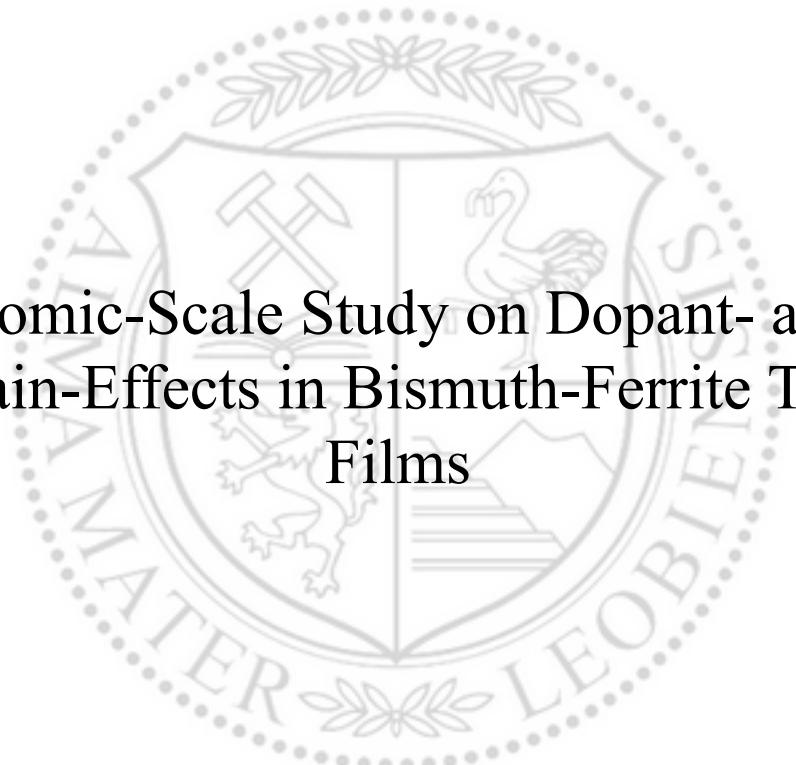




Chair of Materials Physics

Doctoral Thesis



Atomic-Scale Study on Dopant- and
Strain-Effects in Bismuth-Ferrite Thin
Films

Dipl.-Ing. Ulrich Haselmann, BSc

February 2022



AFFIDAVIT

I declare on oath that I wrote this thesis independently, did not use other than the specified sources and aids, and did not otherwise use any unauthorized aids.

I declare that I have read, understood, and complied with the guidelines of the senate of the Montanuniversität Leoben for "Good Scientific Practice".

Furthermore, I declare that the electronic and printed version of the submitted thesis are identical, both, formally and with regard to content.

Date 09.02.2022

DI Ulrich Haselmann

Signature Author
Ulrich Haselmann

“Claims that cannot be tested, assertions immune to disproof are veridically worthless, whatever value they may have in inspiring us or in exciting our sense of wonder.”

Carl Sagan; *The Demon-Haunted World: Science as a Candle in the Dark*; 1995

“In our search for new ideas, beauty plays many roles. It’s a guide, a reward, a motivation. It is also a systematic bias.”

Sabine Hossenfelder; *Lost in Math: How Beauty Leads Physics Astray*; 2018

By the grace of the late birth and the birthplace, I have not been drafted into a war like many others, which only gave me the chance to develop my potential in this form. Dedicated to all those, who haven’t had this chance and the lost potentials.

The provisional title for this thesis was:

Advanced Electron Microscopy of Oxide Heterostructure Interfaces

This work was financially supported by the Austrian Science Fund (FWF): no. P29148–N36.

This thesis is published under the [Creative Commons Attribution 4.0 International \(CC-BY\) License](https://creativecommons.org/licenses/by/4.0/) unless content is copyrighted by another entity.

© 2022; Ulrich Haselmann

Erich Schmid Institute of Materials Science of the Austrian Academy of Sciences, Jahnstraße 12,
8700 Leoben, Austria

Montanuniversität Leoben, Franz Josef-Straße 18, 8700 Leoben, Austria

Acknowledgments

In our days, science is more than ever before a collaborative process. In this place, I want to thank the scientific collaborators and colleagues but also family and friends who, in one way or the other, had a part in the emergence of this work. These acknowledgments are not necessarily complete since I might, by accident, have forgotten someone.

Firstly, I want to express my big gratitude toward my supervisor **PD. Dr. Zaoli Zhang** who always supported and advised me, encouraged me to pursue my ideas, and from whom I learned a lot about science. I also want to thank my mentor **Prof. Christian Mitterer** for his kind support, advice, and helpfulness. I want to express my sincere gratitude to the postdocs who accompanied me each for a part of my journey, **Dr. Arsham Ghasemi** and **Dr. Yurii P. Ivanov** for offering me the possibility to learn from them, lots of discussions and support, their friendship, and the latter also for help with FIB sample preparation. Furthermore, I want to thank all other members or former members of my group for discussions and help, especially **Dr. Zhuo Chen** and **Sergej Raznjevic, MSc.**, of whom the latter lately shared the office with me and is an excellent colleague and friend.

I would like to thank all the people at ESI for the inspiring and helpful environment. Immense thanks go to my dear colleague and friend **Dr. Jakub Zálešák** for doing measurements with me, encouragement and always offering help when needed, and to **Dr. Julian Rosalie** for lots of support with the instruments and countless scientific discussions. Furthermore, I want to thank my office mate during all this time as a PhD candidate, **Dr. Baran Sarac**, for lots of good advice, always having an open ear, a great time in the office with a good dash of humor and his friendship. I also enjoyed lots of good discussions with my dear colleague and friend **Dr. David Gruber** and express my hope to be able to declare a winner on the bet on the origin of dark matter during our lifetime. In particular, I also want to thank **Prof. Jozef Keckes, Dr. Stefan Wurster, Dr. Sophie Cazottes, Dr. Anton Hohenwarter, DI Karoline Freitag, Dr. Karoline Kormout, Silke Kaufmann, Peter Kutleša, Dr. Christoph Gammer, DI Stefan Zeiler, Daniela Brunner, Gabriele Felber, Dr. Oliver Renk, Dr. Juraj Todt, Dr. Michael Reisinger, Prof. Daniel Kiener, Alan Oso, and Prof. Jürgen Eckert.**

I also want to express my greatest gratitude to all my cooperation partners from other institutions, especially **DI Thomas Radlinger, Dr. Georg Haberfehlner, Prof. Gerald Kothleitner, and Prof. Ferdinand Hofer**, for performing analytical probe-corrected STEM and DPC measurements at the Felmi-ZFE (Graz, Austria) with me, without which a lot of the results presented in this thesis

would not have been possible. My sincere gratitude goes to **Dr. Daniel Knez** for providing me his program and code for data analysis and my own Matlab Script to build upon as well as discussions about the interpretation. I want to declare my sincere gratitude to **Dr. Y. Eren Suyolcu** and **Prof. Peter A. van Aken** from the Max-Planck Institute for Solid State Research in Stuttgart (Germany) for also doing analytical probe-corrected STEM measurements with me and their input on the manuscript. I am hugely grateful to **Dr. Maxim Popov** from Materials Center Leoben and **Prof. Lorenz Romaner** from Montanuniversität Leoben for performing the DFT calculations along with feedback and input for the manuscripts. My acknowledgement also goes to our cooperation partners, who fabricated the thin films: **Weijie Pei**, **Dr. Jian Chen**, and **Prof. Yunbin He** from the Hubei University in Wuhan (China), and **Dr. Ping-Chun Wu** and **Prof. Ying-Hao Chu** from the National Chiao Tung University in Hsinchu (Taiwan). I also want to thank **Ass. Prof. Markus Kubicek**, **DI Matthäus Siebenhofer**, **Dr. Martin Rausch**, **DI Tobias Spitaler**, and **Dr. Markus Katzer** for their advice and tips.

I want to thank all of my former colleagues from University of Technology Graz as well as personal friends. Specifically, I want to mention **Dr. Andreas Kautsch**, **Dr. Gernot Krabberger**, **Dr. Manuel Zingl**, **H. Birtan Kalelioglu, BSc.**, **Peter Lackner**, **Dr. Charlotte Reiff**, **Pavel Sonin**, and **Dr. Christian Vetta**.

Last but not least, I would like to thank my family, especially my parents, **Dr. Ulrich Haselmann** and **Isabella Haselmann**, for enabling and encouraging my education and always supporting me, also financially, during BSc. and MSc. degrees. Also, I want to thank my brothers **Dr. Matthias Haselmann** and **Dr. Gernot Haselmann**, as well as **Sabrina Obersteiner, MSc.**, **Vivica Ramdawon, M.A.**, and my nephews **Emil** and **Nikolas** for their company, the good times together and support.

Abstract

BiFeO_3 is one of the most promising functional materials on perovskite basis. It is well known for its multiferroic properties, which it even maintains at temperatures far above room temperature, in the form of coupling between its ferroelectric polarization and antiferromagnetic ordering. With the successful demonstration of a direct switching of the antiferromagnetic domains via an electric field, research interest in BiFeO_3 has enormously increased in the past years because it offers intriguing application prospects. Besides the magnetoelectric properties, BiFeO_3 is also piezoelectric, shows a photovoltaic effect, and is highly birefringent. Additionally, it does not use a toxic and environmentally problematic component like Pb-based perovskites.

Possible applications include smaller, faster, and more energy-efficient digital storage since changing magnetic orientation via the application of an electric field and the magnetoelectric coupling needs much less energy than to have electric current create a magnetic field to rewrite magnetic domains. With an increasing demand for digital data storage, this could be valuable to reduce environmental impact by reduced energy consumption. Other interesting applications include spin valves, spintronic devices, sensors, and optoelectronic devices.

Doping and strain engineering of BiFeO_3 can be used to tune and change the material properties for applications. For example, the antiferromagnetic behavior can be changed to a ferromagnetic one. To understand effects in the material at an atomic scale, advanced transmission electron microscopy is one of the best methods since it delivers not just structural but also elemental and chemical information. This is combined in this work with density functional theory calculations, which showed substantial synergy effects. Scanning electron microscopy, X-Ray diffraction, X-ray photoelectron spectroscopy, and atomic force microscopy were used for additional characterization of the BiFeO_3 thin films.

This dissertation focuses on thin films with Ca as a dopant or co-dopant. Specifically, it contains 3 studies focused on different aspects:

- A new finding of segregation of Ca dopant toward the in-plane compressively strained interface between the Ca and Mn co-doped bismuth ferrite film and a strontium titanate substrate. The Ca segregation triggers atomic and electronic structure changes at the interface. The strain at the interface is reduced according to the Ca concentration gradient. Variations in the interplanar spacing and oxygen vacancies are introduced. The observed segregation behavior is confirmed with density functional theory calculations.

- A study on the interaction of oxygen vacancies and ferroelectric domain walls on the case of a Ca doped BiFeO₃ film. The results revealed that the oxygen vacancies agglomerate in plates which simultaneously represent negatively charged domain walls in a tail-to-tail configuration. The plates appear without any periodicity between each other in out-of-plane as well as in-plane direction. Within the plates, the oxygen vacancies form 1D channels in pseudocubic [010] direction with one site containing lots of vacancies and the adjacent ones on both sites few. Interestingly, no variety between the characteristics of out-of-plane and in-plane plates could be found. Charged defects such as oxygen vacancies are known for their application-decisive pinning effect on domain walls, which on the one hand leads to fatigue mechanisms but on the other hand also counteracts retention failure. Charged defects also strongly influence domain wall conductivity.
- The discovery of a significantly higher Ca solubility in BiFeO₃ than in the secondary Bi₂O₃ phase. The solubility behavior is confirmed and expanded on with density functional theory calculations. Bi₂O₃ can be used to evoke the super-tetragonal phase in BiFeO₃, which has very interesting material properties, without the need of a substrate that imposes very strong compressive strain. Using this effect for the fabrication of functional devices, the different Ca solubility is critical since it could increase the dopant level in the BiFeO₃ matrix.

Kurzfassung

BiFeO_3 ist einer der vielseitigsten Funktionswerkstoffe auf Perovskitbasis. Es ist bekannt für seine multiferroischen Eigenschaften, die es auch bei Temperaturen weit über der Raumtemperatur beibehält, in Form einer Kopplung zwischen ferroelektrischer Polarisation und der antiferromagnetischen Ordnung. Mit der erfolgreichen Demonstration von einem direkten Umschalten der ferroelektrischen Domänen mittels eines elektrischen Feldes hat sich das Forschungsinteresse in BiFeO_3 stark verstärkt in den letzten Jahren, da es faszinierende Anwendungsmöglichkeiten bietet. Neben den magnetoelektrischen Eigenschaften ist BiFeO_3 auch piezoelektrisch, zeigt einen photovoltaischen Effekt und ist stark doppelbrechend. Außerdem werden keine giftigen und umweltproblematischen Komponenten wie bei Perovskiten auf Blei-Basis verwendet.

Zu den möglichen Anwendungen gehören kleinere, schnellere und energieeffizientere digitale Speicher, da die Änderung der magnetischen Ausrichtung mittels Anlegens eines elektrischen Feldes und der magnetoelektrischen Koppelung viel weniger Energie benötigt, als wenn elektrischer Strom ein Magnetfeld erzeugt, um magnetische Domänen neu zu beschreiben. Angesichts der steigenden Nachfrage nach digitaler Datenspeicherung könnte dies ein wertvoller Beitrag zur Verringerung der Umweltbelastung durch geringeren Energieverbrauch sein. Weitere interessante Anwendungen sind Spinventile, Sensoren, spintronische- und optoelektronische Geräte

Durch Dotierung und Verformung von BiFeO_3 lassen sich die Materialeigenschaften für Anwendungen abstimmen und verändern. Zum Beispiel kann das antiferromagnetische Verhalten in ein ferromagnetisches umgewandelt werden. Um Effekte im Material auf atomarer Ebene zu verstehen ist fortgeschrittene Transmissionselektronenmikroskopie eine der besten Methoden, da sie nicht nur strukturelle, sondern auch elementare und chemische Informationen liefert. Dies wird in dieser Arbeit mit Dichtefunktionaltheorie-Berechnungen kombiniert, was große Synergieeffekte hervorbringt. Rasterelektronenmikroskopie, Röntgenbeugung, Röntgenphotoelektronen-Spektroskopie und Rasterkraftmikroskopie wurden zur zusätzlichen Charakterisierung der BiFeO_3 -Dünnschichten eingesetzt.

Diese Dissertation konzentriert sich auf Dünnschichten mit Ca als Dotierungs- oder Kodotierungselement, und enthält 3 Studien, die sich auf verschiedene Aspekte konzentrieren:

- Die Entdeckung einer Segregation der Ca-Dotierelemente in Richtung der kompressiv gespannten Grenzfläche zwischen dem Ca- und Mn-kodotiertem Bismuthferritfilm und

einem Strontiumtitanatsubstrat. Die Ca Segregation löst atomare und elektronische Strukturänderungen an der Grenzfläche aus. Die Verformung an der Grenzfläche wird entsprechend dem Ca-Konzentrationsgradienten verringert. Es werden Variationen im interplanaren Abstand sowie Sauerstoffleerstellen erzeugt. Das beobachtete Segregationsverhalten wird durch Dichtefunktionaltheorie-Berechnungen bestätigt.

- Eine Studie über die Wechselwirkung von Sauerstoffleerstellen und ferroelektrischen Domänenwänden am Beispiel eines Ca-dotierten BiFeO_3 -Films. Die Ergebnisse zeigen, dass sich die Sauerstoffleerstellen in plattenartigen Strukturen anhäufen, welche gleichzeitig negativ geladene Domänenwände darstellen, welche eine Startpunkt-zu-Startpunkt Konfiguration aufweisen. Die Distanz der plattenartigen Strukturen zueinander weist keine Periodizität auf und sie erscheinen sowohl in den Orientierungen parallel als auch senkrecht zur Grenzfläche. Innerhalb der plattenartigen Strukturen bilden die Sauerstoffleerstellen eindimensionale Kanäle in pseudokubischer $[010]$ -Richtung, wobei eine Stelle viele Leerstellen enthält und die beiden Nebenstellen auf beiden Seiten nur wenige. Interessanterweise konnten keine Unterschiede in Struktur und Charakteristik zwischen beiden Orientierungen der plattenartigen Strukturen festgestellt werden. Geladene Defekte, wie Sauerstoffleerstellen, sind für ihren anwendungsentscheidenden Verankerungseffekt auf Domänenwände bekannt, der zu Ermüdungsmechanismen führen kann, aber auch zur Verhinderung von Retentionsversagen genutzt werden kann. Sie beeinflussen auch stark die Leitfähigkeit der Domänenwände.
- Die Entdeckung einer deutlich höheren Ca-Löslichkeit in BiFeO_3 als in der sekundären Bi_2O_3 -Phase. Das Löslichkeitsverhalten wird mit Dichtefunktionaltheorie-Berechnungen bestätigt und das Verständnis davon erweitert. Bi_2O_3 kann verwendet werden um die supertetragonale Phase in BiFeO_3 , die interessante modifizierte Materialeigenschaften hat, hervorzurufen, ohne dass ein Substrat benötigt wird, das eine starke kompressive Verformung an der Grenzfläche auslöst. Für die Herstellung von funktionalen Bauteilen, die diesen Effekt nutzen, ist die unterschiedliche Ca-Löslichkeit ein kritischer Aspekt, der berücksichtigt werden muss, da er den Dotierungsgrad in der BiFeO_3 -Matrix erhöhen kann.

Content

1.	Introduction and Aims	1
2.	Background and Motivation	2
2.1	Multiferroics and Magnetoelectric Coupling	2
2.2	BiFeO ₃ - Bismuth Ferrite	4
2.2.1	Crystallographic description and characteristics.	4
2.3	Structure of the Ferroelectric Domains in BiFeO ₃	7
2.4	Strain effects of BiFeO ₃ in Epitaxy	8
2.5	Doping of BiFeO ₃	12
2.5.1	Substitutional Doping	14
2.5.2	Vacancy Doping	17
2.6	Device Applications of BiFeO ₃	17
2.6.1	Device Applications based on Electronics	17
2.6.2	Device Applications based on Spintronics	20
2.6.3	Device Applications based on Optical Properties	21
3.	Methodology	23
3.1	Thin-Film Fabrication	23
3.2	Transmission Electron Microscopy (TEM)	25
4.	Summary and Discussion of Publication Results	28
4.1	Ca Segregation toward an Epitaxial Heterostructure Interface ⁵⁶	28
4.2	V _o agglomerations at negatively charged domain walls ⁷⁰	30
4.3	Ca solubility in BFO compared to secondary BO phase ¹¹³	31
5.	Conclusion	33
6.	Bibliography	34
7.	PUBLICATIONS	43
	Publication A	44
	Publication A – Supporting Information	68
	Publication B	75
	Publication B – Supporting Information	99
	Publication C	107
	Publication C – Supporting Information	124
8.	Appendix	128

List of Figures

Figure 1. The possible four ordering parameters of multiferroics and the magnetoelectric interactions.....	2
Figure 2. The magnetoelectric family tree.....	3
Figure 3. Crystallographic description of bulk BiFeO ₃ . and antiferromagnetism.....	5
Figure 4. Relation of electric polarization and magnetization in BiFeO ₃	6
Figure 5. Schematic illustrations of the uncharged domain-walls (UCDWs) in rhombohedral BFO	8
Figure 6. Strain effects in BFO films	9
Figure 7. Schematic illustration of the effect of substrate miscut on BFO domain structure.....	10
Figure 8. Magnetic phase diagram of strained BFO films	12
Figure 9. Site preferences of substitutional doping in BFO, oxidation states, and energy level comparison.....	13
Figure 10. Phase diagram of Ca-doped Bi _{1-x} Ca _x FeO _{3-δ} films grown on (001) STO substrate	16
Figure 11. Electronic device applications of BFO	18
Figure 12. Proof of concept for device application using DW conductivity	20
Figure 13. Spin valves with BFO	21
Figure 14. Prototype of 16-bit ferroelectric photovoltaic memory device.. ..	22
Figure 15. Schematic illustration of a pulsed laser deposition (PLD) apparatus and conceptual diagram of phase-stability regions.....	24
Figure 16. Schematic illustrations of a TEM and spherical and chromatic aberration in electromagnetic lenses	26
Figure 17. Ca segregation toward a BCFMO-STO interface	29
Figure 18. V _O agglomerations at negatively CDWs.....	31
Figure 19. Ca solubility in BFO compared to secondary BO phase.....	32

List of Abbreviations

ABF	Annular bright field	HRTEM	high-resolution transmission electron microscopy
ADF	Annular dark field	H-T	head-to-tail (DWs)
AFM	atomic force microscope/microscopy	LAO	LaAlO ₃
BCFCO	(BiCa)(FeCo)O ₃	LSAT	(LaAlO ₃) _{0.3} -(SrAlTaO ₆) _{0.7}
BCFMO	(BiCa)(FeMn)O ₃	MBE	molecular beam epitaxy
BCFO	(BiCa)FeO ₃	NSO	NdScO ₃
BFMO	Bi(FeMn)O ₃	pc	pseudocubic
BFO	BiFeO ₃	PFM	piezoresponse force microscopy
BO	Bi ₂ O ₃	PSO	PrScO ₃
C	cubic	PVD	physical vapor deposition
CBE	conduction band energy	R	rhombohedral
CCMO	(CaCe)MnO ₃	R-BFO	BFO monoclinic phase of space group Cc
CDW	charged domain-wall	SRO	SrRuO ₃
CMO	CaMnO ₃	SSO	SmScO ₃
CVD	chemical vapor deposition	STEM	scanning transmission electron microscopy
DFT	density functional theory	STO	SrTiO ₃
DPC	differential phase contrast	T-BFO	super-tetragonal BFO
DSO	DyScO ₃	T _C	Curie temperature
DW	domain wall	TEM	transmission electron microscopy
EDS	energy-dispersive X-ray spectroscopy	T _N	Néel temperature
EELS	electron energy loss spectroscopy	T-T	tail-to-tail (DWs)
FeFET	ferroelectric field-effect transistor	u.c.	unit cell
FO	Fe ₂ O ₃	UCDW	uncharged domain-wall
FTJ	ferroelectric tunnel junction	VBE	valence band energy
GMR	giant magnetoresistance effect	V _{Bi}	Bismuth vacancy
GPA	geometric phase analysis	V _{Fe}	Iron vacancy
GSO	GdScO ₃	V _O	Oxygen vacancy
HAADF	high-angular annular dark field	w	domain width
hex	hexagonal	Z	atomic number
H-H	head-to-head (DWs)		

1. Introduction and Aims

BiFeO₃ is one of the few single-phase multiferroic materials with direct coupling between order parameters of electric polarization and magnetization, which is even maintained at temperatures high above room temperature. In 2006, the demonstration of successfully controlling the antiferromagnetic domains with an electric field sparked a wave of increased interest in this unique material.¹

The multiferroic properties of BiFeO₃ offer a wide range of very interesting possible applications. A constantly increasing total worldwide consumption of electric energy has been the trend in the last years. A factor for this is the increasing usage of electronic devices. Devices with lower energy consumption for the same or superior tasks are a necessity and would technologically counteract the electric energy consumption trend. The possibility to change magnetic domains directly with an electric field is significantly more power efficient than creating a magnetic field by the flow of an electric current. Therefore, digital storage devices using electric fields and magnetoelectric coupling instead of magnetic fields to write bits would lead to much more power efficient but also smaller and faster data storage technologies. Further applications include spin valves, spintronic devices, optoelectronic applications, and sensors.²⁻⁴

Functional doping of BFO is, besides strain engineering, a way to tune and design properties of the material for applications. Theoretical *ab-initio* calculations can help to highlight and prioritize promising design paths. However, for an exact understanding and analyzation of dopant or strain effects on an atomic level, advanced transmission electron microscopy (TEM) techniques are necessary and a critical experimental method.^{2,5}

The aim of this thesis is to use a range of methods centered around the said TEM techniques to study the aspects and effects of functional doping on BFO and its interlinkage with strain effects. To achieve this, BFO based thin films with the intended functional doping were fabricated and subsequently investigated.

The results highlight the necessity of TEM studies by presenting a previously unknown effect of Ca dopant segregation toward a compressively strained epitaxial interface, by revealing the linkage between agglomerated oxygen vacancies (V_O) and charged domain walls (CDWs) in films with relatively low Ca-doping ratio, and by showing the novel solubility behavior of a Ca dopant in BiFeO₃ compared to a functional secondary phase. All these results have direct relevance for device applications. On a more general scope, this thesis highlights the potential of combining TEM methods with *ab initio* calculations.

2. Background and Motivation

2.1 Multiferroics and Magnetoelectric Coupling

Initially, the term multiferroics referred to materials, which exhibit more than one of the four primary ferroic orderings, which are ferromagnetism, ferroelectricity, ferroelasticity and ferrotoroidicity.⁶ Nowadays, this definition is not strictly maintained but has been expanded to include non-primary orderings like antiferromagnetism.⁷ Figure 1a,b,c,d shows schematic illustrations of these possible four ordering parameters of multiferroic materials, of which at least two must be present.

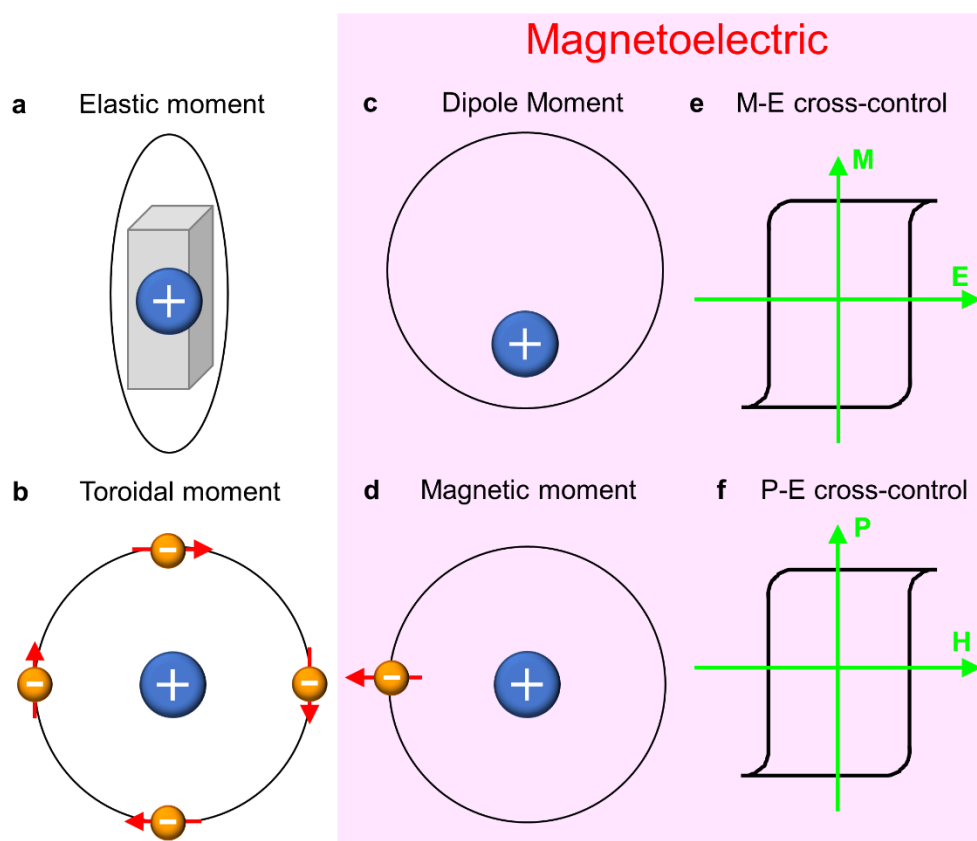


Figure 1. The possible four ordering parameters of multiferroics and the magnetoelectric interactions: (a) elastic moment, (b) toroidal moment, (c) dipole moment, and (d) magnetic moment. The pink back-ground indicates the parameter combination of magnetoelectrics between the (c) electric and (d) magnetic ordering parameters. If they are coupled, (e) an applied electric-field (\mathbf{E}) influences the magnetic moment (magnetization, \mathbf{M}) or (f) and an applied magnetic-field (\mathbf{H}) influences the dipole moment (polarization, \mathbf{P}).⁸ Idea adapted from ref.⁸.

If magnetic and electric order parameters are present, the material is called magnetoelectric (indicated by the pink background in Figure 1) but is today frequently just labeled multiferroic. In multiferroics, the order parameters can be coupled so that one ferroic property can be influenced by the other.^{7,9–11} An especially exciting variant is magnetoelectric coupling.^{7,12,13} Thereby, the magnetization can be switched by an electric field, as is displayed in Figure 1e. Also, the opposite variant of switching the polarization by a magnetic field is possible (see Figure 1f).⁸

Spaldin and Ramesh distinguish two conventional mechanisms for ferroelectricity, which are the two left ‘roots’ of the magnetoelectric family tree (see Figure 2):⁷

- Transition metals with empty d orbitals (d^0), e.g., Ti^{4+} in BaTiO_3
- Lone pair stereochemical activity, e.g., Bi^{3+} in BiFeO_3 , Pb^{2+} in PbTiO_3 , or Ge^{2+} in GeTe

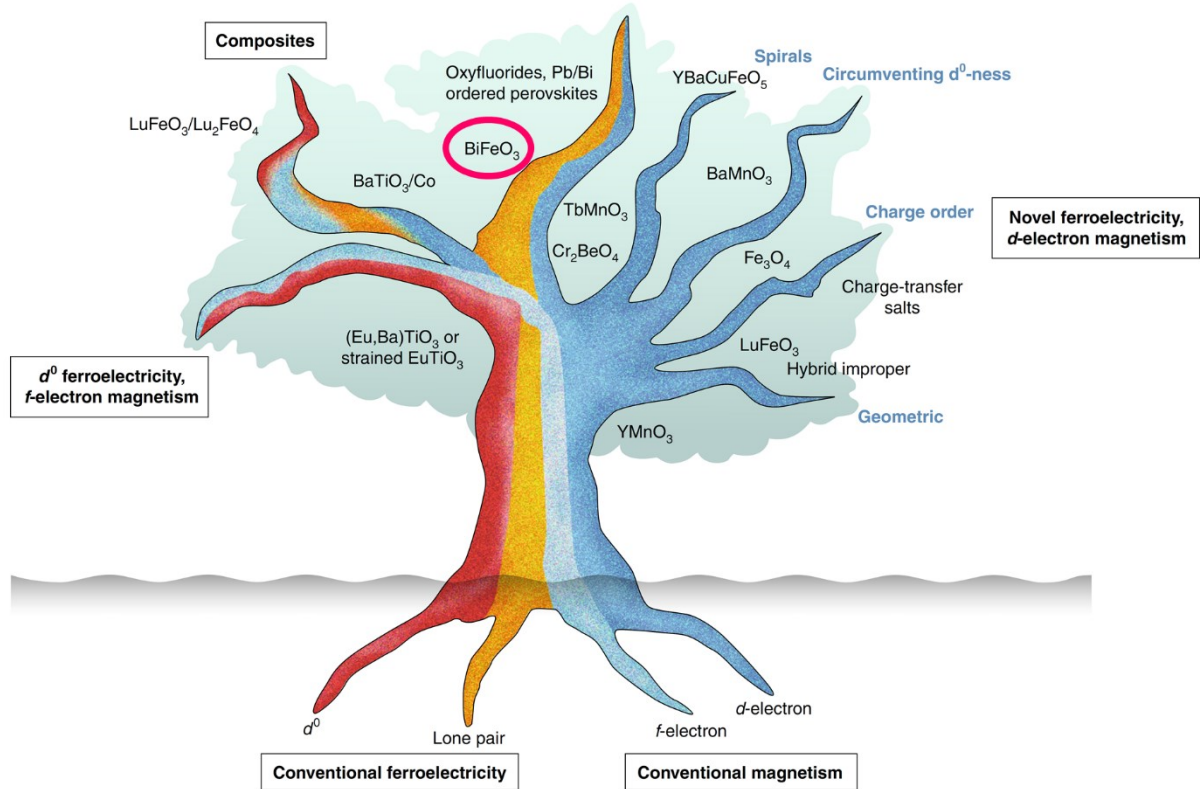


Figure 2. The magnetoelectric family tree. Magnetoelectricity can arise from four different ‘root’ sources. The different possible combinations of these ‘root’ sources resulting in magnetoelectric materials are visualized in the branches of the tree. The branches also suggest less explored options that might be fruitful in the future. BiFeO_3 , which is the focus of this thesis, is marked by a magenta oval.⁷ Adapted with permission from ref.⁷, Springer Nature Limited, Copyright 2019

They also mention two established routes to magnetism, which are the two ‘roots’ on the right side of the tree (see Figure 2):⁷

- Partially filled localized *f*-electron states on rare-earth ions, e.g., Eu²⁺ in (Eu, Ba)TiO₃ or in strained EuTiO₃
- Partially occupied *d* levels in transition metals, e.g., Fe³⁺ in BiFeO₃ or in PbFeO₃

To conclude, in BiFeO₃, the magnetoelectricity arises from the lone pair stereochemical activity of the Bi³⁺ ions and the partially occupied *d* levels in the Fe³⁺ ions.⁷

2.2 BiFeO₃ - Bismuth Ferrite

BiFeO₃ (BFO) has a magnetoelectric coupling between its ferroelectricity and antiferromagnetism. The magnetoelectric coupling is maintained until the Néel temperature of $T_N \approx 370^\circ\text{C}$, at which the antiferromagnetic behavior becomes paramagnetic. The Curie Temperature is even higher with $T_C \approx 830^\circ\text{C}$, at which the ferroelectricity turns to paraelectricity. That means that for device applications, making use of the magnetoelectric coupling, the functionality is maintained far above room temperature up to the Néel temperature of 370°C , which is rare among single-phase magnetoelectric materials.^{1,14}

2.2.1 Crystallographic description and characteristics.

The exact crystallographic description of BFO is a little complicated but is often simplified to a pseudocubic (pc) perovskite-type unit cell with a rhombohedral distortion. The pseudocubic unit cell, which is indicated by the thin dashed lines in Figure 3a, contains one chemical formula unit of BFO ($1 \times \text{BiFeO}_3$). The $8 \times 1/8$ Bi atoms are sitting on the corners of the cube (violet spheres in Figure 3a, A-sites), and one Fe atom (orange spheres in Figure 3a, B-site) sits near the center of the cube but is shifted along the $\langle 111 \rangle_{pc}$ direction due to the ferroelectric properties. $6 \times 1/2$ O atoms (red spheres in Figure 3a) are sitting on the 6 cube faces forming an oxygen octahedron (orange-colored faces). The pseudocubic perovskite-type lattice parameter is $a_{pc} = 3.965 \text{ \AA}$, and the angle is not rectangular but slightly distorted to $\alpha_{pc} = 89.3 - 89.4^\circ$.¹⁴⁻¹⁶

The oxygen octahedron is tilted so that the O atoms on the cube faces are off-centric. In the adjacent perovskite cube in $[111]_{pc}$ direction, the octahedron is tilted inversely. This different tilt is only taken into account by enlarging the pseudocubic unit cell to the rhombohedral one (thick black lines in Figure 3a). The unit vectors of the rhombohedral unit cell are the red, green and blue arrows in Figure 3a and have the following directional relations $[110]_{pc} // [100]_R$, $[101]_{pc} // [010]_R$,

$[011]_{pc} // [001]_R$, and $[111]_{pc} // [111]_R$.^{15,17} It has the R3c space group (SG. 161) with lattice parameters of $a_R = 5.6343 \text{ \AA}$ and $\alpha_R = 59.348^\circ$. The rhombohedral unit cell (violet Bi spheres and thick black lines in Figure 3b) can be alternatively written in a hexagonal notation (other Bi spheres in grey color and thin lines), which is sometimes also used in literature. The directional relations are $[001]_{hex} // [111]_{pc} // [111]_R$ and the hexagonal unit cell has lattice parameters of $a_{hex} = 5.5787 \text{ \AA}$ and $c_{hex} = 13.8688 \text{ \AA}$.^{15,17,18}

BFO has a G-type antiferromagnetic short-range ordering. That means that each spin in one direction (sitting on the Fe³⁺ ion) is surrounded by six antiparallel spins on the next nearest Fe neighbors. A schematic depiction can be found in Figure 3c, which shows the pseudocubic distribution of the Fe atoms (orange spheres) and the arrangement of parallel and antiparallel spins (green and violet arrows).^{14,19,20}

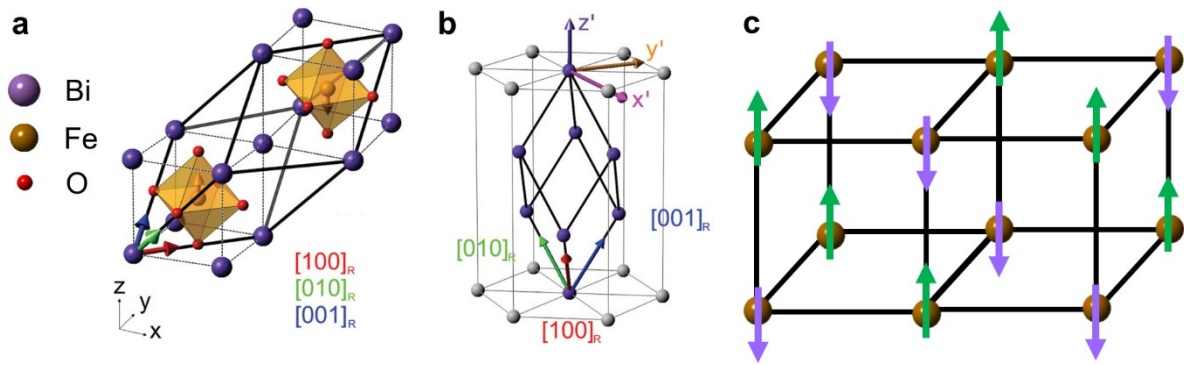


Figure 3. Crystallographic description of bulk BiFeO₃ and antiferromagnetism. (a) Relation between the rhombohedral lattice system (thick black lines) and pseudocubic perovskite structure to which it is often simplified. The orange arrows indicate the spin. x , y , and z are the cartesian axes of the pseudocubic structure, while the red, green, and blue arrows are the unit vectors of the rhombohedral cell.¹⁵ (b) The rhombohedral structure (violet spheres, thick lines) can also be regarded as a trigonal crystal system.¹⁵ (a) and (b) are reproduced under the [Creative Commons Attribution 3.0 License](#) from ref.¹⁵, American Physical Society, Copyright 2013. (c) G-type antiferromagnetic ordering in 3 dimensions, where each next nearest neighbor of a spin has a reverse orientation. Here, the corners of the cubes are the positions of the Fe atoms.²⁰

In a pseudocubic unit cell of BFO, the possible polarization orientations are always oriented in $\langle 111 \rangle_{pc}$ direction as depicted in Figure 4a, e.g. for $[111]_{pc}$ (turquoise arrow) and $[1-11]_{pc}$ (dark blue arrow). Even though the magnetic spin ordering is G-type antiferromagnetic, the spins are not perfectly antiparallel but there is a slight canting, that originates from the magnetoelectric coupling to the polarization (see next paragraph) and leaves a net magnetic moment per spin-pair. This is schematically displayed by the green, purple, and magenta (net magnetic moment) arrows in Figure 4b. However, superimposed on this local spin-structure is a superstructure of a spin cycloid.

The spin orientation does a full rotation in the plane spanned by the polarization vector $\langle 111 \rangle_{pc}$ and by the cycloid propagation vector in the $\langle 10 - 1 \rangle_{pc}$. The wavelength of this rotation is 62-64 nm. This spin rotation also cancels out the net magnetic moment. However, the spin cycloid can be demolished by doping or by epitaxial strain in thin films, which then gives rise to a remnant magnetization.^{14,19-24}

If the electric polarization is changed, for example, by an external electric field, due to the magnetoelectric coupling, the easy plane of spin rotation is also changed. An example can be seen in Figure 4a by the two blue planes of spin rotation for either the turquoise $[111]_{pc}$ polarization or the dark blue $[1-11]_{pc}$ polarization. The magnetic easy plane can only be switched if the polarization changes direction – 180° switching of the polarity does not affect the magnetic orientation.^{14,16,23,24} Experimentally, this switching behavior was first demonstrated in 2006 by Zhao *et al.*¹ The BFO thin film, which they used, had no spin rotation and the magnetic easy plane was perpendicular to the ferroelectric polarization. Due to the fact that the experiment needed piezoelectric force microscopy and X-ray photoelectron microscopy for manipulation and characterization of the ordering parameters, further modifications are necessary to reach applicability.¹

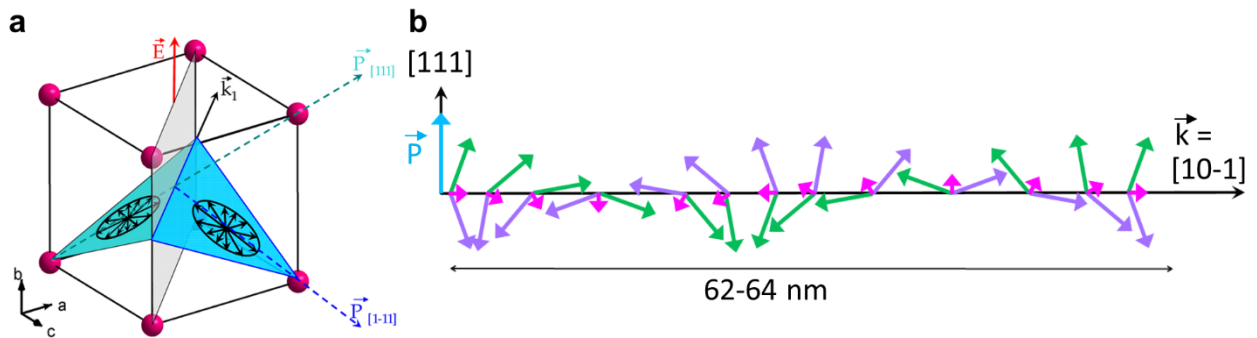


Figure 4. Relation of electric polarization and magnetization in BiFeO₃. (a) Schematic illustration of the orientation of two vectors of ferroelectric polarization (\vec{P}) separated by a domain wall (DW, in light grey) in the pseudocubic unit cell. Here it would be a 71° uncharged domain-wall (UCDW). The magnetic easy planes (planes of magnetic spin rotation) are located in the blue planes linked to the ferroelectric polarization orientation. By applying an electric field (\vec{E}), the polarization can be switched, changing also the magnetic easy plane and the spins.¹⁶ Reprinted with permission of ref.¹⁶, American Physical Society, Copyright 2008. (b) Schematic depiction of the spin cycloid. The antiferromagnetic spins are canted (green and purple). Therefore, they don't cancel out but result in a net magnetic moment (magenta arrow), which in turn is averaged out in space because of the cycloidal rotation. The spins rotate within the plane spanned by the cycloidal propagation vector (\vec{k} , black) and the polarization (\vec{P} , turquoise).^{14,25,26}

Besides being piezoelectric, BFO also has interesting optical properties. It has a moderate band gap at room temperature between 2.6-3.0 eV, which lies in the visible range. The bulk photovoltaic effect gives rise to photovoltages much larger than the band gap, but the photocurrents are unluckily too low for light-harvesting applications.² However, BFO is highly birefringent, which means that the refractive index can be changed with the polarization.

2.3 Structure of the Ferroelectric Domains in BiFeO₃

Starting from here, crystallographic directions and planes are by default in the pseudocubic system unless it is indicated otherwise (with subscripts). The 8 possible ferroelectric variants are linked to 4 different ferroelastic deformations. Thereby, antiparallel polarizations result in the same ferroelastic deformation (see (Figure 5a)).²⁷

Places where the orientation of the polarization in the BFO changes are ferroelectric domain-walls (DWs). There are 2 general possibilities for domain walls: Uncharged domain-walls (UCDWs), for which the relative orientation of the polarization vectors to each other is head-to-tail (H-T), and charged domain-walls (CDW), for which the relative orientation is either head-to-head (H-H) or tail-to-tail (T-T). These 3 options respectively introduce either zero, net positive, or net negative bound charges at the DWs. Since all the polarization vectors are oriented in the $\langle 111 \rangle$ directions (see Figure 5a), there are geometrically only 3 possible angles between the ferroelectric polarization vectors: 71°, 109°, and 180°. ²⁷⁻²⁹

Due to the minimization of elastic and electrostatic energy, not every possible combination of relative polarization and domain wall orientation appears in rhombohedral BFO. For UCDWs, there are only 3 types: ²⁷⁻²⁹

- 109° UCDW with the DW-plane orientation in $\{100\}$ (Figure 5b, e)
- 71° UCDW with the DW-plane orientation in $\{110\}$ (Figure 5c, e)
- 180° UCDW with the DW-plane orientation in $\{110\}$ (Figure 5d, e)

According to Wang et al. there are 4 types of CDW in rhombohedral BFO:²⁷

- 109° CDW with the DW-plane orientation in $\{100\}$
- 109° CDW with the DW-plane orientation in $\{110\}$
- 180° CDW with the DW-plane orientation in $\{100\}$
- 71° CDW with the DW-plane orientation in $\{100\}$

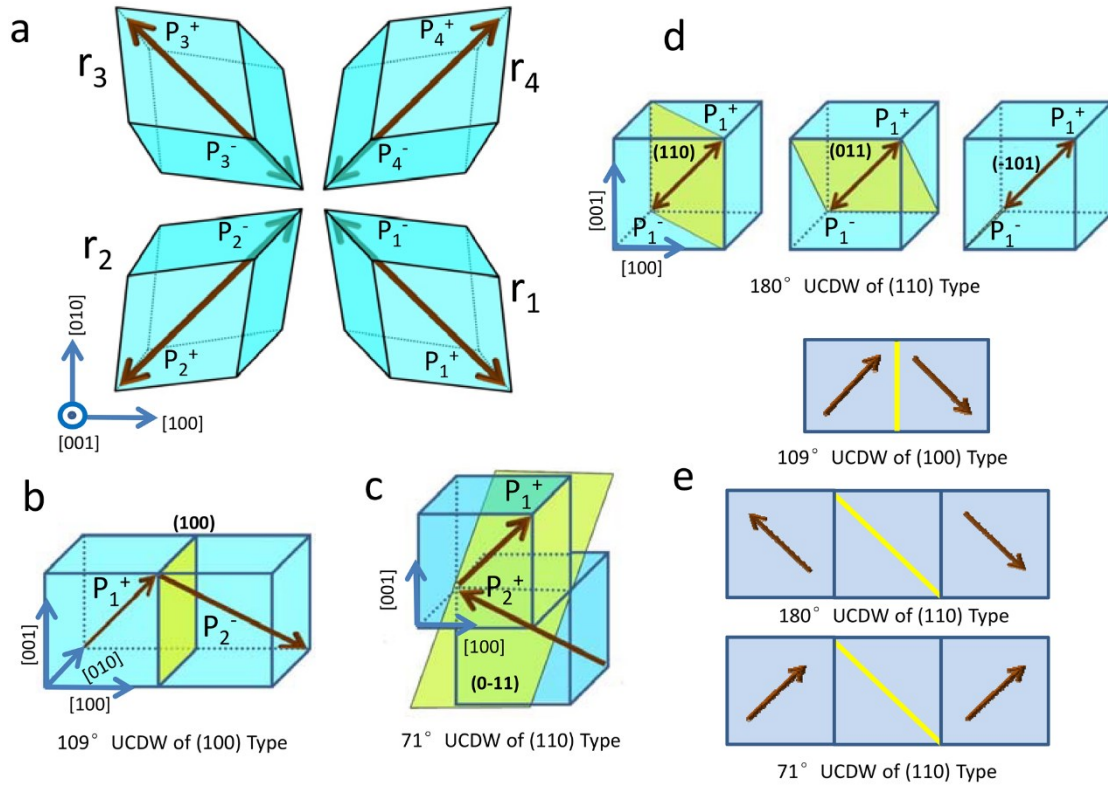


Figure 5. Schematic illustrations of the uncharged domain-walls (UCDWs) in rhombohedral BFO. (a) The 4 ferroelastic (r₁ - r₄) and 8 ferroelectric variants in BFO, which are always oriented in <111> directions. (b), (c), (d) The 3 types of possible UCDW variants. The DWs are marked by the bright green planes and the arrows mark the polarization directions in the domains (e) Edge-on projection of these 3 UCDWs. The yellow lines mark the DWs.²⁷⁻²⁹ Reprinted with permission from ref.²⁷, WILEY-VCH Verlag GmbH & Co. KGaA, Copyright 2015

2.4 Strain effects of BiFeO₃ in Epitaxy

Epitaxy means the continuation of a single-crystalline thin layer on top of a thick single crystal (substrate). Thereby, ideally, the in-plane lattice parameters of the film should coincide with those of the substrate.^{30,31} When the film is deposited onto a substrate of another crystal formula (heteroepitaxial growth), the lattice parameters often differ, and the film is forced to grow strained onto the substrate surface. The strain energy accumulates until a critical thickness (30-70 nm when grown along the [001] direction), at which the film begins to release the strain energy through the formation of misfit edge dislocations, elastic domains, twins, and so on.³⁰ Figure 6a shows in the bottom section a collection of commercially available substrates and their lattice parameter compared to BFO marked in the top section with the red overlay. For some applications, electrically conducting electrode materials, which are compatible with the epitaxy and allow the retention of strain, are required. A selection of these materials can be found in the middle section.³²

Strain effects of BiFeO₃ in Epitaxy

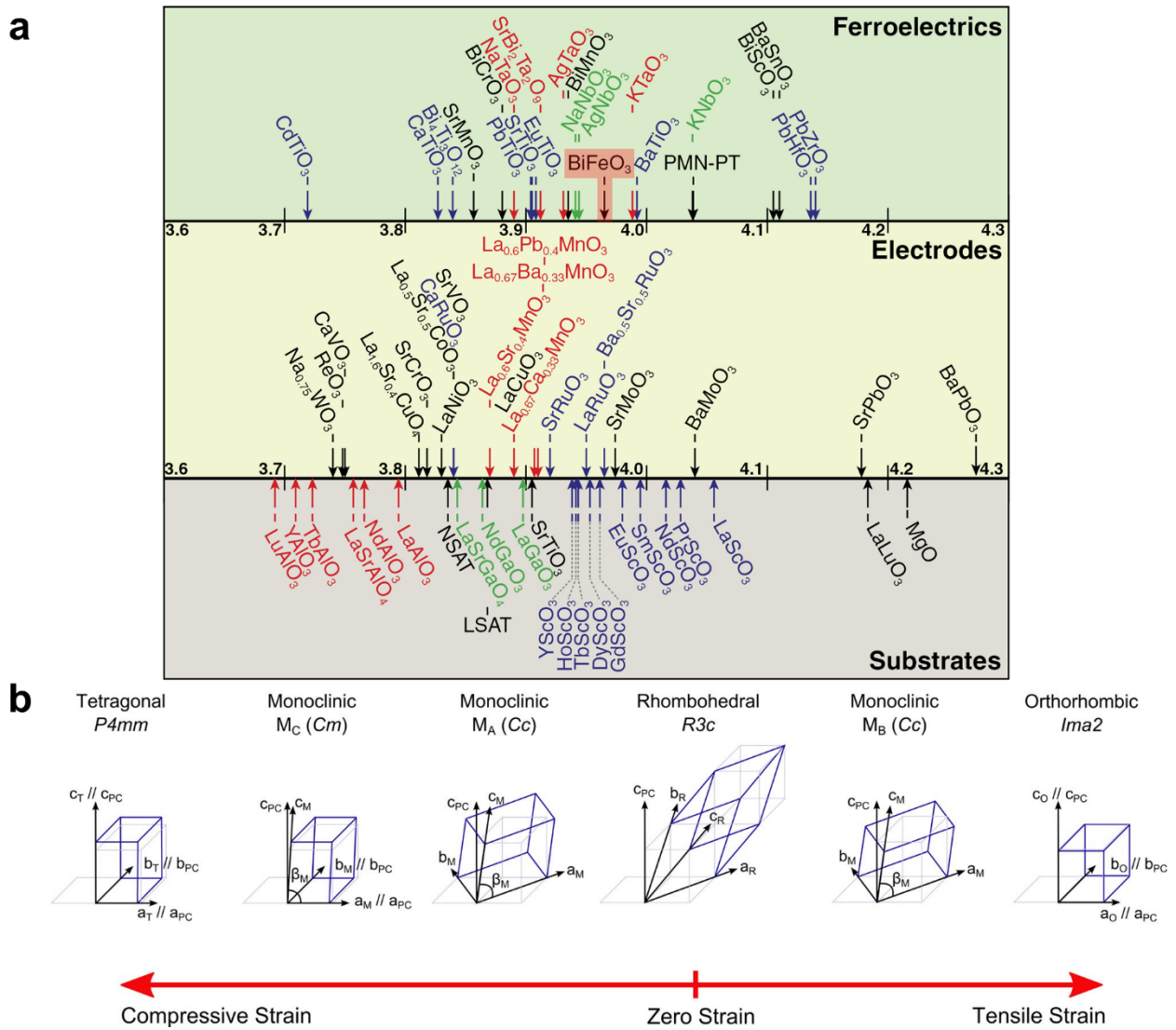


Figure 6. Strain effects in BFO films: (a) relationship of lattice parameters of commercially available substrates (bottom area), electrode materials (middle area), and ferroelectrics with BFO marked (top panel).³² Reprinted with permission from ref.³², IOP Publishing Ltd, Copyright 2016 (b) Crystal structures of BFO depending on the strain state introduced by the substrate. The unit cells (blue lines) are compared with the pseudocubic unit cell (light grey lines).² Reprinted with permission from ref.², IOP Publishing Ltd, Copyright 2014

The critical thickness of BFO is compared to other materials quite large due to the quite large “flexibility” of the BFO structure, where both strong cationic shifts and oxygen octahedra tilts can compensate for the epitaxial stress. The regular bulk rhombohedral symmetry of BFO is distorted by misfit strain and leads, depending on the size and if it is compressive or tensile, to new crystal structures.³⁰ A schematic illustration of them can be found in Figure 6b. Under moderate strain between -3% and +2% on a (001)_C substrate, BFO has a monoclinic phase of space group *Cc*., which is usually called the R-phase.^{30,33,34} When growing toward larger compressive strain, the oxygen octahedra tilts disappear, and the symmetry transforms into a *Cm* one, while keeping the

monoclinic structure.^{30,34,35} The ratio of out-of-plane to in-plane lattice parameters (c/a) changes continuously with the misfit strain.^{30,36,37}

The ratio develops roughly linearly under compressive strain until approximately -4.5%, which is reached for a LaAlO₃ (LAO) substrate, where the c/a ratio jumps to unexpectedly high values around 1.23 (for other perovskite materials, the strained tetragonal phase is usually around 1.06 at room temperature). This is a new phase with a strong tetragonality with $P4mm$ symmetry and is usually referred to in literature as super-tetragonal or T-phase (see Figure 6b). The tetragonal phase shows no lateral component of the ferroelectric polarization in contrast to the monoclinic or rhombohedral phases.^{30,36,38} A high misfit strain is not necessarily a condition to get the T-phase since a buffer layer of β -Bi₂O₃ can be used to stabilize the super-tetragonal phase on a STO substrate (misfit strain of only -1.4%) or other substrates.³⁹

BFO has an untypical behavior of its T_C under strain. While in classical ferroelectrics like BaTiO₃ or PbTiO₃, T_C increases with epitaxial strain, in BFO, it decreases with compressive strain.³⁷ If an (001) STO substrate (with an SrRuO₃ electrode layer) is miscut 4° along [100], instead of the normal film on STO with all 4 ferroelastic variants and all 8 possible polarization directions (see bottom part of Figure 7a), only 2 ferroelastic variants coinciding with 4 polarization directions grow due to the constrains of the steps (see bottom part of Figure 7b). If the 4° miscut is instead done in [110] direction, only 1 ferroelastic variant and 2 polarization directions, which are antiparallel to each other, grow on the substrate (see Figure 7c).^{40,41}

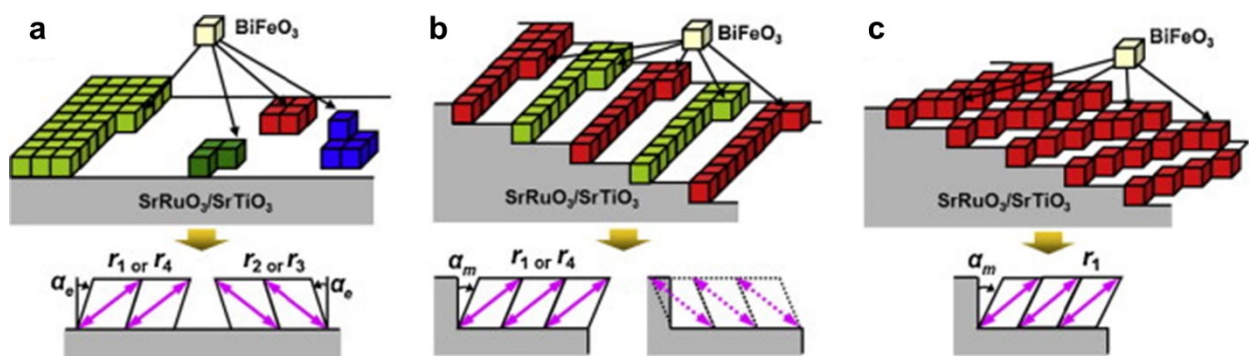


Figure 7. Schematic illustration of the effect of substrate miscut on BFO domain structure. (a) on exact (001) STO single crystal substrate all 4 ferroelastic variants appear. (b) on a 4° miscut along [100] only 2 ferroelastic variants appear. (c) on a 4° miscut along [110] only a single ferroelastic variant grows.^{40,41} Reprinted with permission of ref.⁴⁰, Elsevier Ltd., Copyright 2013

Both the work of Landau and Lifshitz⁴² in 1935 and of Kittel⁴³ in 1946 lead to the realization that in ferromagnetic thin films, the domain size scales as the square root of film thickness, which is known as Kittel's law. Later, it could be shown that this law is also valid for ferroelectric⁴⁴ and multiferroic⁴⁵ materials. The situation can be understood as a competition between the surface energy (demagnetization, depolarization, strain), which is directly proportional to the width of the domain (w), and the DW energy, which is proportional to the number-density of DWs and thus inversely proportional to w . The width of the domains w is also connected to the film thickness d . Simplification leads to the expression $w = C \times \sqrt{d}$, with C being a constant. So thinner films lead to smaller domains.^{14,30}

Concerning the polar properties, the strategy of strain engineering in ferroelectrics is to enhance the out-of-plane polarization value.³⁰ However, in the R-type phase, no matter the growth directions, the polarization direction stays in the [111] direction and differs only minor by around 15% with respect to the 100 $\mu\text{C}/\text{cm}^2$ value for bulk BFO.^{30,46-48} However, for the T-phase (super-tetragonal) polarization, values of approximately 150 $\mu\text{C}/\text{cm}^2$ are reached. In contrast, the piezoelectric properties appear to be much more strain sensitive. In the R-phase, by varying the misfit strain by $\sim 3.5\%$, the piezoelectric coefficient d_{33} increases from ~ 20 pm/V to ~ 50 pm/V, which is an enlargement by 250%.^{30,47} The T-phase itself shows only a slightly improved piezoelectric coefficient, but a mixture of R- and T-phase shows a huge enlargement of 600% to ~ 120 pm/V.^{30,36,49}

Concerning the effect of strain on the magnetism of BFO, between 0 and -1.75% strain, the antiferromagnetic spins arrange in a spin cycloid along [1-10] direction. For strains smaller than -1.75% and larger than $+0.5\%$, a G-type antiferromagnetic phase forms with spin-canting, but without cycloids, and with the spin orientation close to [001]. Because of the spin canting, this G-type antiferromagnetic phase shows a remnant magnetization. Between 0- 0.5% strain, a new type of cycloid with the propagation along the [110] direction forms, which is not perpendicular to the direction of the ferroelectric polarization anymore. However, it still lies in the cycloid plane. For the super-tetragonal phase at low temperature, a C-type antiferromagnetic ordering is adopted instead of the G-type antiferromagnetic ordering. Two studies^{50,51} both foresee a strain-induced enhancement of M-E cross-control or P-H cross-control (see Figure 1e,f).^{22,30,52,53}

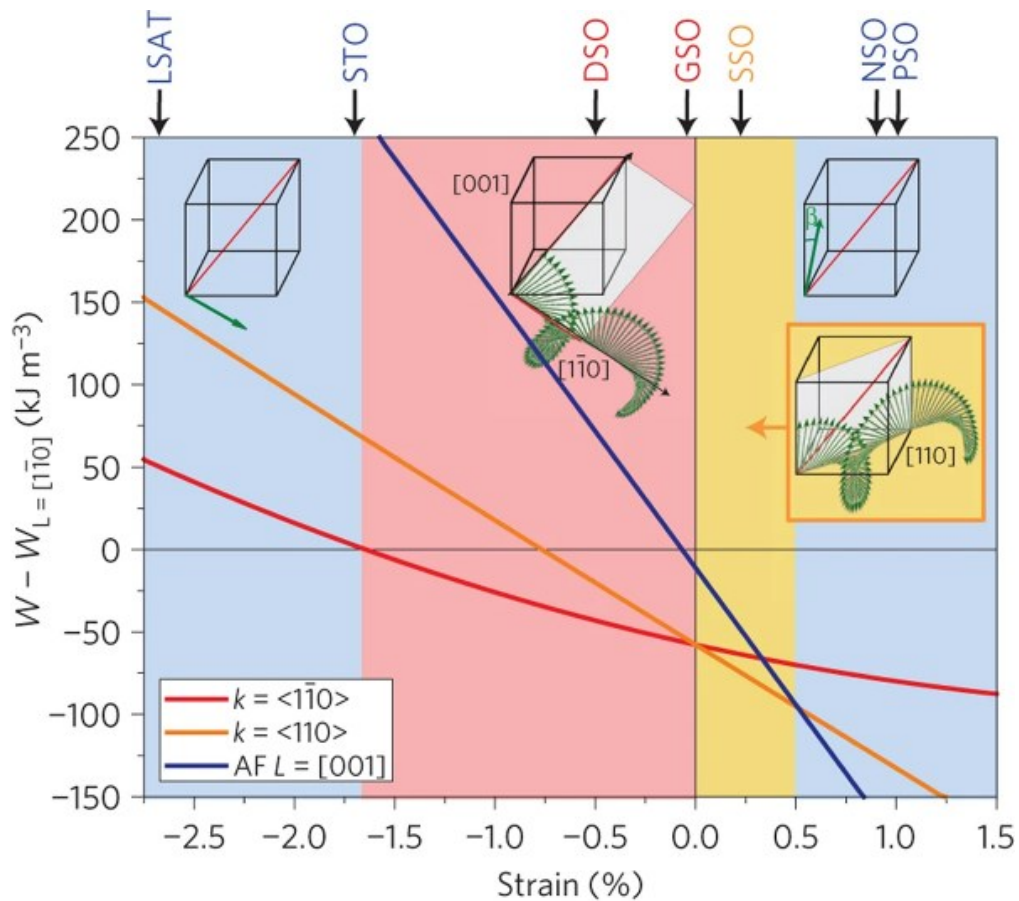


Figure 8. Magnetic phase diagram of strained BFO films. The energy of the bulk-like type 1 cycloid in [1-10] direction is displayed by the red curve, of the type 2 cycloid with the propagation vector along [110] by the yellow curve, and of an antiferromagnetic ordering with the spins oriented close to [001] by the blue curve are displayed relative to an antiferromagnetic ordering with spins along in-plane [1-10]. On the top are substrates labelled for the according strain values like (LaAlO₃)_{0.3}-(SrAlTaO₆)_{0.7} (LSAT), DyScO₃ (DSO), GdScO₃ (GSO), SmScO₃ (SSO), NdScO₃ (NSO), and PrScO₃ (PSO).^{30,52} Reprinted by permission from ref.⁵², Macmillan Publishers Limited, Copyright 2013

2.5 Doping of BiFeO₃

Doping can be used to change, modify, tune, or specifically design certain properties of BFO. This work differentiates between 2 types of doping:

- Substitutional doping
- Vacancy doping.

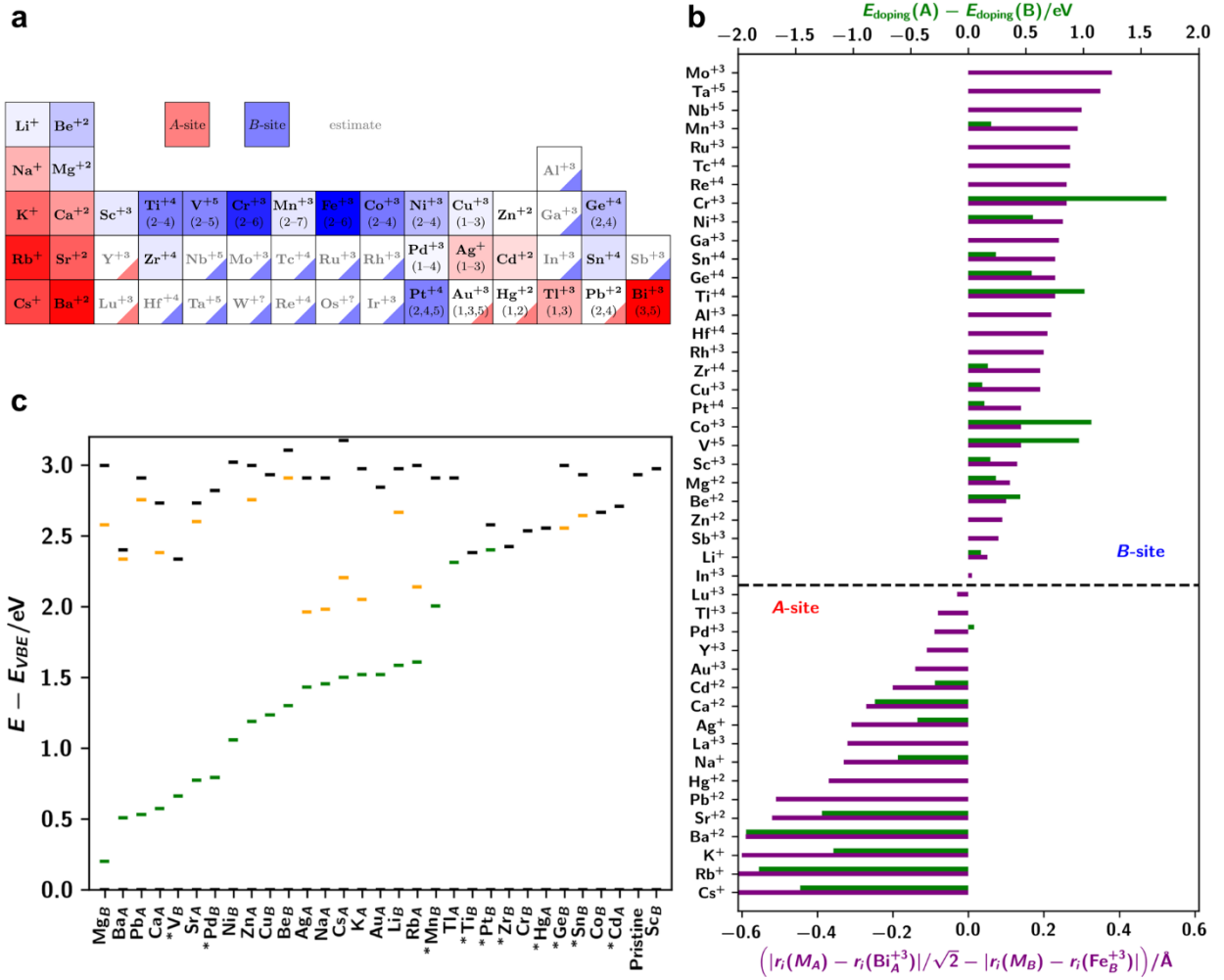


Figure 9. Site preferences of substitutional doping in BFO, oxidation states, and energy level comparison. (a) Preferred doping sites for either the A-site substituting Bi (red) or the B-site substituting Fe (blue) for metallic elements according to the DFT calculations.⁵ The intensity of the color marks the size of the thermodynamic preference toward the indicated site. The effect of the elements in grey letters wasn't calculated, but their effect was estimated. Superscript numbers indicate the observed oxidation state in BFO. If the element is known to appear in various oxidation states, they are given in brackets below the elemental symbol letters. For elements where the site preference coloring is only done in the bottom right corner, it was not calculated but predicted from an examination of the ionic radii and trends within the periodic table.⁵ (b) Site preference according to the ionic radii (purple bars) and DFT energies (green bars). The left side (negative energies) indicates A-site preference, while the right side indicates B-site preference.⁵ (c) Comparison of the energy levels of dopants on their most stable substitution site. Black markers indicate the Fe-dominated CBE, green ones mark the maxima of the first acceptor/donor state and orange bars show the optional shifted iron states, which appear below the CBE in case an Fe oxidation takes place. The energy values are given by the difference between them and the O-dominated VBE. The asterisks indicate n-type doping or only partially filled acceptor bands. In all other cases (elements without asterisks) each green bar (marking the energy of the acceptor band) indicates the energy of the first electronic excitation from

the VBE.⁵ All 3 subfigures are reprinted with permission of ref.⁵, American Physical Society, Copyright 2018.

2.5.1 Substitutional Doping

In the perovskite BFO, a Bi atom sits on the so-called A-site and Fe on the B-site (ABO₃ as generalization for perovskite structures). Usually in BFO substitutional doping, the dopants replace either the Bi or Fe on their respective sites. Which dopant replaces which atom can be to some degree predicted by considering the ionic radii or, if the behavior of other dopant elements is known, by considering trends and relations within the periodic table. However, to non-experimentally receive very reliable predictions, theoretical calculations, specifically density functional theory (DFT) calculations, are necessary. In 2018, Gebhardt and Rappe⁵ theoretically calculated the behavior of a wide range of possible BFO dopants in an extensive work. Figure 9a shows a part of the periodic table (without lanthanoids and actinoids) with the indication of the site preferences of the chemical elements: Red means A-site and blue means B-site. The intensity of the color indicates how large the thermodynamic preference toward the indicated site is. Figure 9b compares the site preferences according to the ionic radii (purple bars) with the result according to the DFT calculations (green bars). An interesting case is Pd³⁺, which would ionic radii wise tend toward the A-site, but DFT calculations show a small tendency toward the B-site. Zn²⁺ is another one since the DFT calculations show no preference for either of the sites over the other but ionic radii predict a slight tendency toward B-sites. Additionally Zn²⁺ is the only transition metal element which behaves similar to alkali and alkaline earth elements (p-type doping).⁵

In general, A-site substitutional doping influences the band structure indirectly usually by control of the band width and control of the band filling. A-site substitutions by dopants with smaller ionic radii can introduce a larger buckling in the Fe-O-Fe bond angle, which leads to a smaller tolerance factor and in turn also to a more insulating behavior (leakage currents are an unwanted behavior for most applications).⁵⁴ The research on A-site acceptor doping has been mostly concentrated on Ba²⁺, Ca²⁺, Sr²⁺ and Pb²⁺.⁵⁵ For instance, Ba²⁺ doping of BFO results in a larger permittivity, a smaller dielectric loss and a better ferroelectric hysteresis loop. This is caused by the smaller concentration of charge defects (see Chapter 2.5.2) and a structural transition.⁵ The Ca²⁺ dopant is charge-compensated by the formation of oxygen vacancies (V_O, see Chapter 2.5.2).⁵⁶ The Seebeck-coefficient and electrical-conductivity dependence on the oxygen partial pressure cannot be easily explained by a single point defect model. Parallel conduction pathways across undoped grains and defect-containing domain-walls can explain this behavior.⁵⁷ In theory replacing the

trivalent Bi³⁺ by some divalent element like Ca²⁺ should give rise to novel conducting states of a hole-doped BFO. In reality, formation of V_O often counteract this effect.⁵⁴ Figure 10 shows the phase diagram of Ca-doped Bi_{1-x}Ca_xFeO_{3-δ} films grown on (001) STO substrate proposed by Yang et al.⁵⁸ It shows that the film changes crystal symmetry from monoclinic to (pseudo)-tetragonal, the polarization behavior from ferroelectric to paraelectric and a super-structure arises.⁵⁸ Ca²⁺ and Sr²⁺ doping leads to an improved magnetization. On the other hand, doping with Ce⁴⁺ is one of the few donor dopants (produces electron carriers) for the A-site. Doping with the rare earth elements Dy³⁺ and Sm³⁺ leads to the rise of a morphotropic phase boundary in BFO, which means a significantly increased piezoelectric response (110 pm/V). This stems from the introduction of a mixture between the rhombohedral and tetragonally distorted phase and resulting double hysteresis loop of the polarization. If, like in the case Dy³⁺ and Sm³⁺, the dopant has the same valence as the replaced ion, it is called isovalent doping. If the dopant has a different valence, it is called aliovalent doping. A-site doping can also introduce a magnetic moment which is given by $\mu = |\mu(M_A^{+i})| + |3 - i|$ with μ being the magnetic moment induced by the A-site doping, $|\mu(M_A^{+i})|$ being the intrinsic magnetic moment of the A-site dopant with the oxidation state +i, and i being the oxidation state of the dopant.^{5,54-56,59-61}

By changing the electronic structure near the Fermi level, B-site substitutional doping can have a strong influence on the physical properties since the conduction band of BFO is related to the d-orbital state of the Fe³⁺ in BFO. The d-orbital of Fe³⁺ is filled with 5 electrons (d⁵ configuration) and is responsible for the antiferromagnetism of the BFO with the total spin of one Fe atom being (almost) antiparallel to all nearest Fe neighbors (G type antiferromagnetism, see Figure 3c). The valence shell configuration of the dopant determines its own magnetization, which typically aligns with the antiferromagnetic spin structure of the iron sites and lowers the magnetism reduction due to the antiferromagnetic ordering. The introduced magnetic moment is given by $\mu = 5 - |\mu(M_B^{+i})| + |3 - i|$ with μ being the magnetic moment induced by the B-site doping, $|\mu(M_B^{+i})|$ being the intrinsic magnetic moment of the B-site dopant with the oxidation state +i, and i being the oxidation state. The isovalent doping with Mn³⁺, which has a d⁴ configuration, and Cr³⁺ which has a d³ configuration both introduce net magnetism in an antiferromagnetic ordering. Both dopants have a ferromagnetic exchange interaction with iron. Therefore, for an optimal ferromagnetic state one needs to maximize the amount of Fe³⁺ - Mn³⁺/Cr³⁺ neighbors (stabilize a superlattice structure of BFO and BiCrO₃/BiMnO₃ grown one by one in [111] direction). B-site doping of dopants like Ti⁴⁺, Cr³⁺ or Mn³⁺ has been also proven effective to reduce the leakage current. Zr⁴⁺ is also found to reduce the leakage current but additionally improve ferroelectric properties and remnant polarization at moderate doping levels up to 20%.^{5,54,55,62}

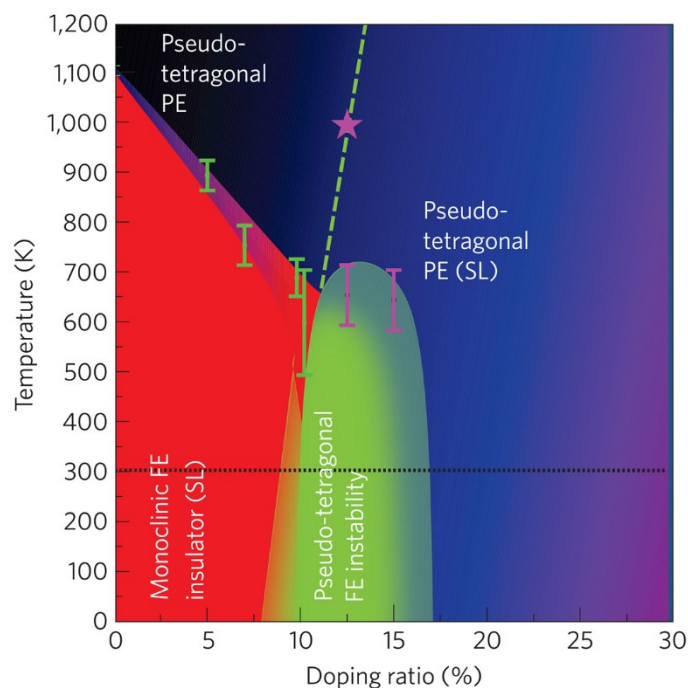


Figure 10. Phase diagram of Ca-doped Bi_{1-x}Ca_xFeO_{3-δ} films grown on (001) STO substrate. The standard, monoclinic, ferroelectric (FE), and insulating state is present until a dopant level of approximately 10% at room temperature (indicated by the black dashed line) and indicated by the red area. Between 10% and ~17%, it turns into a pseudo-tetragonal state, which is still ferroelectric and indicated by the green area. Above this dopant level, a pseudo-tetragonal paraelectric state follows, which shows the formation of ordered oxygen vacancy superstructures and is indicated by the blue area. Going to high temperatures above the red area, a pseudo-tetragonal paraelectric state with no V_O superstructure formation forms, which is separated by the one with superstructures by the green dashed line and which is indicated by the black area. The green and magenta error bars indicate a hysteresis loop effect in the phase diagram.⁵⁸ Reprinted with permission of ref.⁵⁸, Macmillan Publishers Limited, Copyright 2009

Depending on the dopant, they can introduce acceptor/donor states at various energies. The difference between the VBE, which is dominated by the O anions, and the CBE, which is dominated by the Fe state, shows only minor changes for most dopants, as can be seen by the black bars in Figure 9c. However, the energy difference between the acceptor state and the VBE, which is also the first excitation energy, changes significantly (from 0.20 eV to 2.30 eV), as shown by the green bars in Figure 9c. This could be useful to tune the properties for optoelectronic applications in sensors and photovoltaic devices.⁵

Simultaneous co-doping of A- and B-sites offers even more possibilities to vary and to combine the effects of different dopants with each other. For example, Ca and Co co-doping results in a large improvement in the saturation magnetization compared to samples doped with either one of them alone.⁶³ Therefore, this dopant combination is promising for receiving a ferromagnetic

system instead of an antiferromagnetic one. However, the results have not always been consistent in previous works.^{63,64}

2.5.2 Vacancy Doping

Vacancy doping means that some of the crystal lattice positions of the 3 different ions (Bi, Fe and O) are vacant of said ion. There are 3 types of vacancies which can appear in BFO:

- V_O (oxygen vacancies)
- V_{Bi} (Bismuth vacancies)
- V_{Fe} (Iron vacancies)

V_O can be introduced by controlling the growth parameters during thin-film deposition, e.g., by controlling the oxygen partial pressure in the deposition chamber or with p-type dopants like Ca.⁵⁴ Under normal oxygen-rich conditions during deposition, the defect formation energy of V_{Bi} is lower than that V_O, leading to V_{Bi} vacancies dominating. Both increase the conductivity of the film.⁶⁵ V_{Bi} creates a relatively small net magnetic moment of ~1 μB, while V_{Fe} creates a much larger one of ~5 μB. V_O has no influence on the net magnetization. Under oxidizing conditions, V_{Bi} and V_{Fe} are the dominant defects, while under reducing conditions V_O and V_{Bi} are dominant.^{66,67} V_O can have a significant effect on domain wall conductivity.^{54,55,68–70}

2.6 Device Applications of BiFeO₃

Due to its multifunctional properties, BFO has a wide variety of possible device applications making use of either a single functionality like, e.g., the ferroelectricity or piezoelectric response or the synergy between multiple functionalities, like, e.g., the magnetoelectric effect.²

2.6.1 Device Applications based on Electronics

Usually, electronic device applications exploit the large ferroelectric polarization of BFO. They can operate either in a planar geometry, where the current flows in a conductive channel adjacent to the ferroelectric, or in a perpendicular geometry, where the current flows across the ferroelectric. The former one includes ferroelectric field-effect transistors (FeFETs), while the latter one includes switchable diodes, ferroelectric tunnel junctions (FTJs), and memristors. This classification is also schematically illustrated in Figure 11.²

In FeFETs, the conductivity of the channel material needs to be very sensitive to changes in the carrier density. Because of its sizeable ferroelectric polarization, BFO is an attractive gate oxide

for FeFETs. Yamada et al.⁷¹ built a prototype of such a device (see Figure 11a,b) using CaMnO₃ (CMO), which is a Mott insulator, as channel material. CMO was sandwiched between a YAO substrate and a super-tetragonal (T-)BFO layer on top. The T-BFO phase was necessary due to the otherwise small lattice parameter of YAO (see Figure 6a) and CMO but also provides the advantage of a larger ferroelectric polarization. The as-grown downward polarization is the OFF state, while an upward polarization is the ON state (see Figure 11b). The temperature-resistivity diagram in Figure 11c shows that, even toward room temperature (RT), the resistivity difference between ON and OFF is significant for a 20 unit cell (u.c.) thick CMO layer.^{2,71}

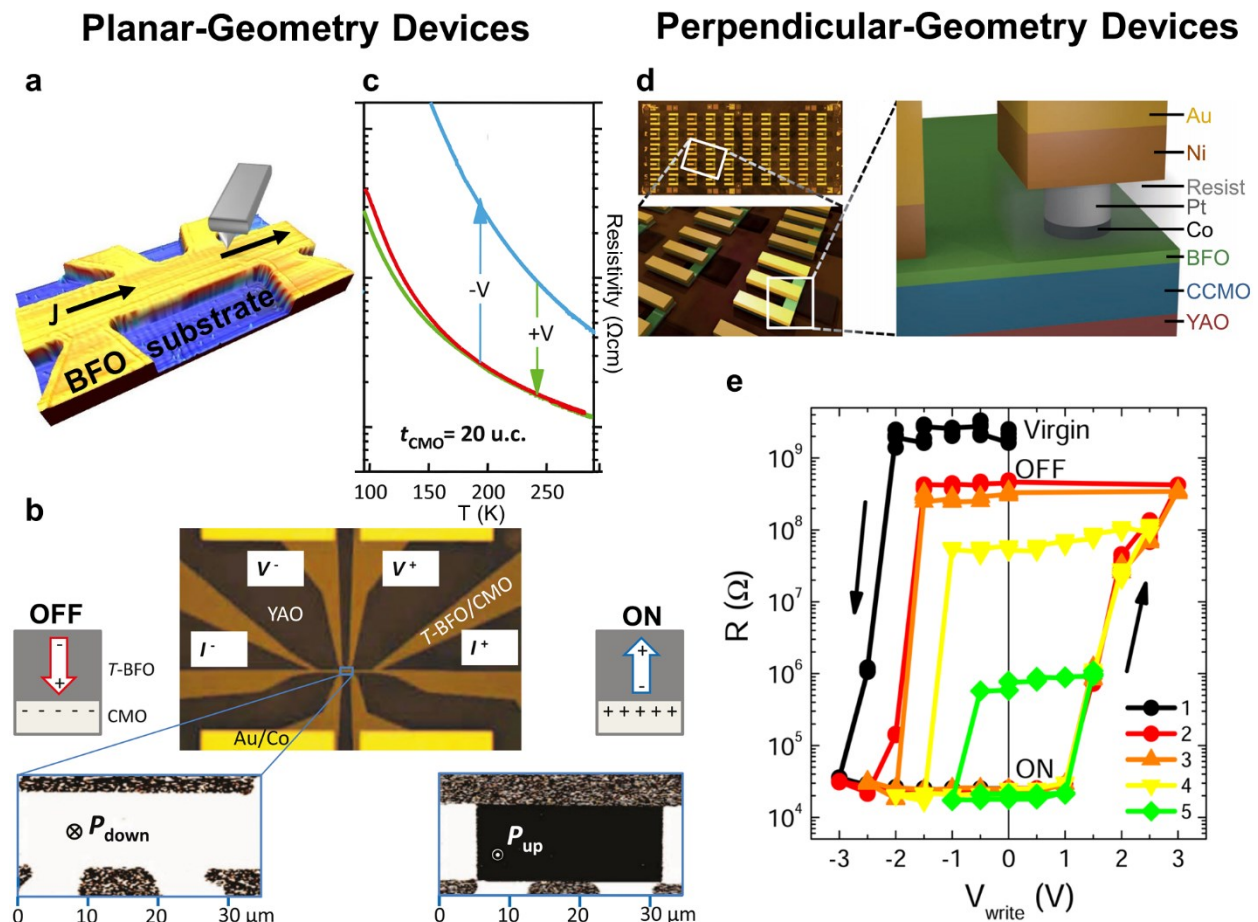


Figure 11. Electronic device applications of BFO: It can be differentiated between Planar-Geometry Devices (e.g., FeFET) or Perpendicular-Geometry Devices (switchable diode, FTJs, memristors). (a) AFM image of a FeFET device. Reprinted with permission from ref.⁷², American Physical Society, Copyright 2011 (b) Photograph of a FeFET device using a heterostructure of super-tetragonal (T-)BFO and CaMnO₃ (CMO) grown on a YAlO₃ (YAO) substrate. The conduction pathways for the 4-point measurement are indicated in the photo. The left side shows schematics and piezoresponse force microscopy (PFM) of the device in the regular poled-downwards state, and the right one shows it in the poled-upwards state. (c) Resistivity-temperature diagram for the FeFET with 20 u.c. thick CMO layer. (b) and (c) are reproduced under the [Creative Commons Attribution 3.0 License](https://creativecommons.org/licenses/by/3.0/) from ref.⁷¹, Copyright 2013, The Authors (d) Illustrations of 5 x 10 fully patterned ferroelectric tunnel

junctions (FTJ), which behave as memristors. Reprinted from ref.⁷³ with the permission of AIP Publishing, Copyright 2014. (e) Hysteresis of Resistance for an FTJ. The number 1 indicates the first switching from a virgin to the ON state. The typical reproducible hysteresis can be seen under 2 and 3. 4 and 5 show intermediate states. Reprinted with permission of ref.⁷⁴, American Chemical Society, Copyright 2013. ^{2,71-74}

One of the perpendicular geometry application cases is a switchable diode. A prototype was first presented by Choi. et al.⁷⁵ using an Ag/BFO/Ag structure. Current-voltage diagrams showed a strongly asymmetric behavior, as it is typical for p-n junction diodes. This asymmetry can be reversed by flipping the polarization direction of the BFO.^{2,75}

For a current stemming from a tunneling effect, if the tunneling barrier is ferroelectric, polarization switching leads to a change in the tunnel resistance. Thereby, usually, one of the interfaces with the BFO barrier is epitaxially grown Ce-doped CMO (CCMO) (see Figure 11d). The resistance difference in such devices is quite large and even at room temperature several magnitudes, as can be seen in Figure 11e. After the initial switching (black curve number 1), the characteristics after each switching process stay largely the same (red and orange curve number 2 and 3) and show an endurance of up to several million cycles. These BFO-based FTJs can therefore also be used as a new type of memristor, in which the resistance is not determined by changing the defect distribution via applied voltage but a purely polarization-based effect.^{2,73,74,76}

The fact that DWs in BFO are conductive enables further applications. The work of Seidel et al.⁷⁷, which kicked off this so-called field of DW nanoelectronics, falls under the class of perpendicular-geometry devices and presented a proof of concept for a device application that can be seen in Figure 12a. Thereby, an electrode made from SRO was combined with a BFO in in-plane geometry. The structure was grown in (110) orientation on a STO substrate. The domains were switched by applying a bias to the tip of the PFM, which for non-proof of concept devices, has to be achieved with another technical solution than PFM. Depending on the number of domains, which were switched from the regular downwards polarization to the upwards polarization (180° DW), with each domain creating two domain walls, the measurements in Figure 12b show a step-like increase of the current with each DW pair created. This process is also reversible, when one written domain is deleted again. The original study, including theoretical calculations, concluded that only 109° and 180° DWs are conductive and that it originates from the step in the electrostatic potential related to the change in polarization direction. However, this has proven wrong, and it was shown that conduction also occurs in 71° DWs.⁷⁸ According to the current knowledge, the conductivity in DWs is caused by the agglomeration of charged defects, like V_O or V_{Bi} at the DWs.^{2,68-70,77,78}

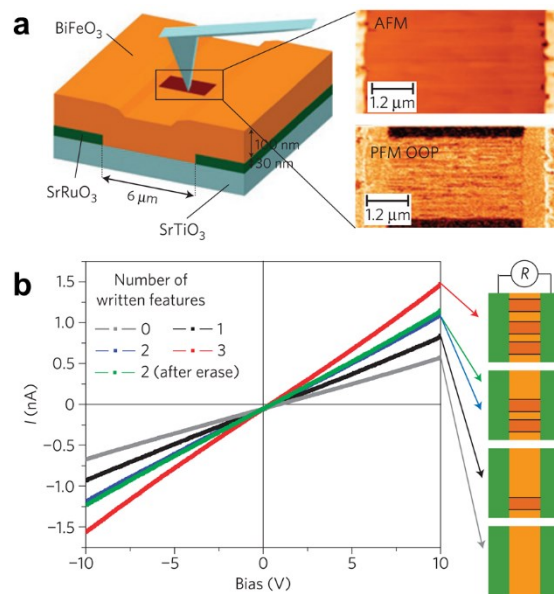


Figure 12. Proof of concept for device application using DW conductivity (a) Schematic illustration (left) of an electrode (SRO) – ferroelectric (BFO) heterostructure. The right side shows an AFM and a PFM image of a region after the polarization was changed with the PFM. (b) Voltage-Current characteristics of the device for 0, 1, 2 and 3 areas with switched polarization, which creates 2 DWs for each area.⁷⁷ Reprinted with permission from ref.⁷⁷, Copyright 2009, Nature Publishing Group

2.6.2 Device Applications based on Spintronics

The magnetoelectric coupling makes BFO a promising candidate in the field of spintronics. The principle of controlling magnetic properties by an electric field could enable very energy-efficient spintronic devices, in which information is stored magnetically and written electrically. In BFO, switching the ferroelectric polarization 71° or 109° leads to a change in the magnetization. The antiferromagnetic properties of BFO can be used to induce exchange bias in standard ferromagnets with high Curie temperatures. This results, depending on the BFO domain structure, in either an enhanced coercive field (stripe-like domains) or in an additional shift of the hysteresis loop of the ferromagnet (mosaic-like domains).^{29,79} The magnetoelectric coupling in BFO allows to manipulate this exchange bias effect by an electric field. For a planar geometry, this has been demonstrated by changing the magnetic state of a Co₉Fe layer on top of a BFO structure, as displayed in Figure 13a-e.^{80,81} For device applicability, this concept needs to be transferred to a vertical geometry since this allows lower voltages for operation and is therefore better compatible with standard electronics. Thereby, a spin valve is used, which means that between two or more conducting magnetic materials, electrical resistivity changes depending on the relative magnetization to each other. This is caused by the giant magnetoresistance (GMR) effect.

Figure 13f shows a device setup to control the exchange bias of a Co₇₁Fe₈B₂₀/Cu/Co spin valve structure.^{2,29,79–84}

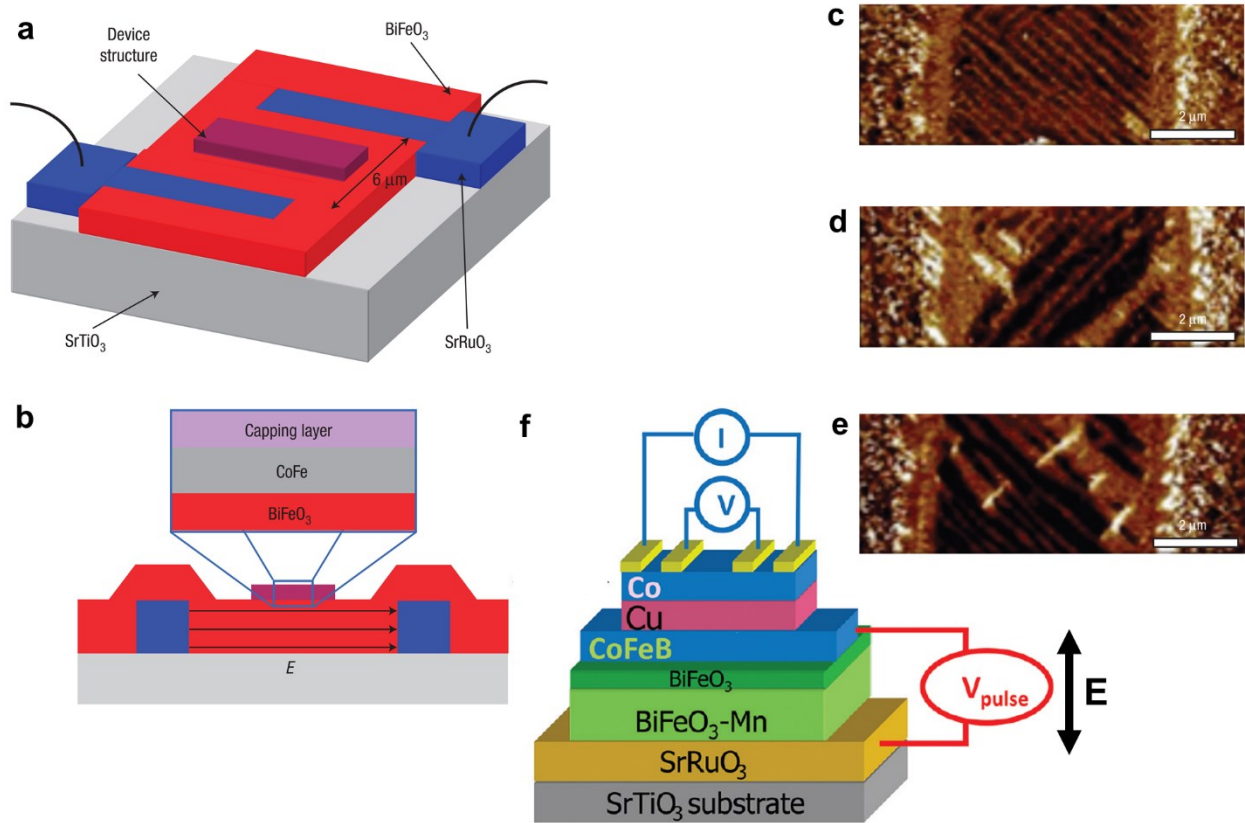


Figure 13. Spin valves with BFO. (a) Parallel projection and (b) cross-sectional schematic of an electrode device that allows electrical control of local ferromagnetism in CoFe device structures. In-plane PFM images showing the domain structure for a device in the (c) as-grown state, (d) after applying the electrical field and (e) after applying the electrical field in the antiparallel direction.⁸⁰ (a)-(e) reprinted with permission of ref.⁸⁰, Copyright 2008, Nature Publishing Group (f) Vertical spin valve device, which is better for standard integrated electronics.⁸² Reprinted with permission of ref.⁸², Copyright 2012, American Chemical Society.

2.6.3 Device Applications based on Optical Properties

The birefringence of BFO is very interesting for applications. Changing the ferroelectric polarization either by 71° or by 109° results in a large change of the refractive index (≈ 0.2). For plasmonic resonators, this switching capability could be very interesting, and concepts have been presented. Additionally to birefringence, also the other electro-optical coefficients are large, and the super-tetragonal phase of BFO is even more promising due to its larger ferroelectric distortion. Therefore, it is expected to cause even higher electro-optical coefficients.^{2,85,86}

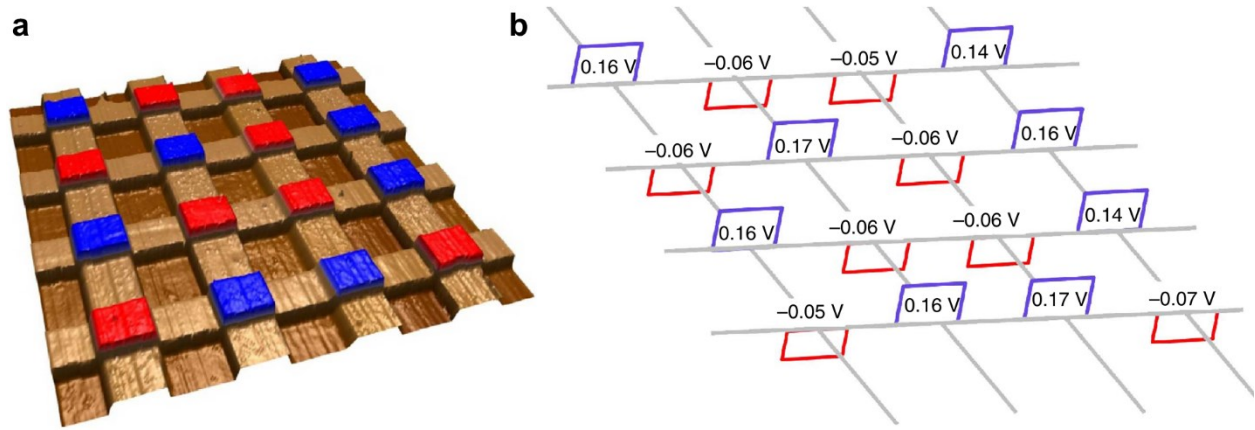


Figure 14. Prototype of 16-bit ferroelectric photovoltaic memory device. (a) Topography of the memory device with crossbar architecture to be able to control and read the voltage signal from each bit. The colors indicate the ferroelectric polarization state of the bit. Blue illustrates polarization up and red illustrates polarization down. (b) When light is shone on the array (20 mW/cm²), depending on the polarization, voltages with different signs are received.⁸⁷ Reprinted with Permission of ref.⁸⁷, Copyright 2013, Nature Publishing Group.

The bulk-photovoltaic effect can also be used for a new type of FeRAM (ferroelectric random-access memories), where the BFO is the active storage medium. The first prototype was presented by Guo et al.⁸⁷, in the form of a 16-bit device with a cross-bar circuit architecture based on a La_{0.7}Sr_{0.3}MnO₃/BFO heterostructure. The crossbar architecture allows the electric polarization of the BFO patches either in upwards (blue color in Figure 14a) or downwards direction (red color in Figure 14a). To read the stored bits, the device is irradiated with a halogen lamp with 20 mW/cm², and, over the crossbar architecture, the bias at each bit is readout. While upwards polarization leads to a positive voltage, downwards polarization results in a negative voltage readout (see Figure 14b). Such devices show no fatigue after 10⁸ cycles ($\approx 10^5$ cycles is the limit for flash memories) and no deterioration within 4 months.^{2,87–89}

Bulk phase BFO also shows photostriction, which means a change in dimension when irradiated with light. It stems from the combination of inverse piezoelectricity and the bulk photovoltaic effect and is also influenced by magnetic fields.^{2,90}

An interesting effect, without much industrial relevance at the moment, is the fact that water and acidic solution can be used to imprint and delete domains on BFO films allowing to “write” patterns into the domain structure tow-view wise (e.g., in the form of letters) with a minimum resolution of around 30 μm .^{88,91}

3. Methodology

3.1 Thin-Film Fabrication

Pulsed laser deposition (PLD), which occasionally is also named pulsed laser ablation deposition (PLAD), is often used for perovskite thin-film fabrication. It belongs to the physical vapor deposition (PVD) techniques. It is well established in research, due to the high-quality perovskite thin films it can produce, but is only scarcely used for industrial fabrication.^{92,93}

In a PLD system, a high-power pulsed laser beam is focused with lenses (see Figure 15a) on a target of the material to be deposited and which is placed within a vacuum chamber. The target is rotated to ensure a homogenous ablation. The hit of the laser on the target generates a plume of material. The material is thereby transported into the chamber and deposits on the heated substrate on the other side of the chamber placed in the line of the plume (see Figure 15a). The target-substrate distance is usually between 5-10 cm. Also, multiple targets can be used simultaneously in the deposition chamber to fabricate multilayers and superlattices. If the substrate is rotated too, that further improves film quality. One advantage of PLD is that it congruently evaporates the target and produces layers with the same chemical composition as the target, which is especially crucial for multi-component films like perovskites, which often also incorporate one or two dopants.⁹²⁻⁹⁴

Typically, a KrF excimer laser which has a light wavelength of 248 nm and a repetition rate of 4-15 Hz is used. The deposition rate is usually between 1-12 nm/min, and good quality films are normally reached with a laser fluence of 1-4 J/cm². For oxygen perovskites, additional O₂ gas is introduced into the chamber (see gas cylinder in Figure 15a). Before heating the substrate and introducing the O₂, the chamber is commonly evacuated to 10⁻⁴ Pa, and the O₂ pressure is around 10 Pa. The growth temperature for BFO is normally around 700°C. At too low temperature, BFO can't be grown at all anymore (see Figure 15b).⁹²⁻⁹⁴

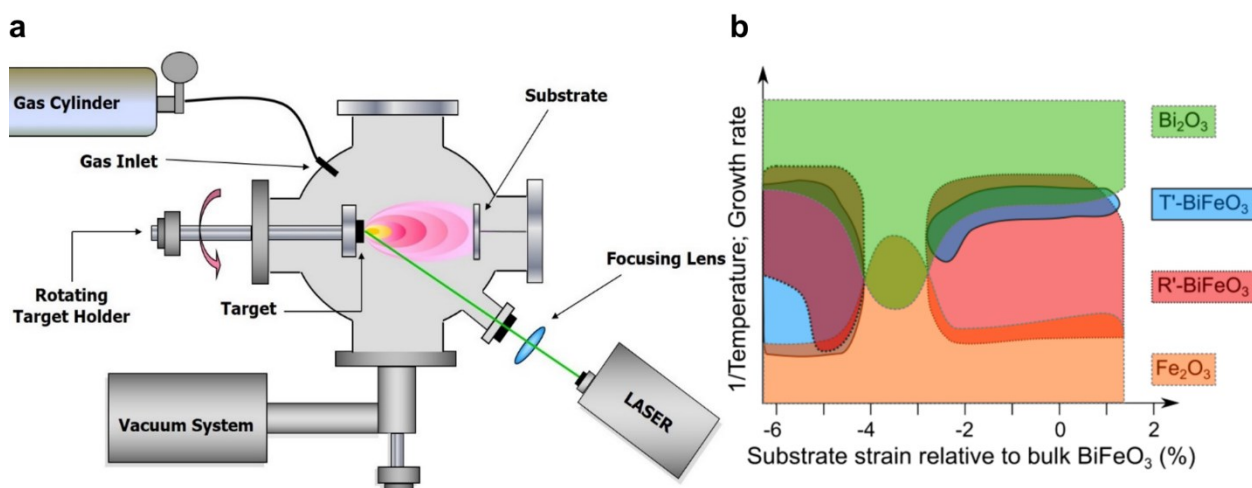


Figure 15. Schematic illustration of a pulsed laser deposition (PLD) apparatus and conceptual diagram of phase-stability regions. (a) In a PLD apparatus, a laser beam hits the rotating target, which has a composition tuned to the intended thin film composition and vaporizes it in the form of a material plume. In this way, the material is deposited on the target substrate, which is normally also rotating.⁹³ Reprinted under the [Creative Commons Attribution 4.0 License](https://creativecommons.org/licenses/by/4.0/) from ref.⁹³, Copyright 2020, Authors of ref.⁹³ (b) Phase-stability regions in BFO thin-film fabrication in dependence of the strain introduced by the substrate (x-axis) and the inverse temperature and growth rate (y-axis). R-BiFeO₃ (R-BFO) means the monoclinic BFO under moderate compressive or tensile strain. The super-tetragonal BFO phase (indicated as T-BiFeO₃) can form under strong compressive strain but also under moderate compressive or tensile strain requiring the secondary chemical phase Bi₂O₃ (BO). Another secondary phase is Fe₂O₃ (FO).⁹⁵ Reprinted from ref.⁹⁵ with the permission of AIP Publishing, Copyright 2016

Different regions of phase stability exist depending on the strain introduced by the substrate on the BFO thin film, the substrate temperature during growth, and the growth rate, as can be seen in the conceptual diagram in Figure 15b. The monoclinic BFO (R-phase) (red in Figure 15b) forms between approximately -2.5% and 1.5% strain at medium range temperature and growth rate. Epitaxial BFO films generally do not form between approximately -4% and -2.5% of strain. At strain values < -4%, the super-tetragonal (T-) phase forms either as a single phase or in a phase mixture with the R-phase. The super-tetragonal phase can also be reached at moderate strains by decreasing the substrate temperature and the growth rate to produce a secondary chemical phase Bi₂O₃ (BO) in the deposit, which in turn gives rise to the super-tetragonal phase. Another secondary chemical phase which can be in the film is Fe₂O₃ (FO).^{39,95}

Compared to molecular beam epitaxy (MBE)³⁶, PLD has less high vacuum requirements, higher growth rates with still good film quality, and is cheaper, but MBE, in turn, offers better control over component concentration, which can be used to fabricate exotic superlattices or single atomic layers, intentionally varied dopant gradients, and films with a potentially even better quality and

no unwanted secondary phases. Compared to PLD, chemical vapor deposition (CVD)⁹⁶ has higher growth rates and is easier upscalable, especially for industrial applications, but to date results in significantly lower film quality, specifically, since there are many parameters, which need to be tuned with complicated relationships.²⁶

3.2 Transmission Electron Microscopy (TEM)

Optical microscopes have been for hundreds of years a valuable tool for the understanding of the small-scale structure of all kinds of research objects. According to the Rayleigh criterium, the smallest distance between two point features which can be resolved is given by:⁹⁷

$$d = \frac{0.61\lambda}{\mu \times \sin(\beta)}$$

In this formula, μ is the refractive index of the viewing medium, β is the semi-angle of collection, and λ is the wavelength. Assuming that $\mu \sin(\beta) \approx 1$, for green light ($\lambda = 550$ nm) in a visual-light microscope, the resolution limit is ≈ 336 nm, which is over 800 times larger than the pseudocubic lattice parameter of BFO. Using electrons instead of visible light has the advantage that, because of the particle-wave dualism, the wavelength of electrons is given by:⁹⁷

$$\lambda = \underbrace{h / \left[2m_0 eV \left(1 + \frac{eV}{2m_0 c^2} \right) \right]^{1/2}}_{\text{relativistic effects included}} \approx \underbrace{\frac{1.22}{\sqrt{E(\text{in eV})}}}_{\text{non-relativistic approximation}}$$

Here h is the Planck's constant, m_0 the rest mass of an electron, c the speed of light, and $1\text{eV} = 1.602\text{e-}19$ J. So for electrons with 200 kV, the theoretical resolution limit stemming from the Rayleigh criterion would be ≈ 3 pm.⁹⁷

Different forms of electron microscopes have been developed to make use of this better resolution of electrons. The transmission electron microscope (TEM; see Figure 16a) is the earliest form, which was invented by Ernst Ruska (Nobel Prize in 1986 for his work on electron optics and the design of the first TEM) and Max Knoll in 1931 and is simultaneously also today the electron microscope variant which provides the highest resolutions. Thereby the electrons are transmitted through a very thin specimen (< 100 nm). A small part of the electrons interacts in some form with the sample, which is used to create the image signal.^{97,98}

Transmission Electron Microscopy (TEM)

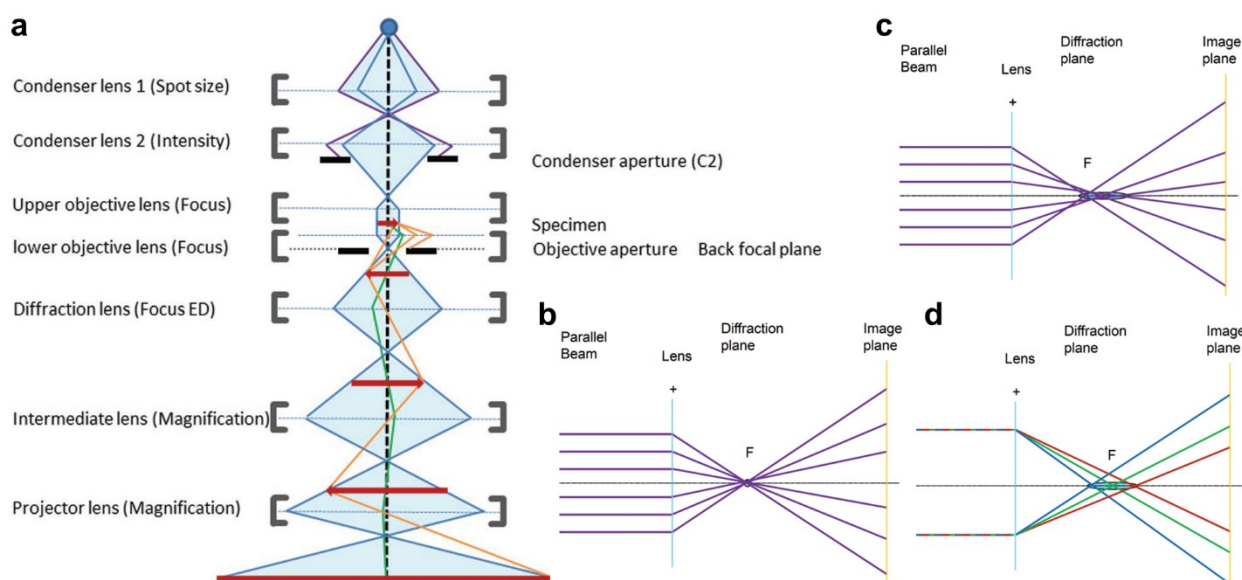


Figure 16. Schematic illustrations of a TEM and spherical and chromatic aberration in electromagnetic lenses. (a) The TEM schematic indicates lenses by grey brackets, apertures by black bars, the specimen and (intermediate) images of the specimen by red arrows, and the paths of scattered electrons in orange and green. (b) A perfect lens would have one single focus point. (c) Electron beams far from the optic axis are focused stronger than those close to the optic axis, which results in a focus area of least confusion rather than a point. This is called spherical aberration. (d) Chromatic aberration stems from electrons having different speeds (energies). Slower electrons (blue lines) are focused more compared to faster electrons (red lines), resulting again in a focus range.⁹⁸ Reprinted under the [Creative Commons Attribution 4.0 License](#) from ref.⁹⁸, Copyright 2020, Authors of ref.⁹⁸

However, electromagnetic lenses are not aberration free, which severely limits the reachability of the theoretical Rayleigh criterion. While in a perfect electron lens, all parallel electron beams would be focused into one point (see Figure 16b), due to the so-called spherical aberration, electron beams far from the optical axis are focused stronger than the ones closer to the optical axis resulting in a focus area rather than a focus point. Additionally, electrons with slightly lower energies (slower speeds) would also be focused stronger than higher energy ones. The latter can be omitted by having a low energy spread of the primary electrons. To correct spherical aberrations, starting in the 1990s, spherical-aberration correctors (often called Cs correctors) consisting of multipole lenses (quadrupole, hexapole, octupole and so on) were developed⁹⁹, which correct for the spherical aberration and other lens errors.⁹⁷⁻⁹⁹

The atomic-resolved phase-contrast image is often called high-resolution TEM (HRTEM). If spherical aberration in the objective lens (image forming system) is corrected, it is often called “image-side Cs-corrected” or “image-corrected”. Alternatively, the beam can be focused into an

electron probe and scanned across the surface which is then called scanning transmission electron microscopy (STEM) and uses differently diffracted electrons or secondary signals (secondary electrons, energy-dispersive X-ray spectroscopy, electron energy loss spectroscopy) for imaging. If the spherical aberration in condenser lenses (probe forming system) is corrected, it is often called “probe-side Cs-corrected” or “probe-corrected”. There are numerous different imaging modes, from which often the information can be collected simultaneously. With a probe-corrected STEM in crystalline samples, single-atom columns can be resolved, and chemical information about their composition, oxidation state, bonds, and other aspects can be gained. These possible imaging modes include (without completeness):^{97,98}

- High-angle annular dark-field (HAADF)^{100,101}
- Annular bright-field (ABF)¹⁰²
- Differential phase contrast (DPC)¹⁰³
- Energy-dispersive X-ray spectroscopy (EDS)^{104,105}
- Electron energy loss spectroscopy (EELS)¹⁰⁶

4. Summary and Discussion of Publication Results

The results of the publications presented in this work are focused on different aspects and effects of doping in BFO thin films, which are experimentally studied, mainly with various advanced TEM techniques and sophisticated data analysis software developed in part by the author of this thesis. BFO is a magnetoelectric material showing coupling of ferroelectric and antiferromagnetic order parameters at temperatures far above room temperature. This makes it very interesting for countless applications, but a better understanding of general processes within the material and further property tuning via doping or strain engineering is crucial for widespread industrial applications.

This thesis presents:

- a novel phenomenon of segregation of Ca dopant toward a compressively strained heterostructure interface
- a study on the effect that negatively charged domain walls in BFO based films coincide with agglomerated oxygen vacancies
- the report of a novel solubility behavior of Ca in BFO compared to a functional secondary phase, which can be used for phase engineering

4.1 Ca Segregation toward an Epitaxial Heterostructure Interface⁵⁶

For studying the Ca segregation toward an epitaxial heterostructure interface with compressive strain, thin-film systems of $\text{Bi}_{0.9}\text{Ca}_{0.1}\text{Fe}_{0.95}\text{Mn}_{0.05}\text{O}_3$ (BCFMO) were compared with $\text{BiFe}_{0.95}\text{Mn}_{0.05}\text{O}_3$ (BFMO), each grown on STO substrate. A-site doping with Ca^{2+} is thereby known to introduce oxygen vacancies, which increases conductivity.⁵⁴ B-site doping with Mn^{3+} in turn is known to decrease conductivity.⁵ Additionally, depending on the concentration, Ca can lead to structural changes, changes of the behavior of the electric polarization (ferroelectric to paramagnetic), a rise of a ferromagnetic residual magnetization (see Chapter 2.5.1), and an enhancement of the electromagnetic coupling.^{61,107} Mn^{3+} doping has been shown to restore the antiferromagnetic behavior of BFO.⁶¹ So while these dopants are very useful to tune material properties, segregation processes are an essential aspect to consider since they can lead to concentration gradients at surfaces, grain boundaries, or heterostructure interfaces. Thereby, on the one hand it can change functionality by a depletion of the bulk but on the other hand also

change functionality by modifying the interfaces.¹⁰⁸ There are countless studies available on segregation toward surfaces because there is a plethora of surface sensitive but also surface-limited analysis techniques. In comparison, for studies toward nonsurface interfaces, besides analytical TEM, only atom probe tomography and coherent Bragg rod analysis remain. Therefore, even for perovskite materials, nonsurface segregation has been rarely studied, and for BFO systems, even less so.⁵⁶

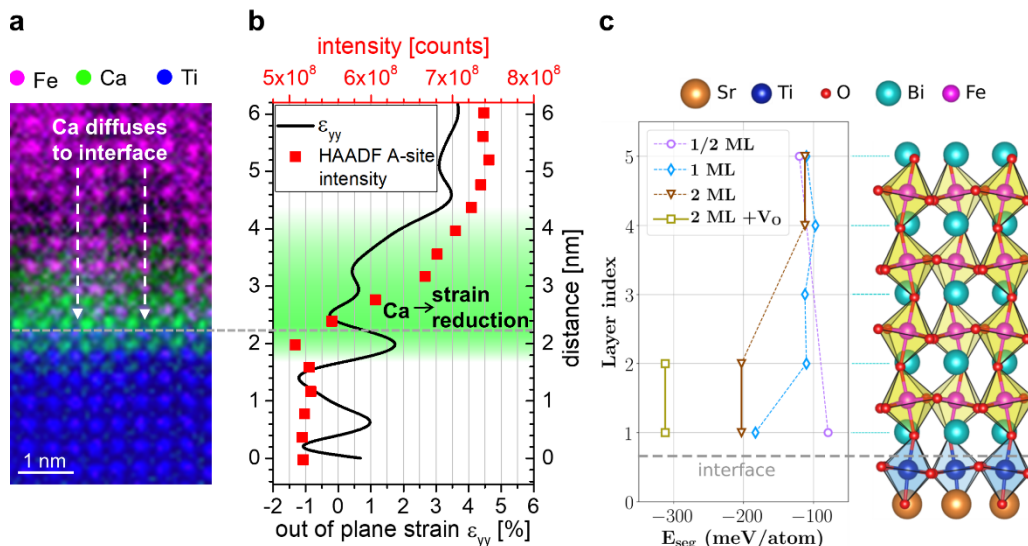


Figure 17. Ca segregation toward a BCFMO-STO interface. (a) Elemental Map of the BCFMO/STO interface gained via EELS. It is clearly visible that the Ca is segregated toward the interface, which is marked by the grey-dashed line. (b) Diagram of summarized HAADF A-site intensities (in [100] direction) across the interface (red x-label on the top) in comparison with the out-of-plane strain (black x-label on the bottom). The green-colored area indicates the zone with increased Ca segregation due to the strain. (c) DFT calculations of the segregation energy (E_{seg}) for monolayers (ML) of Ca depending on their position at the interface.⁵⁶ Adapted under the [Creative Commons Attribution 4.0 License](https://creativecommons.org/licenses/by/4.0/) from ref.⁵⁶, Copyright 2020, American Chemical Society

In publication A⁵⁶, a Ca segregation towards a BCFMO-STO interface was shown with analytical STEM techniques in atomic resolution, including EELS (Figure 17a) and EDS. EELS and EDS data showed that the Ca had segregated toward the interface and that several nm from the interface, the Ca content dropped below detectability. On the other hand, a concentration gradient of Mn could not be found anywhere in the film. A comparison of the geometric phase analysis (GPA) data of the film with Ca and one film without Ca, showed that the out-of-plane strain in the film with the Ca agglomeration was delayed at the interface in comparison to the other film, in which the out-of-plane strain increased immediately. Analysis of the EELS spectra showed no change of Fe polarization at the interface caused by the Ca and therefore suggested a formation of V_O instead. Since the intensity of HAADF images is approximately proportional to the sum of atomic numbers

squared (Z^2), the A-site intensities of a large-scale HAADF image were summed up in the in-plane direction [100] and compared with the out-of-plane strain of GPA analysis (Figure 17b). This showed a direct correlation between the Ca concentration at the interface and the amount of strain reduction. Finally, these experimental results were compared with DFT calculations which suggested that only complete monolayers in the crystal matrix minimize the energy and also that this energy minimization is larger with simultaneous formation of V_O instead of a change of the Fe oxidation (Figure 17c). Thereby, the calculations fully support the experimental results.⁵⁶

In conclusion, these results showed that significant segregation of Ca dopants in a BFO based film toward the interface can happen and that this is mainly driven by strain relief (significantly smaller ionic radii of Ca^{2+} compared to Bi^{3+}) but also by the chemical interactions of the Ca-rich layer with the interface. For the understanding of segregation behavior, these results are of great importance, especially since for device applications, this might result in a functionality breakdown. The DFT results indicate the rise of a 2D electron-gas state at the interface due to the Ca agglomeration. Therefore, the mechanism could also be used for purposely creating 2D systems. Additionally, the Ca-rich buffer layer seems to prevent antiphase boundaries at the interface.⁵⁶

4.2 V_O agglomerations at negatively charged domain walls⁷⁰

For Ca doping ratios $\geq 20\%$, the oxygen vacancies arrange in ordered superstructures, which appear as dark stripes in HAADF images. For Ca dopant levels $\leq 10\%$, usually no ordered superstructures appear. Randomly distributed dark stripes in the HAADF images can also have other causes than oxygen vacancies. These V_O can play a critical role in the retention failure of BFO based functional devices.^{58,70,109}

In publication B⁷⁰, randomly distributed dark stripes in HAADF images of a $Bi_{0.9}Ca_{0.1}FeO_3$ (BCFO) film were investigated (see Figure 18a). For the specific task of the data analysis, a Matlab script building up on a program developed by D. Knez¹¹⁰ was written (see Appendix) to analyze polarization, atomic site intensities, interatomic spacing, and other aspects in the image data. The evaluation of these data showed that the dark stripes always represent a T-T CDW and also always show a relative lattice enlargement of 11%. Additionally, the A-A distances across the defect show an alternating pattern, as can be seen in Figure 18c. From these 3 indicators, considering the previous results from Geng et al.¹¹¹ and Campanini et al.¹¹², it could be concluded that the defects also represent agglomerated oxygen vacancies. From the alternating A-A distances and the relative lattice enlargement of 11% it follows, that within the defects in the $FeO_{2-\delta}$ plane $\delta \approx 1$, meaning

that approximately every second oxygen site accommodates a vacancy. Within the dark stripes, the V_O form 1D channels in [010] direction with lots of vacancies on one site alternating with few vacancies on the two adjacent sites. Both in-plane defects and out-of-plane defects show exactly the same characteristics indicating their same nature and no preference of any sort.⁷⁰

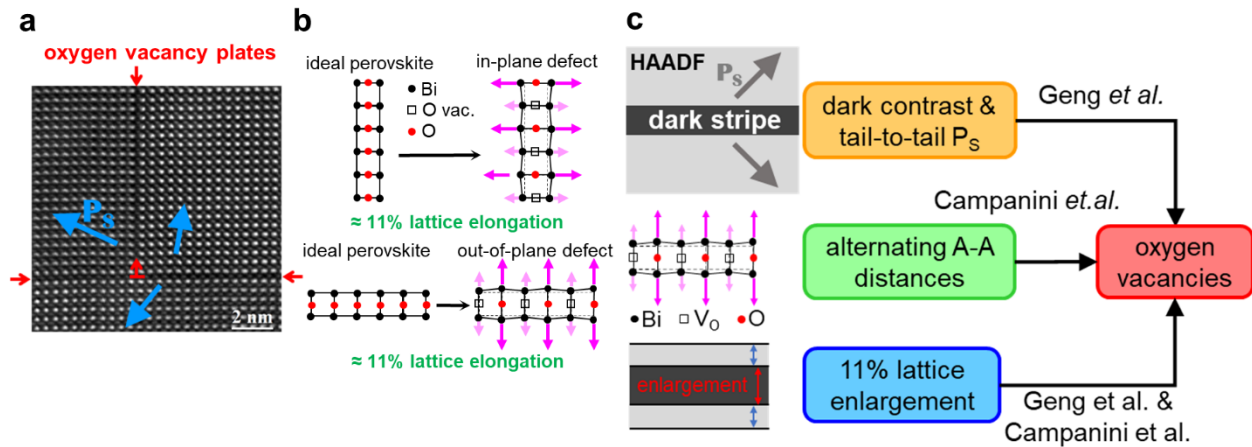


Figure 18. V_O agglomerations at negatively CDWs. (a) HAADF image of an in- and out-of-plane defect with contact point. The red arrows mark the defects, while the blue arrows indicate the projected ferroelectric polarization direction P_s . (b) Crystallographic arrangement of the Bi cations and O anions in the FeO_{2-8} plane for the regular perovskite structure and for the two types of defects. (c) The path of indicators and deductions, which lead to the identification of agglomerated V_O as the nature of the defects. Thereby, results of previous works by Geng *et al.*¹¹¹ and Campanini *et al.*¹¹² were used.⁷⁰ Adapted under the [Creative Commons Attribution 4.0 License](https://creativecommons.org/licenses/by/4.0/) from ref.⁷⁰, Copyright 2021 by the authors, Published by American Chemical Society

The results of publication B⁷⁰ are of high relevance because the demonstration of the close linkage of V_O ordered in plates, which represent negative CDWs, is noteworthy for influencing, controlling, and purposely designing domains and DWs in multiferroics due to the pinning effect of V_O . Because charged defects in the DW region have a critical influence on the domain wall conductivity, this result is also very relevant for the relatively novel field of DW nanoelectronics and, thereby, give interesting insights into the functionalities, mechanisms, and interactions of DWs and ordered V_O .⁷⁰

4.3 Ca solubility in BFO compared to secondary BO phase¹¹³

In a BFO system, BO is one of the secondary phases, whose formation is promoted if the substrate temperature and/or the growth rate is lower than necessary for pure BFO growth (see Chapter 3.1 and Figure 15b). This secondary BO phase can give rise to the formation of the super-tetragonal

phase in the BFO primary phase. Normally the super-tetragonal phase can only be created by strong compressive in-plane strain from the substrate but using secondary BO to create super-tetragonal BFO allows the fabrication of this exotic phase on a wide range of substrates. The advantage of the super-tetragonal phase is that it provides an approximately 50% larger polarization, which is also oriented only in [001] direction.^{30,36,38} Therefore, the super-tetragonal phase plays an important role in many device concepts (see Chapter 2.6.1 and 2.6.3).^{95,113–116}

Publication C¹¹³ shows a $\text{Bi}_{0.8}\text{Ca}_{0.2}\text{Fe}_{0.95}\text{Co}_{0.05}\text{O}_3$ (BCFCO) thin film deposited on STO substrate containing the secondary BO phase in the form of one unit cell thick plates (see Figure 19a). EELS and EDS data not only confirm the BO phase nature but also show that the Ca content in the BO phase is significantly lower than in the bismuth ferrite matrix (see Figure 19b, c). DFT calculations support these observations by showing that the solution enthalpy is considerably lower in BFO for the two considered charge compensation mechanisms: Fe oxidation and V_O formation (see Figure 19d). Additionally, DFT calculations predict at the growth temperature of the film a nearly 50 times higher Ca content in BFO than in BO for the more likely compensation case of V_O formation.^{56,113}

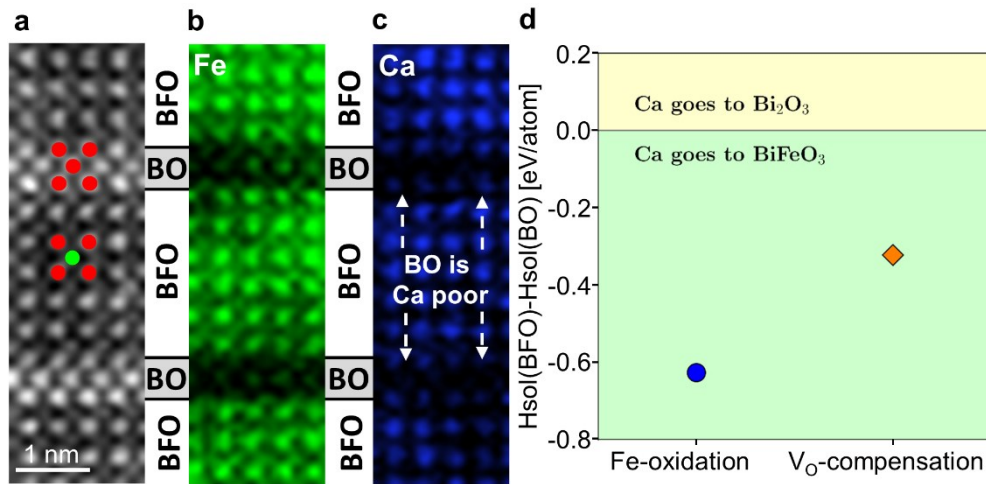


Figure 19. Ca solubility in BFO compared to secondary BO phase. (a) HAADF image containing two plates (one unit cell thick) of BO phase. The red circles indicate Bi positions, the green circles Fe positions. (b) EELS elemental map of Fe showing low signal in the BO stripes, as is expected. (c) EELS elemental map of Ca showing a reduced Ca content in the BO stripes. (d) DFT calculations for relative enthalpy of Ca solution in BFO compared to the secondary BO phase for two charge compensation mechanisms: Through Fe-oxidation or through V_O formation.¹¹³ Adapted from ref.¹¹³

The results of publication C¹¹³ on the Ca solubility in these two phases have never been reported in literature before. While the secondary BO phase is usually implemented to receive the super-

tetragonal phase, Ca doping is also applied to tune other material properties of BFO. Since dissolution of the majority of the available Ca in the BFO phase leads to changes in the intended dopant levels, this could shift the intended material characteristics (depending on the BO phase ratio). Additionally, other studies have shown that bismuth oxide layers can have an influence on the domain structure and publication C¹¹³ also presents further evidence of that, without being a specific focus point of it. The results also serve as a highly relevant data point for the assessment of a ternary BO – FO – CaO system in a thermodynamic database like CALPHAD, which so far does not exist.¹¹³

5. Conclusion

In summary, this thesis centers around the study of dopant- and substrate strain effects in BFO systems on a subnanometer scale. Thereby, novel insights about segregation behaviors of dopants (Ca), the connection between charged domain walls and V_O , and the previously unknown Ca solubility in a system of BFO and secondary BO are found. These findings contribute specifically to the fundamental understanding of BFO and perovskites in general. Not only this, but the results are also highly relevant for the design, operation, and reliability of multiferroic device applications in the present and future.

In this way, the results also highlight the importance of state-of-the-art advanced TEM capabilities, without which the findings would not have been possible. It also demonstrates the potentially significant gains of combining experimental techniques with modern *ab initio* methods, which require in term high-performance supercomputers.

6. Bibliography

- (1) Zhao, T.; Scholl, A.; Zavaliche, F.; Lee, K.; Barry, M.; Doran, A.; Cruz, M. P.; Chu, Y. H.; Ederer, C.; Spaldin, N. A.; Das, R. R.; Kim, D. M.; Baek, S. H.; Eom, C. B.; Ramesh, R. Electrical Control of Antiferromagnetic Domains in Multiferroic BiFeO₃ Films at Room Temperature. *Nat. Mater.* **2006**, *5* (10), 823–829. <https://doi.org/10.1038/nmat1731>
- (2) Sando, D.; Barthélémy, A.; Bibes, M. BiFeO₃ Epitaxial Thin Films and Devices: Past, Present and Future. *J. Phys. Condens. Matter* **2014**, *26* (47), 473201. <https://doi.org/10.1088/0953-8984/26/47/473201>
- (3) Fiebig, M.; Lottermoser, T.; Meier, D.; Trassin, M. The Evolution of Multiferroics. *Nat. Rev. Mater.* **2016**, *1* (8), 16046. <https://doi.org/10.1038/natrevmats.2016.46>
- (4) Elnozahy, M. S. Accommodating a High Penetration of PHEVs and PV Electricity in Residential Distribution Systems. *PhD Thesis* 2015, University of Waterloo
- (5) Gebhardt, J.; Rappe, A. M. Doping of BiFeO₃: A Comprehensive Study on Substitutional Doping. *Phys. Rev. B* **2018**, *98* (12), 125202. <https://doi.org/10.1103/PhysRevB.98.125202>
- (6) Schmid, H. Multi-Ferroic Magnetoelectrics. *Ferroelectrics* **1994**, *162* (1), 317–338. <https://doi.org/10.1080/00150199408245120>
- (7) Spaldin, N. A.; Ramesh, R. Advances in Magnetoelectric Multiferroics. *Nat. Mater.* **2019**, *18*, 203–212. <https://doi.org/10.1038/s41563-018-0275-2>
- (8) Dong, S.; Liu, J. M.; Cheong, S. W.; Ren, Z. Multiferroic Materials and Magnetoelectric Physics: Symmetry, Entanglement, Excitation, and Topology. *Adv. Phys.* **2015**, *64* (5–6), 519–626. <https://doi.org/10.1080/00018732.2015.1114338>
- (9) Spaldin, N. A.; Fiebig, M. The Renaissance of Magnetoelectric Multiferroics. *Science* **2005**, *309* (July), 391–392. <https://doi.org/10.1126/science.1113357>
- (10) Liu, H.; Yang, X. A Brief Review on Perovskite Multiferroics. *Ferroelectrics* **2017**, *507* (1), 69–85. <https://doi.org/10.1080/00150193.2017.1283171>
- (11) Eerenstein, W.; Mathur, N. D.; Scott, J. F. Multiferroic and Magnetoelectric Materials. *Nature* **2006**, *442*, 759–765. <https://doi.org/10.1038/nature05023>
- (12) Ramesh, R.; Spaldin, N. A. Multiferroics: Progress and Prospects in Thin Films. *Nat. Mater.* **2009**, 20–28. https://doi.org/10.1142/9789814287005_0003
- (13) Areas to Watch. *Science* **2007**, *318* (5858), 1848–1849. <https://doi.org/10.1126/science.318.5858.1848>
- (14) Catalan, G.; Scott, J. F. Physics and Applications of Bismuth Ferrite. *Adv. Mater.* **2009**, *21* (24), 2463–2485. <https://doi.org/10.1002/adma.200802849>
- (15) Doig, K. I.; Aguesse, F.; Axelsson, A. K.; Alford, N. M.; Nawaz, S.; Palkar, V. R.; Jones, S. P. P.; Johnson, R. D.; Synowicki, R. A.; Lloyd-Hughes, J. Coherent Magnon and Acoustic Phonon Dynamics in Tetragonal and Rare-Earth-Doped BiFeO₃ Multiferroic Thin Films. *Phys. Rev. B* **2013**, *88* (9), 094425(8). <https://doi.org/10.1103/PhysRevB.88.094425>
- (16) Lebeugle, D.; Colson, D.; Forget, A.; Viret, M.; Bataille, A. M.; Gukasov, A. Electric-Field-Induced Spin Flop in BiFeO₃ Single Crystals at Room Temperature. *Phys. Rev. Lett.* **2008**, *100* (22), 1–4. <https://doi.org/10.1103/PhysRevLett.100.227602>

Bibliography

- (17) Park, J. G.; Le, M. D.; Jeong, J.; Lee, S. Structure and Spin Dynamics of Multiferroic BiFeO₃. *J. Phys. Condens. Matter* **2014**, *26*, 433202 (33pp). <https://doi.org/10.1088/0953-8984/26/43/433202>
- (18) Megaw, H. D.; Darlington, C. N. W. Geometrical and Structural Relations in the Rhombohedral Perovskites. *Acta Crystallogr.* **1975**, *A31*, 161. <https://doi.org/10.1107/S0567739475000332>
- (19) Bernardo, M. S. Synthesis, Microstructure and Properties of BiFeO₃-Based Multiferroic Materials: A Review. *Bol. la Soc. Esp. Ceram. y Vidr.* **2014**, *53* (1), 1–14. <https://doi.org/10.3989/cyv.12014>
- (20) Martin, L. W.; Crane, S. P.; Chu, Y. H.; Holcomb, M. B.; Gajek, M.; Huijben, M.; Yang, C. H.; Balke, N.; Ramesh, R. Multiferroics and Magnetoelectrics: Thin Films and Nanostructures. *J. Phys. Condens. Matter* **2008**, *20* (43), 434220. <https://doi.org/10.1088/0953-8984/20/43/434220>
- (21) Wang, N.; Cheng, J.; Pyatakov, A.; Zvezdin, A. K.; Li, J. F.; Cross, L. E.; Viehland, D. Multiferroic Properties of Modified BiFeO₃-PbTiO₃-Based Ceramics: Random-Field Induced Release of Latent Magnetization and Polarization. *Phys. Rev. B* **2005**, *72* (10), 1–5. <https://doi.org/10.1103/PhysRevB.72.104434>
- (22) Feiming, B.; Wang, J.; Wuttig, M.; Lie, J.; Wang, N.; Pyatakov, A. P.; Zvezdin, A. K.; Cross, L. E.; Viehland, D. Destruction of Spin Cycloid in (111)c-Oriented BiFeO₃ Thin Films by Epitaxial Constraint: Enhanced Polarization and Release of Latent Magnetization. *Appl. Phys. Lett.* **2005**, *86* (3), 032511. <https://doi.org/10.1063/1.1851612>
- (23) Lee, S.; Ratcliff, W.; Cheong, S. W.; Kiryukhin, V. Electric Field Control of the Magnetic State in BiFeO₃ Single Crystals. *Appl. Phys. Lett.* **2008**, *92* (19), 10–13. <https://doi.org/10.1063/1.2930678>
- (24) Heron, J. T.; Schlom, D. G.; Ramesh, R. Electric Field Control of Magnetism Using BiFeO₃-Based Heterostructures. *Appl. Phys. Rev.* **2014**, *1* (2), 021303. <https://doi.org/10.1063/1.4870957>
- (25) Mishra, M. K.; Mahaling, R. N. Single or Both Site Doped BiFeO₃—Which Is Better Candidate for Profound Electronic Device Applications? *Chinese J. Phys.* **2018**, *56* (3), 965–973. <https://doi.org/10.1016/j.cjph.2018.03.026>
- (26) Srihari, N. V.; Vinayakumar, K. B.; Nagaraja, K. K. Magnetoelectric Coupling in Bismuth Ferrite - Challenges and Perspectives. *MDPI Coatings* **2020**, *10* (12), 1221. <https://doi.org/doi:10.3390/coatings10121221>
- (27) Wang, W. Y.; Tang, Y. L.; Zhu, Y. L.; Xu, Y. Bin; Liu, Y.; Wang, Y. J.; Jagadeesh, S.; Ma, X. L. Atomic Level 1D Structural Modulations at the Negatively Charged Domain Walls in BiFeO₃ Films. *Adv. Mater. Interfaces* **2015**, *2* (9), 1500024. <https://doi.org/10.1002/admi.201500024>
- (28) Streiffer, S. K.; Parker, C. B.; Romanov, A. E.; Lefevre, M. J.; Zhao, L.; Speck, J. S.; Pompe, W.; Foster, C. M.; Bai, G. R. Domain Patterns in Epitaxial Rhombohedral Ferroelectric Films. I. Geometry and Experiments. *J. Appl. Phys.* **1998**, *83* (5), 2742–2753. <https://doi.org/10.1063/1.366632>
- (29) Martin, L. W.; Chu, Y. H.; Holcomb, M. B.; Huijben, M.; Yu, P.; Han, S. J.; Lee, D.; Wang, S. X.; Ramesh, R. Nanoscale Control of Exchange Bias with BiFeO₃ Thin Films. *Nano Lett.* **2008**, *8* (7), 2050–2055. <https://doi.org/10.1021/nl801391m>
- (30) Yang, Y.; Infante, I. C.; Dkhil, B.; Bellaiche, L. Strain Effects on Multiferroic BiFeO₃ Films. *Comptes Rendus Phys.* **2015**, *16* (2), 193–203. <https://doi.org/10.1016/j.crhy.2015.01.010>
- (31) Ohring, M. *Materials Science of Thin Films: Deposition and Structure*, 2nd Edit.; Academic Press, 2002.
- (32) Damodaran, A. R.; Agar, J. C.; Pandya, S.; Chen, Z.; Dedon, L.; Xu, R.; Apgar, B.; Saremi, S.; Martin, L. W. New Modalities of Strain-Control of Ferroelectric Thin Films. *J. Phys. Condens. Matter* **2016**, *28* (26),

Bibliography

263001. <https://doi.org/10.1088/0953-8984/28/26/263001>
- (33) Hatt, A. J.; Spaldin, N. A.; Ederer, C. Strain-Induced Isosymmetric Phase Transition in BiFeO₃. *Phys. Rev. B* **2010**, *81* (5), 054109(5). <https://doi.org/10.1103/PhysRevB.81.054109>
- (34) Dupé, B.; Infante, I. C.; Geneste, G.; Janolin, P. E.; Bibes, M.; Barthélémy, A.; Lisenkov, S.; Bellaiche, L.; Ravy, S.; Dkhil, B. Competing Phases in BiFeO₃ Thin Films under Compressive Epitaxial Strain. *Phys. Rev. B* **2010**, *81* (14), 144128(5). <https://doi.org/10.1103/PhysRevB.81.144128>
- (35) Pailloux, F.; Couillard, M.; Fusil, S.; Bruno, F.; Saidi, W.; Garcia, V.; Carrétéro, C.; Jacquet, E.; Bibes, M.; Barthélémy, A.; Botton, G. A.; Pacaud, J. Atomic Structure and Microstructures of Supertetragonal Multiferroic BiFeO₃ Thin Films. *Phys. Rev. B* **2014**, *89* (10), 104106(9). <https://doi.org/10.1103/PhysRevB.89.104106>
- (36) Zeches, R. J.; Rossell, M. D.; Zhang, J. X.; Hatt, A. J.; He, Q.; Yang, C.-H.; Kumar, A.; Wang, C. H.; Melville, A.; Adamo, C.; Sheng, G.; Chu, Y.-H.; Ihlefeld, J. F.; Erni, R.; Ederer, C.; Gopalan, V.; Chen, L. Q.; Schlom, D. G.; Spaldin, N. A.; Martin, L. W.; Ramesh, R. A Strain-Driven Morphotropic Phase Boundary in BiFeO₃. *Science* (80-.). **2009**, *326* (5955), 977–980. <https://doi.org/10.1126/science.1177046>
- (37) Infante, I. C.; Lisenkov, S.; Dupé, B.; Bibes, M.; Fusil, S.; Jacquet, E.; Geneste, G.; Petit, S.; Courtial, A.; Juraszek, J.; Bellaiche, L.; Barthélémy, A.; Dkhil, B. Bridging Multiferroic Phase Transitions by Epitaxial Strain in BiFeO₃. *Phys. Rev. Lett.* **2010**, *105* (5), 057601. <https://doi.org/10.1103/PhysRevLett.105.057601>
- (38) Béa, H.; Dupé, B.; Fusil, S.; Mattana, R.; Jacquet, E.; Warot-Fonrose, B.; Wilhelm, F.; Rogalev, A.; Petit, S.; Cros, V.; Anane, A.; Petroff, F.; Bouzouane, K.; Geneste, G.; Dkhil, B.; Lisenkov, S.; Ponomareva, I.; Bellaiche, L.; Bibes, M.; Barthélémy, A. Evidence for Room-Temperature Multiferroicity in a Compound with a Giant Axial Ratio. *Phys. Rev. Lett.* **2009**, *102* (21), 217603. <https://doi.org/10.1103/PhysRevLett.102.217603>
- (39) Liu, H.; Yang, P.; Yao, K.; Ong, K. P.; Wu, P.; Wang, J. Origin of a Tetragonal BiFeO₃ Phase with a Giant *c/a* Ratio on SrTiO₃ Substrates. *Adv. Funct. Mater.* **2012**, *22* (5), 937–942. <https://doi.org/10.1002/adfm.201101970>
- (40) Giencke, J. E.; Folkman, C. M.; Baek, S. H.; Eom, C. B. Tailoring the Domain Structure of Epitaxial BiFeO₃ Thin Films. *Curr. Opin. Solid State Mater. Sci.* **2014**, *18* (1), 39–45. <https://doi.org/10.1016/j.cossms.2013.11.003>
- (41) Jang, H. W.; Ortiz, D.; Baek, S. H.; Folkman, C. M.; Das, R. R.; Shafer, P.; Chen, Y.; Nelson, C. T.; Pan, X.; Ramesh, R.; Eom, C. B. Domain Engineering for Enhanced Ferroelectric Properties of Epitaxial (001) BiFeO₃ Thin Films. *Adv. Mater.* **2009**, *21* (7), 817–823. <https://doi.org/10.1002/adma.200800823>
- (42) Landau, L.; Lifshits, E. On the Theory of the Dispersion of Magnetic Permeability in Ferromagnetic Bodies. *Phys. Zeitsch. der Sow.* **1935**, *8*, 153–169. <https://doi.org/10.1016/b978-0-08-036364-6.50008-9>
- (43) Kittel, C. Theory of the Structure of Ferromagnetic Domains in Films and Small Particles. *Phys. Rev.* **1946**, *70* (11–12), 965–971. <https://doi.org/10.1103/PhysRev.70.965>
- (44) Mitsui, T.; Furuichi, J. Domain Structure of Rochelle Salt and KH₂PO₄. *Phys. Rev.* **1953**, *90* (2), 193–202. <https://doi.org/10.1103/PhysRev.90.193>
- (45) Daraktchiev, M.; Catalan, G.; Scott, J. F. Landau Theory of Ferroelectric Domain Walls in Magnetoelectrics. *Ferroelectrics* **2008**, *375*, 122–131. <https://doi.org/10.1080/00150190802437969>
- (46) Jang, H. W.; Baek, S. H.; Ortiz, D.; Folkman, C. M.; Das, R. R.; Chu, Y. H.; Shafer, P.; Zhang, J. X.;
-

Bibliography

- Choudhury, S.; Vaithyanathan, V.; Chen, Y. B.; Felker, D. A.; Biegalski, M. D.; Rzchowski, M. S.; Pan, X. Q.; Schlom, D. G.; Chen, L. Q.; Ramesh, R.; Eom, C. B. Strain-Induced Polarization Rotation in Epitaxial (001) BiFeO₃ Thin Films. *Phys. Rev. Lett.* **2008**, *101* (10), 107602(4). <https://doi.org/10.1103/PhysRevLett.101.107602>
- (47) Daumont, C.; Ren, W.; Infante, I. C.; Lisenkov, S.; Allibe, J.; Carrétéro, C.; Fusil, S.; Jacquet, E.; Bouvet, T.; Bouamrane, F.; Prosandeev, S.; Geneste, G.; Dkhil, B.; Bellaiche, L.; Barthélémy, A.; Bibes, M. Strain Dependence of Polarization and Piezoelectric Response in Epitaxial BiFeO₃ Thin Films. *J. Phys. Condens. Matter* **2012**, *24* (16), 162202. <https://doi.org/10.1088/0953-8984/24/16/162202>
- (48) Bá, H.; Bibes, M.; Zhu, X. H.; Fusil, S.; Bouzehouane, K.; Petit, S.; Kreisel, J.; Barthély, A. Crystallographic, Magnetic, and Ferroelectric Structures of Bulklike BiFeO₃ Thin Films. *Appl. Phys. Lett.* **2008**, *93* (7), 91–94. <https://doi.org/10.1063/1.2940327>
- (49) Infante, I. C.; Juraszek, J.; Fusil, S.; Dupé, B.; Gemeiner, P.; Diéguez, O.; Pailloux, F.; Jouen, S.; Jacquet, E.; Geneste, G.; Pacaud, J.; Íñiguez, J.; Bellaiche, L.; Barthélémy, A.; Dkhil, B.; Bibes, M. Multiferroic Phase Transition near Room Temperature in BiFeO₃ Films. *Phys. Rev. Lett.* **2011**, *107* (23), 237601(4). <https://doi.org/10.1103/PhysRevLett.107.237601>
- (50) Wojdeł, J. C.; Íñiguez, J. Ab Initio Indications for Giant Magnetoelectric Effects Driven by Structural Softness. *Phys. Rev. Lett.* **2010**, *105* (3), 037208(4). <https://doi.org/10.1103/PhysRevLett.105.037208>
- (51) Prosandeev, S.; Kornev, I. A.; Bellaiche, L. Magnetoelectricity in BiFeO₃ Films: First-Principles-Based Computations and Phenomenology. *Phys. Rev. B* **2011**, *83* (2), 020102(4). <https://doi.org/10.1103/PhysRevB.83.020102>
- (52) Sando, D.; Agbelele, A.; Rahmedov, D.; Liu, J.; Rovillain, P.; Toulouse, C.; Infante, I. C.; Pyatakov, a P.; Fusil, S.; Jacquet, E.; Carrétéro, C.; Deranlot, C.; Lisenkov, S.; Wang, D.; Le Breton, J.-M.; Cazayous, M.; Sacuto, A.; Juraszek, J.; Zvezdin, a K.; Bellaiche, L.; Dkhil, B.; Barthélémy, A.; Bibes, M. Crafting the Magnonic and Spintronic Response of BiFeO₃ Films by Epitaxial Strain. *Nat. Mater.* **2013**, *12*, 641–646. <https://doi.org/10.1038/nmat3629>
- (53) Escorihuela-Sayalero, C.; Diéguez, O.; Íñiguez, J. Strain Engineering Magnetic Frustration in Perovskite Oxide Thin Films. *Phys. Rev. Lett.* **2012**, *109* (24), 247202(5). <https://doi.org/10.1103/PhysRevLett.109.247202>
- (54) Yang, C. H.; Kan, D.; Takeuchi, I.; Nagarajan, V.; Seidel, J. Doping BiFeO₃: Approaches and Enhanced Functionality. *Phys. Chem. Chem. Phys.* **2012**, *14* (46), 15953–15962. <https://doi.org/10.1039/c2cp43082g>
- (55) Feng, Y.; Wu, J.; Chi, Q.; Li, W.; Yu, Y.; Fei, W. Defects and Aliovalent Doping Engineering in Electroceramics. *Chem. Rev.* **2020**, *120*, 1710–1787. <https://doi.org/10.1021/acs.chemrev.9b00507>
- (56) Haselmann, U.; Haberfehlner, G.; Pei, W.; Popov, M. N.; Romaner, L.; Knez, D.; Chen, J.; Ghasemi, A.; He, Y.; Kothleitner, G.; Zhang, Z. Study on Ca Segregation toward an Epitaxial Interface between Bismuth Ferrite and Strontium Titanate. *ACS Appl. Mater. Interfaces* **2020**, *12* (10), 12264–12274. <https://doi.org/10.1021/acsami.9b20505>
- (57) Schrade, M.; Masó, N.; Perejón, A.; Pérez-Maqueda, L. A.; West, A. R. Defect Chemistry and Electrical Properties of BiFeO₃. *J. Mater. Chem. C* **2017**, *5* (38), 10077–10086. <https://doi.org/10.1039/c7tc03345a>
- (58) Yang, C. H.; Seidel, J.; Kim, S. Y.; Rossen, P. B.; Yu, P.; Gajek, M.; Chu, Y. H.; Martin, L. W.; Holcomb, M. B.; He, Q.; Maksymovych, P.; Balke, N.; Kalinin, S. V.; Baddorf, A. P.; Basu, S. R.; Scullin, M. L.;
-

Bibliography

- Ramesh, R. Electric Modulation of Conduction in Multiferroic Ca-Doped BiFeO₃ Films. *Nat. Mater.* **2009**, *8*, 485–493. <https://doi.org/10.1038/nmat2432>
- (59) Hegab, A. F.; Ahmed Farag, I. S.; El-Shabiny, A. M.; Nassaar, A. M.; Ramadan, A. A.; Moustafa, A. M. Role of Sr Doping on Transport and Magnetic Properties of Bismuth Ferrite in Correlation with Defect Formation. *J. Mater. Sci. Mater. Electron.* **2017**, *28* (19), 14460–14470. <https://doi.org/10.1007/s10854-017-7308-5>
- (60) Fujino, S.; Murakami, M.; Anbusathaiah, V.; Lim, S. H.; Nagarajan, V.; Fennie, C. J.; Wuttig, M.; Salamanca-Riba, L.; Takeuchi, I. Combinatorial Discovery of a Lead-Free Morphotropic Phase Boundary in a Thin-Film Piezoelectric Perovskite. *Appl. Phys. Lett.* **2008**, *92* (20), 2006–2009. <https://doi.org/10.1063/1.2931706>
- (61) Khomchenko, V. A.; Pereira, L. C. J.; Paixão, J. A. Mn Substitution-Induced Revival of the Ferroelectric Antiferromagnetic Phase in Bi_{1-x}CaxFeO_{3-x/2} Multiferroics. *J. Mater. Sci.* **2015**, *50* (4), 1740–1745. <https://doi.org/10.1007/s10853-014-8735-9>
- (62) Dai, H. Y.; Gu, L. T.; Xie, X. Y.; Li, T.; Chen, Z. P.; Li, Z. J. The Structure, Defects, Electrical and Magnetic Properties of BiFe_{1-x}ZrxO₃ Multiferroic Ceramics. *J. Mater. Sci. Mater. Electron.* **2018**, *29* (3), 2275–2281. <https://doi.org/10.1007/s10854-017-8143-4>
- (63) Quan, C.; Han, Y.; Gao, N.; Mao, W.; Zhang, J.; Yang, J.; Li, X.; Huang, W. Comparative Studies of Pure, Ca-Doped, Co-Doped and co-doped BiFeO₃ Nanoparticles. *Ceram. Int.* **2015**, *42* (1), 537–544. <https://doi.org/10.1016/j.ceramint.2015.08.142>
- (64) Xu, Q.; Zai, H.; Wu, D.; Qiu, T.; Xu, M. X. The Magnetic Properties of Bi(Fe_{0.95}Co_{0.05})O₃ Ceramics. *Appl. Phys. Lett.* **2009**, *95* (11), 2007–2010. <https://doi.org/10.1063/1.3233944>
- (65) Geneste, G.; Paillard, C.; Dkhil, B. Polarons, Vacancies, Vacancy Associations, and Defect States in Multiferroic BiFeO₃. *Phys. Rev. B* **2019**, *99* (2), 024104(20). <https://doi.org/10.1103/PhysRevB.99.024104>
- (66) Yang, R.; Lin, S.; Fang, X.; Gao, X.; Zeng, M.; Liu, J. First-Principles Study on the Magnetic Properties in Mg Doped BiFeO₃ with and without Oxygen Vacancies. *J. Appl. Phys.* **2013**, *114* (23), 233912. <https://doi.org/10.1063/1.4850975>
- (67) Paudel, T. R.; Jaswal, S. S.; Tsymbal, E. Y. Intrinsic Defects in Multiferroic BiFeO₃ and Their Effect on Magnetism. *Phys. Rev. B* **2012**, *85* (10), 104409(8). <https://doi.org/10.1103/PhysRevB.85.104409>
- (68) Rojac, T.; Bencan, A.; Drazic, G.; Sakamoto, N.; Ursic, H.; Jancar, B.; Tavcar, G.; Makarovic, M.; Walker, J.; Malic, B.; Damjanovic, D. Domain-Wall Conduction in Ferroelectric BiFeO₃ Controlled by Accumulation of Charged Defects. *Nat. Mater.* **2017**, *16* (3), 322–327. <https://doi.org/10.1038/nmat4799>
- (69) Bencan, A.; Drazic, G.; Ursic, H.; Makarovic, M.; Komelj, M.; Rojac, T. Domain-Wall Pinning and Defect Ordering in BiFeO₃ Probed on the Atomic and Nanoscale. *Nat. Commun.* **2020**, *11*, 1762. <https://doi.org/10.1038/s41467-020-15595-0>
- (70) Haselmann, U.; Suyolcu, Y. E.; Wu, P.; Ivanov, Y. P.; Knez, D.; van Aken, P. A.; Chu, Y.; Zhang, Z. Negatively Charged In-Plane and Out-Of-Plane Domain Walls with Oxygen-Vacancy Agglomerations in a Ca-Doped Bismuth-Ferrite Thin Film. *ACS Appl. Electron. Mater.* **2021**, *3* (10), 4498–4508. <https://doi.org/10.1021/acsaem.1c00638>
- (71) Yamada, H.; Marinova, M.; Altuntas, P.; Crassous, A.; Bégon-Lours, L.; Fusil, S.; Jacquet, E.; Garcia, V.; Bouzheouane, K.; Gloter, A.; Villegas, J. E.; Barthélémy, A.; Bibes, M. Ferroelectric Control of a Mott Insulator. *Sci. Rep.* **2013**, *3*, 2834. <https://doi.org/10.1038/srep02834>
- (72) Crassous, A.; Bernard, R.; Fusil, S.; Bouzheouane, K.; Le Bourdais, D.; Enouz-Vedrenne, S.; Briatico, J.;
-

Bibliography

- Bibes, M.; Barthélémy, A.; Villegas, J. E. Nanoscale Electrostatic Manipulation of Magnetic Flux Quanta in Ferroelectric/Superconductor BiFeO₃/YBa₂Cu₃O_{7- δ} Heterostructures. *Phys. Rev. Lett.* **2011**, *107* (24), 247002(5). <https://doi.org/10.1103/PhysRevLett.107.247002>
- (73) Boyn, S.; Girod, S.; Garcia, V.; Fusil, S.; Xavier, S.; Deranlot, C.; Yamada, H.; Carrétéro, C.; Jacquet, E.; Bibes, M.; Barthélémy, A.; Grollier, J. High-Performance Ferroelectric Memory Based on Fully Patterned Tunnel Junctions. *Appl. Phys. Lett.* **2014**, *104* (5), 052909. <https://doi.org/10.1063/1.4864100>
- (74) Yamada, H.; Garcia, V.; Fusil, S.; Boyn, S.; Marinova, M.; Gloter, A.; Xavier, S.; Grollier, J.; Jacquet, E.; Carrétéro, C.; Deranlot, C.; Bibes, M.; Barthélémy, A. Giant Electroresistance of Super-Tetragonal BiFeO₃-Based Ferroelectric Tunnel Junctions. *ACS Nano* **2013**, *7* (6), 5385–5390. <https://doi.org/10.1021/nn401378t>
- (75) Choi, T.; Lee, S.; Choi, Y. J.; Kiryukhin, V.; Cheong, S.-W. Switchable Ferroelectric Diode and Photovoltaic Effect in BiFeO₃. *Science* **2009**, *324*, 5923. <https://doi.org/10.1126/science.1168636>
- (76) Boyn, S.; Grollier, J.; Lecerf, G.; Xu, B.; Locatelli, N.; Fusil, S.; Girod, S.; Carrétéro, C.; Garcia, K.; Xavier, S.; Tomas, J.; Bellaiche, L.; Bibes, M.; Barthélémy, A.; Saïghi, S.; Garcia, V. Learning through Ferroelectric Domain Dynamics in Solid-State Synapses. *Nat. Commun.* **2017**, *8*, 14736. <https://doi.org/10.1038/ncomms14736>
- (77) Seidel, J.; Martin, L. W.; He, Q.; Zhan, Q.; Chu, Y. H.; Rother, A.; Hawkrige, M. E.; Maksymovych, P.; Yu, P.; Gajek, M.; Balke, N.; Kalinin, S. V.; Gemming, S.; Wang, F.; Catalan, G.; Scott, J. F.; Spaldin, N. A.; Orenstein, J.; Ramesh, R. Conduction at Domain Walls in Oxide Multiferroics. *Nat. Mater.* **2009**, *8* (3), 229–234. <https://doi.org/10.1038/nmat2373>
- (78) Farokhipoor, S.; Noheda, B. Conduction through 71° domain Walls in BiFeO₃ Thin Films. *Phys. Rev. Lett.* **2011**, *107* (12), 127601(4). <https://doi.org/10.1103/PhysRevLett.107.127601>
- (79) Béa, H.; Bibes, M.; Ott, F.; Dupé, B.; Zhu, X. H.; Petit, S.; Fusil, S.; Deranlot, C.; Bouzheouane, K.; Barthélémy, A. Mechanisms of Exchange Bias with Multiferroic BiFeO₃ Epitaxial Thin Films. *Phys. Rev. Lett.* **2008**, *100* (1), 017204(4). <https://doi.org/10.1103/PhysRevLett.100.017204>
- (80) Chu, Y. H.; Martin, L. W.; Holcomb, M. B.; Gajek, M.; Han, S. J.; He, Q.; Balke, N.; Yang, C. H.; Lee, D.; Hu, W.; Zhan, Q.; Yang, P. L.; Fraile-Rodríguez, A.; Scholl, A.; Wang, S. X.; Ramesh, R. Electric-Field Control of Local Ferromagnetism Using a Magnetoelectric Multiferroic. *Nat. Mater.* **2008**, *7* (6), 478–482. <https://doi.org/10.1038/nmat2184>
- (81) Heron, J. T.; Trassin, M.; Ashraf, K.; Gajek, M.; He, Q.; Yang, S. Y.; Nikonov, D. E.; Chu, Y. H.; Salahuddin, S.; Ramesh, R. Electric-Field-Induced Magnetization Reversal in a Ferromagnet-Multiferroic Heterostructure. *Phys. Rev. Lett.* **2011**, *107* (21), 217202(5). <https://doi.org/10.1103/PhysRevLett.107.217202>
- (82) Allibe, J.; Fusil, S.; Bouzheouane, K.; Daumont, C.; Sando, D.; Jacquet, E.; Deranlot, C.; Bibes, M.; Barthélémy, A. Room Temperature Electrical Manipulation of Giant Magnetoresistance in Spin Valves Exchange-Biased with BiFeO₃. *Nano Lett.* **2012**, *12* (3), 1141–1145. <https://doi.org/10.1021/nl202537y>
- (83) Allibe, J.; Infante, I. C.; Fusil, S.; Bouzheouane, K.; Jacquet, E.; Deranlot, C.; Bibes, M.; Barthémy, A. Coengineering of Ferroelectric and Exchange Bias Properties in BiFeO₃ Based Heterostructures. *Appl. Phys. Lett.* **2009**, *95* (18), 182503. <https://doi.org/10.1063/1.3247893>
- (84) Zhang, X.; Wang, Y. H.; Zhang, D. L.; Zhang, G. Q.; Yang, H. L.; Miao, J.; Xu, X. G.; Jiang, Y. Electric-Field-Induced Change of the Magnetoresistance in the Multiferroic Spin-Valve Based on BiFeO₃ Film. *IEEE Trans. Magn.* **2011**, *47* (10), 3139–3142. <https://doi.org/10.1109/TMAG.2011.2148102>
-

Bibliography

- (85) Chu, S. H.; Singh, D. J.; Wang, J.; Li, E. P.; Ong, K. P. High Optical Performance and Practicality of Active Plasmonic Devices Based on Rhombohedral BiFeO₃. *Laser Photonics Rev.* **2012**, *6* (5), 684–689. <https://doi.org/10.1002/lpor.201280022>
- (86) Babicheva, V. E.; Zhukovsky, S. V.; Lavrinenko, A. V. Bismuth Ferrite as Low-Loss Switchable Material for Plasmonic Waveguide Modulator. *Opt. Express* **2014**, *22* (23), 28890. <https://doi.org/10.1364/oe.22.028890>
- (87) Guo, R.; You, L.; Zhou, Y.; Lim, Z. S.; Zou, X.; Chen, L.; Ramesh, R.; Wang, J. Non-Volatile Memory Based on the Ferroelectric. *Nat. Commun.* **2013**, *4*, 1990. <https://doi.org/10.1038/ncomms2990>
- (88) Yin, L.; Mi, W. Progress in BiFeO₃-Based Heterostructures: Materials, Properties and Applications. *Nanoscale* **2020**, *12* (2), 477–523. <https://doi.org/10.1039/c9nr08800h>
- (89) Lu, Z.; Li, P.; Wan, J. G.; Huang, Z.; Tian, G.; Pan, D.; Fan, Z.; Gao, X.; Liu, J. M. Controllable Photovoltaic Effect of Microarray Derived from Epitaxial Tetragonal BiFeO₃ Films. *ACS Appl. Mater. Interfaces* **2017**, *9* (32), 27284–27289. <https://doi.org/10.1021/acsami.7b06535>
- (90) Kundys, B.; Viret, M.; Colson, D.; Kundys, D. O. Light-Induced Size Changes in BiFeO₃ Crystals. *Nat. Mater.* **2010**, *9* (10), 803–805. <https://doi.org/10.1038/nmat2807>
- (91) Tian, Y.; Wei, L.; Zhang, Q.; Huang, H.; Zhang, Y.; Zhou, H.; Ma, F.; Gu, L.; Meng, S.; Chen, L. Q.; Nan, C. W.; Zhang, J. Water Printing of Ferroelectric Polarization. *Nat. Commun.* **2018**, *9*, 3809. <https://doi.org/10.1038/s41467-018-06369-w>
- (92) Schwarzkopf, J.; Fornari, R. Epitaxial Growth of Ferroelectric Oxide Films. *Prog. Cryst. Growth Charact. Mater.* **2006**, *52*, 159–212. <https://doi.org/10.1016/j.pcrysgrow.2006.06.001>
- (93) De Bonis, A.; Teghil, R. Ultra-Short Pulsed Laser Deposition of Oxides, Borides and Carbides of Transition Elements. *Coatings* **2020**, *10* (5), 501. <https://doi.org/10.3390/COATINGS10050501>
- (94) Sando, D.; Young, T.; Bulanadi, R.; Cheng, X.; Zhou, Y.; Weyland, M.; Munroe, P.; Nagarajan, V. Designer Defect Stabilization of the Super Tetragonal Phase in >70-Nm-Thick BiFeO₃ Films on LaAlO₃ Substrates. *Jpn. J. Appl. Phys.* **2018**, *57* (9), 0902B2. <https://doi.org/10.7567/JJAP.57.0902B2>
- (95) Sando, D.; Xu, B.; Bellaiche, L.; Nagarajan, V. A Multiferroic on the Brink: Uncovering the Nuances of Strain-Induced Transitions in BiFeO₃. *Appl. Phys. Rev.* **2016**, *3* (1), 011106. <https://doi.org/10.1063/1.4944558>
- (96) Moniz, S. J. A.; Quesada-Cabrera, R.; Blackman, C. S.; Tang, J.; Southern, P.; Weaver, P. M.; Carmalt, C. J. A Simple, Low-Cost CVD Route to Thin Films of BiFeO₃ for Efficient Water Photo-Oxidation. *J. Mater. Chem. A* **2014**, *2* (9), 2922–2927. <https://doi.org/10.1039/c3ta14824f>
- (97) Williams, D. B.; Carter, C. B. *Transmission Electron Microscopy*; Springer, 2009.
- (98) Franken, L. E.; Grünewald, K.; Boekema, E. J.; Stuart, M. C. A. A Technical Introduction to Transmission Electron Microscopy for Soft-Matter: Imaging, Possibilities, Choices, and Technical Developments. *Small* **2020**, *16* (14), 1906198. <https://doi.org/10.1002/sml.201906198>
- (99) Urban, K.; Kabius, B.; Haider, M.; Rose, H. A Way to Higher Resolution: Spherical-Aberration Correction in a 200 KV Transmission Electron Microscope. *J. Electron Microsc. (Tokyo)*. **1999**, *48* (6), 821–826. <https://doi.org/10.1093/oxfordjournals.jmicro.a023753>
- (100) Pennycook, S. J.; Jesson, D. E. High-Resolution Z-Contrast Imaging of Crystals. *Phys. Rev. Lett.* **1990**, *64* (8), 938–941. <https://doi.org/10.1103/PhysRevLett.64.938>
-

Bibliography

- (101) Klenov, D. O.; Stemmer, S. Contributions to the Contrast in Experimental High-Angle Annular Dark-Field Images. *Ultramicroscopy* **2006**, *106*, 889–901. <https://doi.org/10.1016/j.ultramic.2006.03.007>
- (102) Findlay, S. D.; Shibata, N.; Sawada, H.; Okunishi, E.; Kondo, Y.; Ikuhara, Y. Dynamics of Annular Bright Field Imaging in Scanning Transmission Electron Microscopy. *Ultramicroscopy* **2010**, *110* (7), 903–923. <https://doi.org/10.1016/j.ultramic.2010.04.004>
- (103) Lohr, M.; Schregle, R.; Jetter, M.; Wächter, C.; Wunderer, T.; Scholz, F.; Zweck, J. Differential Phase Contrast 2.0-Opening New “Fields” for an Established Technique. *Ultramicroscopy* **2012**, *117*, 7–14. <https://doi.org/10.1016/j.ultramic.2012.03.020>
- (104) Kothleitner, G.; Neish, M. J.; Lugg, N. R.; Findlay, S. D.; Grogger, W.; Hofer, F.; Allen, L. J. Quantitative Elemental Mapping at Atomic Resolution Using X-Ray Spectroscopy. *Phys. Rev. Lett.* **2014**, *112* (8), 085501. <https://doi.org/10.1103/PhysRevLett.112.085501>
- (105) D’Alfonso, A. J.; Freitag, B.; Klenov, D.; Allen, L. J. Atomic-Resolution Chemical Mapping Using Energy-Dispersive x-Ray Spectroscopy. *Phys. Rev. B* **2010**, *81* (10), 100101(4). <https://doi.org/10.1103/PhysRevB.81.100101>
- (106) Kimoto, K.; Asaka, T.; Nagai, T.; Saito, M.; Matsui, Y.; Ishizuka, K. Element-Selective Imaging of Atomic Columns in a Crystal Using STEM and EELS. *Nature* **2007**, *450*, 702–704. <https://doi.org/10.1038/nature06352>
- (107) Catalan, G.; Sardar, K.; Church, N. S.; Scott, J. F.; Harrison, R. J.; Redfern, S. A. T. Effect of Chemical Substitution on the Néel Temperature of Multiferroic Bi_{1-x}CaxFeO₃. *Phys. Rev. B* **2009**, *79* (21), 212415. <https://doi.org/10.1103/PhysRevB.79.212415>
- (108) Cai, Z.; Kubicek, M.; Fleig, J.; Yildiz, B. Chemical Heterogeneities on La_{0.6}Sr_{0.4}CoO_{3-δ} Thin Films- Correlations to Cathode Surface Activity and Stability. *Chem. Mater.* **2012**, *24* (6), 1116–1127. <https://doi.org/10.1021/cm203501u>
- (109) Jang, H.; Kerr, G.; Lim, J. S.; Yang, C. H.; Kao, C. C.; Lee, J. S. Orbital Reconstruction in a Self-Assembled Oxygen Vacancy Nanostructure. *Sci. Rep.* **2015**, *5*, 12402. <https://doi.org/10.1038/srep12402>
- (110) Knez, D.; Dražić, G.; Chaluvadi, S. K.; Orgiani, P.; Fabris, S.; Panaccione, G.; Rossi, G.; Ciancio, R. Unveiling Oxygen Vacancy Superstructures in Reduced Anatase Thin Films. *Nano Lett.* **2020**, *20* (9), 6444–6451. <https://doi.org/10.1021/acs.nanolett.0c02125>
- (111) Geng, W. R.; Tian, X. H.; Jiang, Y. X.; Zhu, Y. L.; Tang, Y. L.; Wang, Y. J.; Zou, M. J.; Feng, Y. P.; Wu, B.; Hu, W. T.; Ma, X. L. Unveiling the Pinning Behavior of Charged Domain Walls in BiFeO₃ Thin Films via Vacancy Defects. *Acta Mater.* **2020**, *186*, 68–76. <https://doi.org/10.1016/j.actamat.2019.12.041>
- (112) Campanini, M.; Erni, R.; Yang, C. H.; Ramesh, R.; Rossell, M. D. Periodic Giant Polarization Gradients in Doped BiFeO₃ Thin Films. *ACS Nanoletters* **2018**, *18* (2), 717–724. <https://doi.org/10.1021/acs.nanolett.7b03817>
- (113) Haselmann, U.; Radlinger, T.; Pei, W.; Popov, M. N.; Spitaler, T.; Romaner, L.; Ivanov, Y. P.; Chen, J.; He, Y.; Kothleitner, G.; Zhang, Z. Ca Solubility in a BiFeO₃ Based System with a Secondary Bi₂O₃ Phase on a Nanoscale. *J. Phys. Chem. C* **2022**, at the time of submission of the dissertation in the “under review” status
- (114) Yun, K. Y.; Ricinschi, D.; Kanashima, T.; Noda, M.; Okuyama, M. Giant Ferroelectric Polarization beyond 150 μC/cm² in BiFeO₃ Thin Film. *Jpn. J. Appl. Phys.* **2004**, *43* (No. 5A), L647–L648. <https://doi.org/10.1143/jjap.43.l647>
-

Bibliography

- (115) Wang, J.; Neaton, J. B.; Zheng, H.; Nagarajan, V.; Ogale, S. B.; Liu, B.; Viehland, D.; Vaithyanathan, V.; Schlom, D. G.; Waghmare, U. V.; Spaldin, N. A.; Rabe, K. M.; Wuttig, M.; Ramesh, R. Epitaxial BiFeO₃ Multiferroic Thin Film Heterostructures. *Science* **2003**, *299* (5613), 1719–1722. <https://doi.org/10.1126/science.1080615>
- (116) Das, R. R.; Kim, D. M.; Baek, S. H.; Eom, C. B.; Zavaliche, F.; Yang, S. Y.; Ramesh, R.; Chen, Y. B.; Pan, X. Q.; Ke, X.; Rzechowski, M. S.; Streiffer, S. K. Synthesis and Ferroelectric Properties of Epitaxial BiFeO₃ Thin Films Grown by Sputtering. *Appl. Phys. Lett.* **2006**, *88* (24), 242904. <https://doi.org/10.1063/1.2213347>

7. PUBLICATIONS

Publication A:⁵⁶

Haselmann, U.; Haberkorn, G.; Pei, W.; Popov, M. N.; Romaner, L.; Knez, D.; Chen, J.; Ghasemi, A.; He, Y.; Kothleitner, G.; Zhang, Z.

Study on Ca Segregation toward an Epitaxial Interface between Bismuth Ferrite and Strontium Titanate.

Published in: *ACS Appl. Mater. Interfaces* **2020**, *12* (10), 12264–12274.
<https://doi.org/10.1021/acsami.9b20505>.

Reprinted under the [Creative Commons Attribution 4.0 License](https://creativecommons.org/licenses/by/4.0/) from ref.⁵⁶, Copyright 2020, American Chemical Society

Publication B:⁷⁰

Haselmann, U.; Suyolcu, Y. E.; Wu, P.; Ivanov, Y. P.; Knez, D.; van Aken, P. A.; Chu, Y.; Zhang, Z.

Negatively Charged In-Plane and Out-Of-Plane Domain Walls with Oxygen-Vacancy Agglomerations in a Ca-Doped Bismuth-Ferrite Thin Film.

Published in: *ACS Appl. Electron. Mater.* **2021**, *3* (10), 4498–4508.
<https://doi.org/10.1021/acsaelm.1c00638>.

Reprinted under the [Creative Commons Attribution 4.0 License](https://creativecommons.org/licenses/by/4.0/) from ref.⁷⁰, Copyright 2021 by the authors, Published by American Chemical Society

Publication C:¹¹³

Haselmann, U.; Radlinger, T.; Pei, W.; Popov, M. N.; Spitaler, T.; Romaner, L.; Ivanov, Y. P.; Chen, J.; He, Y.; Kothleitner, G.; Zhang, Z.

Ca Solubility in a BiFeO₃ Based System with a Secondary Bi₂O₃ Phase on a Nanoscale.

Submitted to: *J. Phys. Chem. C* **2022**; at the time of submission of the dissertation in the “under review” status

Publication A

Study on Ca Segregation toward an Epitaxial Interface between Bismuth Ferrite and Strontium Titanate

Ulrich Haselmann¹, Georg Haberfehlner², Weijie Pei³, Maxim N. Popov⁴, Lorenz Romaner⁴, Daniel Knez⁵, Jian Chen³, Arsham Ghasemi¹, Yunbin He^{3*}, Gerald Kothleitner^{2,5}, and Zaoli Zhang^{1,6*}

¹ Erich Schmid Institute of Materials Science, Austrian Academy of Sciences, Leoben, Austria

² Institute for Electron Microscopy and Nanoanalysis, Graz University of Technology, Graz, Austria

³ School of Materials Science & Engineering, Hubei University, Wuhan, Hubei, China

⁴ Materials Center Leoben Forschung GmbH, Leoben, Austria

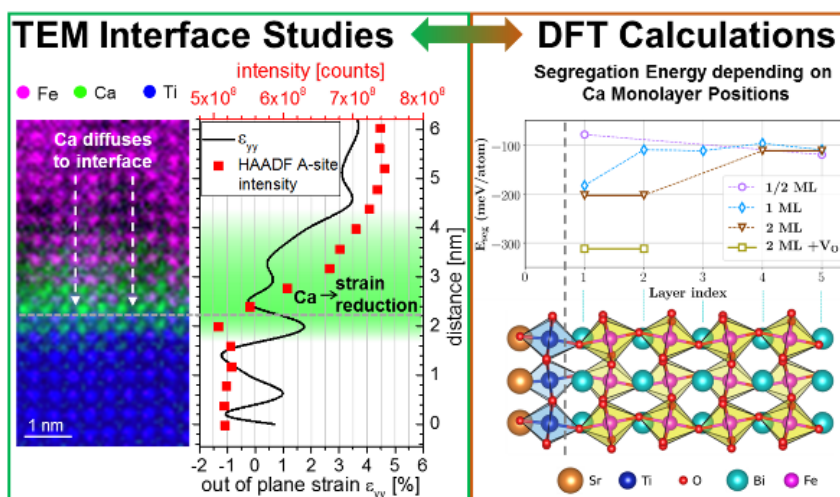
⁵ Graz Centre for Electron Microscopy, Austrian Cooperative Research, Graz, Austria

⁶ Institute of Material Physics, Montanuniversität Leoben, Leoben, Austria

*Corresponding authors: zaoli.zhang@oeaw.ac.at, ybhe@hubu.edu.cn

ABSTRACT:

Segregation is a crucial phenomenon, which has to be considered in functional material design. Segregation processes in perovskite oxides have been the subject of ongoing scientific interest, since they can lead to a modification of properties and a loss of functionality. Many studies in oxide thin films have focused on segregation toward the surface using a variety of surface sensitive analysis techniques. In contrast, here, we report a Ca segregation toward an in-plane compressively strained heterostructure interface in a Ca- and Mn-codoped bismuth ferrite film. We are using advanced transmission electron microscopy



techniques, X-ray photoelectron spectroscopy and density functional theory (DFT) calculations. Ca segregation is found to trigger atomic and electronic structure changes at the interface. This includes the reduction of the interface strain according to the Ca concentration gradient, interplanar spacing variations and oxygen vacancies at the interface. The experimental results are supported by DFT calculations, which explore two segregation scenarios, i.e., one without oxygen vacancies and Fe oxidation from 3+ to 4+ and one with vacancies for charge compensation. Comparison with electron energy loss spectroscopy (EELS) measurements confirms the second segregation scenario with vacancy formation. The findings contribute to the understanding of segregation and indicate promising effects of a Ca rich buffer layer in this heterostructure system.

KEYWORDS: BiFeO₃, oxide heterostructure interface, segregation, atomic-resolution TEM, EELS and EDS, oxygen vacancy, density functional theory (DFT)

1. INTRODUCTION

Perovskite materials have a structure of 2 or more cations and oxygen in the arrangement ABO₃ and provide a huge variety of physical phenomena and functional properties.¹ One of the most promising properties is the coupling between ferroelectricity and the magnetic properties in multiferroic materials, which has attracted significant attention in the past years. Besides the fascinating physics underlying this effect, its potential applications include memory devices with superior speed and storage density,^{2,3} spin valves, spintronic devices and sensors.⁴ BiFeO₃ is among the few single-phase magnetoelectric multiferroics with Néel and Curie temperatures far above room temperature and is therefore a material of strong relevance to practical applications. The successful demonstration of the electrical control of antiferromagnetic domains further increased the interest in BiFeO₃ (BFO).⁵

Doping of BFO with cations such as Ca or Mn offers further possibilities for tuning the magnetic and electric properties. In particular, it has been shown that Ca doping on the A-site leads to an increase in the oxidation state of Fe atoms which has experimentally been determined to be 4+ at 300K and a pairing of 3+ and 5+ at 15K.⁶ Furthermore, Mn doping on the B-site has shown to restore the weak ferromagnetic behavior received through Ca doping to the antiferromagnetic behavior of pure BiFeO₃.⁷

For such doping-related phenomena, segregation processes of cations are a critical aspect since they can lead to strong agglomeration at surfaces, grain boundaries or interfaces and a depletion

of the bulk. With this they have a significant influence on the behavior and function.⁸ Therefore, a deeper understanding of the processes underlying the segregation process is required in order to prevent property degradation.

There are many studies available on segregation toward surfaces, since there is a variety of surface sensitive but also surface limited analysis techniques. This includes low-energy ion scattering (LEIS), Auger-electron spectroscopy (AES), X-ray photon spectroscopy (XPS), secondary ion mass spectroscopy (SIMS), atomic force microscopy (AFM) and scanning tunneling microscopy (STM).⁹ Different factors for segregation, which have been so far identified⁹ include non-stoichiometry of the cations,¹⁰ the charge and the radius of the dopants,^{11–13} the crystallinity of the sample,⁸ lattice strain,¹⁴ temperature history,^{11,15} external electrical polarization,¹⁶ and the gas atmosphere, in particular, the oxygen partial pressure.¹¹

Since experimental studies of segregation processes toward nonsurface interfaces require either cross-sectional transmission electron microscopy (TEM) analysis, atom probe tomography (APT) or coherent Bragg rod analysis (COBRA)¹⁷, the segregation toward nonsurface interfaces is not as widely studied for perovskites. In the study of Yoon *et al.* the motivation for the choice of Ta and La as dopants in $\text{Ca}_{1/4}\text{Cu}_{3/4}\text{Ti}_{1-x}\text{Ta}_x\text{O}_3$ and $\text{Ca}_{1/4-y}\text{La}_y\text{Cu}_{3/4}\text{TiO}_3$ was to minimize the influence of the dopant radius and focus on the space charge effect.¹⁸ Thereby it was demonstrated that besides the influence of the electrostatic potential near the interface, the segregation behavior is the same whether the segregation is toward a surface, the interfaces with secondary Cu excess phases or a grain boundary with or without amorphous materials in between.¹⁸ Interestingly, for epitaxial $\text{La}_{2/3}\text{Ca}_{1/3}\text{MnO}_3$ thin films on (100) and (110) SrTiO_3 (STO) substrates, a Ca enrichment close to the surface could only be observed for very thin films but not for films above 14 nm thickness.¹⁹

In studies of heterostructures for solid oxide cells, it was shown that in $(\text{LaSr})\text{CoO}_3/\text{LaSrCoO}_4$ heterostructures a Sr enrichment in the interfacial region stabilizes it against detrimental Sr segregation receiving a much better surface exchange coefficient.^{20,21} In a $(\text{NdSr})\text{CoO}_3/(\text{NdSr})\text{CoO}_4$ multilayered structure, higher Sr and Co segregation could be observed for consistent crystal orientation, while grain boundaries hindered it.^{20,22}

Segregation processes in BiFeO_3 have been scarcely studied. For a BiFeO_3 thin film on a (100) LaAlO_3 chemical interdiffusion of La atoms into the first atomic layers of the film with the suspected reason for stress reduction were found.²³ For B-site Ti doping in BiFeO_3 nanograins a segregation toward the grain boundary has been observed²⁴.

Exsolution effects can be seen in a $\text{Bi}_2\text{FeMnO}_3$ thin film on STO substrate, which has led to Mn^{4+} -rich antiphase boundary (APB) defects, which nucleate at the substrate where they have Ti at the core and form a stepped structure. Below this APBs the film is highly strained, while above it is relaxed and close to bulk state.²⁵ Besides Nd nanorods formed through exsolution^{26,27}, Ti rich APBs are formed in Nd and Ti co-doped BFO separating tetragonal distorted regions with strong polar ordering at each side of the defect²⁸. Similar structures have been reported in other BFO based systems.^{29,30}

In this work, we demonstrate the segregation of the Ca dopant in a bismuth ferrite thin film at the interface with a strontium titanate substrate, which was formed via diffusion during and shortly after the thin film deposition, while still at high deposition temperatures of 700°C , using various transmission electron microscopy (TEM) techniques as well as density functional theory (DFT) calculations. Atomic-resolution scanning transmission electron microscopy (STEM) with simultaneous recording of high-angle annular dark field (HAADF) images, electron energy loss spectroscopy (EELS), and energy-dispersive X-ray (EDS) spectroscopy reveal that the vast majority of available Ca is agglomerated at the interface. Its concentration at the interface leads to the formation of oxygen vacancies, while the oxidation state of Fe^{3+} of an undoped BiFeO_3 film is maintained. High-resolution transmission electron microscopy (HRTEM) examinations were performed to analyze the local strain states via geometric phase analysis (GPA) at the interface and revealed that, in contrast to a film without Ca, its agglomeration at the interface leads to a reduction of the compressive strain exerted by the substrate. The intensity analysis of large area HAADF data and GPA analysis showed that the strain reduction is directly linked to the Ca content at the interface. DFT calculations showed that the Ca agglomeration at the interface was energetically more favorable and the interatomic distances from the calculations show good agreement with the measured ones. To our knowledge, this is the first observation of A-site dopant diffusion toward interfaces in BiFeO_3 and the understanding of this process is crucial to prevent device failure in future applications.

2. EXPERIMENTAL AND CALCULATION DETAILS

2.1. Thin Film Fabrication. Two Bismuth Ferrite thin films were fabricated via pulsed laser deposition (PLD): A Ca- and Mn codoped $\text{Bi}_{0.98}\text{Ca}_{0.02}\text{Fe}_{0.95}\text{Mn}_{0.05}\text{O}_3$ (BCFMO) film and an only Mn-doped $\text{BiFe}_{0.95}\text{Mn}_{0.05}\text{O}_3$ (BFMO) film. The thin films were deposited on a single-crystalline (100) oriented SrTiO_3 substrate (Kejing Materials Technology Co. Ltd., China) by PLD

technique using a KrF excimer laser (Lambda Physik COMPEX PRO 205F, $\lambda = 248$ nm) as the ablation source with a pulse repetition rate of 5 Hz. The laser beam energy was fixed at 320 mJ/pulse for the Ca doped and at 280 mJ/pulse for the non-Ca-doped film. Prior to film deposition the substrates were ultrasonically cleaned with acetone, alcohol and pure water and subsequently blown dry with high-purity nitrogen gas. Afterward they were immediately loaded into the PLD chamber. The vacuum chamber was evacuated to about 10^{-4} Pa. During film deposition, the substrate was kept at a temperature of 700°C and the oxygen pressure was fixed at 3.0 Pa. The total deposition time for both film samples was 30 min resulting in a thickness of approximately 50 nm for the Ca doped film and 20 nm for the non-Ca doped film. The crystalline structure of the films was investigated using high-resolution X-ray diffraction (HRXRD) with a four-circle single-crystal diffractometer (D8 discover, Bruker, Germany) and a Cu $K\alpha 1$ monochromatic radiation source ($\gamma = 1.5406$ Å). X-Ray Photoelectron Spectroscopy (XPS) using an ESCALAB 250Xi (Thermo Fisher Scientific) was performed to confirm that there was a constant Ca level in the target during deposition and to investigate the surfaces of the thin films.

2.2. Sample Preparation. Cross-sectional TEM samples were prepared via the sandwich technique using two film pieces glued together film side to film side in a Ti holder. Afterward, the holder and samples were ground from both sides to reach a residual thickness of ≈ 80 μm and then dimpled from one side to a residual thickness of ≈ 11 μm . For final thinning conventional Ar^+ ion beam milling was done using a Gatan precision ion polishing system (PIPS) Model 691 at 3 keV acceleration voltage and first 6° for 20 min and subsequent 4° for a short time until the sample showed a thin area.

2.3. Data Acquisition. High-resolution transmission electron microscope (HRTEM) investigations were performed on a JEOL JEM 2100F with an image-side C_s corrector operating at 200 keV and using a Gatan Orius SC1000 camera. An indicated magnification of 600 000 resulting in a pixel size of 0.21 Å and an exposure time of 0.7s was used. The analytical STEM investigations were carried out on a FEI Titan³ operated at 300 keV at a convergence angle of 19.7 mrad. For analytical data collection a GIF quantum³¹ energy filter (Gatan) and a super-X EDX detector³² (FEI) were used with simultaneous HAADF image acquisition with 38 mrad inner and 137 mrad outer detection angles on the Gatan 806 HAADF STEM detector. The EELS collection semiangle was 20.5 mrad, the dispersion index was 5, and for the spectrometer channel width 0.25 eV was chosen. All EELS spectra were recorded in the dual mode with the energy

range of the core loss region from 300 eV to 812 eV. The analytical EELS and EDX STEM data were recorded with a pixel size of 0.69 Å. The pixel time for HAADF and EDX data acquisition was 10 ms. EELS pixel time was split into 9.95 ms for the core loss region and 0.05 ms for the zero-loss region. The HAADF survey image before the EDX line scan was recorded with a pixel size of 0.23 Å and a pixel time of 3.05 μs summing up 5 frames. For the EDX line scan, a step size of 0.7 Å was chosen and summing up the signal in the perpendicular direction above 64 pixels with a pixel width of 0.57 Å and a single pixel time of 7.5 ms totaling to 500 ms exposure time per line scan step. The HAADF data without analytical data collection was gained using the Fischione HAADF detector with 49 mrad inner and 242 mrad outer detection angles. The pixel size was 0.11 Å with a pixel time of 18 μs.

2.4. Data Evaluation. For the EELS elemental atomic resolution map data were preprocessed with the DM plugin temDM MSA basic version³³ applying principal component analysis (PCA) using components 1-7. The EELS and the EDX data were processed using the built-in functions of Gatan Digital Micrograph 2.3. To determine automatically the edge onset, a MatLab program was written. For the strain analysis, GPA for Digital Micrograph v4.0 from HREM Research Company was used. For the detailed intensity analysis in the HAADF images a homemade MatLab script written in MathWorks Inc. MatLab (version R2017b) was used. Thereby, the positions of the atomic columns in the image are determined by searching for local maxima. The experimental image was filtered with a batch principal component analysis (patchPCA) to reduce the influence of noise on the performance of the algorithm. The peak positions are refined by Gaussian fitting with subpixel precision and are then used as a basis for Voronoi tessellation. Based on these received cells, the absolute intensity from the unfiltered image is determined, and integrated over a defined area corresponding to each atomic column. Columns that lie not entirely in the image are excluded.³⁴ The integrated column intensity is a robust measurement as it has been shown to be insensitive to probe shape and defocusing.³⁵ Image simulations for the comparison with HRTEM images were done with JEMS Version 4.7031U2018b21 using 200 keV acceleration voltage, $C_c = 1.2$ mm, $C_s = -5$ μm, $C_5 = 10$ mm, an energy spread of 0.8 eV, a lens stability of 0.1 ppm, a magnetic noise of 20 pm, a voltage stability of 0.5 ppm, and a beam half convergence of 1.0 nm⁻¹. The real HRTEM images were filtered with the HRTEM filter from D. R. G. Mitchell, version 1.3 from February 2007 using the standard values of 5 steps, a delta of 2%, 20 cycles, BW b = 3 and BW Ro = 0.5. With SRIM software, deposition kinetic simulations were done. Thereby the assumption was that Ca and Bi have the same velocity in the deposition process and when assuming a primary energy for Bi of 1 keV the

resulting Ca value was 0.191 keV. The deposition was simulated for 200 nm thick layers, being either STO or BFO.

2.5. DFT Calculations. Ab initio calculations were performed using projector augmented wave (PAW)³⁶ method as implemented in the VASP code.³⁷⁻⁴⁰ The electron exchange-correlation effects were treated using PBEsol⁴¹ generalized gradient approximation. To cope with the d-electron delocalization problem, the DFT+U method of Dudarev *et al.*⁴² was employed. The U parameters applied to Ti and Fe sites were set equal to 4 eV, in accordance with previous studies.^{43,44} The energy cut-off used for the basis set expansion was 520 eV. The supercell used for modeling the interface between STO and BFO consisted of the stoichiometric slabs of STO and BFO joined together along [001] to result in a TiO₂-BiO stacking at the interface and a vacuum layer (see Figure S1). The individual slabs were constructed from fully relaxed BFO (R3c) and STO. Since STO was used as a substrate for BFO, the equilibrium lattice parameter of STO was imposed when constructing the interface model with the exception of the last SrO and TiO₂ layers. The thickness of the slabs and the vacuum layer were chosen so as to minimize the surface-induced effects, and, in addition, the dipole correction was applied.⁴⁵ The G-type antiferromagnetic order was maintained in BFO. The Brillouin zone integration was performed using a 6x6x1 k-point grid. All atoms in STO slab were fixed, except for those belonging to the two atomic layers adjacent to BFO. The positions of all other atoms were relaxed until the residual forces were less than 10⁻² eV/Å. The segregation energy was calculated as:

$$E_{\text{seg}} = \frac{E(n * \text{Ca@IF}) - E(\text{IF}) - n * [E(\text{Ca@Bulk}) - E(\text{Bulk})]}{n}.$$

Here, $E(n * \text{Ca@IF})$, $E(\text{Ca@Bulk})$, $E(\text{IF})$, $E(\text{Bulk})$ are the total energies of the supercell containing n Ca atoms at the interface, a 4x4x4 BFO supercell with one Ca atom, and similar supercells containing no Ca atoms. In the case of V_O charge compensation, oxygen vacancies were introduced in close proximity to the Ca atoms. The structural models were visualized using the VESTA software.⁴⁶

3. RESULTS AND DISCUSSION

3.1. Atomic Structure and Chemical Composition at the Interface. The interface structure and composition were investigated in the [010]_c zone axis orientation regarding

the cubic STO substrate, which also corresponds to the $[010]_{pc}$ (pseudocubic) axis of the bismuth ferrite thin films. The HAADF image in Figure 1a shows that the film-substrate interface of the Ca- and Mn-codoped film is perfectly epitaxial without any visible defects. Both the elemental maps for Fe, Ca, and Ti gained from EELS image data (see Figure 1b), and the elemental ratio as line profiles from the EDS data for all cationic elements (see Figure 1c) reveal that the Ca is concentrated in the film area close to the interface sitting as expected on the A-site (Bi) position in between the B-site positions (Fe). In the first A-site layer of the film Ca is even the majority atomic species with an approximate ratio of 3:2 with regard to the Bi atoms on these positions. The Ca concentration in the film decreases with increasing distance from the substrate-film interface and is below detectability after an interface distance of approximately 7 nm (Figure 2a,b). Due to the XPS data of the PLD target we can be sure that the Ca level is constant during the deposition (Figure S2).

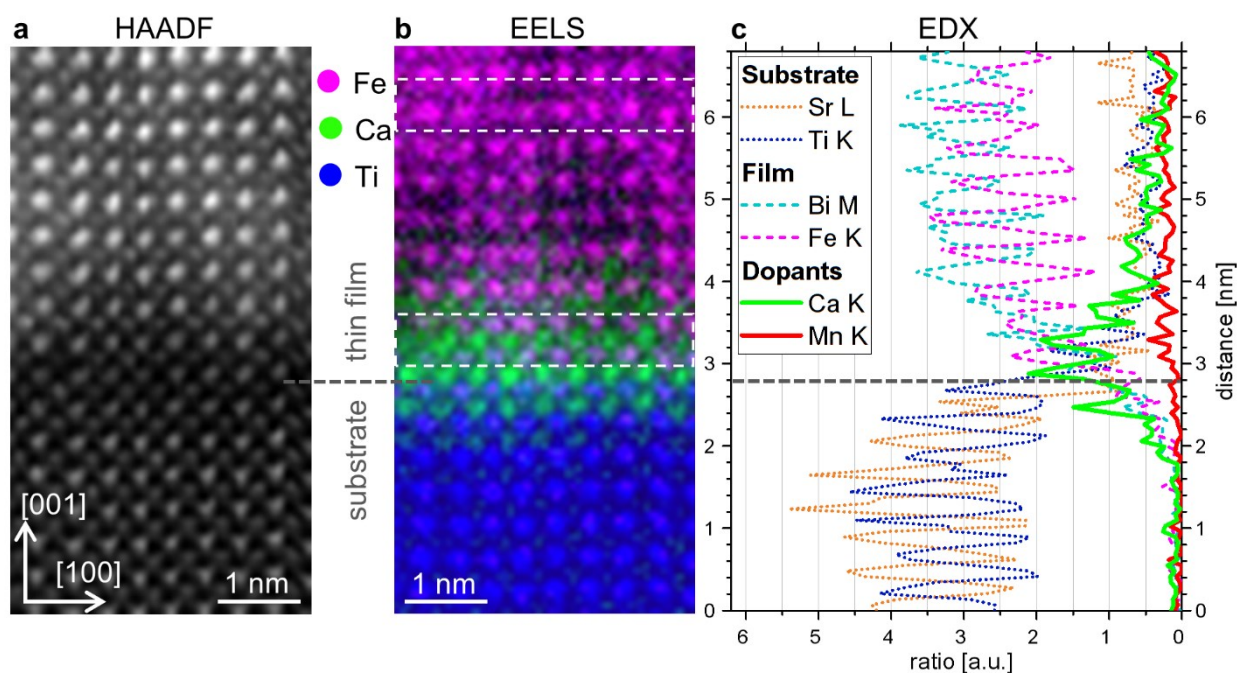


Figure 1. Interface structure and chemical composition of the Ca doped film. (a) HAADF image of the interface along the $[010]_c$ zone axis. (b) Elemental map from the area of the HAADF image in (a) for the elements Ti (blue), Ca (green) and Fe (magenta) gained by processing the EELS spectrum image data. The gray dashed line indicates the exact position of the substrate film interface. The white dashed rectangles indicate the area considered for the Fe oxidation state analysis in Figure 3. (c) Profiles of elemental ratios from all sample elements including the dopants Ca and Mn (red) gained from EDS data by summing up along the $[100]$ orientation.

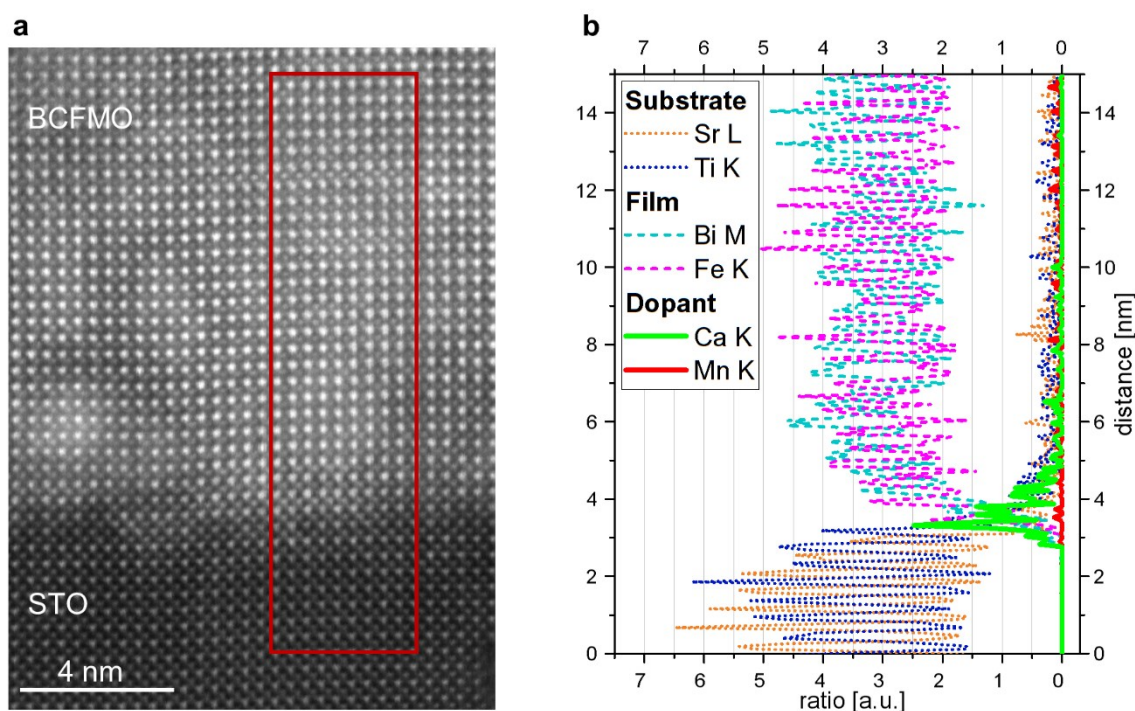


Figure 2. Ca content far from the interface. (a) HAADF image of the interface of the Ca doped film. The red rectangle indicates the area where the EDS line scan was gained from. (b) EDS line profile with the elemental ratio indicates that in approximately 7 nm from the interface, the film contains no Ca anymore.

To exclude the possibility that deposition kinetic effects are the cause for the Ca agglomeration at the interface, SRIM simulations were conducted and the backscattering ratios and implantation depths of Ca and Bi on STO and BFO targets were compared. However, neither of these two values provided an explanation for the Ca agglomeration.

Therefore, the conclusion is, that the Ca gradient toward the interface must have been formed during and shortly after the thin film deposition, while the high substrate temperature of 700°C, which corresponds for BiFeO₃ to 0.79*T_m (T_m: melting point temperature, 79% of the melting point temperature), significantly facilitated diffusion of the originally homogeneously distributed Ca and enabled its segregation at the interface. To our knowledge, there is no data about Ca diffusion in BiFeO₃. The study of Francois-Saint-Cyr *et al.* investigated the diffusion coefficients for a range of different elements in amorphous SiO₂.⁴⁷ Thereby, Ca showed by far the highest diffusion coefficient D in the range of 10⁻¹⁶ cm/s² at a temperature of T = 1000°C = 0.64*T_m and is even larger than the one for oxygen diffusion.⁴⁷ In crystalline MgO at T = 700°C = 0.31*T_m the Ca diffusion coefficient is in the range of 10⁻¹⁵ cm/s².⁴⁸ Lanthanide cobalt oxides (LnCoO₃) show tracer diffusion coefficients in the range of 10⁻¹⁴ cm/s² for T = 700°C = 0.57*T_m.^{49,50} Assuming an average of these values as Ca diffusion coefficient in BiFeO₃, the average diffusion distance

during 1h at 700°C (30 min deposition time including the time before and during cooling) corresponds to average diffusion distance of 50 nm (for a value of $D = 10^{-15}$ cm²/s). Considering that the film thickness is 50 nm, it is reasonable that diffusion and segregation of the Ca from the whole film area toward the interface are reasonable.

In addition, Figure 1 shows a clear indication of intermixing between the film and substrate material which is typical for this kind of heterostructure.²³ In the first two layers of the substrate, a clear Ca signal can be detected in the EELS and EDS signals and additionally also a Bi signal in the first layer (EDS). In addition, Sr and Ti can be clearly identified in the first two layers of the thin film. The termination layer of the substrate is identified as TiO₂ (Figure 1b), which is the expected one for an untreated STO substrate. Opposite to the Ca, the Mn dopant shows a homogenous distribution within the film.

Note that since no defects at the film interface could be found, of a Ca rich buffer layer at an BFMO/STO interface could manifest as successful strategy against the unwanted formation of Mn rich APB at the interface.²⁵ However, further studies are necessary, since the effect reported by MacLaren *et al.*²⁵ appeared at films with much higher Mn doping ratios of 50% compared to 5% used in this study, which might also critically influence the formation of APBs.

3.2. Influence of Ca on the interfacial electronic structure. Ca is an alkaline earth metal and offers only two electrons in the *sp* valence complex in contrast to Bi, which has three electrons. Hence, Ca leads to p-type or hole doping. There are two n-type or electron-doping mechanisms, which can occur and counteract the p-type doping through Ca. These mechanisms are either the creation and implementation of oxygen vacancies or the oxidation of a fraction of Fe³⁺ into Fe⁴⁺.⁵¹⁻⁵³ For example, in the CaFeO₃ perovskite, where all Bi atoms are replaced with Ca, the Fe atoms are found in the 4+ oxidation state.^{53,54} Therefore, to understand the interface structure and chemistry better, analyzing the Fe oxidation states is crucial.

Electron energy-loss near edge structures (ELNES) of Fe-L and O-K edges can be used to determine the oxidation state of the Fe atoms.^{55,56} It has been previously shown that the energy onset difference (ΔE) between the O-K and Fe-L₃ edge shows a clear correlation with the Fe oxidation state, where an increase would mean a shift from 3+ to a larger oxidation states.^{55,56} However, as can be seen in Figure 3a, there is no change in ΔE in a Ca rich interface region compared to a Ca poor region (3 nm away from the interface). The exact locations where the spectra have been recorded are indicated by the white rectangles in Figure 1b. Furthermore, the

measured energy onset difference of $\Delta E = 178.00 \pm 0.25$ eV corresponds within the measurement tolerance to the values in the literature of 178.25 ± 0.30 eV⁵⁶ and 178.5 ± 0.25 eV.⁵⁵ We defined the edge onset as the point where the edge exceeds 15% of the edge maximum, to prevent falsifying influence from pre-peaks and noise, as suggested by Tan *et al.*⁵⁵ In Figure 3b it becomes obvious that, while the O-K edge shape changes in the Ca rich interface region compared to the Ca poor region, the onset remains unchanged. The change in the edge simply stems from the overlapping of the two different O-K edge shapes in the substrate and the film (Figure S3). Likewise, the onset position of the Fe-L₃ edge does not change as can be seen in Figure 3c. Additionally, the ratio of the Fe-L₃ and L₂ edges is also an indication of the oxidation state and known to have its maximum for Fe³⁺.⁵⁵ The L₃/L₂ ratio, which does not decrease in the Ca rich area as becomes obvious in Figure 3c for the normalized Fe-L edges, is a further indication that a shift to higher Fe oxidation states does not take place. Summarizing, we find that Fe atoms in the Ca rich interface region remain in the 3+ oxidation state, which suggests that oxygen vacancies are present at the interface to counteract the p-type doping of Ca.

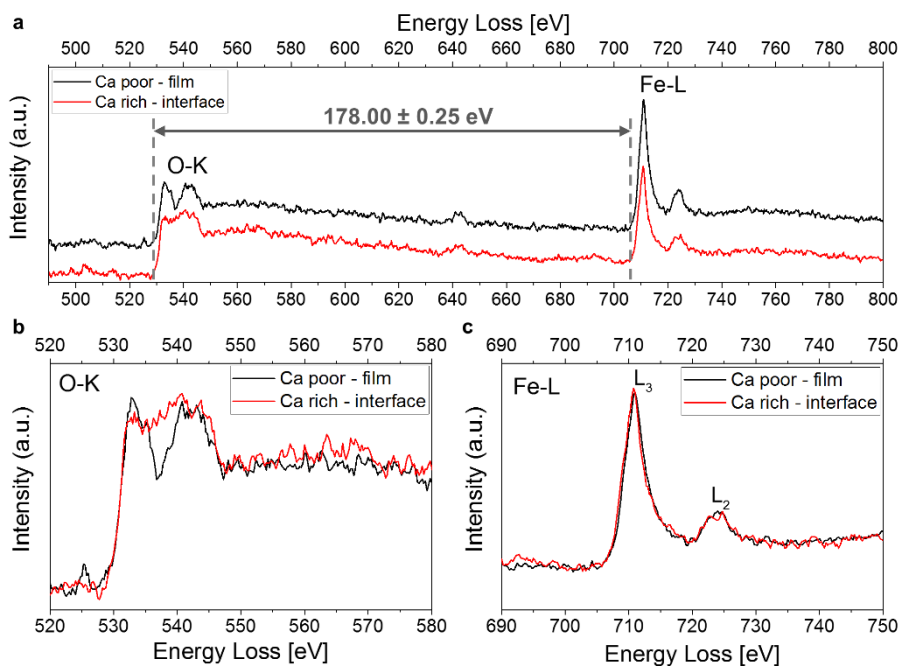


Figure 3. EELS analysis of the Fe oxidation state at the Ca-rich interface. (a) Energy onset difference (ΔE) between O-K and Fe-L₃ edges for the Ca-rich region directly at the interface (red) and for the Ca-poor region at a distance of approximately 3 nm from the interface (black). The position where the spectrum stems from is indicated in Figure 1b by the dashed white rectangles. Compared to the Ca-poor region the Ca rich interface shows no change in ΔE . (b) EELS region of the O-K edges enlarged showing that there is no relative shift in the edge onsets. (c) Energy region of the Fe-L₃ and L₂ edges enlarged showing again no relative shift in the edge onset. The Fe-L edge intensities are normalized by integrating the background subtracted intensity from 708 to 761 eV showing that the L₃/L₂ peak ratio does not change as well.

3.3. Influence of Ca Segregation on the Strain State of the Film. To see if the Ca agglomeration on the interface has an influence on the strain state of the thin film, HRTEM investigations together with GPA were carried out. Figure 4a demonstrates that, in the Ca doped thin film, identifying the exact atomic layer where the film starts in the HRTEM image is not a trivial matter. Ca agglomeration at the interface leads to very similar image contrast because of more similar Z per column compared to those of the Sr columns in STO. This leads to a similar contrast between the substrate and the first few layers of the film. To overcome this issue, image simulations were conducted via JEMS. For that, a supercell modeling the interface based on an STO unit cell (Pm-3m symmetry) was created by 15 times multiplication in the $[001]_c$ direction. Figure S4a shows the resulting crystallographic atomic model, whereby the Sr and Ti cations were replaced completely or partly on the corresponding positions by Ca, Bi, and Fe to model the heterostructure interface according to the cation concentration displayed in Figure S4b. The simulated HRTEM image for a sample thickness of 10.54 nm in Figure S4c displays that the contrast in the first 2-3 A-side rows of the film (with 60, 4, and 20 atom % Ca compared to Bi) is almost identical to the contrast in STO. It is important to note that for these imaging conditions, the bright spots in the cells containing only Bi and Fe on the cation positions (unit cells 10 and 11) indicate the Fe positions and not the Bi ones. The simulated image accurately corresponds to the real HRTEM image in Figure S4d.

The image simulations allow one to determine the location of the interface in the film with the Ca agglomeration in Figure 4a. GPA analysis of the HRTEM image shows no significant in-plane lattice strain ϵ_{xx} , which is the supposed situation for an epitaxial interface, as depicted in Figure 4b,d by the strain distribution and integrated profile. The out-of-plane lattice strain ϵ_{yy} of the film (cf. Figure 4c,d) is on average around 3%. This elongation along the $[001]$ direction is expected, since the lattice of BFO is, simplified to a pseudocubic system, with a lattice constant of 3.965 Å approximately 1.5% larger than the lattice parameter of STO.^{4,57} The novel aspect is that the increase of the out-of-plane strain directly after the heterostructure interface in the first 2 nm of the film is delayed. In Figure 4c,d the out-of-plane strain value of the film is reached notably later than for the non-Ca-doped film in Figure 4e,f,g,h, whose strain increase sets in immediately at the interface. The fact that the area with the delayed out-of-plane strain has a very similar HRTEM image contrast compared to the substrate indicates that it corresponds to the area of Ca agglomeration. This leads to the conclusion that Ca agglomeration at the interface results in a reduction of the out-of-plane strain, which is a probable driving force behind the segregation process of Ca.

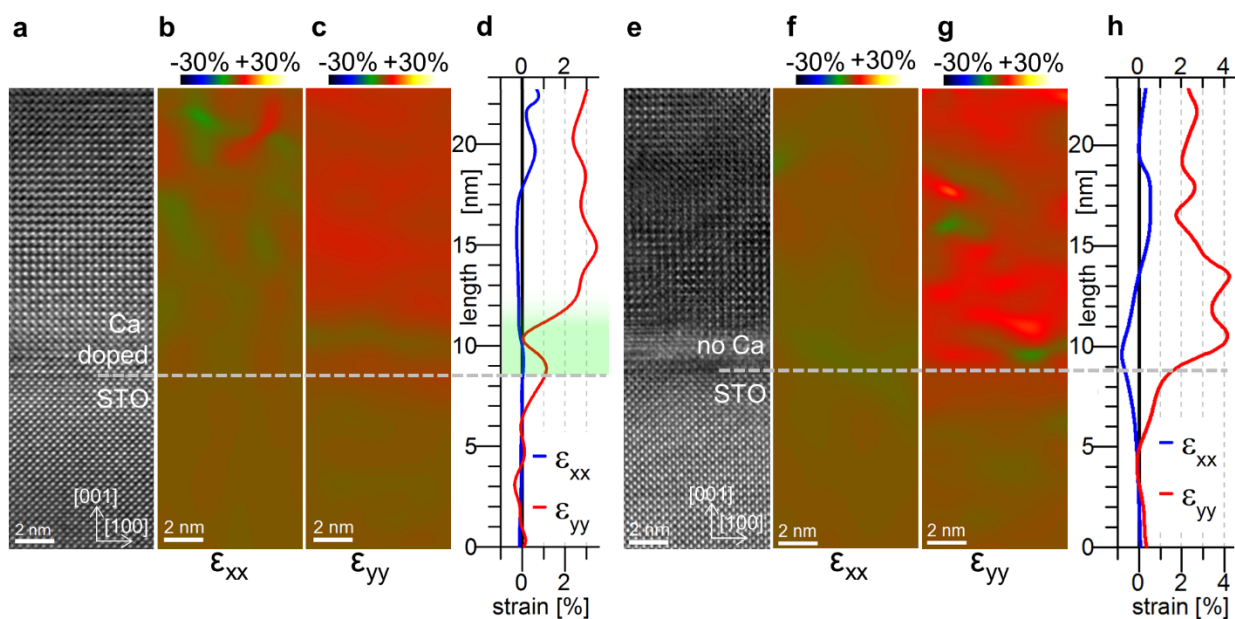


Figure 4. GPA strain analysis from HRTEM images for the films with and without Ca agglomeration at the interface. (a) HRTEM image, (b) in-plane (ϵ_{xx}) and (c) out-of-plane (ϵ_{yy}) strain maps and (d) line profiles of the strains averaged over the width of the strain maps in [100] direction of the film with Ca agglomeration at the interface. The green square indicates the region where the out-of-plane strain is reduced compared to the rest of the film. (e) HRTEM image, (f) in-plane (ϵ_{xx}), and (g) out-of-plane (ϵ_{yy}) strain maps, and (h) averaged line profiles of the strains for the film without Ca doping.

Compared to HRTEM, HAADF images have the advantage that the column intensity is directly proportional to Z^{58} and, therefore, allows direct conclusions regarding the Ca content at the interface, in comparison to the indirect approach from HRTEM analysis where more detailed knowledge about the chemical composition and simulations is necessary. The atomic resolution HAADF image of the interface area with Ca agglomeration in Figure 5a has due to shorter recording times compared to spectral images less severe distortions stemming from drift while covering simultaneously a larger area. The color-coded intensity map shown in Figure 5b is calculated by integrating the intensities for each atomic position. Knowing from the EDS data that the first film layer contains 60 atom % Ca compared to 40 atom % Bi on the A-site positions, resulting in an average Z number (assuming that the columns have everywhere the same thickness and same number of atoms in projection direction) of $Z_m \approx 54.7$ (larger than the Z value of 38 for Sr), it can be clearly identified where the film starts.

While in HRTEM images, phase shifts caused by thickness or Z variations might introduce errors into the GPA analysis^{59,60}, the nature of the scanning procedure itself introduces errors into STEM images. However, distortions in the slow-scan direction caused by sample drift and the so-called “fly-back” error are significantly larger than in the fast-scanning direction. Without using more elaborate techniques to correct scanning artefacts, like, for example, the method developed by Sang and LeBeau,⁶¹ by aligning the fast scanning direction parallel to the principal axis of the strain a reliable strain value in the fast scanning direction is received.^{62,63} Therefore, the fast scanning direction in Figure 5 was oriented perpendicular to the interface allowing to analyze the out-of-plane strain ϵ_{yy} and link it to the Ca concentration in the interface area. Figure 5c shows the out-of-plane strain received via GPA analysis (black curve) and the intensity values (red squares), both from the area marked by the white rectangle in Figure 5a,b, which shows the least drift in the image, and averaged along the direction parallel to the interface.

In Figure 5c, the averaged intensity increases in the first six A-site rows (≈ 2.4 nm) of the film after the interface indicating the decreasing Ca content. Starting from the seventh A-site layer, the intensities reach a plateau value and remain there with little changes indicating that the chemical composition stays largely unchanged. Simultaneously, the out-of-plane strain starts increasing after the interface from the substrate level and reaches its plateau value of $\approx 3.5\%$ in the film, exactly when in the intensity analysis no Ca can be detected anymore. This indicates a direct correlation between the lattice strain and the Ca content. The significantly reduced strain by integrating Ca in the film structure at the interface is one possible driving force behind the observed Ca segregation.

Additionally, it can be seen in Figure 5c that, while the intensity in the substrate side is very uniform, the last A-site layer of the substrate shows a reduced intensity indicating the interdiffusion of Ca in the top substrate layer, as already observed in Figure 1.

The strain data in Figure 4 and especially the direct correlation between Ca content and the strain value in Figure 5c indicate that the strain reduction and thereby minimization of elastic energy is the driving force for the segregation to the interface. The ionic radii for Ca^{2+} compared to Bi^{3+} , which it replaces on the A-sites, are 1.18 \AA compared to 1.24 \AA (both for coordination number 9).⁶⁴ The -4.8% smaller cation radius for Ca instead of Bi leads to a smaller lattice parameter and subsequent reduction of strain, if it segregates to the BFMO/STO interface. The observed segregation process in this study is related to segregation processes toward the surface for larger dopant radii, *e.g.* described by Lee *et al.*¹¹ Therefore, for a deeper understanding DFT calculations have to be done.

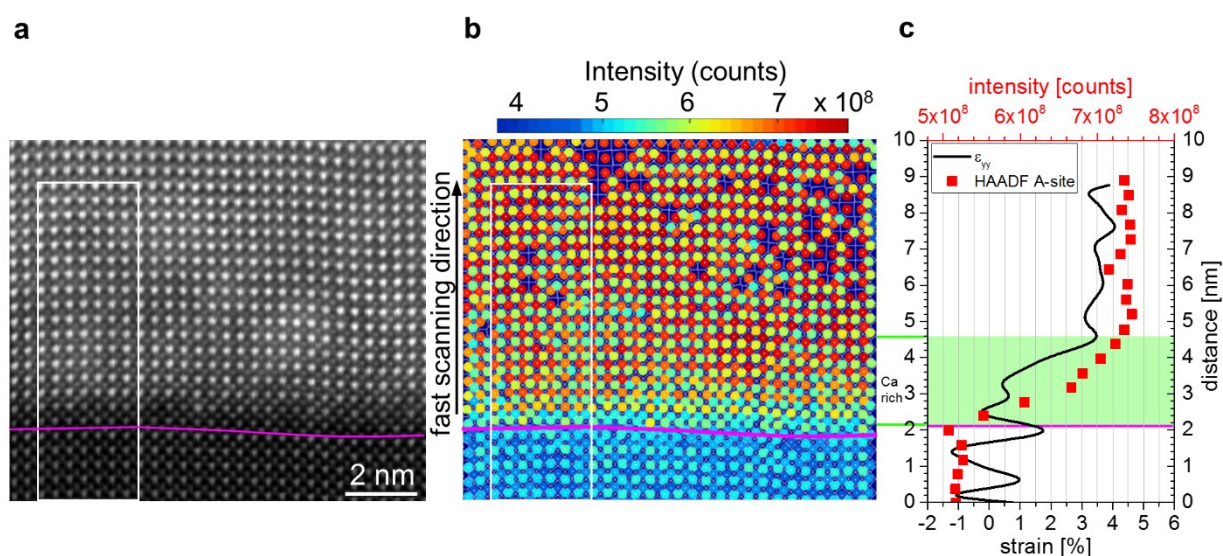


Figure 5. Correlation of the Ca content and out-of-plane (ϵ_{yy}) lattice strain. (a) HAADF image of the heterostructure interface, where the primary scanning direction was vertical. The white rectangle indicates the area used for the strain and intensity analysis. The magenta curve indicates the interface (not a straight line due to the small image drift in the right half of the image). (b) Intensity map by integrating over the atomic positions of the HAADF image in (a). (c) Out-of-plane strain (ϵ_{yy} , black curve) received via GPA from (a), which is possible to receive reliably, since the primary scanning direction is oriented parallel, compared with the intensity of the A-site positions (red squares) in (b). Both were averaged horizontally within the white rectangle in (a) and (b). The green overlay indicates the area where the intensity analysis revealed the presence of Ca and the increase of the out-of-plane strain is simultaneously delayed.

3.4. Density Functional Theory (DFT) Calculations. DFT modeling was used to investigate the energetics of Ca segregation to the STO/BFO interface by means of calculating the segregation energies, i.e., the energy change upon relocating Ca from bulk BFO to the interface. When this energy is negative, it indicates the propensity toward Ca segregation. Two segregation scenarios were explored: (1) a Bi atom in the BiFeO₃ is replaced with a Ca atom; and (2) a complex of two Bi atoms at the interface is replaced with two Ca atoms and one oxygen vacancy. The first case corresponds to Fe oxidation from 3+ to 4+ while the second case corresponds to charge compensation by the vacancy mechanism. The resulting segregation energies are presented in Figure 6. In the case of the Fe-oxidation mechanism, one observes a slightly negative segregation energy for the 1/2 monolayer (ML) of Ca-coverage at interface, which becomes more prominent for 1 ML and even more so for 2 ML, reaching the value of about -0.2 eV per Ca atom (crystallographic models are shown in Figure S1). To verify whether the p-doping introduced by Ca was indeed compensated by Fe oxidation, the electronic density of states (DOS) and the

volumes of the FeO_6 -octahedra were analyzed. Ca-doping leads to the emergence of the acceptor gap state localized on the FeO_6 octahedra next to Ca (see Figure S5b). Also, the volumes of these octahedra decreased as compared to the volumes of FeO_6 units away from Ca. These two observations confirm the shift of the oxidation state of Fe^{3+} to Fe^{4+} , in agreement with the analysis of Gebhardt and Rappe.⁵³ When considering the second segregation scenario, i.e., involving the oxygen-vacancies, the segregation energy was found to be even lower (-0.3 eV per Ca atom). In this case no acceptor state occurs (see Figure S5c). Though both considered scenarios are found to favor Ca segregation, only the one that assumes formation of the oxygen vacancies is supported by the EELS assessment presented before and is also consistent with the previous reports on the effect of Ca doping in BiFeO_3 .⁶⁵ These findings give strong evidence of charge compensation by O-vacancies and, most importantly, confirm the tendency for Ca segregation to the STO/BFO interface.

The analytical STEM data from Figure 1 suggest that the Ca:Bi ratio is approximately 6:4 in the first film layer. The energetically most favorable configurations in the DFT calculations appear to have higher Ca/Bi ratios. This is not a contradiction, since the Ca atoms can cluster in the investigated TEM sample, which was ≈ 25 nm thick ($t/\lambda = 0.22$) and corresponds to 60 pseudocubic unit cells. It also needs to be kept in mind that channeling effects influence EELS and EDX results in atomic resolution and, in both techniques, cause signals from neighboring columns.⁶⁶

Figure 6b compares experimental and theoretical results of the out-of-plane cation distances received either from the HAADF image in Figure 5a or from the relaxed unit cells of the DFT simulations. The distances of the DFT calculations start in the last substrate layer, because the parameters of the other cells in the substrate are fixed. According to the results from Figure 5c, the first A-site distances in the film are smaller compared to the plateau level reached deeper into the film. The distances received from the DFT simulations show that for 1 ML of Ca in the first layer of the film, the interplanar distances are very similar to the ones from the HAADF data showing the absolute minimum of the distances between the first two Bi layers. For 2 ML of Ca in the first and second layer of the film, the minimum is on the same position as for 1 ML but also compared to the experimental data much more pronounced, since it concentrates more Ca at the interface than observed in the sample. The spacings received from the DFT simulations from the third film layer onward do not approach the experimental ones further from the interface, mostly, because thermal lattice expansion was not included in the calculations, the finite model size, and also due to limitations of the employed exchange-correlation functional.

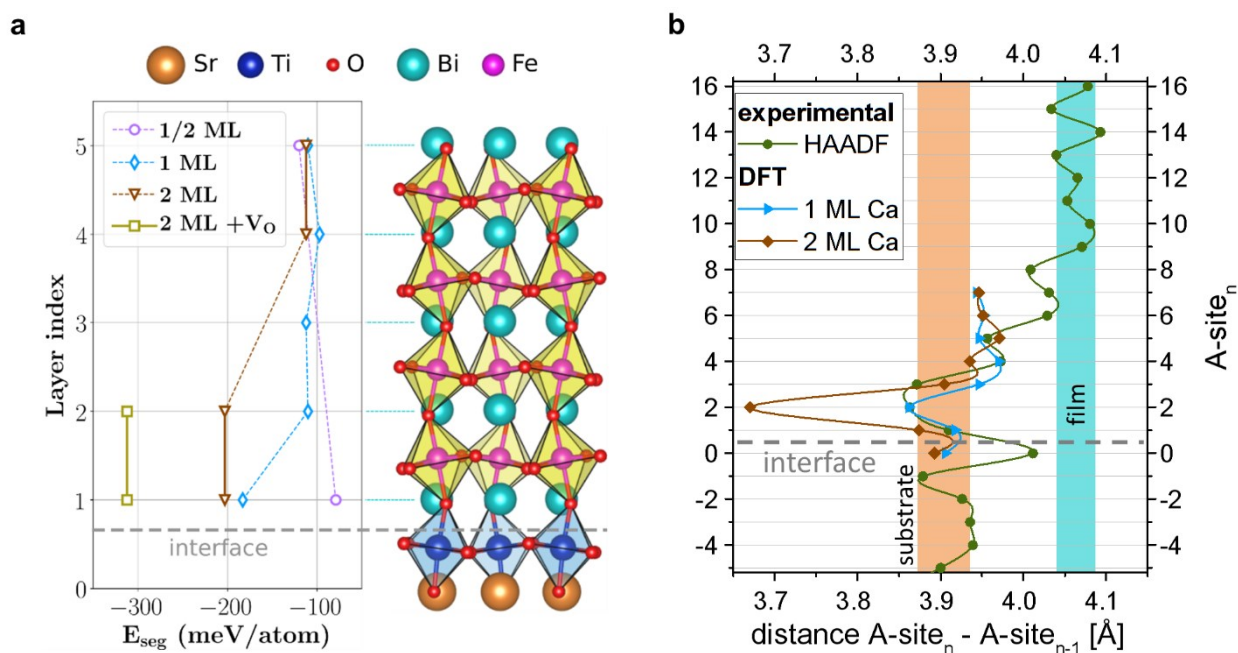


Figure 6. DFT calculations for Ca agglomerations at the interface and comparison of lattice spacing for experimental and theoretical data. (a) Segregation energy received from DFT calculations for Ca agglomerations of the 1/2 monolayer, 1 ML positioned at the A-site film layers 1-5, 2 ML with the Ca at either layers 1 and 2 or 4 and 5 and 2 ML of Ca at the interface with one oxygen vacancy (V_{O}). The last A-site layer of the substrate was assigned the y-axis value 0, while the film starts with the value 1. (b) Comparison of the A-site distances between experimental and calculated results. The experimental data are gained from the HAADF image in Figure 5a by averaging horizontally over the area within the white rectangle. The theoretical data are the values for the relaxed unit cells of the DFT simulations with 1 ML of Ca directly in the first A-site layer and 2 ML of Ca in the first and second A-site layers.

In the literature, segregation phenomena have been studied in metals and compounds including oxides.^{11,67-70} There are two primary mechanisms identified, that drive segregation: minimizing the Coulomb energy in non-metals and the strain relief.^{11,67,68} In the case of Ca segregation to the STO/BFMO interface, it seems to be defined in-part by the strain relief, as judged from the comparison of the ionic radii of Bi^{3+} and Ca^{2+} , but also by the chemical interactions of the Ca-rich layer with the interface. No significant amount of Ca found on the upper surface of the BFO film requires further investigation, as surface segregation is often observed in perovskite materials.¹¹ One of the possible explanations could be that surface Ca has evaporated while the film is at high temperatures, as it is relatively volatile.

4. CONCLUSION

In summary, we have fabricated a BFO thin film with a minor initial Ca doping in the target of $\text{Bi}_{0.98}\text{Ca}_{0.02}\text{Fe}_{0.95}\text{Mn}_{0.05}\text{O}_3$. The advanced STEM investigations of the film revealed that the Ca had diffused completely to the area of the compressive strain interface. An estimation of the value for the diffusion coefficient demonstrated that diffusion in this scale is reasonable. EELS investigations showed that in the Ca rich areas no shift in oxidation state took place indicating the formation of oxygen vacancies at the interface. HRTEM strain analysis of the interface revealed that compared to the Ca free film, the increase of the out-of-plane lattice strain at the interface is delayed due to the Ca at the interface. Analytical HAADF information of the interface region together with strain analysis proves the direct causality of Ca and strain reduction at the interface. Finally, in accordance with the measurement results, DFT calculations confirmed that it is energetically more favorable when Ca is agglomerated at the interface and the received lattice spacings from the calculations fit to the measured ones.

This study is of great importance to accordingly understand the segregation behavior of dopants at oxide heterostructure interfaces and its effects on the atomic and electronic structure. Especially in light of functional devices using these materials, segregation behavior must be considered and addressed with prevention strategies if necessary. Alternatively, the process could be used purposely to engineer electric and magnetic properties of the two-dimensional system realized at the BFO/STO interface. A Ca-rich buffer layer at a BFMO/STO interface may be a successful prevention strategy against the unwanted formation of antiphase boundaries at the interface, since they could not be observed here.

ASSOCIATED CONTENT

Supporting Information

The Supporting Information is available free of charge on the ACS Publications at:

<https://pubs.acs.org/doi/10.1021/acsami.9b20505>

Calculation of the average *Z* number for the first film layer, three exemplary examples for the supercells used in the DFT calculations, XPS results showing that Ca distribution in the target was uniform during deposition, the superposition of the O-K edge from the substrate and film at the interface, image simulations to confirm the observed HRTEM contrast in the interface

region, atom- and position-resolved electronic density of states (DOS) of an undoped STO/BFO interface and 2 ML Ca-doped interfaces compensated either by charge shift from Fe³⁺ to Fe⁴⁺ or by oxygen vacancies, HAADF overview images of the film-substrate interface for the BCFMO and BFMO films, XRD data and XPS spectra from both films and a low-magnification bright field (BF) TEM image

AUTHOR INFORMATION

Author Contributions

Z.Z. conceived and supervised the project. U.H. prepared the Ca doped TEM samples, performed the TEM and HRTEM investigations and data analysis, and wrote the main part of the manuscript with input from all other authors. G.H. and G.K. performed the analytical STEM measurements and supported the interpretation. W. P., J. C., and Y.H. fabricated the thin films and did the XPS and XRD investigations. D.K. wrote the program for the intensity analysis and supported the usage of it. M.N.P. and L.R. did the DFT calculations and the interpretation of the results for the observed film structure. A.G. contributed to the data evaluation, interpretation, and discussion of the results. Z.Z. contributed to the writing of the manuscript. All authors read through the manuscript and contributed to the discussion of the results.

ORCID

Ulrich Haselmann: 0000-0001-5664-8656

Georg Haberfehlner: 0000-0003-4136-9384

Maxim N. Popov: 0000-0002-4923-0785

Lorenz Romaner: 0000-0003-4764-130X

Daniel Knez: 0000-0003-0755-958X

Arsham Ghasemi: 0000-0002-4529-7843

Gerald Kothleitner: 0000-0002-2116-7761

Zaoli Zhang: 0000-0002-7717-2500

Notes

The authors declare no competing interests.

ACKNOWLEDGMENTS

We kindly acknowledge the financial support by the Austrian Science Fund (FWF): No. P29148-N36. U.H. thanks G. Felber for preparing the non Ca doped sample and also her and H. Felber for their general support with the sample preparation. U.H. also expresses his thanks to Y.P. Ivanov, J. Zálešák and M. Kubicek for very helpful discussions. U.H. and Z.Z. thank C. Mitterer and M. Rausch from the University of Leoben for their kind help using SRIM and enlightening discussion and express their gratitude to S. Wurster for performing general bulk sample checks in SEM. G.H., D.K., and G.K. acknowledge support from the European Union's Horizon 2020 research and innovation program under grant agreement No. 823717 – ESTEEM3. Y.H. acknowledges financial support from the National Key R&D Program of China (Grant No. 2019 YFB 1503500) and the National Natural Science Foundation of China (Project Nos. 51572073, 11774082). M.N.P. and L.R. gratefully acknowledge the financial support under the scope of the COMET program within the K2 Center “Integrated Computational Material, Process and Product Engineering (IC-MPPE)” (Project No 859480). This program is supported by the Austrian Federal Ministries for Transport, Innovation and Technology (BMVIT) and for Digital and Economic Affairs (BMDW), represented by the Austrian research funding association (FFG), and the federal states of Styria, Upper Austria and Tyrol.

REFERENCES

- (1) Zubko, P.; Gariglio, S.; Gabay, M.; Ghosez, P.; Triscone, J.-M. Interface Physics in Complex Oxide Heterostructures. *Annu. Rev. Condens. Matter Phys* **2011**, *2*, 141–165.
- (2) Scott, J. F. Data Storage: Multiferroic Memories. *Nat. Mater.* **2007**, *6*, 256–257.
- (3) Roy, A.; Gupta, R.; Garg, A. Multiferroic Memories. *Adv. Condens. Matter Phys.* **2012**, No. 926290.
- (4) Catalan, G.; Scott, J. F. Physics and Applications of Bismuth Ferrite. *Adv. Mater.* **2009**, *21*, 2463–2485.
- (5) Zhao, T.; Scholl, A.; Zavaliche, F.; Lee, K.; Barry, M.; Doran, A.; Cruz, M. P.; Chu, Y. H.; Ederer, C.; Spaldin, N. A.; Das, R. R.; Kim, D. M.; Baek, S. H.; Eom, C. B.; Ramesh, R. Electrical Control of Antiferromagnetic Domains in Multiferroic BiFeO₃ Films at Room Temperature. *Nat. Mater.* **2006**, *5*, 823–829.
- (6) Woodward, P. M.; Cox, D. E.; Moshopoulou, E.; Sleight, A. W.; Morimoto, S. Structural Studies of Charge Disproportionation and Magnetic Order in CaFeO₃. *Phys. Rev. B* **2000**, *62*, 844–855.
- (7) Khomchenko, V. A.; Pereira, L. C. J.; Paixão, J. A. Mn Substitution-Induced Revival of the Ferroelectric Antiferromagnetic Phase in Bi_{1-x}CaxFeO_{3-x/2} Multiferroics. *J. Mater. Sci.* **2015**, *50*, 1740–1745.
- (8) Cai, Z.; Kubicek, M.; Fleig, J.; Yildiz, B. Chemical Heterogeneities on La_{0.6}Sr_{0.4}CoO_{3-δ} Thin Films—Correlations to Cathode Surface Activity and Stability. *Chem. Mater.* **2012**, *24*, 1116–1127.

- (9) Li, Y.; Zhang, W.; Zheng, Y.; Chen, J.; Yu, B.; Chen, Y.; Liu, M. Controlling Cation Segregation in Perovskite-Based Electrodes for High Electro-Catalytic Activity and Durability. *Chem. Soc. Rev.* **2017**, *46*, 6345–6378.
- (10) Neagu, D.; Tsekouras, G.; Miller, D. N.; Ménard, H.; Irvine, J. T. S. In Situ Growth of Nanoparticles through Control of Non-Stoichiometry. *Nat. Chem.* **2013**, *5*, 916–923.
- (11) Lee, W.; Han, J. W.; Chen, Y.; Cai, Z.; Yildiz, B. Cation Size Mismatch and Charge Interactions Drive Dopant Segregation at the Surfaces of Manganite Perovskites. *J. Am. Chem. Soc.* **2013**, *135*, 7909–7925.
- (12) Suyolcu, Y. E.; Wang, Y.; Sigle, W.; Baiutti, F.; Cristiani, G.; Logvenov, G.; Maier, J.; van Aken, P. A. Octahedral Distortions at High-Temperature Superconducting La₂CuO₄ Interfaces: Visualizing Jahn–Teller Effects. *Adv. Mater. Interfaces* **2017**, *4*, No. 1700731.
- (13) Suyolcu, Y. E.; Wang, Y.; Baiutti, F.; Al-Temimy, A.; Gregori, G.; Cristiani, G.; Sigle, W.; Maier, J.; Van Aken, P. A.; Logvenov, G. Dopant Size Effects on Novel Functionalities: High-Temperature Interfacial Superconductivity. *Sci. Rep.* **2017**, *7*, No. 453.
- (14) Jalili, H.; Han, J. W.; Kuru, Y.; Cai, Z.; Yildiz, B. New Insights into the Strain Coupling to Surface Chemistry, Electronic Structure, and Reactivity of La_{0.7}Sr_{0.3}MnO₃. *J. Phys. Chem. Lett.* **2011**, *2*, 801–807
- (15) Kubicek, M.; Rupp, G. M.; Huber, S.; Penn, A.; Opitz, A. K.; Bernardi, J.; Stöger-Pollach, M.; Hutter, H.; Fleig, J. Cation Diffusion in La_{0.6}Sr_{0.4}CoO_{3-δ} below 800°C and Its Relevance for Sr Segregation. *Phys. Chem. Chem. Phys.* **2014**, *16*, 2715–2726.
- (16) Huber, A. K.; Falk, M.; Rohnke, M.; Luerßen, B.; Gregoratti, L.; Amati, M.; Janek, J. In Situ Study of Electrochemical Activation and Surface Segregation of the SOFC Electrode Material La_{0.75}Sr_{0.25}Cr_{0.5}Mn_{0.5}O_{3±δ}. *Phys. Chem. Chem. Phys.* **2012**, *14*, 751–758.
- (17) Feng, Z.; Yacoby, Y.; Gadre, M. J.; Lee, Y. L.; Hong, W. T.; Zhou, H.; Biegalski, M. D.; Christen, H. M.; Adler, S. B.; Morgan, D.; Shao-Horn, Y. Anomalous Interface and Surface Strontium Segregation in (La_{1-y}Sr_y)₂CoO_{4±δ}/La_{1-x}Sr_xCoO_{3-δ} Heterostructured Thin Films. *J. Phys. Chem. Lett.* **2014**, *5*, 1027–1034.
- (18) Yoon, H. I.; Lee, D. K.; Bae, H. Bin; Jo, G. Y.; Chung, H. S.; Kim, J. G.; Kang, S. J. L.; Chung, S. Y. Probing Dopant Segregation in Distinct Cation Sites at Perovskite Oxide Polycrystal Interfaces. *Nat. Commun.* **2017**, *8*, No. 1417.
- (19) Estradé, S.; Rebled, J. M.; Arbiol, J.; Peiró, F.; Infante, I. C.; Herranz, G.; Sánchez, F.; Fontcuberta, J.; Córdoba, R.; Mendis, B. G.; Bleloch, A. L. Effects of Thickness on the Cation Segregation in Epitaxial (001) and (110) La_{2/3}Ca_{1/3}MnO₃ Thin Films. *Appl. Phys. Lett.* **2009**, *95*, No. 072507.
- (20) Zhao, C.; Li, Y.; Zhang, W.; Zheng, Y.; Lou, X.; Yu, B.; Chen, J.; Chen, Y.; Liu, M.; Wang, J. Heterointerface Engineering for Enhancing the Electrochemical Performance of Solid Oxide Cells. *Energy Environ. Sci.* **2020**, *13*, 53-85.
- (21) Zhao, C.; Liu, X.; Zhang, W.; Zheng, Y.; Li, Y.; Yu, B.; Wang, J.; Chen, J. Measurement of Oxygen Reduction/Evolution Kinetics Enhanced (La,Sr)CoO₃/(La,Sr)₂CoO₄ Hetero-Structure Oxygen Electrode in Operating Temperature for SOCs. *Int. J. Hydrogen Energy* **2019**, *4*, 19102–19112.
- (22) Zheng, Y.; Li, Y.; Wu, T.; Zhao, C.; Zhang, W.; Zhu, J.; Li, Z.; Chen, J.; Wang, J.; Yu, B.; Zhang, J. Controlling Crystal Orientation in Multilayered Heterostructures toward High Electro-Catalytic Activity for Oxygen Reduction Reaction. *Nano Energy* **2019**, *62*, 521–529.
- (23) Krishnan, P. S. S. R.; Morozovska, A. N.; Eliseev, E. A.; Ramasse, Q. M.; Kepaptsoglou, D.; Liang, W.-I.;

- Chu, Y.-H.; Munroe, P.; Nagarajan, V. Misfit Strain Driven Cation Inter-Diffusion across an Epitaxial Multiferroic Thin Film Interface. *J. Appl. Phys.* **2014**, *115*, No. 054103.
- (24) Bernardo, M. S.; Jardiel, T.; Peiteado, M.; Mompean, F. J.; Garcia-Hernandez, M.; Garcia, M. A.; Villegas, M.; Caballero, A. C. Intrinsic Compositional Inhomogeneities in Bulk Ti-Doped BiFeO₃: Microstructure Development and Multiferroic Properties. *Chem. Mater.* **2013**, *25*, 1533–1541.
- (25) MacLaren, I.; Sala, B.; Andersson, S. M. L.; Pennycook, T. J.; Xiong, J.; Jia, Q. X.; Choi, E. M.; MacManus-Driscoll, J. L. Strain Localization in Thin Films of Bi(Fe,Mn)O₃ Due to the Formation of Stepped Mn⁴⁺-Rich Antiphase Boundaries. *Nanoscale Res. Lett.* **2015**, *10*, 407.
- (26) Maclaren, I.; Wang, L. Q.; Schaffer, B.; Ramasse, Q. M.; Craven, A. J.; Selbach, S. M.; Spaldin, N. A.; Miao, S.; Kalantari, K.; Reaney, I. M. Novel Nanorod Precipitate Formation in Neodymium and Titanium Codoped Bismuth Ferrite. *Adv. Funct. Mater.* **2013**, *23*, 683–689.
- (27) Reaney, I. M.; Maclaren, I.; Wang, L.; Schaffer, B.; Craven, A.; Kalantari, K.; Miao, S.; Karimi, S.; Sinclair, D. C. Defect Chemistry of Ti-Doped Antiferroelectric Bi_{0.85}Nd_{0.15}FeO₃. *Appl. Phys. Lett.* **2012**, *100*, No. 182902.
- (28) MacLaren, I.; Wang, L.; Morris, O.; Craven, A. J.; Stamps, R. L.; Schaffer, B.; Ramasse, Q. M.; Miao, S.; Kalantari, K.; Sterianou, I.; Reaney, I. M. Local Stabilisation of Polar Order at Charged Antiphase Boundaries in Antiferroelectric (Bi_{0.85}Nd_{0.15})(Ti_{0.1}Fe_{0.9})O₃. *APL Mater.* **2013**, *1*, No. 021102.
- (29) Liu, Y.; Zhu, Y. L.; Tang, Y. L.; Wang, Y. J.; Li, S.; Zhang, S. R.; Han, M. J.; Ma, J. Y.; Suriyaprakash, J.; Ma, X. L. Controlled Growth and Atomic-Scale Mapping of Charged Heterointerfaces in PbTiO₃/BiFeO₃ Bilayers. *ACS Appl. Mater. Interfaces* **2017**, *9*, 25578–25586.
- (30) Batuk, D.; Batuk, M.; Filimonov, D. S.; Zakharov, K. V.; Volkova, O. S.; Vasiliev, A. N.; Tyablikov, O. A.; Hadermann, J.; Abakumov, A. M. Crystal Structure, Defects, Magnetic and Dielectric Properties of the Layered Bi_{3n+1}Ti₇Fe_{3n-3}O_{9n+11} Perovskite-Anatase Intergrowths. *Inorg. Chem.* **2017**, *56*, 931–942.
- (31) Gubbens, A.; Barfels, M.; Trevor, C.; Twesten, R.; Mooney, P.; Thomas, P.; Menon, N.; Kraus, B.; Mao, C.; McGinn, B. The GIF Quantum, a next Generation Post-Column Imaging Energy Filter. *Ultramicroscopy* **2010**, *110*, 962–970.
- (32) Schlossmacher, P.; Klenov, D. O.; Freitag, B.; von Harrach, H. S. Enhanced Detection Sensitivity with a New Windowless XEDS System for AEM Based on Silicon Drift Detector Technology. *Microsc. Today* **2010**, July, 14–20.
- (33) Potapov, P. Why Principal Component Analysis of STEM Spectrum-Images Results in “Abstract”, Uninterpretable Loadings? *Ultramicroscopy* **2016**, *160*, 197–212.
- (34) Jones, L.; MacArthur, K. E.; Fauske, V. T.; Van Helvoort, A. T. J.; Nellist, P. D. Rapid Estimation of Catalyst Nanoparticle Morphology and Atomic-Coordination by High-Resolution Z-Contrast Electron Microscopy. *Nano Lett.* **2014**, *14*, 6336–6341.
- (35) E, H.; MacArthur, K. E.; Pennycook, T. J.; Okunishi, E.; D’Alfonso, A. J.; Lugg, N. R.; Allen, L. J.; Nellist, P. D. Probe Integrated Scattering Crosssections in the Analysis of Atomic Resolution HAADF STEM Images. *Ultramicroscopy* **2013**, *133*, 109–119.
- (36) Blochl, P. E. Projector Augmented-Wave Method. *Phys. Rev. B* **1994**, *50*, 17953.
- (37) Kresse, G.; Hafner, J. Ab Initio Molecular Dynamics for Liquid Metals. *J. Non. Cryst. Solids* **1993**, *47*, 558–561.

- (38) Kresse, G.; Hafner, J. Ab Initio Molecular-Dynamics Simulation of the Liquid-Metamorphous-Semiconductor Transition in Germanium. *Phys. Rev. B* **1994**, *49*, 14251.
- (39) Kresse, G.; Furthmüller, J. Efficient Iterative Schemes for Ab Initio Total-Energy Calculations Using a Plane-Wave Basis Set. *Phys. Rev. B* **1996**, *54* (16), 11169.
- (40) Kresse, G.; Joubert, D. From Ultrasoft Pseudopotentials to the Projector Augmented-Wave Method. *Phys. Rev. B* **1999**, *59*, 1758.
- (41) Perdew, J. P.; Ruzsinszky, A.; Csonka, G. I.; Vydrov, O. A.; Scuseria, G. E.; Constantin, L. A.; Zhou, X.; Burke, K. Restoring the Density-Gradient Expansion for Exchange in Solids and Surfaces. *Phys. Rev. Lett.* **2008**, *100*, No. 136406.
- (42) Dudarev, S. L.; Botton, G. A.; Savrasov, S. Y.; Humphreys, C. J.; Sutton, A. P. Electron-Energy-Loss Spectra and the Structural Stability of Nickel Oxide: An LSDA+U Study. *Phys. Rev. B* **1998**, *57*, 1505.
- (43) Shenton, J. K.; Bowler, D. R.; Cheah, W. L. Effects of the Hubbard U on Density Functional-Based Predictions of BiFeO₃ Properties. *J. Phys. Condens. Matter* **2017**, *29*, No. 445501.
- (44) Chen, C.; Lv, S.; Li, J.; Wang, Z.; Liang, X.; Li, Y.; Viehland, D.; Nakajima, K.; Ikuhara, Y. Two-Dimensional Electron Gas at the Ti-Diffused BiFeO₃/SrTiO₃ Interface. *Appl. Phys. Lett.* **2015**, *107*, No. 031601.
- (45) Neugebauer, J.; Scheffler, M. Adsorbate-Substrate and Adsorbate-Adsorbate Interactions of Na and K Adlayers on Al(111). *Phys. Rev. B* **1992**, *46*, 16067.
- (46) Momma, K.; Izumi, F. VESTA: A Three-Dimensional Visualization System for Electronic and Structural Analysis. *J. Appl. Crystallogr.* **2008**, *41*, 653–658.
- (47) Francois-Saint-Cyr, H. G.; Stevie, F. A.; McKinley, J. M.; Elshot, K.; Chow, L.; Richardson, K. A. Diffusion of 18 Elements Implanted into Thermally Grown SiO₂. *J. Appl. Phys.* **2003**, *94*, 7433–7439
- (48) Rungis, J.; Mortlock, A. J. The Diffusion of Calcium in Magnesium Oxide. *Philos. Mag.* **1966**, *14*, 821–827.
- (49) Palcut, M.; Wiik, K.; Grande, T. Cation Self-Diffusion in LaCoO₃ and La₂CoO₄ Studied by Diffusion Couple Experiments. *J. Phys. Chem. B* **2007**, *111*, 2299–2308.
- (50) Petrov, A. N.; Rabinovich, L. Y.; Zhukovskij, V. M.; Zhukovskaya, A. S. Diffusion of Metallic Components in Sintered Rare Earth Orthocobaltites LnCoO₃ (Ln=La, Pr, Nd, Sm, Eu, Gd). *Dokl. Akad. Nauk SSSR* **1987**, *372*, 292.
- (51) Khomchenko, V. A.; Kiselev, D. A.; Vieira, J. M.; Kholkin, A. L.; Sá, M. A.; Pogorelov, Y. G. Synthesis and Multiferroic Properties of Bi_{0.8}A_{0.2}FeO₃ (A = Ca, Sr, Pb) Ceramics. *Appl. Phys. Lett.* **2007**, *90*, No. 242901.
- (52) Khomchenko, V. A.; Kiselev, D. A.; Vieira, J. M.; Jian, L.; Kholkin, A. L.; Lopes, A. M. L.; Pogorelov, Y. G.; Araujo, J. P.; Maglione, M. Effect of Diamagnetic Ca, Sr, Pb, and Ba Substitution on the Crystal Structure and Multiferroic Properties of the BiFeO₃ Perovskite. *J. Appl. Phys.* **2008**, *103*, No. 024105.
- (53) Gebhardt, J.; Rappe, A. M. Doping of BiFeO₃: A Comprehensive Study on Substitutional Doping. *Phys. Rev. B* **2018**, *98*, 125202.
- (54) Jiang, L.; Saldana-Greco, D.; Schick, J. T.; Rappe, A. M. Enhanced Charge Ordering Transition in Doped CaFeO₃ through Steric Templating. *Phys. Rev. B* **2014**, *89*, 235106. <https://doi.org/10.1103/PhysRevB.89.235106>.
- (55) Tan, H.; Verbeeck, J.; Abakumov, A.; Van Tendeloo, G. Oxidation State and Chemical Shift Investigation in Transition Metal Oxides by EELS. *Ultramicroscopy* **2012**, *116*, 24–33.

- (56) Rojac, T.; Bencan, A.; Drazic, G.; Sakamoto, N.; Ursic, H.; Jancar, B.; Tavcar, G.; Makarovic, M.; Walker, J.; Malic, B.; Damjanovic, B. Domain-Wall Conduction in Ferroelectric BiFeO₃ Controlled by Accumulation of Charged Defects. *Nat. Mater.* **2017**, *16*, 322–327.
- (57) Kubel, F.; Schmid, H. Structure of a Ferroelectric and Ferroelastic Monodomain Crystal of the Perovskite BiFeO₃. *Acta Crystallogr. Sect. B*, **1990**, *46*, 698–702.
- (58) Klenov, D. O.; Stemmer, S. Contributions to the Contrast in Experimental High-Angle Annular Dark-Field Images. *Ultramicroscopy* **2006**, *106*, 889–901.
- (59) Chung, J.; Rabenberg, L. Effects of Strain Gradients on Strain Measurements Using Geometrical Phase Analysis in the Transmission Electron Microscope. *Ultramicroscopy* **2008**, *108*, 1595–1602.
- (60) Guerrero, E.; Galindo, P.; Yáñez, A.; Ben, T.; Molina, S. I. Error Quantification in Strain Mapping Methods. *Microsc. Microanal.* **2007**, *13*, 320–328.
- (61) Sang, X.; LeBeau, J. M. Revolving Scanning Transmission Electron Microscopy: Correcting Sample Drift Distortion without Prior Knowledge. *Ultramicroscopy* **2014**, *138*, 28–35.
- (62) Chung, J.; Lian, G.; Rabenberg, L. Practical and Reproducible Mapping of Strains in Si Devices Using Geometric Phase Analysis of Annular Dark-Field Images from Scanning Transmission Electron Microscopy. *IEEE Electron Device Lett.* **2010**, *31*, 854–856.
- (63) Zhu, Y.; Ophus, C.; Ciston, J.; Wang, H. Interface Lattice Displacement Measurement to 1 pm by Geometric Phase Analysis on Aberration-Corrected HAADF STEM Images. *Acta Mater.* **2013**, *61*, 5646–5663.
- (64) Shannon, R. D. Revised Effective Ionic Radii and Systematic Studies of Interatomic Distances in Halides and Chalcogenides. *Acta Cryst.* **1976**, *A32*, 751–766.
- (65) Park, H. S.; Lim, J. S.; Suh, J.; Yang, C. H. Real-Time Observation of Filamentary Conduction Pathways in Ca-Doped BiFeO₃. *Appl. Phys. Lett.* **2019**, *115*, No. 183901.
- (66) Kothleitner, G.; Neish, M. J.; Lugg, N. R.; Findlay, S. D.; Grogger, W.; Hofer, F.; Allen, L. J. Quantitative Elemental Mapping at Atomic Resolution Using X-Ray Spectroscopy. *Phys. Rev. Lett.* **2014**, *112*, 085501
- (67) Chung, S. Y.; Choi, S. Y.; Yoon, H. I.; Kim, H. S.; Bae, H. Bin. Subsurface Space-Charge Dopant Segregation to Compensate Surface Excess Charge in a Perovskite Oxide. *Angew. Chem. Int. Ed.* **2016**, *55*, 9680–9684
- (68) Harrington, G. F.; Skinner, S. J.; Kilner, J. A. Can Solute Segregation in Ceramic Materials Be Reduced by Lattice Strain? *J. Am. Ceram. Soc.* **2018**, *101*, 1310–1322.
- (69) Scheiber, D.; Romaner, L.; Pippan, R.; Puschnig, P. Impact of Solute-Solute Interactions on Grain Boundary Segregation and Cohesion in Molybdenum. *Phys. Rev. Mater.* **2018**, *2*, 093609.
- (70) Popov, M. N.; Bochkarev, A. S.; Razumovskiy, V. I.; Puschnig, P.; Spitaler, J. Point Defects at the $\Sigma 5(012)[100]$ Grain Boundary in TiN and the Early Stages of Cu Diffusion: An Ab Initio Study. *Acta Mater.* **2018**, *144*, 496–504.

Publication A – Supporting Information

Study on Ca Segregation towards an Epitaxial Interface between Bismuth Ferrite and Strontium Titanate

Ulrich Haselmann¹, Georg Haberfehlner², Weijie Pei³, Maxim N. Popov⁴, Lorenz Romaner⁴, Daniel Knez⁵, Jian Chen³, Arsham Ghasemi¹, Yunbin He^{3}, Gerald Kothleitner^{2,5} and Zaoli Zhang^{1,6*}*

¹ Erich Schmid Institute of Materials Science, Austrian Academy of Sciences, Leoben, Austria

² Institute for Electron Microscopy and Nanoanalysis, Graz University of Technology, Graz, Austria

³ School of Materials Science & Engineering, Hubei University, Wuhan, Hubei, China

⁴ Materials Center Leoben Forschung GmbH, Leoben, Austria

⁵ Graz Centre for Electron Microscopy, Austrian Cooperative Research, Graz, Austria

⁶ Institute of Material Physics, Montanuniversität Leoben, Leoben, Austria

***Corresponding authors:** zaoli.zhang@oeaw.ac.at, ybhe@hubu.edu.cn

Assuming incoherent scattering, the detected intensity I is proportional to $Z_1^2 + Z_2^2 + \dots + Z_n^2$ with the Z for each atom in the column. To calculate the average Z -number (Z_m), which we define as being the Z -number if the column would only consist of 1 hypothetical chemical element and not a mixture, (here 60at.% Ca and 40at.% Bi are assumed from the EDX data for the first film layer) the following formula is used:

$$Z_m = \sqrt{c_1 \times Z_1^2 + c_2 \times Z_2^2} = \sqrt{0.4 \times 83^2 + 0.6 \times 20^2} \approx 54.7 \quad (1)$$

c_n ... atomic concentration [1]

Z_n ... Z of element [1]

Figure S1 shows as examples for the supercells used in the DFT calculations those with no Ca, 2 ML of Ca directly at the interface and 2 ML of Ca and two oxygen vacancies at the interface.

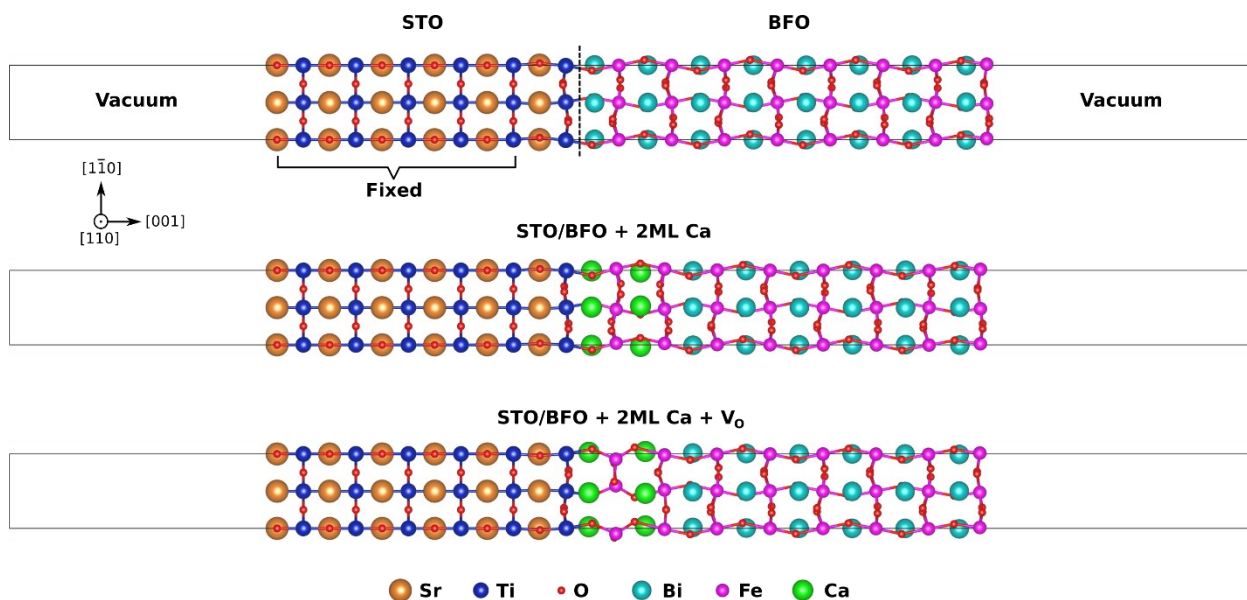


Figure S1. Supercells used in DFT calculations: (Top) STO/BFO interface model; (Middle) the interface with 2ML of Ca (4 atoms); (Bottom) the interface with 2ML of Ca and 2 oxygen vacancies. All presented structures correspond to equilibrium geometries obtained after ionic relaxation. Fixed layers in STO slab highlighted in the top panel were maintained throughout all calculations.

Figure S2 shows the X-Ray Photoelectron Spectroscopy (XPS) data of the PLD target used for the fabrication of the film with the Ca agglomeration at the interface, recorded at different (laser ablated and unablated) areas on the target surface. It clearly shows that both XPS spectra contain similarly large Ca $2p_{1/2}$ and Ca $2p_{3/2}$ peaks, which indicate that the Ca distribution in the target is homogenous.

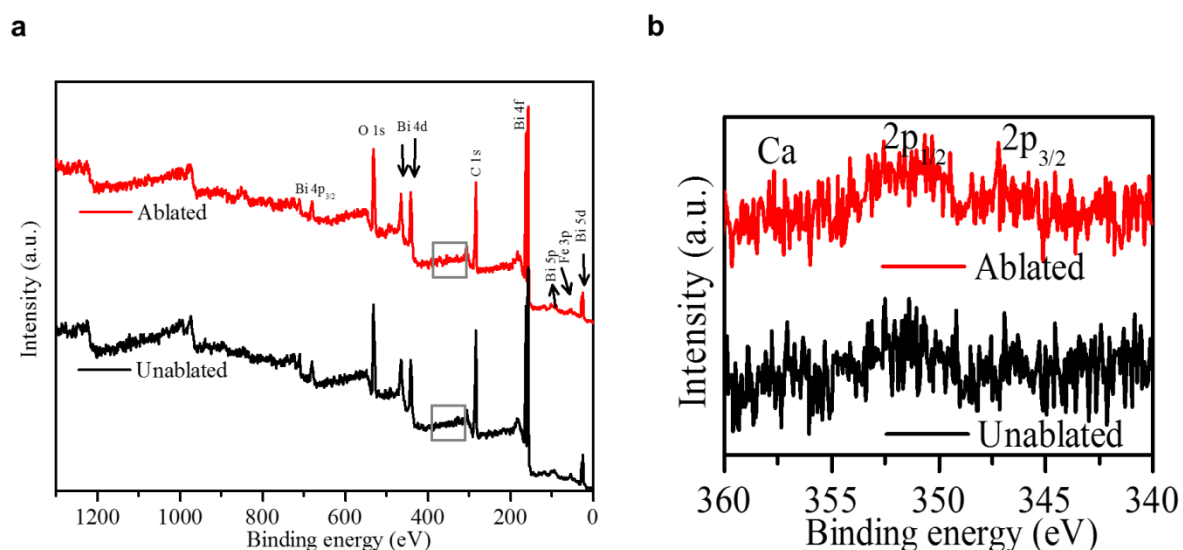


Figure S2. XPS data of the ablated (after deposition) and unablated (before deposition) surface of the PLD target from which the Bi film with the Ca agglomeration stems. (a) Whole XPS spectrum (b) Enlarged area of the Ca $2p_{1/2}$ and Ca $2p_{3/2}$ peaks indicated by the grey squares in (a).

The unusual O-K edge form at the substrate-film interface displayed by the red curve in Figure S3 stems from a superposition of the typical edge shapes of the SrTiO_3 substrate (blue) and the film. The dashed grey lines in Figure S3 are eye guides to show where local maxima of one curve compensate local minima or slopes of the other curve leading to a flat top form of the O-K edge at the interface.

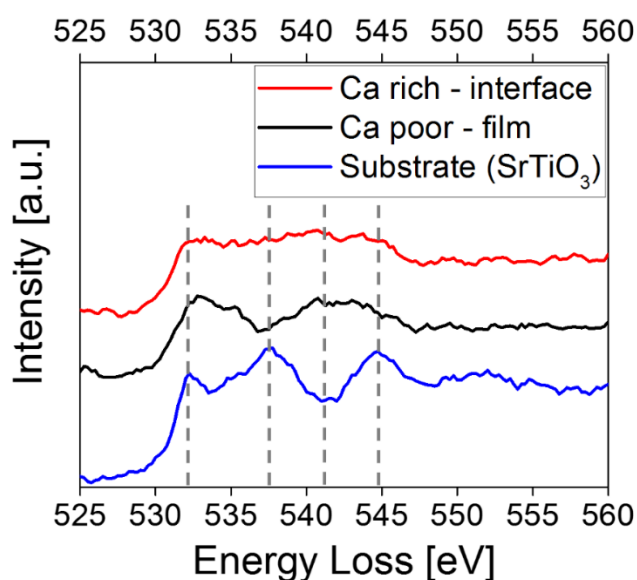


Figure S3. Formation by superposition of the O-K edge signal at the substrate-film interface (red) by the 2 characteristic O-K edges for the SrTiO_3 substrate (blue) and the Bismuth Ferrite film (black). The grey dashed lines are eye guides to follow local maxima of one curve to local minima or slopes of the other one.

To precisely identify the interface in the HRTEM images, image simulations were conducted. Therefore, a supercell modelling the interface based on a STO unit cell (Pm-3m symmetry) was created by 15 times duplication in [001]_c direction. Figure S4a shows the resulting crystallographic atomic model, whereby the Sr and Ti cations were replaced completely or partly on the necessary positions by Ca, Bi and Fe to model the heterostructure interface according to the cation concentration displayed in Figure S4b. The simulated HRTEM image for a sample thickness of 10.54 nm in Figure S4c displays that the contrast in the first 2-3 Å-side rows of the film is almost identical to the contrast in STO. The simulated image accurately corresponds to the real HRTEM image in Figure S4d.

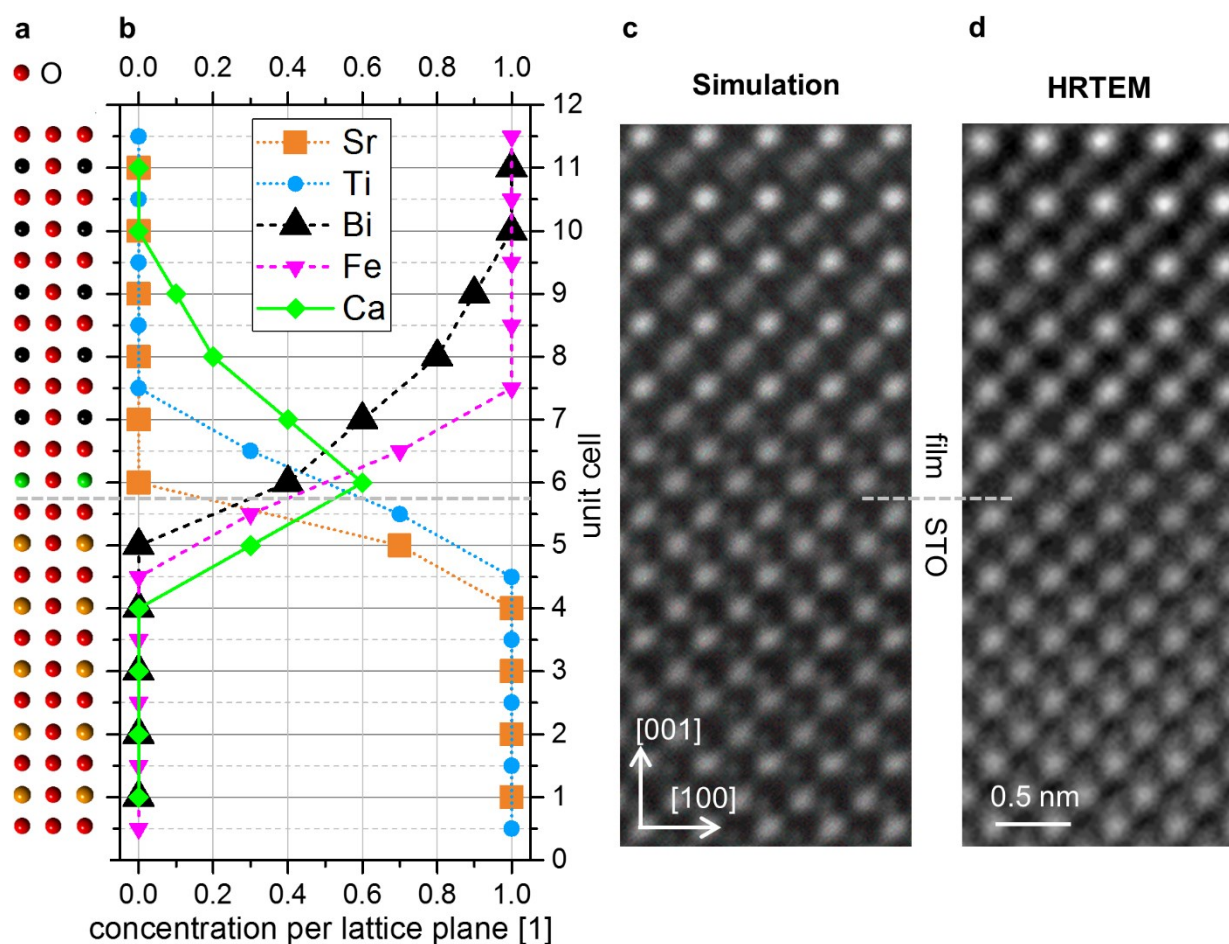


Figure S4. Comparison of image simulation and HRTEM image to verify the correct assignment of the interface in the film with Ca cluster at the interface. (a) Model of the supercell used for image simulations seen from the [010] zone axis consisting of 15 pseudocubic unit cells. The color is determined by the majority element in this column. (b) Diagram of the cation composition per lattice plane to model the heterostructure interface for the image simulations (c) Image simulation with JEMS® for $C_s = -5 \mu\text{m}$, an over focus of 35 nm, a sample thickness of 10.54 nm and tilted 0.54° away from the [010] zone axis in the direction of the [111]. (d) HRTEM image with applied ABSF filter to reduce effects of amorphous layers. The grey dashed lines indicate the position of the interface.

In Figure S5 the atom- and position-resolved electronic density of states are compared for an undoped STO/BFO interface, for a 2 ML Ca-doped interface, which compensates with charge shifts from Fe^{3+} to Fe^{4+} and for the same interface but this time compensated by oxygen vacancies. In the 2ML Ca-doped interface with Fe charge shift an acceptor gap state localized on the FeO_6 octahedra emerges (see Figure S5b), but if oxygen vacancies are assumed instead, no acceptor state occurs (Figure S5c).

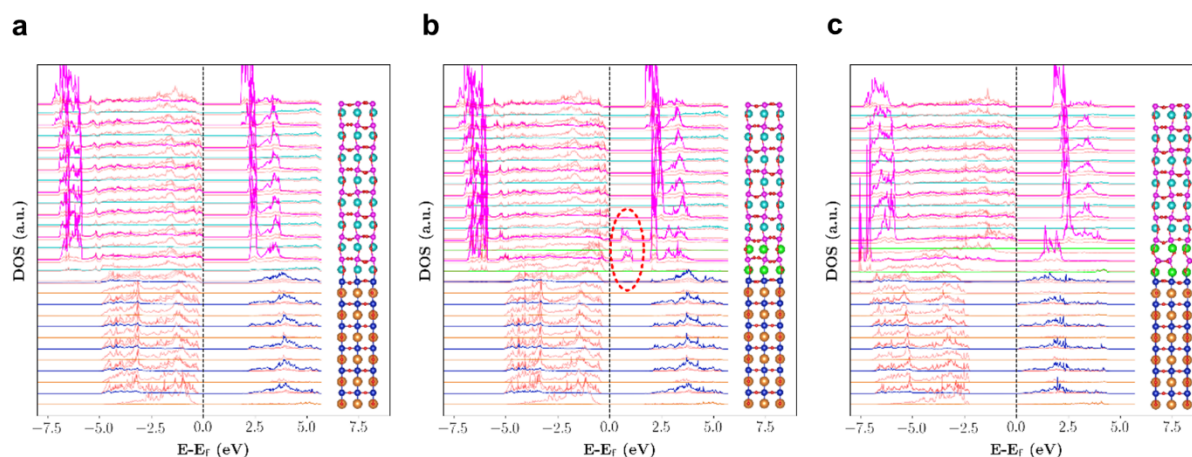


Figure S5. Atom- and position-resolved electronic density of states (DOS) of: (a) STO/BFO interface, (b) 2ML Ca-doped interface, compensated by the charge shift of Fe from 3+ to 4+; and (c) 2ML Ca-doped interface, compensated by oxygen vacancies. Structural models correspond to the geometries after relaxation. The color code is consistent with the one used in the manuscript.

Figure S6a,b shows in the exemplary HAADF images that neither in the film the Ca segregation to the interface (BCFMO) nor at the film without Ca and only Mn doping (BFMO) any antiphase boundaries (APBs) or line defect appear at the interface.

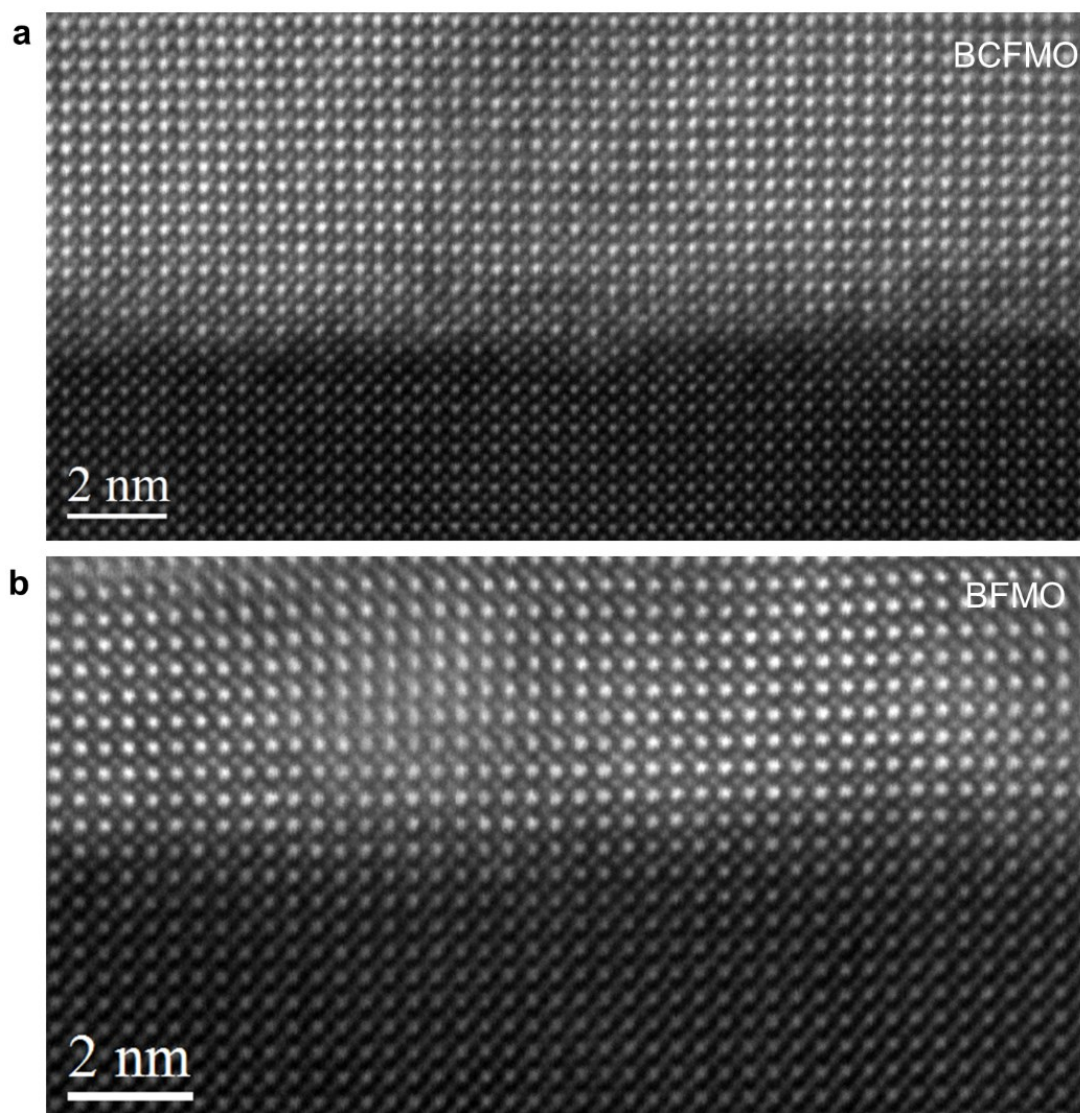


Figure S6. HAADF images of the films with (a) Ca segregated to the interface (BCFMO) and (b) without Ca (BFMO)

Figure S7a shows the XRD data of the Ca doped film and the film without Ca doping. The film without Ca doping contains also an Fe_2O_3 phase, which could be also seen in the TEM images. XPS spectra of both, the Ca-doped film and Ca-free film show that weak signals of Ca are only detected from the surface of the Ca doped film, as can be seen in Figure S7b. However, the weakness of the Ca signals suggests that there is no segregation of Ca towards the surface.

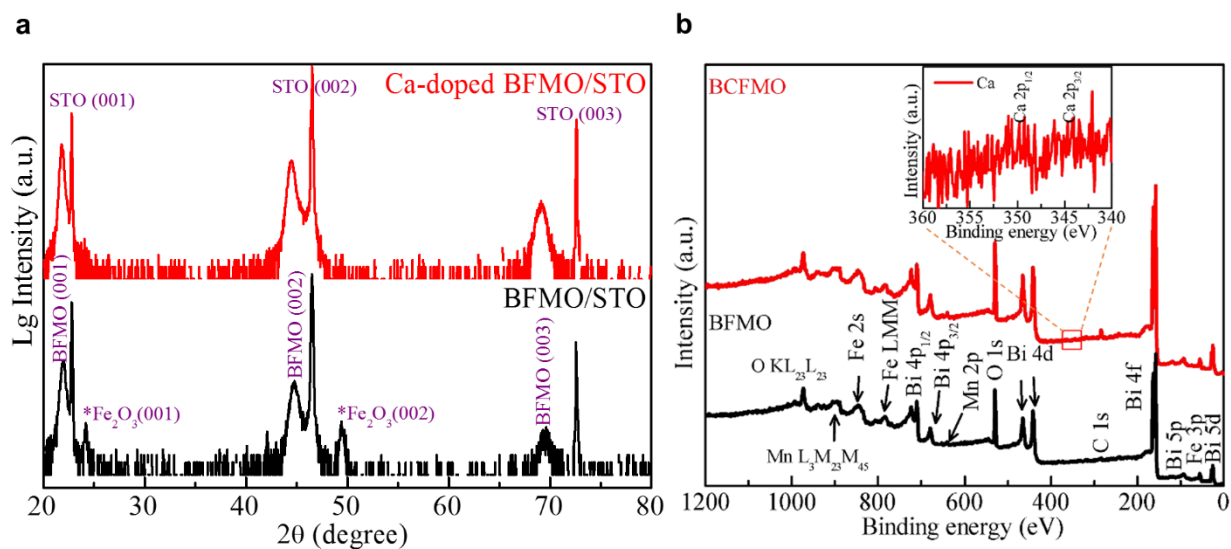


Figure S7. (a) XRD data of the of the Ca doped BFMO film and the film without Ca. (b) XPS spectra from the surfaces of the Ca doped film and the film without Ca.

Figure S8 shows a Bright Field (BF)-TEM image of the Ca doped film, demonstrating the good film quality and that no undesired effects take place at the film surface.

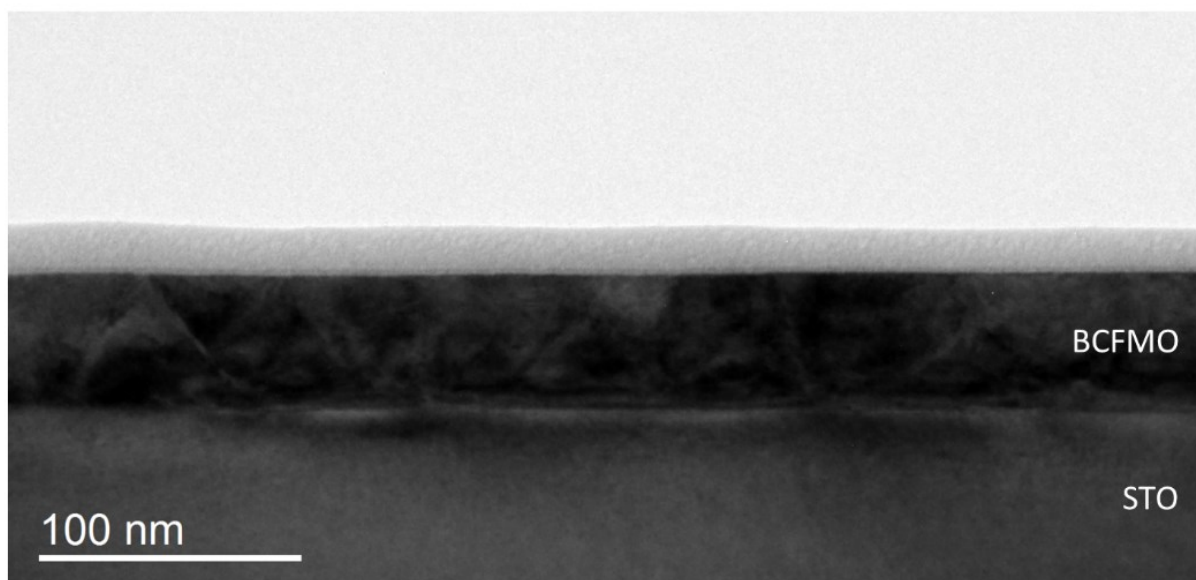


Figure S8. BF-TEM image of the Ca doped film with a magnification of 50k.

Publication B

Negatively Charged In-Plane and Out-of-Plane Domain Walls with Oxygen-Vacancy Agglomerations in a Ca-doped Bismuth-Ferrite Thin Film

Ulrich Haselmann¹, Y. Eren Suyolcu^{2,3}, Ping-Chun Wu⁴, Yurii P. Ivanov^{1,5,6}, Daniel Knez⁷, Peter A. van Aken³, Ying-Hao Chu⁴ and Zaoli Zhang^{*1,8}

¹ Erich Schmid Institute of Materials Science, Austrian Academy of Sciences, 8700 Leoben, Austria

² Department of Materials Science and Engineering, Cornell University, New York 14850, United States

³ Max Planck Institute for Solid State Research, 70569 Stuttgart, Germany

⁴ Department of Materials Science and Engineering, National Chiao Tung University, Hsinchu 30010, Taiwan

⁵ Department of Materials Science & Metallurgy, University of Cambridge, Cambridge CB3 0FS, UK

⁶ School of Natural Sciences, Far Eastern Federal University, 690950, Vladivostok, Russia

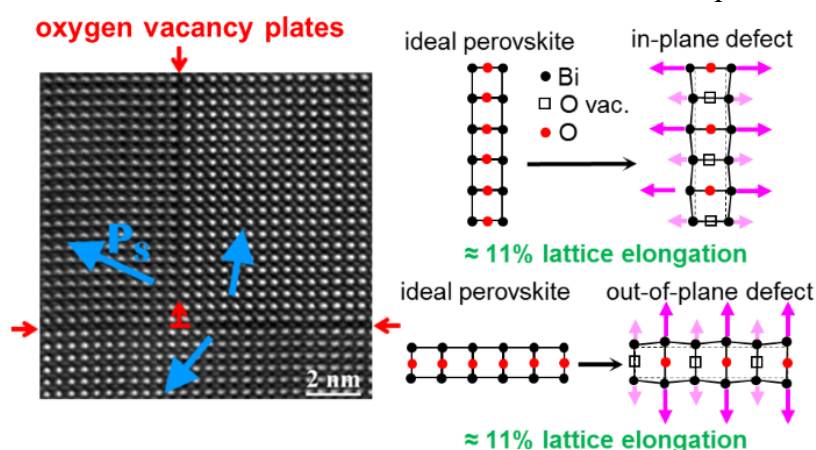
⁷ Graz Centre for Electron Microscopy, Austrian Cooperative Research, 8010 Graz, Austria

⁸ Institute of Material Physics, Montanuniversität Leoben, 8700 Leoben, Austria

Corresponding Author: *E-Mail: zaoli.zhang@oeaw.ac.at

ABSTRACT:

The interaction of oxygen vacancies and ferroelectric domain walls is of great scientific interest because it leads to different domain-structure behavior. Here, we use high-resolution scanning transmission electron microscopy to study the ferroelectric domain structure and oxygen-vacancy ordering in a compressively strained $\text{Bi}_{0.9}\text{Ca}_{0.1}\text{FeO}_{3-\delta}$ thin film. It was found that atomic plates, in which agglomerated oxygen vacancies are ordered, appear without any periodicity between the plates in out-of-plane and in-plane orientation. The oxygen non-stoichiometry with $\delta = 1$ in $\text{FeO}_{2-\delta}$ planes is identical in both orientations



and shows no preference. Within the plates, the oxygen vacancies form 1D channels in pseudocubic [010] direction with a high number of vacancies, that alternate with oxygen columns with few vacancies. These plates of oxygen vacancies always coincide with charged domain walls in a tail-to-tail configuration. Defects such as ordered oxygen vacancies are thereby known to lead to a pinning effect of the ferroelectric domain walls (causing application-critical aspects, such as fatigue mechanisms and countering of retention failure) and to have a critical influence on the domain-wall conductivity. Thus, intentional oxygen vacancy defect engineering could be useful for the design of multiferroic devices with advanced functionality.

KEYWORDS: BiFeO₃, oxygen vacancy, ordering in oxygen vacancy plates, charged domain wall, aberration-corrected STEM, domain-wall pinning, domain-wall nanoelectronics

1. INTRODUCTION

Multiferroic materials showing a coupling between ferroelectric and magnetic order parameters are referred to as magnetoelectric multiferroics and have attracted much attention in the past years.¹⁻⁴ For example, in a magnetoelectric multiferroic, an electrical stimulation results in an effect on the magnetic order parameters.⁵⁻⁷ This behavior is intriguing for numerous applications such as new kinds of memory devices promising significantly improved speed and storage density,^{8,9} spin valves, spintronic devices, and sensors.¹⁰ Single-phase multiferroic materials with high Néel and Curie temperatures, which are critical for practical applicability, are relatively rare. One of those is BiFeO₃ with a high antiferromagnetic Néel temperature of $T_N \approx 370^\circ\text{C}$ and an even higher ferroelectric Curie temperature of $T_C \approx 830^\circ\text{C}$. In particular, the control of the antiferromagnetic domains via the manipulation of the ferroelectric ones has been successfully demonstrated.¹¹ Additionally, the domain walls of BiFeO₃ have a higher conductivity than the domains itself,¹² promising the prospect of resistance-switching devices in the field of domain-wall nanoelectronics.¹³

Perovskite oxides such as BiFeO₃ become even more versatile through the incorporation of substitutional elements on the A- (Bi) or B site (Fe), which enables us to manipulate and design the electronic and magnetic properties within certain limitations.^{14,15} Ca as an A-site dopant has been shown to tune the material's behavior from antiferromagnetic toward ferromagnetic¹⁶ but also to enhance the magnetoelectric coupling¹⁷ and to enable a conductivity modulation through the application of an electric field.¹⁸ Ca doping in BiFeO₃ can induce oxygen vacancies because the replacement of Bi³⁺ with Ca, which is an alkaline earth metal and therefore cannot have a higher oxidation state than 2+, has a hole doping effect. Stoichiometrically in Bi_{1-x}Ca_xFeO_{3-δ} that

would lead to $\delta = x/2$ oxygen vacancies.^{18–20} It has been reported that for doping ratios of $x \geq 0.2$ the oxygen vacancies arrange in ordered superstructures.^{18,20–23} Thereby, the Ca is not uniformly distributed but can segregate to the energetically most favorable position.^{19,24,25} When relatively thick films are under compressive (tensile) strain, these superstructures are expected to be arranged parallel (perpendicular) to the interface, as shown in a study for LaCoO_{3-x} films.²⁶ For thin, tensile strained films where the surface energy becomes dominant compared to the bulk energy, the effect is seen that in order to minimize the surface energy, the perpendicular arranged oxygen defects, become parallel.²⁷ While for doping ratios $x \leq 0.1$, there are reports for some vacancy ordering under certain conditions,²⁸ other results indicate that they are in most cases not ordered in superstructures.^{20,21,28}

Improved magnetic behavior¹⁶ and the coupling between the electric and magnetic ordering parameters¹⁷ alone are often not enough for potential device applications, because regions where the ferroelectric polarization has been switched are at times unstable and do not stay in their switched state but relax back to the original state. This process is known as “retention failure” and can lead to a loss of functionality of the device.²⁹ Generally, it has been accepted that electrostatic boundary conditions at the ferroelectric/electrode interface are a cause for the back switching. Strong fields, that lead to depolarization, can arise at uncompensated interfaces^{29–31} as well as impurity defects.²⁹ However, defects are also a method to counter retention failure by acting as pinning centers hindering the movement of domain walls but simultaneously leading to the fatigue phenomena by degradation of switchable polarization.^{29,32} Besides phase boundaries³³, dislocations³⁴ and pre-existing ferroelastic domains³⁵, these defects can also be oxygen vacancies^{36–38}, leading to another potential improvement of material properties by Ca doping.

In this study, we investigate a Ca-doped $\text{Bi}_{0.9}\text{Ca}_{0.1}\text{FeO}_{3-\delta}$ (BCFO) film deposited on a SrTiO_3 substrate covered with a 55 nm thick SrRuO_3 interlayer. While there are no ordered superstructures, there are randomly ordered features in the atomic resolution image, which are either parallel or perpendicular to the interface. We show by atomic-resolution scanning transmission electron microscopy (STEM) with high-angle annular dark-field (HAADF), electron energy-loss spectroscopy (EELS) and the comparison with characteristic results from previous works, that these features are oxygen-deficient planar defects and, simultaneously, negatively charged domain walls with a tail-to-tail configuration. The atomic-resolution experimental results are compared with STEM image simulations and the HAADF images are evaluated with software scripts to determine the atomic-column locations, intensities, interatomic spacings, and ferroelectric polarization. Thereby, we found that while reduced intensities on the Fe sites of the planar defects do not indicate any Fe vacancies, either an increased Ca concentration or Bi-vacancy

concentration is detected on the A-site around the defect. The film is under compressive strain, which should favor planar defects parallel to the interface, but the defects occur in both directions, showing the same characteristics and presumably containing a similar amount of oxygen vacancies. Our work confirms that charged domain walls in BiFeO₃ oriented both, in-plane and out-of-plane, can be coupled to a local accumulation of oxygen vacancies. This coupling is expected to lead to pinning of the domain walls and an improved resistivity against retention failure.

2. EXPERIMENTAL DETAILS

2.1. Thin-Film Fabrication. The thin-film was fabricated by pulsed laser deposition (PLD) using a KrF excimer laser (Coherent, Inc., 248 nm) with a pulse repetition rate of 10 Hz on a single crystalline (001)-oriented SrTiO₃ (STO) (Shinkosha, Co., Ltd.) substrate. Before the thin-film deposition, the substrate was cleaned by acetone and ethanol in an ultrasonic cleaner. First, using a total deposition time of 30 min, a 55 nm thick SrRuO₃ (SRO) intermediate layer was epitaxially grown with an energy of 220 mJ/pulse onto the STO substrate. Afterward, a 10% Ca-doped Bi_{0.9}Ca_{0.1}FeO_{3- δ} (BCFO) thin film was deposited with a deposition time of 45 min and an energy of 220 mJ/pulse onto the SrRuO₃ intermediate layer, resulting in a film thickness of 60 nm. The vacuum chamber was first kept at a pressure of about 10⁻⁷ Torr. During the deposition the substrate was maintained at a temperature of 700°C with an oxygen environment of 100 mTorr. Cross-sectional samples for the TEM investigations were prepared using a Helios Nanolab FIB-SEM by a standard focused ion beam protocol.³⁹⁻⁴¹

2.2. Data Acquisition. A probe-aberration-corrected (DCOR, CEOS GmbH) JEOL JEM-ARM200F with a cold field-emission electron source operated at 200 kV and equipped with a Gatan GIF Quantum ERS spectrometer was used for all STEM analyses. STEM imaging and EELS analysis were performed at a semi convergence angle of 20 mrad, resulting in a probe size of 0.8 Å.⁴² Detailed imaging parameters for the HAADF images can be found in the Table S1. For the EELS spectral image, a collection semi-angle of 111 mrad, a pixel time of 10 ms with 48 * 170 pixel and an energy channel width of 1 eV have been used. High-resolution transmission electron microscopy (HRTEM) using a JEOL JEM 2100 F with an image-side C_s corrector, an acceleration voltage of 200 kV and a Gatan Orius SC1000 camera was additionally used to evaluate the strain state of the film

2.3. Data Evaluation. The strain analysis was performed with the Geometric Phase Analysis (GPA) software package v4.0 from HREM research company for Digital Micrograph 2.3 from Gatan. For the analysis of HAADF images concerning intensities, site spacings, and ferroelectric polarization two homemade MatLab scripts written in MathWorks Inc. MatLab (version R2017b) were used. Prior to applying the scripts, the experimental images were filtered with a principal component analysis (PCA) script for Digital Micrograph written by S. Lichtert, T. Hayian, and J. Verbeeck to reduce image noise.⁴³ At the beginning of the first MatLab scrip, the locations of atomic columns in the image are ascertained by searching for local maxima. Gaussian fitting with sub-pixel precision is used to refine the peak locations and then as a basis for Voronoi tessellation. These received cells are utilized to determine the absolute intensity from the unfiltered image by integrating over a defined area corresponding to each atomic column. Columns at the edge of the image that lie not entirely in it are excluded.^{24,44} The integrated column intensity is a robust measurement, as it is insensitive to the probe shape and the defocus.^{24,45} The second MatLab script was written to evaluate (i) the fitted atomic-column positions from the first script according to the spacings between the atomic sites, (ii) the polarization due to shifts of the central Fe atom and (iii) to visualize the data. The EELS spectra were processed using the built-in functions of Digital Micrograph and additionally filtered in OriginPro 2016 using a Savitzky-Golay filter with a window of 9 data points for denoising. HAADF-image simulations with the software Dr. Probe⁴⁶ were performed for a sample thickness of 30 nm (76 BiFeO₃ unit cells), an acceleration voltage of 200 kV, a semi convergence angle of 20.9 mrad, a spherical aberration of 0 μm , a defocus value of 0 nm, an effective source radius of 0.10 \AA , a scanning step size of 10 pm, and a HAADF detector ranging from 49 to 250 mrad. Those parameters were chosen so that the simulation results are comparable with the experimental parameters used for HAADF acquisition.

3. RESULTS

3.1. Large-Scale Structure of the Film. STEM investigations of the overall thin film cross section showed that the SRO as well as the BCFO film have grown epitaxially on the STO substrate, as can be seen in Figure S1. The in-plane strain is only slightly increased over the thickness of the 55 nm wide SRO layer and the first 20 nm of the film covered in that image frame, while the out-of-plane strain is immediately increased at the STO/SRO interface and only marginally decreases over the width of the SRO thin film layer and the adjacent BCFO thin film.

These strain characteristics are expected for a good quality epitaxial growth, because the pseudocubic SRO and pure BiFeO₃ (BFO) lattice parameters are approximately 0.6%⁴⁷ and 1.5%^{10,48} larger than the lattice parameter for bulk STO. Therefore, the thin films are compressed in the in-plane direction and enlarged in the out-of-plane direction. For the BCFO film, the lattice parameters received from the strain maps in Figure S1b,c are 3.93±0.01 Å for the in-plane direction and 4.01±0.01 Å for the out-of-plane direction, resulting in an enlargement in the out-of-plane direction by 2.0±0.5%. Determining the lattice parameter with HRTEM measurements, which have the advantage that drift distortions are minimized compared to STEM, 3.91±0.01 Å for the in-plane lattice parameter and 4.02±0.01 Å for the out-of-plane lattice parameter are received resulting in measured enlargement of the out-of-plane direction of 2.9±0.5%.

Figure 1a shows a large scale (low magnification) HAADF image of the BCFO film covering almost the entire epitaxial layer. The SRO/BCFO interface is on the bottom side of the imaging frame and not visible. Noticeable in the HAADF image are several stripes with darker contrast than the surrounding areas, which are either parallel to the [100]_{pc} (subscript pc refers to pseudocubic) or the [001]_{pc} direction. Their starting and endpoints are marked with colored arrows, and they are numbered. The map of the out-of-plane lattice strain in Figure 1b shows that the dark lines parallel to the [100]_{pc} (in-plane) direction, which are marked with green arrows and numbers, coincide with an enlarged strain and therefore with an enlarged lattice parameter in the out-of-plane direction. Because the out-of-plane lattice parameter is enlarged, they are called *out-of-plane defects*. Similarly, in the in-plane strain map in Figure 1c, dark lines in the HAADF image parallel to the [001]_{pc} (out-of-plane) direction are marked by the magenta colored arrows and are called *in-plane defects*, because of their enlarged lattice parameter in the in-plane direction. Figure 1d shows a schematic illustration of the film system and the in-plane and out-of-plane defects. The blue arrows in Figure 1a and c mark a single misfit/edge dislocation, which originates at the SRO/BCFO interface and locally reduces the compressive strain. These dislocations are not very frequent and occur approximately once per 500 nm interface length and therefore will not cause a significant relaxation of the film. These edge dislocations are not the focus of this study, because they have already been investigated extensively for BiFeO₃ thin films under compressive strain.^{49,50}

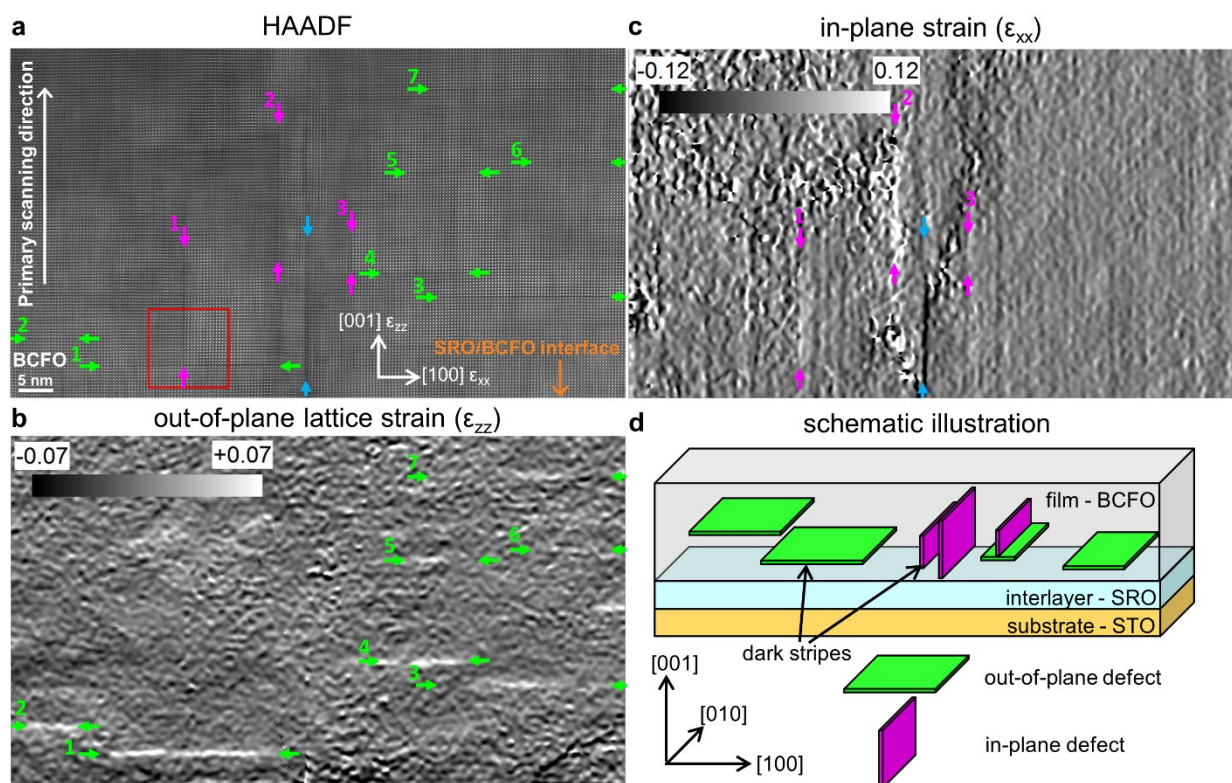


Figure 1. Large-scale structural mapping of the BCFO thin film and its defects. (a) HAADF image of the BCFO film along the $[010]_{pc}$ zone axis. The red square indicates the area shown and analyzed in Figure 2. (b) Map of the out-of-plane strain (ϵ_{zz}) and (c) map of the in-plane strain (ϵ_{xx}). The colored arrows mark the beginning and the end of the dark stripes found in the HAADF image. Green arrows mark dark stripes, where ϵ_{zz} is increased, and are therefore called out-of-plane defects, while magenta arrows indicate dark stripes, where ϵ_{xx} is increased and are therefore called in-plane defects. The blue arrows indicate an edge dislocation relaxing the in-plane strain, which starts at the SRO/BCFO interface (not shown here). (d) Schematic illustration of the thin film and the two types of defects (the best contrast can be seen in the digital version).

3.2. Analysis of In- and Out-Of-Plane Defect with Contact Point. In Figure 1a, the red square indicates an area, where one in-plane defect and one out-of-plane defect (for the difference between the two and the definitions see Figure 1d) touch each other. A more detailed analysis can be seen in Figure 2. In the HAADF image shown in Figure 2a, the in-plane and out-of-plane defects are indicated by red arrows. These defects divide the image in three areas, which are numbered from I to III. The pseudo-cubic $[100]$ direction is defined as the axis a , while the $[001]$ direction is defined as c . Figure 2b shows the map of interatomic distances between A-sites (a_{A-A}) in the a (in-plane) direction. It can be clearly seen that along the a direction there is an elongation of interatomic A-site distances at the in-plane defect, whose position is indicated again by red arrows and ends at the touching point with the out-of-plane defect (marked by the arrow

with a crossbar at the beginning). The out-of-plane defect shows no lattice enlargement in the a direction and is completely invisible in the map. The same interatomic distances in the c (out-of-plane) direction (c_{A-A}) can be found in Figure 2c. In contrast to Figure 2b, the out-of-plane defect can now be observed by an enlarged A-A spacing, while the in-plane defect is not visible. The map of the normalized A-site intensities, where Bi and Ca atoms are sitting, is presented in Figure 2d. In region II, the A-site intensities are the highest, while in region I they are reduced by approximately 20%. The reason for that is, that the images of the A-sites look different in region I and are slightly elongated compared to region II. The root cause for that is probably, that due to the out-of-plane defect, region I is not exactly aligned in zone-axis orientation and is slightly tilted. In region III, the A-site intensities change in a continuous way from the left to the right side of the image. In Figure 2e, the normalized B site intensities (Fe atoms), are displayed. It is quite noticeable that especially at the in-plane defect but also at the out-of-plane defect, the intensities of the B site positions are reduced. In Figure 2f, a map of the electric polarization^{51,52} is displayed, which is obtained from the shift of the Fe atom away from the center of the pseudo-cubic cells, whose edges are formed by the Bi atoms sitting at the corner of the surrounding A-sites (for a schematic illustration see Figure 2a on the right bottom side). The projection of the polarization direction is thereby the vector sum of the negative shift of the Fe atom $-\Delta a$ in a direction and $-\Delta c$ in c direction.^{19,32,53-55} The color bar on the right side of Figure 2f is also valid for Figure 2d,e. It is clear from this map that each of the three regions has a prevalent polarization orientation excluding some minor deviations. The big grey arrows indicate the relative size and orientation obtained from averaging all polarization vectors in each region. In bulk BiFeO₃, the ferroelectric polarizations are oriented along the pseudocubic [111] orientation. However, in thin films, especially in the proximity of defects, it has already been reported before, that the polarization can differ from this direction.^{19,49} The defects clearly represent charged domain walls (CDWs) between all three regions in a tail-to-tail configuration. Between regions I and II, they are either of the kind 71° or 109°, assuming that the polarizations are indeed oriented along the [111] direction and the deviations from it are in fact measurement errors. Because, the b direction ($[010]_{pc}$) can only be observed in projection, we cannot differentiate between 71° and 109° CDWs. Region III deviates from the [111] direction as well. Between regions I and III, there is also a 71° or 109° CDW, and between II and III, there is a 109° or 180° CDW. An optimized version for colorblind readers of Figure 2 is displayed in Figure S2.

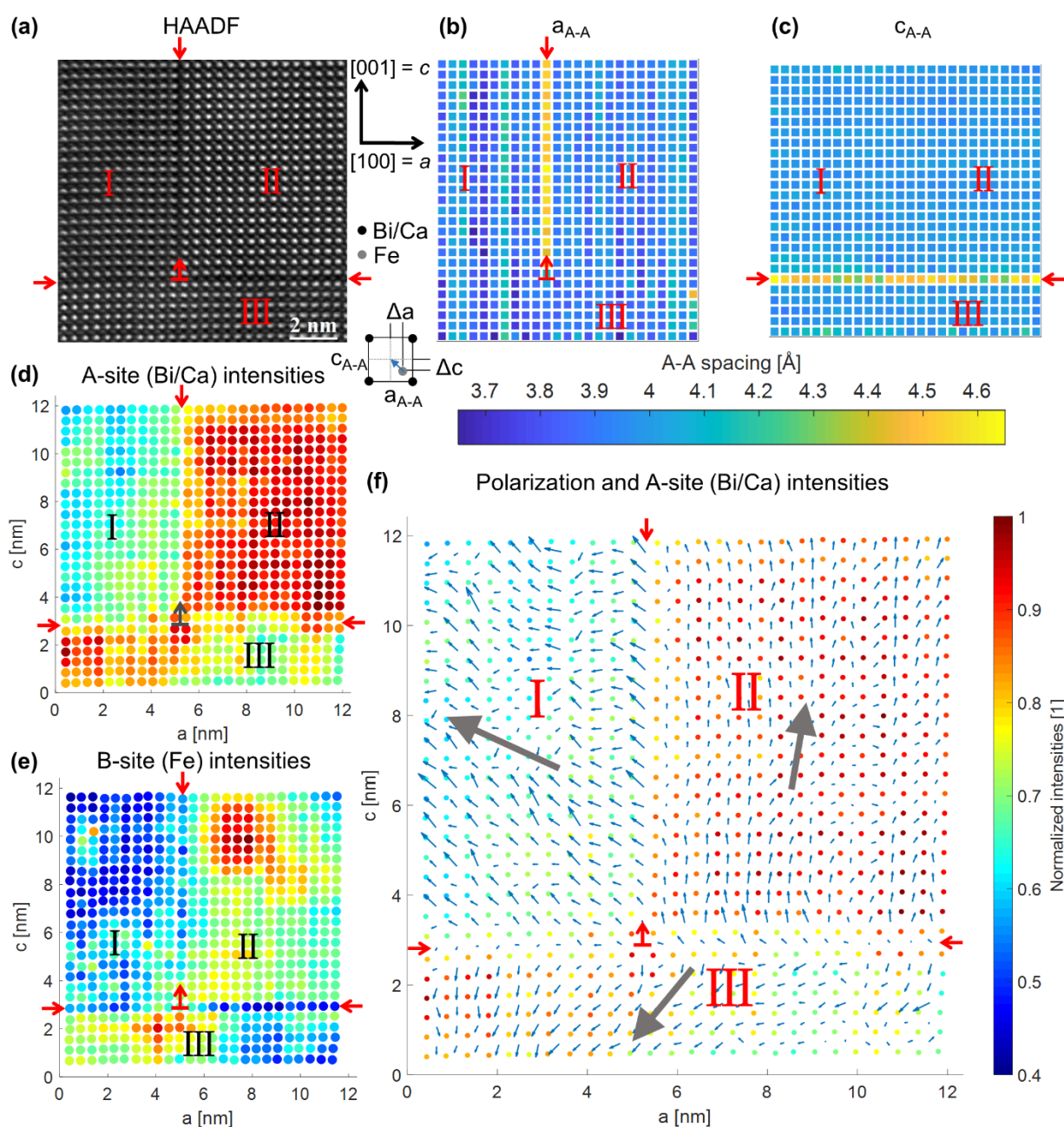


Figure 2. Analysis of high-resolution STEM data of an in-plane and out-of-plane defect, which have a common point of contact (region indicated by the red square in Figure 1) (a) HAADF image showing two defects marked with red arrows. The defects separate the image into three areas designated with roman numbers I to III. On the top right side of the HAADF image, the $[100]_{pc}$ and $[001]_{pc}$ axes are indicated as a and c . At the bottom of the right side is a schematic illustration of the electrical polarization due to shift of the Fe atom from the center of the pseudo-cubic cell. (b) Map of interatomic distances of the A-sites (Bi and Ca atoms) in the a (in-plane)-direction. The in-plane defect marked by the red arrows can be clearly seen by the enlarged lattice parameter. (c) Map of interatomic A-site distances in the c (out-of-plane)-direction. The out-of-plane defect can be clearly observed by the enlarged lattice parameter. (d) A-site intensities (Bi and Ca positions) in the HAADF image normalized to the maximal A-site intensity. (e) B site (Fe) intensities in the HAADF image normalized to the maximal B site intensity. (f) Map of the electrical polarization due to the shift of the Fe atom overlaid

on the fitted positions and intensities of the A-site atoms. The gray arrows in the regions I-III indicate the average polarization direction and magnitude relative to each other. A version optimized for colorblind readers can be found in Figure S2.

3.3. Analysis of In-Plane Defects. To explore the defects in more detail, an in-plane defect (for the definition see Figure 1d) is being analyzed separately in this section. Figure 3a shows the HAADF image of a different in-plane defect (than the one showed in Figure 2). The red arrows mark the defect, which separates the imaged area in regions I and II. In Figure 3b, the HAADF intensities normalized to the maximum A- or B site intensities, which have been averaged along the c direction, are shown. The gray dashed lines indicate the average of the measured intensities. The B site intensities (\bar{I}_B) are reduced exactly at the defect. Similarly, the A-site intensities (\bar{I}_A) in region II on the right side of the defect are noticeably reduced (atomic row 8), while on the left side of the defect (region I) there is a less pronounced intensity decrease on atomic row 7. Figure 3e shows the interatomic distances between A-sites (a_{A-A}) in the a direction (in plane; the associated color bar can be found in Figure 3g). These interatomic distances clearly show a significant elongation exactly at the defect compared to the ideal perovskite structure, as can be seen by the lattice spacing averaged in the c direction in Figure 3f. The distortion is not uniform along the defect, but shows an alternating pattern, where one A-A pair atomic distance shows a larger elongation and the subsequent one has a less pronounced elongation. The analysis of the mean lattice elongation at in-plane defects (five defects analyzed including the in-plane defect shown in Figure 2) yields $11.4 \pm 0.3\%$ of the in-plane lattice parameter. The difference between the values for the lattice elongation of the in-plane defects shown in Figure 2 and Figure 3 are within the measurement errors. The small statistic variance indicates that that all the defects show essentially the same elongation. A summary of the lattice parameters and the lattice elongation values can be found in Table 1. A schematic illustration of this observed defect compared to the ideal perovskite structure can be seen in Figure 3d. In comparison, the interatomic A-site distances in the c direction show no influence of the defect (Figure 3g). The map of the electric polarization due to the shift of Fe atoms from the center of A-site quartets (schematically depicted in Figure 3c) is presented in Figure 3h. From this polarization map, it is obvious that the defect also marks a tail-to-tail CDW between regions I and II. The big gray arrows in Figure 3h show the averaged polarization direction and magnitude for regions I and II. The magnitude of the polarization vector in region II is larger than in region I, which is also depicted by the correct ratio of the norms of the gray vectors in Figure 3h. The reason for that can be seen on the A-sites (B_i) in region II (Figure 3a), which are not nicely circular like the A-sites in region I, but elongated toward the northeast direction of the image. This either seems to stem from a slight tilt introduced by the

defect or there is an astigmatism in region II, while there is none in region I. This slightly increases the magnitude of the polarization in region II, but it does not influence the general polarization direction or the relative polarization relationship between regions I and II. From these directions we can deduce that it can either be a 109° CDW or a 180° CDW. Figure 3i plots the shift of the Fe atoms from the center separated in the Δa and Δc components averaged along c direction, which correspond to the deviation of the Fe atom from the center of the four surrounding A-sites in a and c directions, as schematically depicted in Figure 3c. The Fe displacement values shift exactly at the defect.

Table 1. Lattice parameters of the BCFO thin film and average elongation of the in-plane and out-of-plane defects with the average scanning step size used for the defect analysis.

	Lattice parameter [Å]	Defects		
		elongation [%]	elongation [Å]	average step size [pm]
in-plane	3.93 ± 0.01	11.4 ± 0.3	0.45 ± 0.01	7.46
out-of-plane	4.01 ± 0.01	10.7 ± 1.0	0.43 ± 0.04	12.48

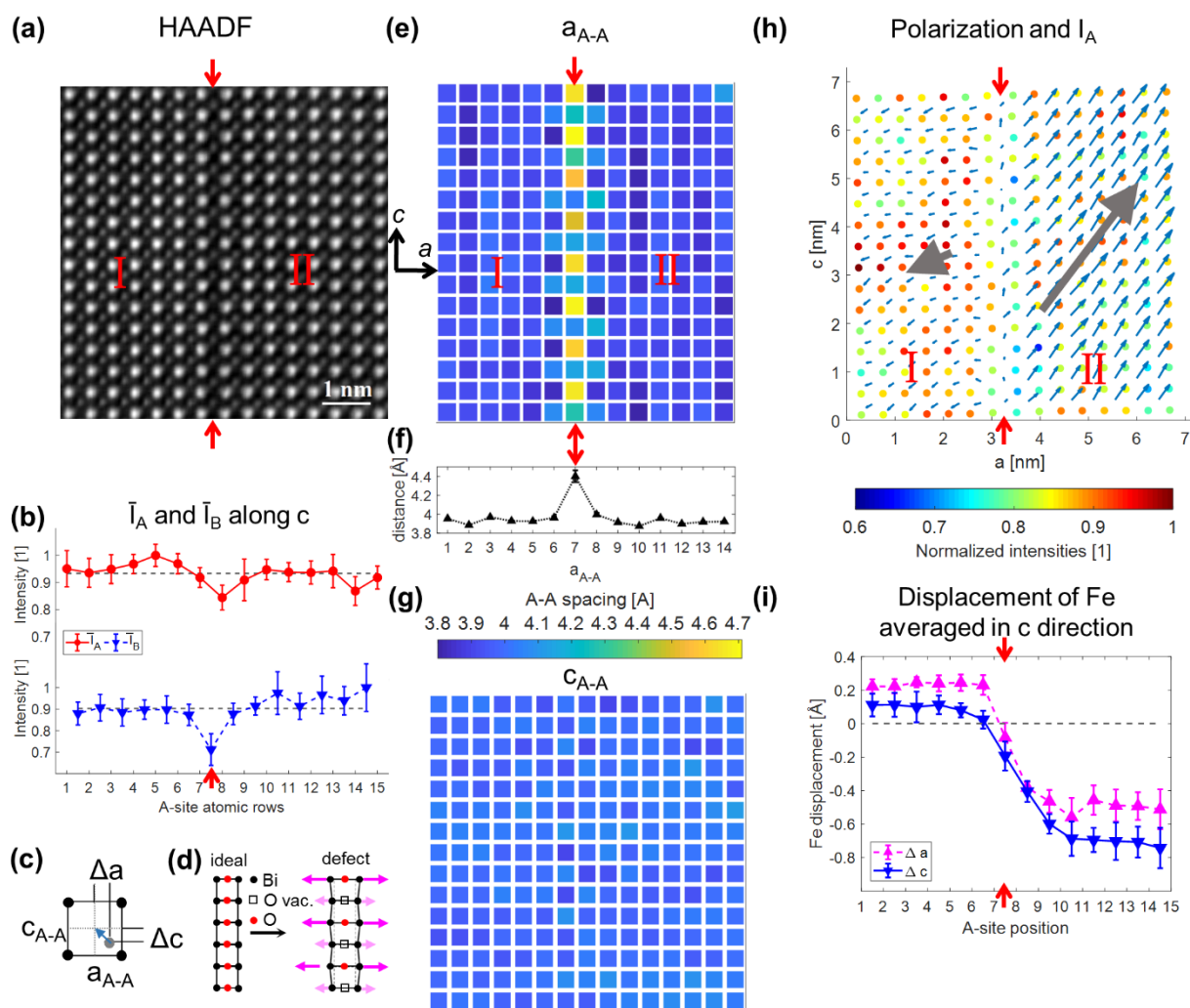


Figure 3. Exemplary analysis of an in-plane defect. (a) HAADF image of the in-plane defect marked by red arrows. (b) A- and B site intensities (\bar{I}_A and \bar{I}_B) averaged along the c direction. The A-sites are numbered in integers, while the B sites are counted as integers of ± 0.5 (half sites). (c) Schematic illustration of the electric polarization due to shift of the central Fe atom by Δa and Δc in the pseudocubic perovskite unit cell. (d) Illustration of the arrangement of the A-site atoms in the ideal perovskite and at the defects including the oxygen stoichiometry in the $\text{FeO}_{2-\delta}$ plane (see discussion section).¹⁹ (e) Map of interatomic A-A-site distances in the a direction (a_{A-A}). The defect is marked by red arrows and shows an enlarged lattice parameter with an alternating pattern of one site having a larger elongation, whereas the next one has a less pronounced one. The color bar can be found in (g). (f) A-A-site distances averaged along the c direction showing the average elongation at the defect. (g) Map of interatomic A-A-site distances in the c direction (c_{A-A}). No variation along the defect is visible. (h) Map of the electric polarization due to shift of Fe atoms overlaid on the fitted positions and intensities of the A-site atoms (I_A). (i) Displacement of Fe atoms separated in Δa and Δc components averaged in the c direction. A version optimized for colorblind readers can be found in Figure S3a.

3.4. Analysis of Out-Of-Plane Defects. In this section, an exemplary analysis of an out-of-plane defect (for the definition see Figure 1d) is presented and compared to the previously described in-plane defects. In Figure 4a, an HAADF image of a defect, which separates the imaged area in regions I and II, is presented. The red arrows mark the position of the defect. The intensities for A- and B sites averaged along the a direction are shown in Figure 4b. The averaged intensities of the B sites (\bar{I}_B) show, similar to the in-plane defect in Figure 3b, a significant intensity decrease at the defect location. The A-site intensities display a weak intensity decrease in atomic row 8 above the defect, but no significant intensity difference can be seen in atomic row 7 below the defect. The map of the interatomic distances between A-sites in the a direction (a_{A-A}) in Figure 4c shows, opposite to the same map for the in-plane defect in Figure 3e, there are no local distortions, because the present defect is an out-of-plane defect. Instead, the map of the interatomic distances in the c direction (c_{A-A}) in Figure 4h shows the same alternating lattice-elongation pattern as for the in-plane defect, having one A-A couple having a large elongation and the subsequent one with a less pronounced elongation. The lattice spacing averaged in the a direction is displayed in Figure 4i, showing a significant overall increase at this defect. The analysis of the mean lattice elongation at out-of-plane defects (5 defects analyzed including the out-of-plane defect of Figure 2) shows a lattice parameter elongation of $10.7 \pm 1.0\%$. The difference between the values for the lattice elongation of the out-of-plane defects in Figure 2 and Figure 4 is also within the measurement errors. No large difference in the lattice elongation of the out-of-plane defects compared to the in-plane defects could be observed, indicating that the nature of all defects is the same. The summary of the out-of-plane lattice-elongation values can be found in Table 1. The map of the electric polarization is presented in Figure 4f. Again the defect turns out to be a tail-to-tail CDW. The gray arrows show the averaged polarization moment for the regions I and II, displaying besides the direction also the relative magnitude of the polarization in regions I and II. The absolute value of the polarization vector in region I is larger than in region 2. Figure 4g shows the Fe site-shift averaged in the a direction and demonstrates that the orientation of the Fe displacements shifts exactly at the defect as observed for the in-plane defects.

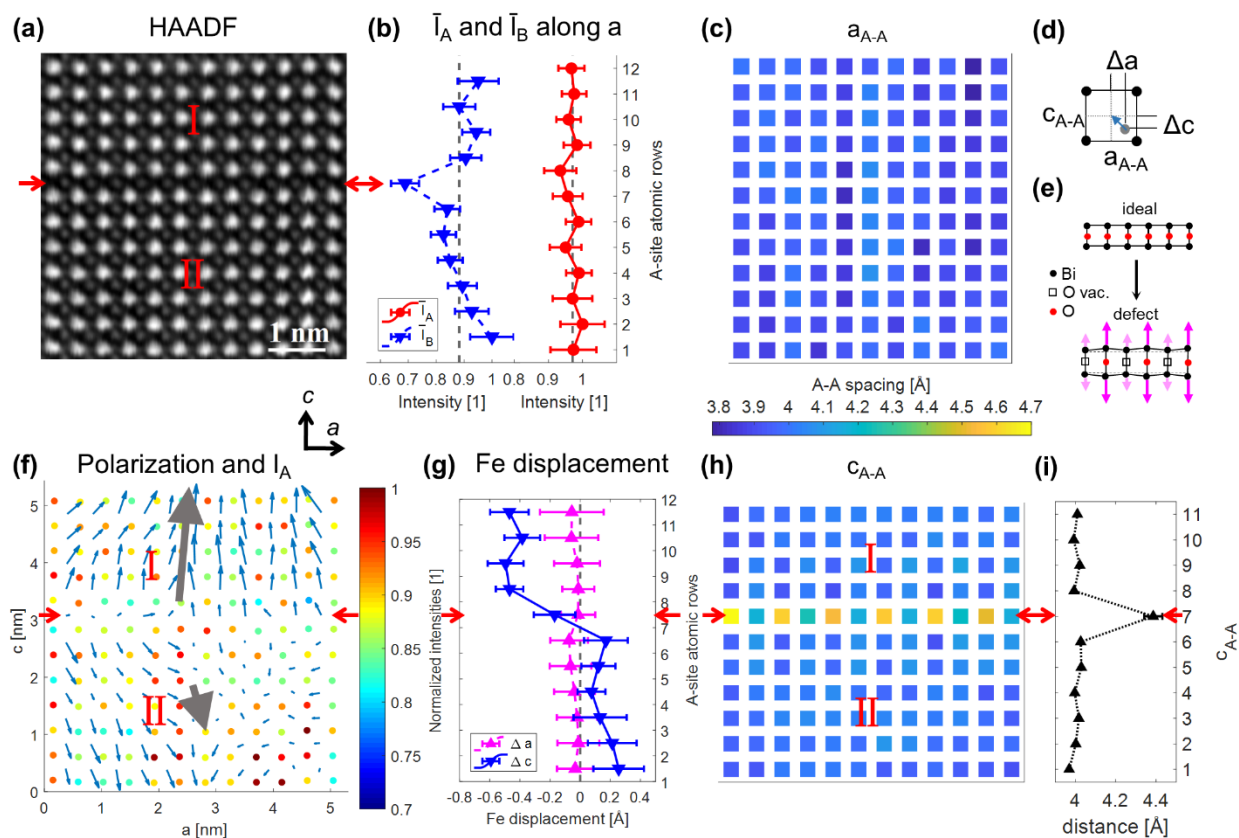


Figure 4. Exemplary analysis of an out-of-plane defect. (a) HAADF image of the defect marked with red arrows. (b) A- and B site intensities (\bar{I}_A and \bar{I}_B) averaged along the a direction. The A-sites are numbered in integers, while the B sites are counted as integers of ± 0.5 (half-sites). (c) Map of interatomic A-site distances in the a direction (a_{A-A}). No variation along the defect is visible. (d) Schematic illustration of the electric polarization due to shift of the central Fe atom by Δa and Δc in the pseudo-cubic perovskite unit cell. (e) Schematic presentation of the A-site atom arrangement in the ideal perovskite and at the defects including the oxygen stoichiometry in the central $\text{FeO}_{2.6}$ plane of the defect (see discussion section).¹⁹ (f) Map of the electric polarization due to the shift of the Fe atom overlaid on the map of the fitted positions and intensities of the A-site atoms (I_A). A version optimized for colorblind readers can be found in Figure S3b. (g) Displacement of Fe atoms displayed for Δa and Δc averaged in the a direction. (h) Map of interatomic A-site distances in the c direction (c_{A-A}). The defect is marked by red arrows and shows an enlarged lattice parameter with a typical alternating A-A distances. (i) A-A-site distances averaged along the c direction displaying an average lattice elongation at the defect.

3.5. Atomic Resolution EELS at the Defects. After revealing information on the structural characteristics, analytical investigations on the defects were performed using STEM_EELS. In Figure 5a, the HAADF image of an in-plane defect is shown. The area of interest for the acquired EELS core-loss spectra is highlighted with a magenta rectangle. The spectral signals of a width of approximately one pseudo-cubic unit cell along the defect (red rectangle in

the EELS map in Figure 5b) and of the undistorted perovskite (blue rectangle) are compared. The distance between the O-K and Fe-L₃ onsets for on and off the defect remains the same, which indicates that the Fe-oxidation state remains the usual Fe³⁺ in the area of the defect.⁵⁶ Additionally, this is supported by the fact, that there is no change in the ELNES fine structure of the Fe or the O edge.⁵⁷ Thus, the Fe oxidation state is not changed by the defect. Concerning the intensity of the O-K edge, the signal from the defect (red curve in Figure 5c) seems slightly weaker than the signal from the undistorted perovskite, indicating that the defect may indeed contain less oxygen (oxygen vacancies).

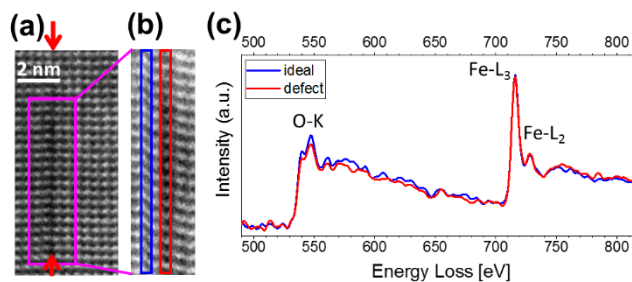


Figure 5. Atomic resolution EELS study at the defects (a) HAADF image of the defect. The magenta rectangle indicates the area where the (b) spectrum image was recorded. The red rectangle marks the area of the defect and the blue one the undistorted perovskite area for comparison. (c) EELS spectra recorded on the defect (red) and beside the defect (blue).

4. DISCUSSION

Considering the data gathered about the the dark stripes, their exact nature becomes evident. Because the areas adjacent to the dark stripes are slightly tilted relative to each other (e.g. Figure 2 region I and II and Figure 3) annular bright field (ABF) images could not be used to analyze the reason for the dark stripes and other indications had to be used. An overview of the three main indicators discussed in the following in detail can be found in Figure 6. In the literature, dark stripes in HAADF images of perovskites have been described as structural modifications due to the local accumulation of oxygen vacancies.^{19,20,26,32,58} Geng *et.al* were able to show directly with EELS for an undoped BFO film that the dark stripes are indeed oxygen deficient. They could confirm this by etching combined with XPS and the fact that films grown with less oxygen partial pressure, showed longer dark stripes in the cross sectional samples.³² Geng *et al.* also observed that the oxygen-vacancy stripes always resulted in a CDW with a tail-to-tail configuration³² (see Figure 6a), where the negative charge of the tail-to-tail domain walls compensates for the positively charged oxygen vacancies.^{59,60} However, in their studies, they were only observing out-

of-plane defects and no in-plane defects, likely due to the much larger compressive strain of -2.6% instead of -1.4%. In our cross sectional samples, we also see dark stripes and they also always coincide with tail-to-tail CDWs (e.g. Figure 2, Figure 3 and Figure 4). Additionally, we see a very slight reduction in the O-K edge intensity of the EELS signal, which could be a direct hint of a reduced oxygen content (Figure 5c). These are apparent indications that the origin of the dark stripes in our samples is also the accumulation of oxygen vacancies.

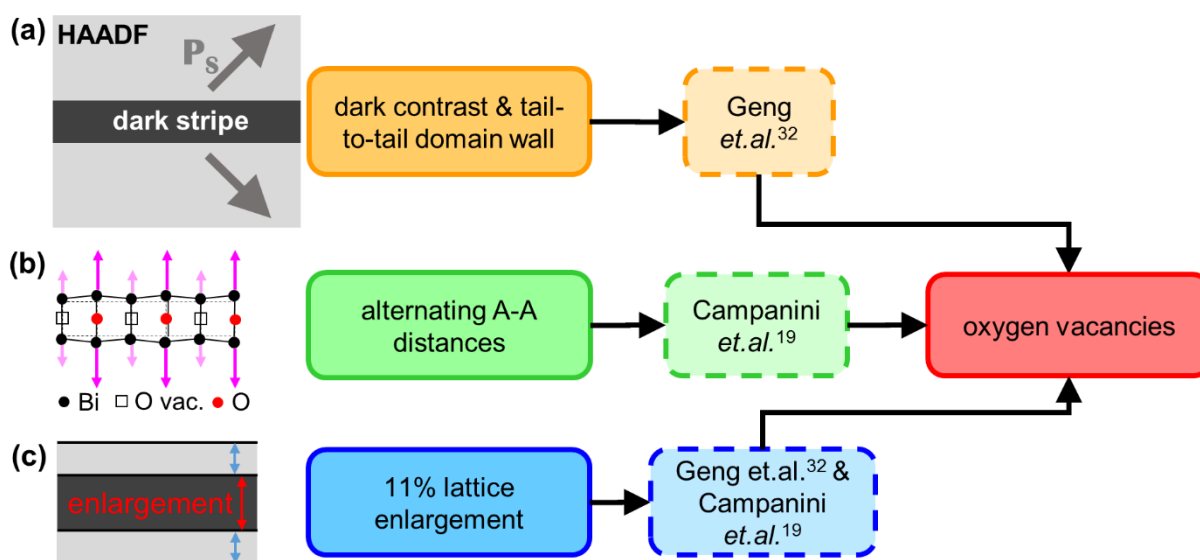


Figure 6: Schematic illustration of the three indicators for the reason of the dark stripes being the agglomeration of oxygen vacancies: (a) Tail-to-tail CDW (negatively charged) with dark contrast in the HAADF images. The accumulation of oxygen vacancies (positively charged) would compensate for the CDW.³² (b) The A-A distances across the dark stripe show one larger elongation followed by one smaller elongation, which is linked to a special ordering of oxygen vacancies reported by Campanini *et al.*¹⁹. (c) Average lattice expansion of around 11% was measured. The same was reported by Geng *et al.*³² for $\delta = 1$ referring to the $\text{FeO}_{2-\delta}$ plane. That means every second oxygen should be missing there, which again fits to the oxygen vacancies and structural changes reported by Campanini *et al.*¹⁹.

Campanini *et al.* (see Figure 6b) also observed these dark stripes in their HAADF images in a $\text{Bi}_{0.8}\text{Ca}_{0.2}\text{FeO}_3$ sample. Mapping of the A site positions showed that across the dark stripes A-A distances are alternating having one larger elongation followed by a smaller one.¹⁹ Campanini *et al.* presented a model structure explaining the A-A distance oscillations with one O site in the $\text{FeO}_{2-\delta}$ plane having few vacancies and the next site having many vacancies as schematically depicted in Figure 3d and Figure 4e. The Fe atoms move further away from the site with many vacancies and increase the adjacent A-A distances.¹⁹ This model was received by directly mapping the O column intensity in ABF (annular bright field) STEM imaging.¹⁹ Mapping the A site positions in our sample across the dark stripes, we also observe alternating A-A distances with

one A-A pair showing a larger elongation and the subsequent one being smaller (Figure 3e and Figure 4h). Thus, this alternating pattern is another evident indication that the nature of these defects is indeed the planar arrangement of oxygen vacancies. These columns with a high amount of oxygen vacancies form one-dimensional (1D) channels oriented in $[010]_{pc}$ direction. Also, the same type of oxygen vacancy channels has been found in 50 at.% doped $\text{Bi}_{0.5}\text{Ca}_{0.5}\text{FeO}_3$.²² It is important to note that while Brownmillerite-like defects have been observed in many perovskite materials, such as, e.g., $\text{LaCoO}_{3-\delta}$ based⁶¹⁻⁶⁴, $\text{SrFeO}_{3-\delta}$ based⁶⁵ or $\text{LaMnO}_{3-\delta}$ based⁶⁶, the oxygen vacancy ordering, which would be the explanation for the structure observed in this study, does not belong to the Brownmillerite-like ordering, because the O vacancy channels are oriented in the $[010]_{pc}$ direction and not in the $[110]_{pc}$ direction.⁶⁶

Geng *et al.* (see Figure 6c) saw a lattice elongation in the dark stripes of around 11%, which they assigned through density functional theory calculations in the $\text{FeO}_{2-\delta}$ layers to a value of $\delta = 1$.³² In our film we also measured a lattice elongation for in-plane and out-of-plane defects of approximately 11%, which also hints on a value of $\delta \approx 1$. According to the result of Campanini *et al.*, the alternating A-A distances indicate that in the $\text{FeO}_{2-\delta}$ layers at the center of the dark lines in the HAADF image (e.g., Figure 2, Figure 3 and Figure 4) every second oxygen site has many vacancies, while the other have few (schematic disposition in Figure 3d and Figure 4e), suggesting also a value of $\delta \approx 1$. Therefore, based on the literature data, the alternating A-A distances as well as the 11% lattice elongation in our sample both in consistency suggest a value of $\delta \approx 1$.

The intensity analysis of the Fe sites within the defects (see Figure 2e and the blue curves in Figure 3b and Figure 4b) shows that its values are reduced by $21 \pm 10\%$ compared to the undistorted structure resulting in the darker contrast. Simulations of a model Bismuth ferrite structure with undistorted regions and defects with a larger A-A spacing but without Fe vacancies using the software Dr. Probe⁴⁶ show an intensity decrease by 14% which is within the variance of the measurement results (see Figure S4). Hence, Fe vacancies as the reason for the reduced Fe site intensities within the defects can be discarded. Looking at the A site intensities of the HAADF images, where Bi atoms and Ca dopants are sitting, their red curves in Figure 3b and Figure 4b show a reduction of intensities around the defect. Opposite to the Fe-site intensities, the simulations show no change in the Bi-site intensities at the defect compared to those of the undistorted structure (see Figure S4). Consequently, these intensity reductions indicate either an agglomeration of Ca or an agglomeration of Bi vacancies at the A sites adjacent to the defect, similar to the behavior observed by Campanini *et al.*¹⁹ Because Ca is an earth alkali metal, it offers only two electrons in the *sp* valence complex and does not exceed the 2+ oxidation state. Hence,

Ca sitting on the Bi^{3+} positions or Bi vacancies act as charge compensation for the oxygen vacancy rich defects, and can explain, why we see no mixed valence states of Fe^{3+} and Fe^{2+} .^{32,67}

The oxygen-deficient defect stripes in our 10 at.% Ca-doped $\text{Bi}_{0.9}\text{Ca}_{0.1}\text{FeO}_{3-\delta}$ thin film show a random spacing between each other and no periodicity, like it has been reported for higher Ca dopant ratios.^{19,28} While here the defects always coincide with CDW within the ferroelectric structure of the film, it does not seem to be the case for higher dopant ratios.¹⁹ Earlier studies on oxygen vacancies in epitaxially grown $\text{LaCoO}_{3-\delta}$ films suggest that under compressive strain from the substrate, out-of-plane oxygen defects appear and under tensile strain in-plane defects occur.^{19,26} Here, the oxygen-deficient defects appear simultaneously in both directions. We expected to see a difference and preference between in-plane and out-of-plane line defects either concerning the amount of oxygen vacancies δ or concerning their exact arrangement. However, the observations indicate no differences concerning these two characteristics. The fact that the ordered oxygen vacancy plates coincide with CDWs in the film could be useful to control domains and domain walls in multiferroics,⁶⁸ due to the pinning effect of oxygen vacancies on domain walls.³⁶⁻³⁸ Because charged defects, of which oxygen vacancies are one type, have shown to have a critical influence on the electrical conductivity of domain walls if they are agglomerated in the domain wall region, our results are also relevant for the field of domain wall nanoelectronics.^{69,70}

5. CONCLUSION

In conclusion, we have shown that a $\text{Bi}_{0.9}\text{Ca}_{0.1}\text{FeO}_{3-\delta}$ film under compressive strain shows oxygen vacancies agglomerated in plates with an alternating pattern concerning the $[010]_{\text{pc}}$ oriented oxygen site columns. Thereby one oxygen column contains few vacancies and the two adjacent columns contain many vacancies forming vacancy channels. Even though the film is under compressive strain from the STO substrate, not just out-of-plane oxygen-deficient plates exist but also in-plane ones. Besides their different orientation, the ordered oxygen vacancies show the same ordering and oxygen vacancy concentration. The oxygen-deficient plates coincide with charged domain walls in tail-to-tail configuration. This leads to a pinning effect of the domain walls, causing critical aspects for device applications such as fatigue phenomena and countering of retention failure. This could be intentionally used to design properties in functional devices. The agglomeration of the oxygen vacancies at the domain wall could influence the domain wall conductivity and be relevant for domain wall nanoelectronics. Finally, our results give interesting insights into the functionalities, mechanisms, and interactions of charged domain walls and ordered oxygen vacancies.

ASSOCIATED CONTENT

Supporting Information

The Supporting Information is available free of charge at

<https://doi.org/10.1021/acsaelm.1c00638>

STEM images and strain analysis about the epitaxial growth quality of the thin film system, versions of Figure 2, Figure 3 and Figure 4 optimized for colorblind readers, the crystallographic data for the supercell model for the Dr. Probe⁴⁶ HAADF image simulations, the HAADF image simulation results, and two HAADF images to compare the BCFO film of this study with an undoped BFO film with comparable fabrication parameters.

AUTHOR INFORMATION

Author Contributions

U.H. performed the HRTEM measurements, developed the method, and analyzed the data and wrote the manuscript. Y.E.S. performed the STEM imaging and analytical measurements together with U.H. and P.A.v.A., P.C.W. and Y.H.C. fabricated the thin film. D.K. wrote the MatLab program for the intensity and atomic positions analysis. U.H. wrote the MatLab script (building on D.K.'s program) for the interatomic spacing and the ferroelectric polarization analysis. Y.P.I. did the FIB preparation of the TEM lamellas. Z.Z. conceived and supervised the project. All authors read through the manuscript and contributed to the discussion of the results.

ORCID

Ulrich Haselmann: 0000-0001-5664-8656

Y. Eren Suyolcu: 0000-0003-0988-5194

Yurii P. Ivanov: 0000-0003-0271-5504

Daniel Knez: 0000-0003-0755-958X

Peter A. van Aken: 0000-0003-1890-1256

Ying-Hao Chu: 0000-0002-3435-9084

Zaoli Zhang: 0000-0002-7717-2500

Notes

The authors declare no competing interests.

ACKNOWLEDGMENTS

U.H. and Z.Z. kindly acknowledge the financial support by the Austrian Science Fund (FWF): no. P29148-N36. U.H. and Z.Z. express their gratitude to Stefan Wurster for performing general bulk sample checks in SEM. U.H. and Z.Z. acknowledge the support from the European Union's Horizon 2020 research and innovation program under grant agreement no. 823717-ESTEEM3.

REFERENCES

- (1) Spaldin, N. A.; Fiebig, M. The Renaissance of Magnetoelectric Multiferroics. *Science* **2005**, *309*, 391–392.
- (2) Eerenstein, W.; Mathur, N. D.; Scott, J. F. Multiferroic and Magnetoelectric Materials. *Nature* **2006**, *442*, 759–765.
- (3) Ramesh, R.; Spaldin, N. A. Multiferroics: Progress and Prospects in Thin Films. *Nat. Mater.* **2009**, *3*, 20–28.
- (4) Fiebig, M.; Lottermoser, T.; Meier, D.; Trassin, M. The Evolution of Multiferroics. *Nat. Rev. Mater.* **2016**, *1*, 16046.
- (5) Spaldin, N. A.; Ramesh, R. Advances in Magnetoelectric Multiferroics. *Nat. Mater.* **2019**, *18*, 203–212.
- (6) Fiebig, M. Revival of the Magnetoelectric Effect. *J. Phys. D: Appl. Phys.* **2005**, *38*, R125–R152.
- (7) Chen, D.; Gao, X.; Liu, J. M. Domain Structures and Magnetoelectric Effects in Multiferroic Nanostructures. *MRS Commun.* **2016**, *6*, 330–340.
- (8) Scott, J. F. Data Storage: Multiferroic Memories. *Nat. Mater.* **2007**, *6*, 256–257.
- (9) Roy, A.; Gupta, R.; Garg, A. Multiferroic Memories. *Adv. Condens. Matter Phys.* **2012**, *2012*, 926290.
- (10) Catalan, G.; Scott, J. F. Physics and Applications of Bismuth Ferrite. *Adv. Mater.* **2009**, *21*, 2463–2485.
- (11) Zhao, T.; Scholl, A.; Zavaliche, F.; Lee, K.; Barry, M.; Doran, A.; Cruz, M. P.; Chu, Y. H.; Ederer, C.; Spaldin, N. A.; Das, R. R.; Kim, D. M.; Baek, S. H.; Eom, C. B.; Ramesh, R. Electrical Control of Antiferromagnetic Domains in Multiferroic BiFeO₃ Films at Room Temperature. *Nat. Mater.* **2006**, *5*, 823–829.
- (12) Seidel, J.; Martin, L. W.; He, Q.; Zhan, Q.; Chu, Y. H.; Rother, A.; Hawkrigde, M. E.; Maksymovych, P.; Yu, P.; Gajek, M.; Balke, N.; Kalinin, S. V.; Gemming, S.; Wang, F.; Catalan, G.; Scott, J. F.; Spaldin, N. A.; Orenstein, J.; Ramesh, R. Conduction at Domain Walls in Oxide Multiferroics. *Nat. Mater.* **2009**, *8*, 229–234.
- (13) Catalan, G.; Seidel, J.; Ramesh, R.; Scott, J. F. Domain Wall Nanoelectronics. *Rev. Mod. Phys.* **2012**, *84*, 119–156.
- (14) Yang, C. H.; Kan, D.; Takeuchi, I.; Nagarajan, V.; Seidel, J. Doping BiFeO₃: Approaches and Enhanced

- Functionality. *Phys. Chem. Chem. Phys.* **2012**, *14*, 15953–15962.
- (15) Chen, D.; Nelson, C. T.; Zhu, X.; Serrao, C. R.; Clarkson, J. D.; Wang, Z.; Gao, Y.; Hsu, S. L.; Dedon, L. R.; Chen, Z.; Yi, D.; Liu, H. J.; Zeng, D.; Chu, Y. H.; Liu, J.; Schlom, D. G.; Ramesh, R. A Strain-Driven Antiferroelectric-to-Ferroelectric Phase Transition in La-Doped BiFeO₃ Thin Films on Si. *Nano Lett.* **2017**, *17*, 5823–5829.
- (16) Khomchenko, V. A.; Pereira, L. C. J.; Paixão, J. A. Mn Substitution-Induced Revival of the Ferroelectric Antiferromagnetic Phase in Bi_{1-x}Ca_xFeO_{3-x/2} Multiferroics. *J. Mater. Sci.* **2015**, *50*, 1740–1745.
- (17) Catalan, G.; Sardar, K.; Church, N. S.; Scott, J. F.; Harrison, R. J.; Redfern, S. A. T. Effect of Chemical Substitution on the Néel Temperature of Multiferroic Bi_{1-x}Ca_xFeO₃. *Phys. Rev. B* **2009**, *79*, 212415.
- (18) Yang, C. H.; Seidel, J.; Kim, S. Y.; Rossen, P. B.; Yu, P.; Gajek, M.; Chu, Y. H.; Martin, L. W.; Holcomb, M. B.; He, Q.; Maksymovych, P.; Balke, N.; Kalinin, S. V.; Baddorf, A. P.; Basu, S. R.; Scullin, M. L.; Ramesh, R. Electric Modulation of Conduction in Multiferroic Ca-Doped BiFeO₃ Films. *Nat. Mater.* **2009**, *8*, 485–493.
- (19) Campanini, M.; Erni, R.; Yang, C. H.; Ramesh, R.; Rossell, M. D. Periodic Giant Polarization Gradients in Doped BiFeO₃ Thin Films. *ACS Nanoletters* **2018**, *18*, 717–724.
- (20) Jang, H.; Kerr, G.; Lim, J. S.; Yang, C. H.; Kao, C. C.; Lee, J. S. Orbital Reconstruction in a Self-Assembled Oxygen Vacancy Nanostructure. *Sci. Rep.* **2015**, *5*, 12402.
- (21) Chen, W. T.; Williams, A. J.; Ortega-San-Martin, L.; Li, M.; Sinclair, D. C.; Zhou, W.; Attfield, J. P. Robust Antiferromagnetism and Structural Disorder in Bi_xCa_{1-x}FeO₃ Perovskites. *Chem. Mater.* **2009**, *21*, 2085–2093.
- (22) Lepoittevin, C.; Malo, S.; Barrier, N.; Nguyen, N.; Van Tendeloo, G.; Hervieu, M. Long-Range Ordering in the Bi_{1-x}Ae_xFeO_{3-x/2} Perovskites: Bi_{1/3}Sr_{2/3}FeO_{2.67} and Bi_{1/2}Ca_{1/2}FeO_{2.75}. *J. Solid State Chem.* **2008**, *181*, 2601–2609.
- (23) Schiemer, J. A.; Withers, R. L.; Liu, Y.; Carpenter, M. A. Ca-Doping of BiFeO₃: The Role of Strain in Determining Coupling between Ferroelectric Displacements, Magnetic Moments, Octahedral Tilting, and Oxygen-Vacancy Ordering. *Chem. Mater.* **2013**, *25*, 4436–4446.
- (24) Haselmann, U.; Haberfehlner, G.; Pei, W.; Popov, M.; Romaner, L.; Knez, D.; Chen, J.; Ghasemi, A.; He, Y.; Kothleitner, G.; Zhang, Z. Study on Ca Segregation towards an Epitaxial Interface between Bismuth Ferrite and Strontium Titanate. *ACS Appl. Mater. Interfaces* **2020**, *12*, 12264–12274.
- (25) Suyolcu, Y. E.; Wang, Y.; Baiutti, F.; Al-Temimy, A.; Gregori, G.; Cristiani, G.; Sigle, W.; Maier, J.; Van Aken, P. A.; Logvenov, G. Dopant Size Effects on Novel Functionalities: High-Temperature Interfacial Superconductivity. *Sci. Rep.* **2017**, *7*, No. 453.
- (26) Zhang, N.; Zhu, Y.; Li, D.; Pan, D.; Tang, Y.; Han, M.; Ma, J.; Wu, B.; Zhang, Z.; Ma, X. Oxygen Vacancy Ordering Modulation of Magnetic Anisotropy in Strained LaCoO_{3-x} Thin Films. *ACS Appl. Mater. Interfaces* **2018**, *10*, 38230–38238.
- (27) Zhang, N.; Tian, X.; Zhu, Y.; Wang, Y.; Tang, Y.; Zou, M.; Ma, J.; Feng, Y.; Geng, W.; Cao, Y.; Ma, X. Thickness Dependence of Oxygen Vacancy Ordering in Strained LaCoO_{3-x} Thin Films. *J. Phys. Chem. C* **2020**, *124*, 12492–12501.
- (28) Seidel, J.; Luo, W.; Suresha, S. J.; Nguyen, P. K.; Lee, A. S.; Kim, S. Y.; Yang, C. H.; Pennycook, S. J.; Pantelides, S. T.; Scott, J. F.; Ramesh, R. Prominent Electrochromism through Vacancy-Order Melting in a Complex Oxide. *Nat. Commun.* **2012**, *3*, 796–799.

- (29) Li, L.; Zhang, Y.; Xie, L.; Jokisaari, J. R.; Beekman, C.; Yang, J. C.; Chu, Y. H.; Christen, H. M.; Pan, X. Atomic-Scale Mechanisms of Defect-Induced Retention Failure in Ferroelectrics. *Nano Lett.* **2017**, *17*, 3556–3562.
- (30) Wang, J.; Xia, Y.; Chen, L. Q.; Shi, S. Q. Effect of Strain and Deadlayer on the Polarization Switching of Ferroelectric Thin Film. *J. Appl. Phys.* **2011**, *110*, 114111
- (31) Stengel, M.; Spaldin, N. A. Origin of the Dielectric Dead Layer in Nanoscale Capacitors. *Nature* **2006**, *443*, 679–682.
- (32) Geng, W. R.; Tian, X. H.; Jiang, Y. X.; Zhu, Y. L.; Tang, Y. L.; Wang, Y. J.; Zou, M. J.; Feng, Y. P.; Wu, B.; Hu, W. T.; Ma, X. L.; Unveiling the Pinning Behavior of Charged Domain Walls in BiFeO₃ Thin Films via Vacancy Defects. *Acta Mater.* **2020**, *186*, 68–76.
- (33) Huang, Y.-C.; Liu, Y.; Lin, Y.-T.; Liu, H.-J.; He, Q.; Li, J.; Chen, Y.-C.; Chu, Y.-H. Giant Enhancement of Ferroelectric Retention in BiFeO₃ Mixed-Phase Boundary. *Adv. Mater.* **2014**, *26*, 6335–6340.
- (34) Vrejoiu, I.; Le Rhun, G.; Zakharov, N. D.; Hesse, D.; Pintilie, L.; Alexe, M. Threading Dislocations in Epitaxial Ferroelectric PbZr_{0.2}Ti_{0.8}O₃ Films and Their Effect on Polarization Backswitching. *Philos. Mag.* **2006**, *86*, 4477–4486.
- (35) Gao, P.; Britson, J.; Jokisaari, J. R.; Nelson, C. T.; Baek, S. H.; Wang, Y.; Eom, C. B.; Chen, L. Q.; Pan, X. Atomic-Scale Mechanisms of Ferroelastic Domain-Wall-Mediated Ferroelectric Switching. *Nat. Commun.* **2013**, *4*, 2791.
- (36) Lubk, A.; Rossell, M. D.; Seidel, J.; He, Q.; Yang, S. Y.; Chu, Y. H.; Ramesh, R.; Hÿtch, M. J.; Snoeck, E. Evidence of Sharp and Diffuse Domain Walls in BiFeO₃ by Means of Unit-Cell-Wise Strain and Polarization Maps Obtained with High Resolution Scanning Transmission Electron Microscopy. *Phys. Rev. Lett.* **2012**, *109*, 047601.
- (37) He, L.; Vanderbilt, D. First-Principles Study of Oxygen-Vacancy Pinning of Domain Walls in PbTiO₃. *Phys. Rev. B* **2003**, *68*, 134103.
- (38) Li, W.; Chen, A.; Lu, X.; Zhu, J. Collective Domain-Wall Pinning of Oxygen Vacancies in Bismuth Titanate Ceramics. *J. Appl. Phys.* **2005**, *98*, 024109.
- (39) Ivanov, Y. P.; Kubicek, M.; Siebenhofer, M.; Viernstein, A.; Hutter, H.; Fleig, J.; Chuvilin, A.; Zhang, Z. Strain-Induced Structure and Oxygen Transport Interactions in Epitaxial La_{0.6}Sr_{0.4}CoO_{3-δ} Thin Films. *Commun. Mater.* **2020**, *1*, 25.
- (40) Ivanov, Y. P.; Meylan, C. M.; Panagiotopoulos, N. T.; Georgarakis, K.; Greer, A. L. In-Situ TEM Study of the Crystallization Sequence in a Gold-Based Metallic Glass. *Acta Mater.* **2020**, *196*, 52–60.
- (41) Ivanov, Y. P.; Soltan, S.; Albrecht, J.; Goering, E.; Schütz, G.; Zhang, Z.; Chuvilin, A. The Route to Supercurrent Transparent Ferromagnetic Barriers in Superconducting Matrix. *ACS Nano* **2019**, *13*, 5655–5661.
- (42) Suyolcu, Y. E.; Wang, Y.; Sigle, W.; Baiutti, F.; Cristiani, G.; Logvenov, G.; Maier, J.; van Aken, P. A. Octahedral Distortions at High-Temperature Superconducting La₂CuO₄ Interfaces: Visualizing Jahn–Teller Effects. *Adv. Mater. Interfaces* **2017**, *4*, No. 1700731.
- (43) Lichtert, S.; Verbeeck, J. Statistical Consequences of Applying a PCA Noise Filter on EELS Spectrum Images. *Ultramicroscopy* **2013**, *125*, 35–42.

- (44) Jones, L.; MacArthur, K. E.; Fauske, V. T.; Van Helvoort, A. T. J.; Nellist, P. D. Rapid Estimation of Catalyst Nanoparticle Morphology and Atomic-Coordination by High-Resolution Z-Contrast Electron Microscopy. *Nano Lett.* **2014**, *14*, 6336–6341.
- (45) E, H.; MacArthur, K. E.; Pennycook, T. J.; Okunishi, E.; D'Alfonso, A. J.; Lugg, N. R.; Allen, L. J.; Nellist, P. D. Probe Integrated Scattering Crosssections in the Analysis of Atomic Resolution HAADF STEM Images. *Ultramicroscopy* **2013**, *133*, 109–119.
- (46) Barthel, J. Dr. Probe: A Software for High-Resolution STEM Image Simulation. *Ultramicroscopy* **2018**, *193*, 1–11.
- (47) Koster, G.; Klein, L.; Siemons, W.; Rijnders, G.; Dodge, J. S.; Eom, C. B.; Blank, D. H. A.; Beasley, M. R. Structure, Physical Properties, and Applications of SrRuO₃ Thin Films. *Rev. Mod. Phys.* **2012**, *84*, 253–298.
- (48) Kubel, F.; Schmid, H. Structure of a Ferroelectric and Ferroelastic Monodomain Crystal of the Perovskite BiFeO₃. *Acta Crystallogr. Sect. B* **1990**, *46*, 698–702.
- (49) Lubk, A.; Rossell, M. D.; Seidel, J.; Chu, Y. H.; Ramesh, R.; Hÿtch, M. J.; Snoeck, E. Electromechanical Coupling among Edge Dislocations, Domain Walls, and Nanodomains in BiFeO₃ Revealed by Unit-Cell-Wise Strain and Polarization Maps. *Nano Lett.* **2013**, *13*, 1410–1415.
- (50) Yang, Y.; Infante, I. C.; Dkhil, B.; Bellaiche, L. Strain Effects on Multiferroic BiFeO₃ Films. *Comptes Rendus Phys.* **2015**, *16*, 193–203.
- (51) Nelson, C. T.; Winchester, B.; Zhang, Y.; Kim, S. J.; Melville, A.; Adamo, C.; Folkman, C. M.; Baek, S. H.; Eom, C. B.; Schlom, D. G.; Chen, L.-Q.; Pan, X. Spontaneous Vortex Nanodomain Arrays at Ferroelectric Heterointerfaces. *Nano Lett.* **2011**, *11*, 828–834.
- (52) Tang, Y. L.; Zhu, Y. L.; Wang, Y. J.; Wang, W. Y.; Xu, Y. B.; Ren, W. J.; Zhang, Z. D.; Ma, X. L. Atomic-Scale Mapping of Dipole Frustration at 90° Charged Domain Walls in Ferroelectric PbTiO₃ Films. *Sci. Rep.* **2014**, *4*, 4115.
- (53) Wang, W. Y.; Tang, Y. L.; Zhu, Y. L.; Xu, Y. B.; Liu, Y.; Wang, Y. J.; Jagadeesh, S.; Ma, X. L. Atomic Level 1D Structural Modulations at the Negatively Charged Domain Walls in BiFeO₃ Films. *Adv. Mater. Interfaces* **2015**, *2*, 1500024
- (54) Campanini, M.; Gradauskaite, E.; Trassin, M.; Yi, D.; Yu, P.; Ramesh, R.; Erni, R.; Rossell, M. D. Imaging and Quantification of Charged Domain Walls in BiFeO₃. *Nanoscale* **2020**, *12*, 9186–9193.
- (55) Jia, C. L.; Nagarajan, V.; He, J. Q.; Houben, L.; Zhao, T.; Ramesh, R.; Urban, K.; Waser, R. Unit-Cell Scale Mapping of Ferroelectricity and Tetragonality in Epitaxial Ultrathin Ferroelectric Films. *Nat. Mater.* **2007**, *6*, 64–69.
- (56) Tan, H.; Verbeeck, J.; Abakumov, A.; Van Tendeloo, G. Oxidation State and Chemical Shift Investigation in Transition Metal Oxides by EELS. *Ultramicroscopy* **2012**, *116*, 24–33.
- (57) Garvie, L. A. J.; Craven, A. J.; Brydson, R. Use of Electron-Energy Loss near-Edge Fine Structure in the Study of Minerals. *Am. Mineral.* **1994**, *79*, 411–425.
- (58) Gazquez, J.; Luo, W.; Oxley, M. P.; Prange, M.; Torija, M. A.; Sharma, M.; Leighton, C.; Pantelides, S. T.; Pennycook, S. J.; Varela, M. Atomic-Resolution Imaging of Spin-State Superlattices in Nanopockets within Cobaltite Thin Films. *Nano Lett.* **2011**, *11*, 973–976.
- (59) Bednyakov, P. S.; Sturman, B. I.; Sluka, T.; Tagantsev, A. K.; Yudin, P. V. Physics and Applications of

- Charged Domain Walls. *npj Comput. Mat.* **2018**, *4*, 65.
- (60) Tian, X. H.; Wang, Y. J.; Tang, Y. L.; Zhu, Y. L.; Ma, X. L. The Effect of Oxygen Vacancy Plate on the Domain Structure in BiFeO₃ Thin Films by Phase Field Simulations. *J. Appl. Phys.* **2020**, *127*, 094102.
- (61) Jang, J. H.; Kim, Y. M.; He, Q.; Mishra, R.; Qiao, L.; Biegalski, M. D.; Lupini, A. R.; Pantelides, S. T.; Pennycook, S. J.; Kalinin, S. V.; Borisevich, Y. In Situ Observation of Oxygen Vacancy Dynamics and Ordering in the Epitaxial LaCoO₃ System. *ACS Nano* **2017**, *11*, 6942–6949.
- (62) Kim, Y.-M.; He, J.; Biegalski, M. D.; Ambaye, H.; Lauter, V.; Christen, H. M.; Pantelides, S. T.; Pennycook, S. J.; Kalinin, S. V.; Borisevich, A. Y. Probing Oxygen Vacancy Concentration and Homogeneity in Solid-Oxide Fuel-Cell Cathode Materials on the Subunit-Cell Level. *Nat. Mater.* **2012**, *11*, 888–894.
- (63) Li, J.; Guan, M.; Nan, P.; Wang, J.; Ge, B. Topotactic Phase Transformations by Concerted Dual-Ion Migration of B-Site Cation and Oxygen in Multivalent Cobaltite La–Sr–Co–O_x Films. *Nano Energy* **2020**, *78*, 105215.
- (64) Guan, X.; Shen, X.; Wang, W.; Wang, W.; Lan, Q.; Zhang, J.; Zhang, J.; Yang, H.; Yao, Y.; Li, J.; Gu, C.; Sun, J.; Yu, R. Two Kinds of Metastable Structures in an Epitaxial Lanthanum Cobalt Oxide Thin Film. *Inorg. Chem.* **2019**, *58*, 13440–13445.
- (65) Tian, J.; Zhang, Y.; Fan, Z.; Wu, H.; Zhao, L.; Rao, J.; Chen, Z.; Guo, H.; Lu, X.; Zhou, G.; Pennycook, S. J.; Gao, X.; Liu, J.-M. Nanoscale Phase Mixture and Multi Field-Induced Topotactic Phase Transformation in SrFeO_x. *ACS Appl. Mater. Interfaces* **2020**, *12*, 21883–21893.
- (66) Parsons, T. G.; D’Hondt, H.; Hadermann, J.; Hayward, M. A. Synthesis and Structural Characterization of La_{1-x}A_xMnO_{2.5} (A = Ba, Sr, Ca) Phases: Mapping the Variants of the Brownmillerite Structure. *Chem. Mater.* **2009**, *21*, 5527–5538.
- (67) Luo, J. M.; Lin, S. P.; Zheng, Y.; Wang, B. Nonpolar Resistive Switching in Mn-Doped BiFeO₃ Thin Films by Chemical Solution Deposition. *Appl. Phys. Lett.* **2012**, *101*, 062902.
- (68) Noguchi, Y.; Matsuo, H.; Kitanaka, Y.; Miyayama, M. Ferroelectrics with a Controlled Oxygen-Vacancy Distribution by Design. *Sci. Rep.* **2019**, *9*, 4225.
- (69) Rojac, T.; Bencan, A.; Drazic, G.; Sakamoto, N.; Ursic, H.; Jancar, B.; Tavcar, G.; Makarovic, M.; Walker, J.; Malic, B.; Damjanovic, D. Domain-Wall Conduction in Ferroelectric BiFeO₃ Controlled by Accumulation of Charged Defects. **2017**, *16*, 322-327.
- (70) Bencan, A.; Drazic, G.; Ursic, H.; Makarovic, M.; Komelj, M.; Rojac, T. Domain-Wall Pinning and Defect Ordering in BiFeO₃ Probed on the Atomic and Nanoscale. *Nat. Commun.* **2020**, *11*, 1762.

Publication B – Supporting Information

Negatively Charged In-Plane and Out-of-Plane Domain Walls with Oxygen-Vacancy Agglomerations in a Ca-doped Bismuth-Ferrite Thin Film

Ulrich Haselmann¹, Y. Eren Suyolcu^{2,3}, Ping-Chun Wu⁴, Yurii P. Ivanov^{1,5,6}, Daniel Knez⁷, Peter A. van Aken³, Ying-Hao Chu⁴ and Zaoli Zhang^{*1,8}

1 Erich Schmid Institute of Materials Science, Austrian Academy of Sciences, 8700 Leoben, Austria

2 Department of Materials Science and Engineering, Cornell University, Ithaca, New York 14850, United States

3 Max Planck Institute for Solid State Research, 70569 Stuttgart, Germany

4 Department of Materials Science and Engineering, National Chiao Tung University, Hsinchu 30010, Taiwan

5 Department of Materials Science & Metallurgy, University of Cambridge, Cambridge CB3 0FS, UK

6 School of Natural Sciences, Far Eastern Federal University, 690950, Vladivostok, Russia

7 Graz Centre for Electron Microscopy, Austrian Cooperative Research, 8010 Graz, Austria

8. Institute of Material Physics, Montanuniversität Leoben, 8700 Leoben, Austria

***Corresponding author:** zaoli.zhang@oeaw.ac.at

In Table. S1 complementary imaging parameters of the HAADF data, which have not been mentioned in section 2. *Experimental Details* in the subsection 2.2. *Data acquisition* are listed. For Figure 3 five subsequent images each with 1.4 μ s pixel time are summed up, resulting in a total pixel time of 7 μ s.

Table. S1. Complementary imaging parameters of the STEM HAADF images.

	collection angle [mrad]	pixel time [μ s]	step size [pm]	size [pixel*pixel]
Figure 1	75-309	10.2	58	1536 * 1024
Figure 2	83-205	10.2	12	1024 * 1536
Figure 3	75-309	$5 * 1.4 = 7$	7	1024 * 1024
Figure 4	83-205	13.6	7.2	1536 * 768
Figure 5	110-270	61	36	512 * 512
Figure S1	110-270	6.8	58	1536 * 1536
<i>Figure S5a</i>	75-309	6.8	58	1536 * 1536
<i>Figure S5b</i>	110-270	5.1	35	1536 * 2048

The High Angle Annular Dark Field (HAADF) image in Figure S1a shows on a lamella in $[110]_{pc}$ zone axis that the SrRuO_3 (SRO) interlayer and the $\text{Bi}_{0.9}\text{Ca}_{0.1}\text{FeO}_3$ (BCFO) layer have grown in a good epitaxial quality on the SrTiO_3 (STO) substrate. The blue dashed lines indicate the interfaces between STO and SRO and SRO and BCFO. GPA analysis for the in-plane strain in Figure S1b shows that there is only a slight in-plane relaxation from the beginning of the SRO layer to the first 20 nm of the BCFO. In comparison, the out-of-plane strain in Figure S1c shows a significant increase with the beginning of the SRO layer, and is only slightly reduced with larger film thickness. The scanning frame was once rotated by 90° so that each for ϵ_{xx} and ϵ_{zz} the primary scanning direction was normal to the direction of the analyzed strain. The Bragg vectors (1-10) and (002) were used, respectively.

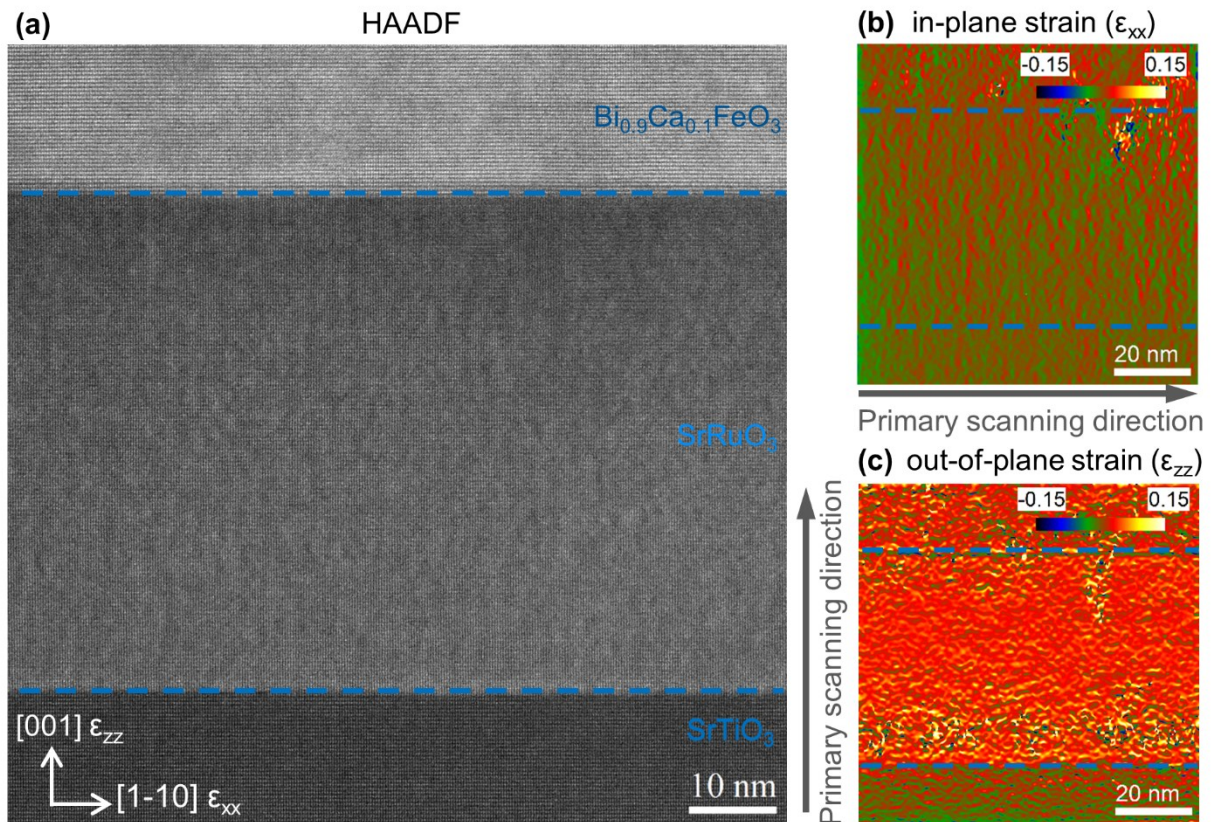


Figure S1. Epitaxial growth quality of the thin film system. (a) HAADF image of a lamella from the pseudo-cubic $[110]_{pc}$ direction. (b) In-plane strain of the film system showing only slight increase along increasing layer thickness. (c) Out-of-plane strain, where clearly a significant increase at the STO-SRO interface can be seen with only slight decrease across the layer thickness. For the GPA analysis, the Bragg vectors $(1-10)$ and (002) were used. The blue dashed lines indicate the respective interfaces.

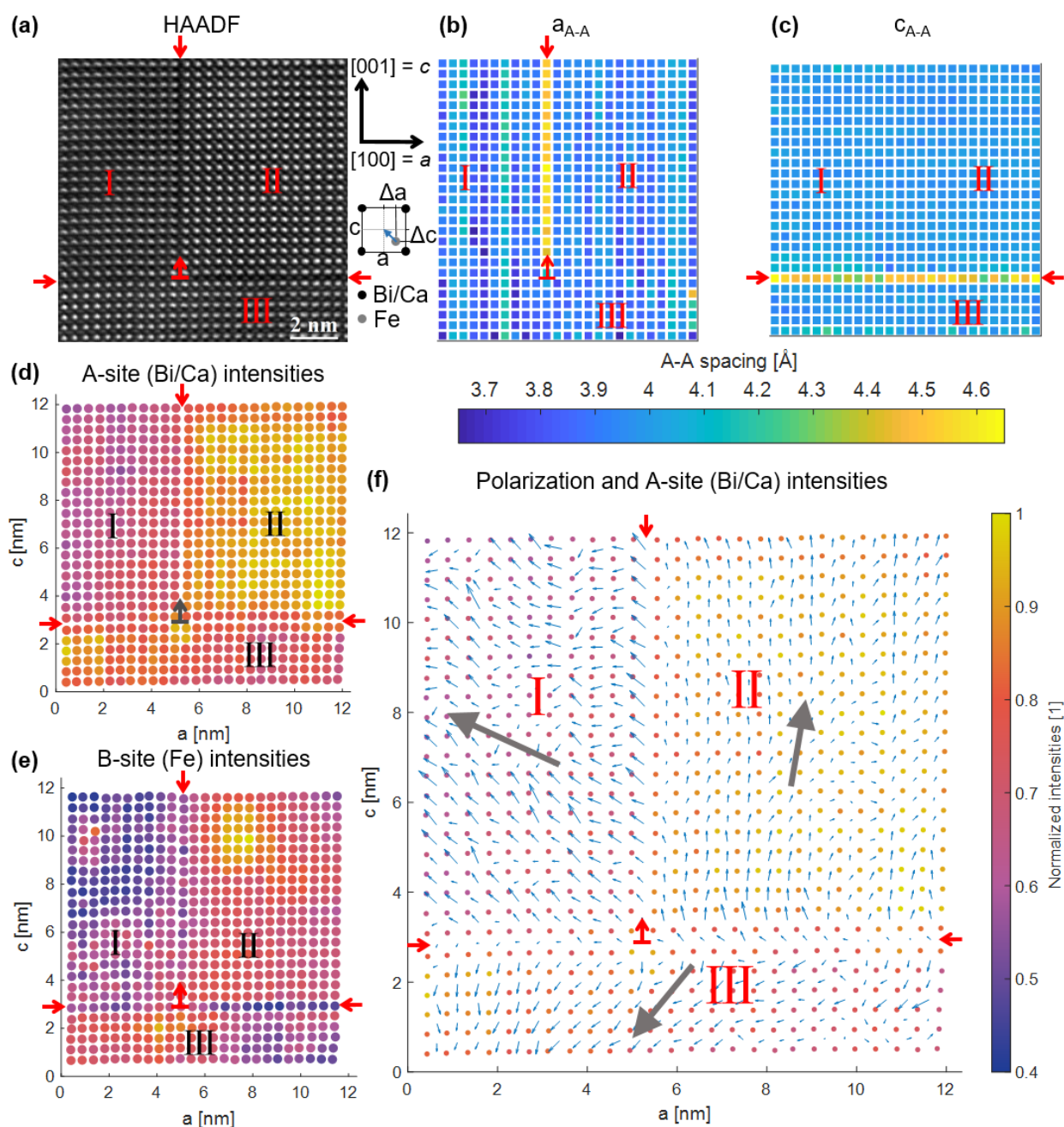


Figure S2 Version of Figure 2 from the main manuscript changed in (d), (e) and (f) to optimize the display for colorblind readers. It shows the analysis of high-resolution STEM data of an in-plane and out-of-plane defect, which have a common point of contact (a) HAADF image showing two defects marked with red arrows. The defects separate the image into three areas designated with roman numbers I-III. On the top right side of the HAADF image, the $[100]_{pc}$ and $[001]_{pc}$ axes are indicated as *a* and *c*. At the bottom of the right side is a schematic illustration of the electrical polarization due to shift of the Fe atom from the center of the pseudo-cubic cell. (b) Map of interatomic distances of the A-sites (Bi and Ca atoms) in a (in-plane)-direction. The in-plane defect marked by the red arrows can be clearly seen by the enlarged lattice parameter. (c) Map of interatomic A-site distances in *c* (out-of-plane)-direction. The out-of-plane defect can be clearly observed by the enlarged lattice parameter. (d) A-site intensities (Bi and Ca positions) in the HAADF image normalized to the maximal A-site intensity. (e) B-site (Fe) intensities in the HAADF image normalized to the maximal B-site intensity. (f) Polarization and A-site (Bi/Ca) intensities.

(f) Map of the electrical polarization due to the shift of the Fe atom overlaid on the fitted positions and intensities of the A-site atoms. The grey arrows in the regions I-III indicate the average polarization direction and magnitude relative to each other.

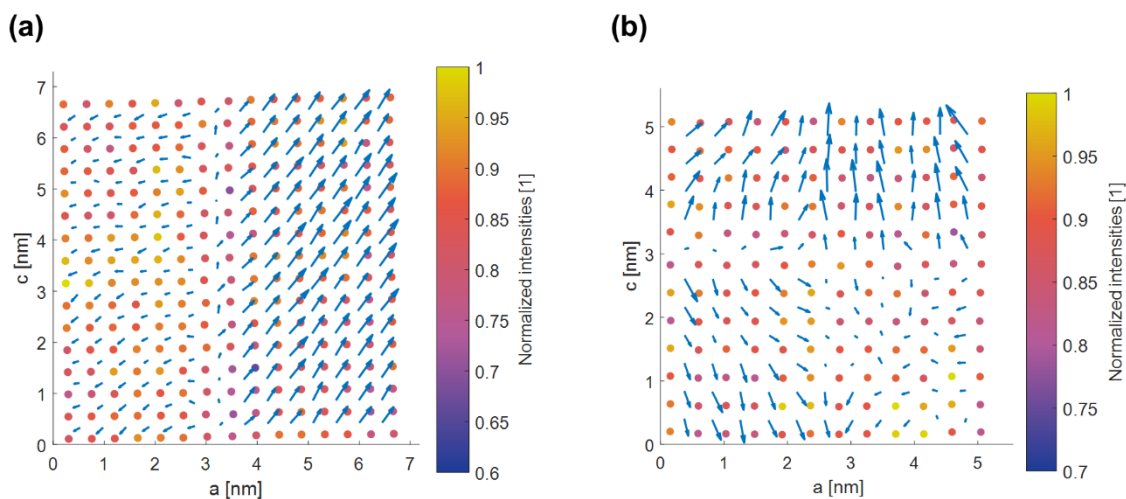


Figure S3 Colorblind version of (a) Figure 3h and (b) Figure 4f.

In Figure S4 the results of HAADF image simulations using the software Dr. Probe¹ are shown. The cation positions of the crystallographic supercell model used for the simulations is depicted in Figure S4a. It was created by multiplying the pseudo-cubic BFO unit cell three times in the *c* direction and modifying the Bi and Fe positions to replicate the defect, its lattice elongation with a value of 12.5% compared to the undistorted lattice and a changed polarization state (polarization within the defect was assumed zero). The thereby modified supercell became in the strict crystallographic sense a new modified unit cell, but we continue to call it small supercell in the text. Its crystallographic data and atomic positions can be found in Table S2. This small supercell (indicated by the grey rectangle in Figure S4a) was then multiplied 2 times each in the *a* and *c* directions to create the supercell model for the image simulations.

The result of the image simulations for a sample thickness of ≈ 30 nm (76 BFO unit cells), an acceleration voltage of $U_{\text{acc}} = 200$ kV, a convergence angle of $\alpha = 20.9$ mrad, a spherical aberration of $C_S = 0$ μm , a defocus value of 0 nm, an electron source radius of $r_s = 0.010$ nm, a scanning step size of 10 pm and a HAADF detector ranging from 49.0 - 250.0 mrad, can be seen in Figure S4b. The pairs of orange arrows in Figure S4a and Figure S4b indicate the area of the defect, where the lattice is elongated and the Fe is not shifted from the center meaning no local polarization there. A comparison of the intensities of the Fe sites in Figure S4c (area of the intensity profile is marked by the magenta rectangle in Figure S4b) shows that at the position in the defect (marked by the red arrow) it is significantly reduced compared to the iron intensities in

the undistorted structure. This intensity reduction happens without a change of atomic composition within this column. For the ideal incoherent scattering case, the detected intensity would be proportional to $Z_1^2 + Z_2^2 + \dots + Z_n^2$ with Z_k being the atomic number of each atom in the column and would not be influenced by an enlarged lattice spacing. In contrast, Figure S4d shows that the intensities of the Bi sites are not influenced by the defect (the area of the intensity profile is marked by the turquoise rectangle in Figure S4b). This is important to keep in mind, since a change in the Bi site intensities of the recorded images means, opposite to the Fe intensities, a compositional change.

Table S2. Crystallographic data of the small supercell created by multiplying the pseudocubic BFO unit cell 3 times in *c* direction (marked by the grey rectangle in Fig. S4a). The cell parameters are $a = b = 3.96 \text{ \AA}$, $c = 11.88 \text{ \AA}$, $\alpha = \beta = \gamma = 90^\circ$.

Atom site label	Atom site type symbol	Occupancy	Atom site fraction x	Atom site fraction y	Atom site fraction z
Bi1	Bi	1	0	0	0
Bi2	Bi	1	0	0	0.32
Bi3	Bi	1	0	0	0.64
Fe1	Fe	1	0.65	0.65	0.208
Fe2	Fe	1	0.65	0.65	0.528
Fe3	Fe	1	0.5	0.5	0.82
O1	O	1	0	0.5	0.16
O2	O	1	0.5	0	0.16
O3	O	1	0.5	0.5	0
O4	O	1	0.5	0.5	0.32
O5	O	1	0	0.5	0.48
O6	O	1	0.5	0	0.48
O7	O	1	0.5	0.5	0.64
O8	O	1	0	0.5	0.82
O9	O	1	0.5	0	0.82

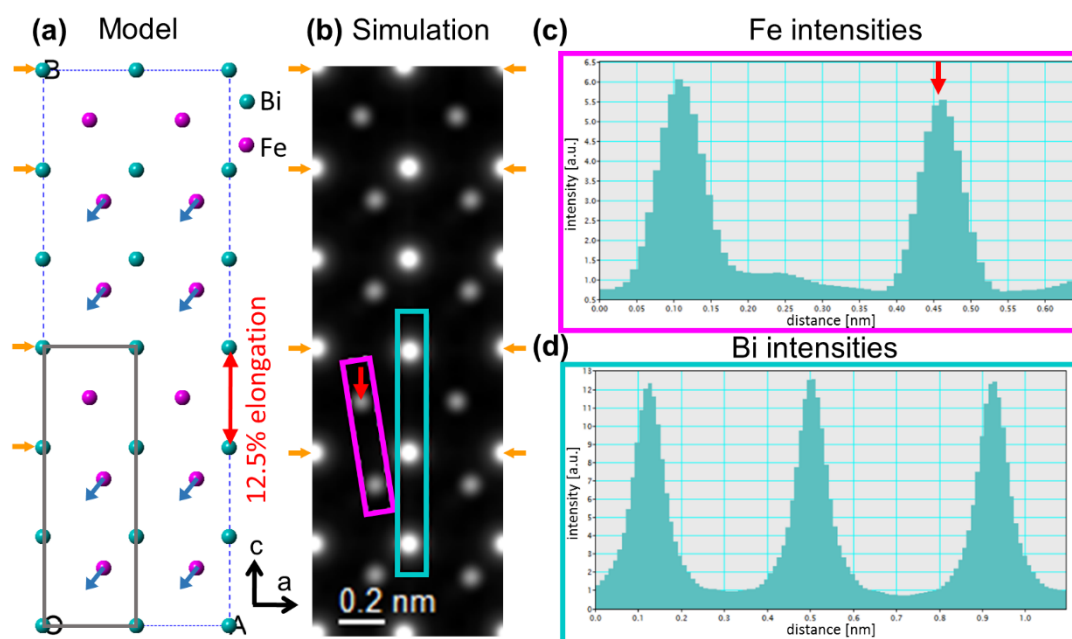


Figure S4. STEM image simulation with the software Dr. Probe¹ (a) Cation model of the supercell used for the simulations (in this depiction the oxygen atoms are faded out for more clarity). The grey rectangle indicates the small supercell, which is multiplied with two in the a and c directions to receive the big supercell covering the whole simulation area. The small supercell consists of 3 pseudo-cubic BFO unit cells, where the atom positions have been modified to model the defect (indicated by the 2 pairs of orange arrows on the left side) and the undistorted cells. The arrows indicate a shift of the central Fe atom and therefore a local polarization. (b) HAADF (49-250 mrad) simulation result from Dr. Probe¹ for a sample thickness of 30 nm and a step size of 10 pm. (c) HAADF intensity of the Fe atoms in the area of the magenta rectangle in (b), which is significantly reduced for the Fe atom in the defect area marked by the red arrow. (d) HAADF intensity of the Bi atoms from the turquoise rectangle in (b), which show no influence from the defect.

Figure S5 shows an overview HAADF image of the BCFO film from this study in comparison with an overview HAADF image from an undoped BFO reference sample. The BFO reference sample was deposited on the same SRO-STO substrate system with the same deposition parameters as the BCFO film with the exception of 15 min deposition time (instead of 45 min) resulting with 20 nm in a third of the thickness. While the BCFO sample clearly shows agglomerated oxygen vacancies, the undoped BFO film shows no agglomerated oxygen vacancies.

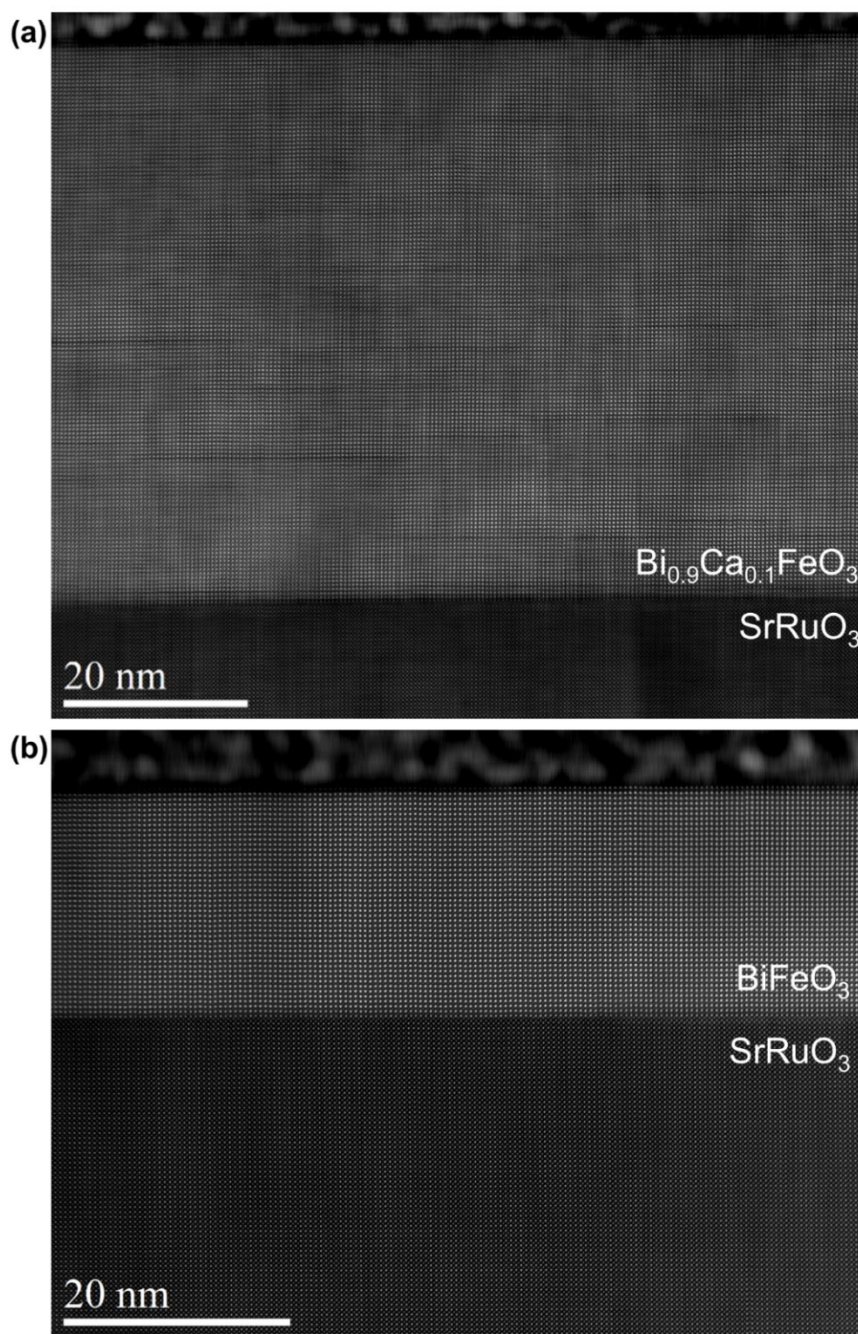


Figure S5. HAADF image comparison of (a) the BCFO film of this study with (b) an undoped BFO film on the same SRO-STO substrate. While the Ca doped film shows agglomerations of oxygen vacancies throughout the film, the BFO film shows none.

References

- (1) Barthel, J. Dr. Probe: A Software for High-Resolution STEM Image Simulation. *Ultramicroscopy* 2018, 193, 1–11.

Publication C

Ca Solubility in a BiFeO₃ Based System with a Secondary Bi₂O₃ Phase on a Nanoscale

Ulrich Haselmann¹, Thomas Radlinger², Weijie Pei³, Maxim N. Popov⁴, Tobias Spitaler⁵, Lorenz Romaner^{4,5}, Yurii P. Ivanov^{6,7}, Jian Chen³, Yunbin He^{*3}, Gerald Kothleitner^{2,8} and Zaoli Zhang^{*1,9}

¹ Erich Schmid Institute of Materials Science, Austrian Academy of Sciences, 8700 Leoben, Austria

² Institute for Electron Microscopy and Nanoanalysis, Graz University of Technology, 8010 Graz, Austria

³ School of Materials Science & Engineering, Hubei University, 430062 Wuhan, Hubei, China

⁴ Materials Center Leoben Forschung GmbH, 8700 Leoben, Austria

⁵ Department of Materials Science, Montanuniversität Leoben, 8700 Leoben, Austria

⁶ Department of Materials Science & Metallurgy, University of Cambridge, Cambridge CB3 0FS, U.K.

⁷ School of Natural Sciences, Far Eastern Federal University, 690950 Vladivostok, Russia

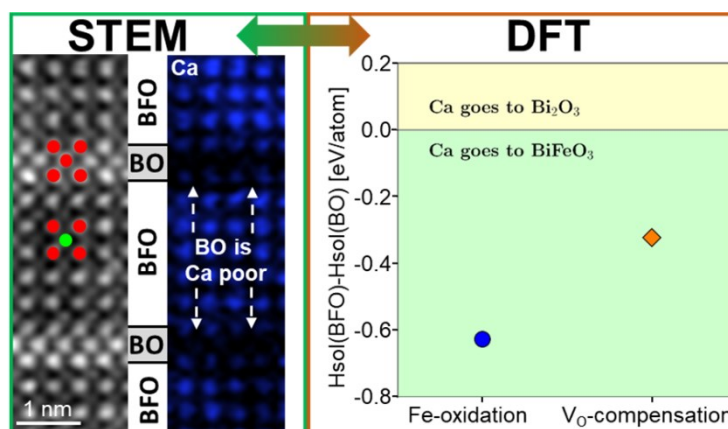
⁸ Graz Centre for Electron Microscopy, Austrian Cooperative Research, 8700 Graz, Austria

⁹ Institute of Material Physics, Montanuniversität Leoben, 8700 Leoben, Austria

*Corresponding authors: zaoli.zhang@oeaw.ac.at, ybhe@hubu.edu.cn

ABSTRACT:

In BiFeO₃ (BFO) a known secondary phase, which can appear under certain growth conditions, is Bi₂O₃ (BO). However, BO is not just an unwanted parasitic phase, but can be used to create the super-tetragonal BFO phase in the film on substrates, which would otherwise grow the regular rhombohedral phase. The super-tetragonal BFO phase has the advantage of much larger ferroelectric polarization of 130-150 $\mu\text{C}/\text{cm}^2$, which is around 50% larger than the ferroelectric polarization of the rhombohedral phase with 80-100 $\mu\text{C}/\text{cm}^2$. Here we report that Ca, which is a common dopant of BFO to tune the properties, the solubility in the secondary BO



phase is significantly lower than in the BFO phase. This leads, starting from the film growth to completely different Ca concentrations in the two phases. We show this with advanced analytical transmission electron microscopy techniques and confirm the experimental results with density functional theory (DFT) calculations. At the film fabrication temperature, caused by the different solubility, an about fifty times higher Ca concentration is expected in the BFO phase than in the secondary one. Depending on the cooling rate after fabrication, this can further increase since a larger Ca concentration difference is expected for lower temperatures. For the fabrication of functional devices making use of Ca dopant and secondary BO phase to create super-tetragonal BFO, this needs to be considered since, depending on the amount of BO phase, it increases the Ca concentration level in the BFO phase. Depending on the size of the permitted tolerances, this can be critical to maintain the intended device functionality.

KEYWORDS: Ca solubility, BiFeO₃, Bi₂O₃, aberration-corrected analytical STEM, DFT

1. INTRODUCTION

Formally, multiferroics are single-phase materials with more than one of the primary ferroic properties, which are ferroelectricity, ferromagnetism, and ferroelasticity. This definition has been broadened to also include antiferroic order but tends to exclude ferroelasticity. The current focus of interest in the scientific community is magnetoelectric multiferroics linking electric and magnetic order parameters, today often only referred by the term multiferroics.¹⁻⁴ An important reason for this interest is a range of highly interesting possible applications. In digital data storage, the reading and writing of a magnetic bit is done by a magnetic-field-generating current that creates waste heat and has a relatively long build-up time. These disadvantages are avoided with the direct control of magnetic order via electric fields in magnetoelectric multiferroics, promising a faster, smaller, and more energy-efficient data storage.^{1,5} Other possible applications are sensors, spin valves, and spintronic devices.⁶

At the moment, BiFeO₃ (BFO) is the leading magnetoelectric multiferroic⁴ with Curie and Neel temperatures high above room temperature ($T_C \approx 830^\circ\text{C}$ and $T_N \approx 370^\circ\text{C}$), which is critical for device applicability.^{7,8} Multiferroic thin films often have fundamentally different properties compared to bulk materials,^{9,10} and therefore can be used to improve the properties of BFO by the choice of the substrate. Another way to tune electronic and magnetic properties is the doping with substitutional elements.¹¹ Ca, which substitutes Bi on the A-sites, can produce O vacancies because as an alkaline earth metal Ca²⁺ replacing Bi³⁺ has a hole doping effect.^{12,13} Additionally, Ca doping has shown to enable modulation of conductivity through application of an electric field,¹³ boost

the magnetoelectric coupling¹⁴ and shift the magnetic order from antiferromagnetic to ferromagnetic.¹⁵ Co, which substitutes the B-site position, leads to a significant increase in the remanent and saturation magnetization at room temperature.^{16–18} Ca and Co co-doped BFO show an even larger improvement in the magnetization compared to samples doped with only one of the two and are promising for receiving in future a ferromagnetic system instead of an antiferromagnetic one.¹⁹

In the BFO system, Bi_2O_3 (BO) is one of the secondary phases, which can form.^{20–28} Secondary BO has also several times been studied in BFO thin films with TEM techniques showing a variety of different nanostructures.^{29–31} A lower substrate temperature than usual and a slower growth rate are reported to promote the formation of the secondary BO phase.³² The BO phase is very useful because it can be utilized to grow tetragonal BFO under low substrate strain conditions instead of having a high compressive strain, which allows a greater substrate material flexibility.^{29,32–38} Tetragonal BFO instead of the normal rhombohedral counterpart has the advantage of having a much larger ferroelectric polarization of 130–150 $\mu\text{C}/\text{cm}^2$ instead of 80–100 $\mu\text{C}/\text{cm}^2$.^{12,39–42}

In this study, we show that the Ca solubility in BiFeO_3 (BFO) is higher than in secondary Bi_2O_3 (BO), resulting in a Ca gradient between the two phases. Atomic-resolution scanning transmission electron microscopy (STEM) with high-angle annular dark-field (HAADF) imaging is used to analyze the BO nanostructure of the film and the local strain structure with geometric phase analysis (GPA). We use electron energy loss spectroscopy (EELS) and energy-dispersive X-ray spectroscopy (EDS), both in atomic-resolution, to confirm the structural model and show a Ca depletion in the secondary BO phase compared to the BFO based film. This experimental result is supported by density functional theory (DFT) calculations, which show that Ca is preferentially dissolved in BFO compared to BO and at the film growth temperature of 700°C at least 10 times higher Ca concentrations are expected in BFO than in BO. To our knowledge, this Ca solubility has not previously been reported and no pseudo-ternary phase diagram between $\text{Bi}_2\text{O}_3 - \text{Fe}_2\text{O}_3 - \text{CaO}$ is available. Since both, Ca-doping, and the implementation of a BO secondary phase, are useful to tune the BFO material properties, knowledge about their interaction is crucial for the future design of BFO based functional devices.

2. EXPERIMENTAL AND CALCULATION DETAILS

2.1. Thin-Film Fabrication. Pulsed laser deposition (PLD) with a KrF excimer laser (Lambda Physik COMPEX PRO 205 F, 248 nm) with a pulse repetition rate of 5 Hz was used to fabricate a Ca- and Co-codoped $\text{Bi}_{0.8}\text{Ca}_{0.2}\text{Fe}_{0.95}\text{Co}_{0.05}\text{O}_3$ (BCFCO) and a BiFeO_3 (BFO) film on

single crystalline (001)-oriented SrTiO₃ (STO) (HeFei Crystal Technical Material Co., Ltd.) substrate. The laser beam energy was fixed at 300 mJ/pulse. The substrate was cleaned by applying acetone, ethanol, and pure water and afterwards blown dry with high purity nitrogen gas before immediately loading it into the PLD chamber. The target-substrate distance was 5.5 cm, and the chamber was evacuated to about 10⁻⁴ Pa. During the deposition, the substrate temperature was kept constant at 700°C, and the oxygen pressure was 3 Pa. The deposition time of 10 min leads to a film thickness of 55 nm for the BCFCO film, which means a growth rate of 0.95 Å/s, and 48 nm for the BFO film, which corresponds to a growth rate of 0.80 Å/s. The crystal structure was probed in θ -2 θ scan mode with a four-circle single-crystal diffractometer (D8 discover, Bruker, Germany) using a Cu K α 1 monochromatic radiation source with a wavelength of 1.5406 Å. The surface topology was investigated with atomic force microscopy (AFM; Solver Nano, NT-MDT) using semi-contact mode.

2.2. Data Acquisition. Cross-sectional TEM samples were fabricated by standard focused ion beam protocol with a Helios Nanolab FIB-SEM.⁴³⁻⁴⁶ A probe-aberration-corrected FEI Titan³ operated at 300 keV at a convergence angle of 19.7 mrad was used to gain all the STEM data. For HAADF imaging, a Fischione HAADF detector was used. Detailed imaging parameters for the HAADF images can be found in Table S1. A GIF quantum⁴⁷ energy filter (Gatan) and a super-X EDX detector⁴⁸ (FEI) were used for the analytical data. The EELS collection semiangle was 26.6 mrad. The EELS spectra were collected in dual mode with an energy range of the core loss region of 290-802 eV and a channel width of 0.25 eV. The pixel time was 100 ms for the core loss region and 0.5 ms for the zero loss region. For the EDS maps in an energy range from 0-20 keV with a channel width of 5 eV, the signal from 77 images with a pixel time of 30 μ s were summed up. For the EDS maps in the Supporting Information, 37 images with a pixel time of 40 μ s were summed up. Drift effects were corrected during the recording with the internal Velox routine from Thermo Fisher. The DPC data in the Supporting Information were collected with a four-segment annular FEI DF4 detector.⁴⁹

2.3. Data Evaluation. For the strain analysis the Geometric Phase Analysis (GPA) software package v4.0 from HREM Research Company for Digital Micrograph 2.3 from Gatan was used. HAADF images were filtered with a Principal Component Analysis (PCA) script for Digital Micrograph to reduce image noise from S. Lichtert, T. Hayian, and J. Verbeeck.⁵⁰ The EELS analytical data were processed in Digital Micrograph 3.43 from Gatan using the build-in MSA Analysis for filtering the data set.⁵¹ The EDS data were processed with Velox from Thermo Fisher using for pre-filtering an 8 pixel wide average filter and for post-filtering a Gaussian with a variance of 1.

2.4. DFT Calculations. For the ab initio calculations, a projector augmented wave (PAW)⁵² method as implemented in the VASP code was used.⁵³⁻⁵⁶ The electron exchange-correlation effects were considered by using PBEsol⁵⁷ generalized gradient approximation. The DFT+U method of Dudarev *et al.*⁵⁸ was utilized to cope with the d-electron delocalization problem. In accordance with previous studies, for the values of the U parameters applied to Ti and Fe sites 4 eV was chosen.^{59,60} The energy cut-off for the basis set expansion was set to 520 eV. To compute enthalpies of solution, we employed supercells constructed from fully relaxed BFO (R3c) and BO (P-42₁c). The BFO supercell, containing 320 atoms, was obtained by a 2x2x2 repetition of the pseudo-cubic unit cell. The BO supercell, containing 240 atoms, was made by a 2x2x3 repetition of the tetragonal unit cell. The G-type antiferromagnetic order was maintained in BFO. The Brillouin zone integration was performed using 2x2x2 k-point grids for the BFO and BO supercells. The positions of all atoms were relaxed until the residual forces were less than 10⁻² eV/Å.

3. RESULTS

3.1 Bi₂O₃ Secondary Phase in the Bismuth Ferrite Matrix. The film structure was investigated in the [010]_c cross-sectional orientation concerning the cubic STO substrate, which also complies with the [010]_{pc} (pseudocubic) zone axis of bismuth ferrite.⁶¹ The HAADF image in Figure 1a shows a cross-section of the Ca- and Co-doped BiFeO₃ film (BCFCO) and the interface with the STO substrate in the bottom part. In the film, approximately 5 nm away from the interface, white stripes with the width of approximately 1 unit cell appear running in the [100] direction. Closer inspection reveals that in these stripes, the B-site intensities are increased (the black arrows mark three exemplary examples), as is typical for a Bi₂O₃ (BO) secondary phase in a Bismuth ferrite matrix. This is caused by the fact that on the pseudocubic lattice positions, the Fe atom on the B-site is replaced with a Bi atom, which has a much higher signal intensity in the HAADF contrast due to the higher Z number. The in-plane strain map in Figure 1b shows almost no strain in the film, as is expected for a good quality epitaxial growth of the film on the substrate. The out-of-plane strain map in Figure 1c unveils a relatively small lattice enlargement of the film in the first 20 nm, which is expected since the pseudocubic lattice parameter of BFO is 3.965 Å, approximately 1.5% larger than that of STO.^{6,62} However, apart from that, the out-of-plane strain map also shows stripes with a very large lattice enlargement, which coincides with the bright stripes in the HAADF image identified as BO and confirms their identification since the pseudocubic lattice parameter of BO is approximately 5.5 Å.²⁹ For comparison, the HAADF image of an undoped BFO film on STO substrate is shown in Figure 1d revealing no signs of the BO

secondary phase. The in-plane strain map in Figure 1e displays some distorted areas stemming from sample damage. However, the out-of-plane strain map in Figure 1f shows, beside an antiphase boundary after the fourth unit cell of the film⁶³, no areas with strongly increased strain, like we see in Figure 1c as indicators of the BO phase. A high magnification HAADF image of the BO phase inside the film is shown in Figure 2. The places where a BO phase is present can be clearly identified by the very bright B-sites, with intensities being similar to those of the A-sites. Overlays in the image illustrate the majority atomic composition on the respective atomic sites in the BO secondary phase and in the film (red indicates Bi atoms and green Fe atoms). In the $[001]_{pc}$ direction (out-of-plane), the BO phase is usually only one unit cell thick, and thus the BO phase seems to form plates stretching mainly in $[100]_{pc}$ and $[010]_{pc}$ direction within the film. As indicated in Figure 2, while the film has an out-of-plane lattice spacing of $\approx 4.0 \text{ \AA}$, the BO phase has a much larger spacing of $\approx 5.5 \text{ \AA}$. As some of the BO stripes end within the image area of Figure 2, the film matrix is visually distorted around the secondary phase to compensate for the much larger spacing.

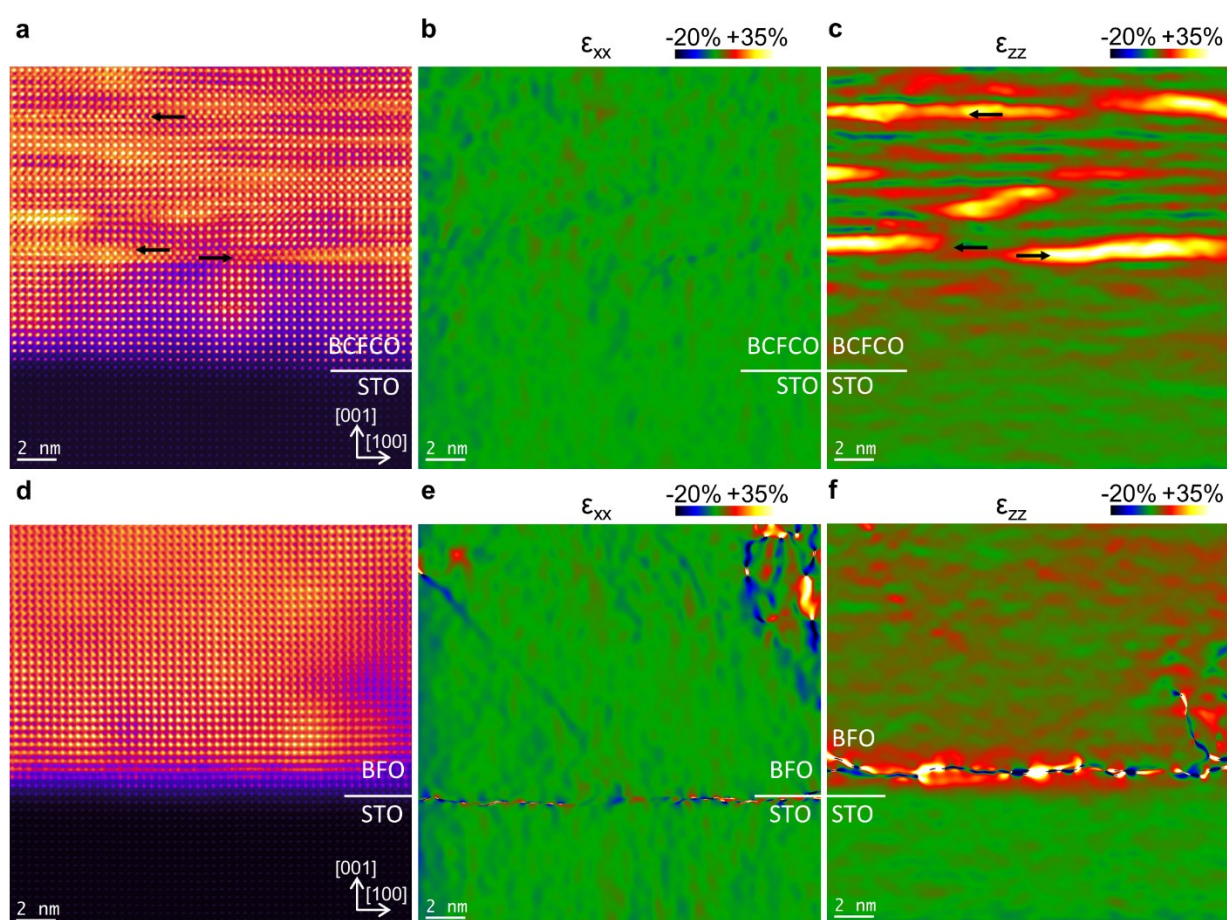


Figure 1. Large Scale structural mapping of a film containing the BO secondary phase and a film without it. (a) HAADF image, (b) in-plane (ϵ_{xx}), and (c) out-of-plane (ϵ_{zz}) strain maps of the film

containing the secondary BO phase. The black arrows indicate examples of lines along the [100] direction where the B-site intensity is increased, indicating the BO phase. (d) HAADF image, (e) in-plane (ϵ_{xx}), and (f) out-of-plane (ϵ_{zz}) strain maps of a film containing no secondary phase.

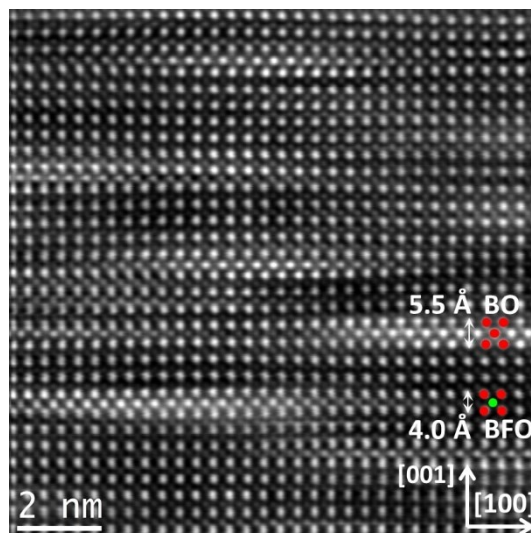


Figure 2. High-resolution HAADF STEM image of the secondary BO phase in the BCFCO film. The overlays indicate the majority atomic composition on the respective atomic sites (red for Bi and green for Fe).

3.2. Elemental Analysis of the Film and the Secondary Phase. Analytical STEM techniques were applied to receive more details on the chemical composition of the film and the secondary phase. Figure 3a shows a HAADF survey image of a film region with multiple stripes of BO secondary phase. The white, overlaid rectangle illustrates an area from which an EELS elemental map was taken. In the HAADF survey image, it clearly shows that this area contains 3 stripes of BO. Figure 3b displays the HAADF image recorded simultaneously with the EELS spectral signals. The three BO stripes oriented in $[100]_{pc}$ direction are clearly visible and indicated by the labeling on the left side. Figure 3c shows the Fe areal density map stemming from the Fe-L edge. As expected, in the stripes of the BO phase, the Fe content is low, with the residual Fe signal likely arising from partial intermixing in projection direction and channeling effects. The Ca areal density map (Ca-L edge), which can be seen in Figure 3d, is very unexpected. Instead of being homogeneously distributed in the BO stripes and the surrounding matrix, which would be expected since the Ca dopant is placed in the Bi columns, the Ca content is smaller in the BO stripes than in the surrounding area. Figure 3e shows the elemental maps of Fe and Ca combined.

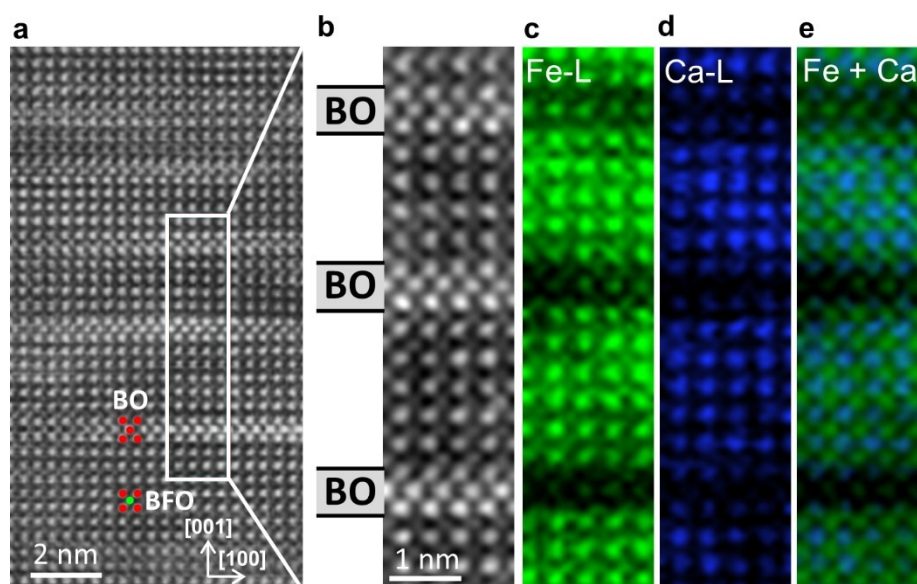


Figure 3. EELS elemental map of 3 plates of BO in the film. (a) HAADF survey image showing a region with several stripes of BO. The white rectangle indicates the area of the EELS elemental map containing 3 BO stripes. (b) Simultaneous HAADF image during mapping. EELS elemental maps of (c) Fe, (d) Ca, and (e) Fe and Ca combined.

To confirm the lower Ca content in the BO stripes, EDS elemental ratio maps were also recorded, which provide the advantage that Bi, which is not well suited for EELS, can be mapped too. Figure 4a displays the HAADF image of the exact area of the EDS map with a BO plate in the upper half of the image. The position of the BO plate with the clearly increased intensity of the B-sites is also indicated on the left side of the image. The elemental map of Bi in Figure 4b clearly reveals a higher Bi content in the BO area, whereas the map of Fe in Figure 4c shows a lower Fe content in the BO area. In Figure 4d, the atomic ratios of Bi and Fe are combined and reveal that, while in the regular BCFCO area, there can be clearly distinguished between Bi and Fe sites, in the BO stripe there cannot be identified the regular Fe lattice sites. This is also indicated by the fact that the BO stripe appears more red and less green than the regular film area, which additionally confirms the BO nature of the stripes.

Figure 4e displays the EDS map of Ca. In the area of the BO stripe, slightly less Ca can be seen. The Ca shortage in BO becomes more apparent in the combined elemental ratio map of Bi and Ca in Figure 4f. In it, the A-sites normally appear violet since red from Bi and blue from Ca color mix, but in the BO stripe it appears only red, indicating the lack of Ca. Figure 4g and h show the O and Co maps, which both have no noticeable inhomogeneities. In Figure 4i, the denoised EDS spectra of the BO are summed up from the area of the red rectangle in Figure 4a, and for comparison signals of the regular film are summed up from the blue rectangle. This confirms the

result of a higher Bi content in the BO area and a lower Fe content indicated by the different intensities of the Bi-M, Bi-L_α, Bi-L_β, and Fe-K_α peaks. The lower Ca content in the BO stripe is confirmed by the comparison of the Ca-K_α peak, where the blue peak from the regular BCFCO film area is higher than the red peak from the BO stripe. Therefore, besides the confirmed BO nature of the plates, both the EDS elemental analysis and the EELS analysis show the lower Ca content in the BO secondary phase.

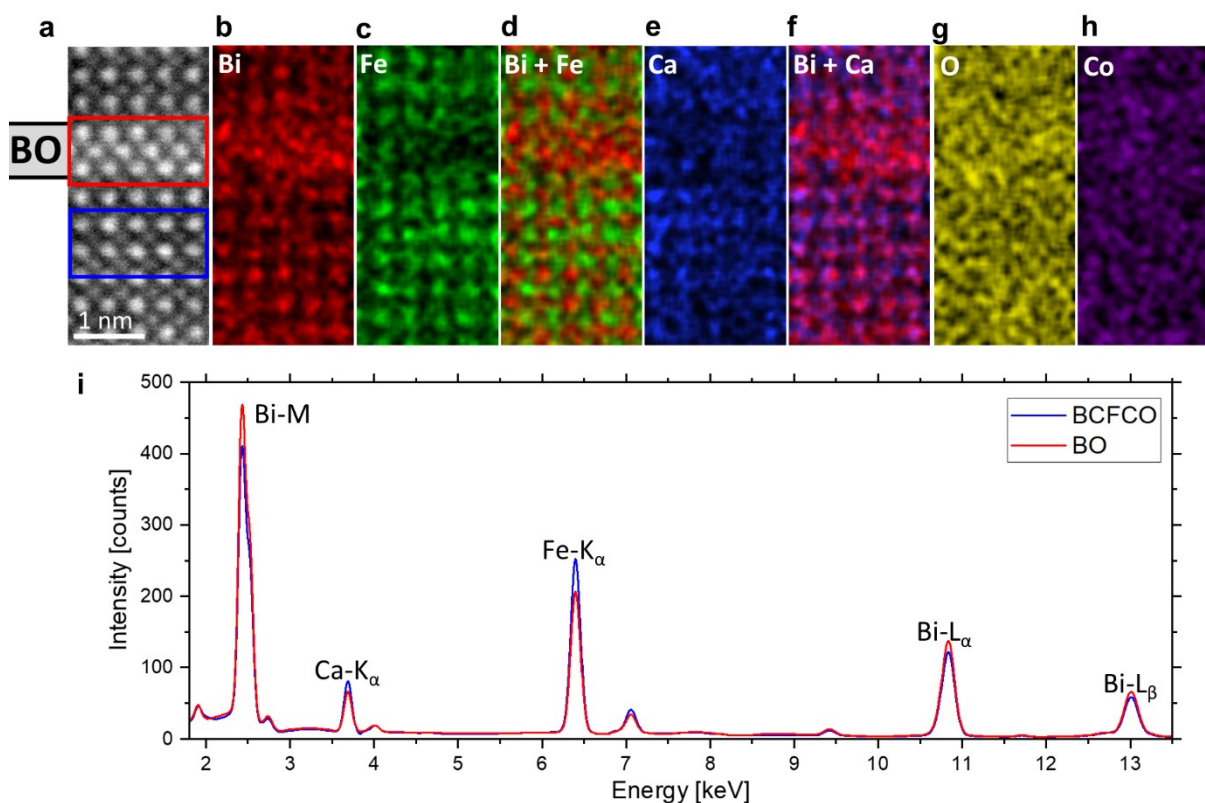


Figure 4. EDS elemental analysis of a BO plate. (a) HAADF image of the EDS mapping area. The BO stripe is indicated on the left side. EDS elemental ratio maps of (b) Bi, (c) Fe, (d) Bi and Fe combined, (e) Ca, (f) Bi and Ca combined, (g) O, and (h) Co. (i) Comparing the background corrected and denoised spectra from the BO area of the red rectangle and the BCFCO area from the blue rectangle in (a). The spectra have the same color as the associated rectangle.

3.3. Solubility of Ca in both phases from DFT calculations. DFT modelling was used to investigate if there is a thermodynamic driving force present that could explain the experimentally observed tendency for Ca depletion in the BO-regions. To this end, the difference of enthalpies of Ca dissolution in BFO and in BO was calculated. According to our TEM analysis, Ca occupies the Bi-sites upon dissolution. This requires a charge-compensation mechanism since Ca is divalent whereas Bi is trivalent. Two mechanisms were considered: 1) shift of the oxidation state of Fe from +3 to +4 (Fe-oxidation); 2) compensation by oxygen vacancies. A more detailed

explanation about these mechanisms can be found elsewhere^{46,61}. The relative enthalpy of solution for the case of Fe-oxidation mechanism was calculated as:

$$H_{\text{sol}}(\text{BFO}) - H_{\text{sol}}(\text{BO}) = [E(\text{BFO}, \text{Ca}) - E(\text{BFO})] - [E(\text{BO}, \text{Ca}) - E(\text{BO})].$$

Here, $E(\text{BFO}, \text{Ca})$ and $E(\text{BO}, \text{Ca})$, are the total energies of the respective supercell containing Ca atoms, while $E(\text{BFO})$ and $E(\text{BO})$ are the energies for the supercells without Ca. The relative enthalpy of solution for the case of O-vacancy compensation was defined similarly:

$$H_{\text{sol}}(\text{BFO}) - H_{\text{sol}}(\text{BO}) = \frac{1}{2} [E(\text{BFO}, 2\text{Ca}, V_{\text{O}}) - E(\text{BFO})] - \frac{1}{2} [E(\text{BO}, 2\text{Ca}, V_{\text{O}}) - E(\text{BO})].$$

Here, $E(\text{BFO}, 2\text{Ca}, V_{\text{O}})$ and $E(\text{BO}, 2\text{Ca}, V_{\text{O}})$, are the total energies of the respective supercell containing two Ca atoms and 1 oxygen vacancy. The oxygen vacancy was always introduced in close proximity to the Ca atoms. The result is presented in Figure 5. When the relative enthalpy is negative, it means that it's energetically more favorable for the Ca to go to the BFO. If it is positive, it preferentially goes to the BO phase. The differential solution enthalpies are negative for both dissolution mechanisms, with approximately -0.32 eV for the mechanism with O vacancies and even larger -0.63 eV for the Fe-oxidation one, as is shown in Figure 5a. Therefore, for both mechanisms, a Ca dissolution in BFO is favored, confirming the experimental observations.

The ratio of the Ca concentration in BFO compared to the concentration in BO can also be determined from the differential solution enthalpies using the Arrhenius law:

$$\frac{c(\text{BFO})}{c(\text{BO})} = \exp \left[-\frac{H_{\text{sol}}(\text{BFO}) - H_{\text{sol}}(\text{BO})}{k_{\text{B}}T} \right],$$

where k_{B} is the Boltzmann's constant and T is the temperature. The result is presented in Figure 5b. The mechanism with the formation of O vacancies has a lower expected Ca ratio but can be considered the more likely case due to our previous results.⁶¹ Nonetheless, at the growth temperature of the film of 700°C, according to the DFT simulations about fifty times more Ca is expected in BFO than in BO. With increasing temperature, the ratio becomes in general smaller. But this also means that the cooling process of the film after the fabrication step increases the Ca gradient in the secondary phase as long as the temperature still enables enough Ca diffusion.⁶¹

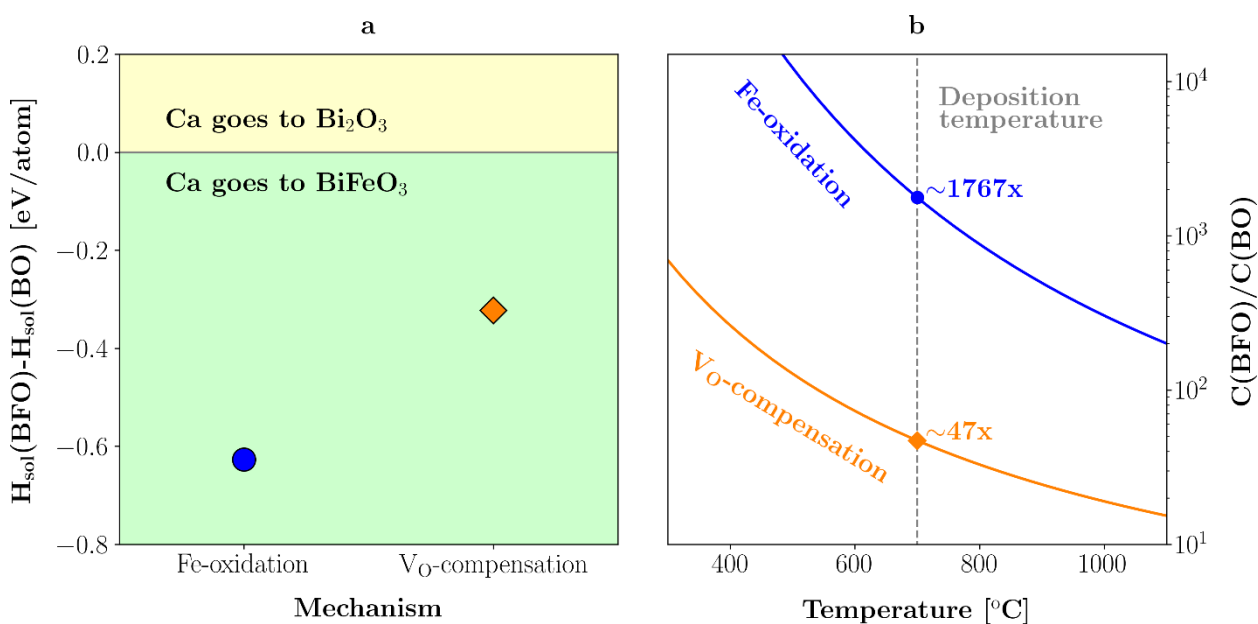


Figure 5. DFT calculations for the Ca solubility in BFO and secondary BO phase. (a) Relative enthalpy of Ca solution for two considered charge-compensation mechanisms: via Fe-oxidation and through introducing oxygen vacancies (VO). Both variants favor Ca dissolution in BFO. (b) Shows the ratio of Ca concentrations for dissolution in BFO to dissolution in BO, estimated using the Arrhenius law and the data from (a). It shows that at the deposition temperature of 700 $^{\circ}\text{C}$ there is about 50 times more Ca expected in BFO than in BO.

4. DISCUSSION

The different Ca solubility in the BO phase observed in this study is of importance for functional device design, as secondary BO phases at the right growth conditions lead to the super-tetragonal BFO phase, which otherwise only appears for films grown on substrates inducing a very strong compressive strain.^{29,32–38} This allows the super-tetragonal phase to be grown on a wider range of substrates, including STO and even polycrystalline substrates.²⁹ Because the super-tetragonal phase provides a much larger ferroelectric polarization^{39,64}, being not limited by the necessity of choosing a narrow range of substrates is very valuable. Since simultaneously Ca doping is applied to specifically and accurately tune the material properties, e.g. to introduce O vacancies, in combination with a BO phase, one must be aware of the solubility effect because it increases the Ca content in the BFO phase. This, depending on the proportion of the BO phase, can have a significant influence and result in a wrong and unintended device functionality.

Previous studies have shown that related phases (Bi_2O_2) have some influence on the ferroelectric polarization structure by having domain walls located at the bismuth oxide layers. However, that

does not mean that every bismuth oxide layer is also a domain wall. Instead, there seems to be a preference for them to be located in the bismuth oxide layers.⁶⁵ We have also found that the BO plates can act as domain walls (see Figure S3). This could potentially be used to manipulate the location or orientation of domain walls or to influence the domain size. However, further studies are necessary for a more thorough understanding.

Note that our results also provide a highly relevant data point for assessing a thermodynamic CALPHAD database of the ternary $\text{Bi}_2\text{O}_3 - \text{Fe}_2\text{O}_3 - \text{CaO}$ system. So far, only relatively little is available in this direction. Indeed, while for the $\text{Bi}_2\text{O}_3 - \text{CaO}$ ⁶⁶ and the $\text{Fe}_2\text{O}_3 - \text{CaO}$ ⁶⁷ systems thermodynamic models have been assessed, this is not the case for the $\text{Bi}_2\text{O}_3 - \text{Fe}_2\text{O}_3$ system for which pseudo-binary phase diagrams have been reported,²⁰⁻²⁷ but the correctness of underlying experimental data is still under debate.²⁸ With further progress in this direction, a thermodynamic model for the ternary $\text{Bi}_2\text{O}_3 - \text{Fe}_2\text{O}_3 - \text{CaO}$ system could be in reach, where the present result provides a decisive contribution regarding Ca solubility and, in this way, also to the design of future multiferroic applications.

5. CONCLUSION

In conclusion, with advanced TEM studies and DFT calculation, we have shown that in a bismuth ferrite system with a secondary bismuth oxide phase, the Ca solubility is lower in the BO phase than the main bismuth ferrite phase. Different Ca solubility can prove problematic while growing BFO films with a secondary BO phase to promote the formation of tetragonal BFO, as it can lead to unintended Ca concentrations in the primary phase. This knowledge is important to keep in mind when designing functional devices. Otherwise, an unexpected Ca concentration can potentially jeopardize the functionality of the device.

ASSOCIATED CONTENT

Supporting Information

The Supporting Information is available free of charge at <http://pubs.acs.org>

Complementary imaging parameters of the STEM data, EELS and EDS elemental map of the interface between the BCFCO film and the STO substrate, DPC analysis of the ferroelectric polarization at a BO plate, XRD data, and AFM data of the film.

AUTHOR INFORMATION

ORCID

Ulrich Haselmann: 0000-0001-5664-8656

Thomas Radlinger:

Weijie Pei:

Maxim N. Popov: 0000-0002-4923-0785

Tobias Spitaler:

Lorenz Romaner: 0000-0003-4764-130X

Yurii P. Ivanov: 0000-0003-0271-5504

Jian Chen:

Yunbin He: 0000-0002-7179-4392

Gerald Kothleitner: 0000-0002-2116-7761

Zaoli Zhang: 0000-0002-7717-2500

Notes

The authors declare no competing interests.

ACKNOWLEDGEMENTS

We kindly acknowledge the financial support by the Austrian Science Fund (FWF): No. P29148-N36. T.R. and G.K. acknowledge support from the European Union's Horizon 2020 research and innovation program under grant agreement No. 823717-ESTEEM3. U.H., Z.Z., T.R. and G.K. kindly thank Ferdinand Hofer for his general support. Y.H. acknowledges financial support from the National Key R&D Program of China (Grant No. 2019YFB1503500) and the National Natural Science Foundation of China (Project Nos. 11774082 and 11975093).

REFERENCES

- (1) Spaldin, N. A.; Fiebig, M. The Renaissance of Magnetoelectric Multiferroics. *Science* 2005, 309, 391–392
- (2) Liu, H.; Yang, X. A Brief Review on Perovskite Multiferroics. *Ferroelectrics* 2017, 507, 69–85.
- (3) Eerenstein, W.; Mathur, N. D.; Scott, J. F. Multiferroic and Magnetoelectric Materials. *Nature* 2006, 442, 759–765.
- (4) Spaldin, N. A.; Ramesh, R. Advances in Magnetoelectric Multiferroics. *Nat. Mater.* 2019, 18, 203–212.
- (5) Fiebig, M.; Lottermoser, T.; Meier, D.; Trassin, M. The Evolution of Multiferroics. *Nat. Rev. Mater.* 2016, 1, 16046.
- (6) Catalan, G.; Scott, J. F. Physics and Applications of Bismuth Ferrite. *Adv. Mater.* 2009, 21, 2463–2485.
- (7) Yin, L.; Mi, W. Progress in BiFeO₃-Based Heterostructures: Materials, Properties and Applications. *Nanoscale* 2020, 12, 477–523.
- (8) Zhao, T.; Scholl, A.; Zavaliche, F.; Lee, K.; Barry, M.; Doran, A.; Cruz, M. P.; Chu, Y. H.; Ederer, C.; Spaldin, N. A.; Das, R. R.; Kim, D. M.; Baek, S. H.; Eom, C. B.; Ramesh, R. Electrical Control of Antiferromagnetic Domains in Multiferroic BiFeO₃ Films at Room Temperature. *Nat. Mater.* 2006, 5, 823–829.
- (9) Ramesh, R.; Spaldin, N. A. Multiferroics: Progress and Prospects in Thin Films. *Nat. Mater.* 2009, 3, 20–28.
- (10) Chen, D.; Nelson, C. T.; Zhu, X.; Serrao, C. R.; Clarkson, J. D.; Wang, Z.; Gao, Y.; Hsu, S. L.; Dedon, L. R.; Chen, Z.; Yi, D.; Liu, H. J.; Zeng, D.; Chu, Y. H.; Liu, J.; Schlom, D. G.; Ramesh, R. A Strain-Driven Antiferroelectric-to-Ferroelectric Phase Transition in La-Doped BiFeO₃ Thin Films on Si. *Nano Lett.* 2017, 17, 5823–5829.
- (11) Yang, C. H.; Kan, D.; Takeuchi, I.; Nagarajan, V.; Seidel, J. Doping BiFeO₃: Approaches and Enhanced Functionality. *Phys. Chem. Chem. Phys.* 2012, 14, 15953–15962.
- (12) Campanini, M.; Erni, R.; Yang, C. H.; Ramesh, R.; Rossell, M. D. Periodic Giant Polarization Gradients in Doped BiFeO₃ Thin Films. *ACS Nanoletters* 2018, 18, 717–724.
- (13) Yang, C. H.; Seidel, J.; Kim, S. Y.; Rossen, P. B.; Yu, P.; Gajek, M.; Chu, Y. H.; Martin, L. W.; Holcomb, M. B.; He, Q.; Maksymovych, P.; Balke, N.; Kalinin, S. V.; Baddorf, A. P.; Basu, S. R.; Scullin, M. L.; Ramesh, R. Electric Modulation of Conduction in Multiferroic Ca-Doped BiFeO₃ Films. *Nat. Mater.* 2009, 8, 485–493.
- (14) Catalan, G.; Sardar, K.; Church, N. S.; Scott, J. F.; Harrison, R. J.; Redfern, S. A. T. Effect of Chemical Substitution on the Néel Temperature of Multiferroic Bi_{1-x}CaxFeO₃. *Phys. Rev. B* 2009, 79, 212415.
- (15) Khomchenko, V. A.; Pereira, L. C. J.; Paixão, J. A. Mn Substitution-Induced Revival of the Ferroelectric Antiferromagnetic Phase in Bi_{1-x}CaxFeO_{3-x/2} Multiferroics. *J. Mater. Sci.* 2015, 50, 1740–1745.
- (16) Bai, L.; Sun, M.; Ma, W.; Yang, J.; Zhang, J.; Liu, Y. Enhanced Magnetic Properties of Co-Doped BiFeO₃ Thin Films via Structural Progression. *Nanomaterials* 2020, 10, 1–13.
- (17) You, S.; Zhang, B. Enhanced Magnetic Properties of Cobalt-Doped Bismuth Ferrite Nanofibers. *Mater. Res. Express* 2020, 7.
- (18) Fan, Y.; Zhou, Y.; Shen, M.; Xu, X.; Wang, Z.; Mao, W.; Zhang, J.; Yang, J.; Pu, Y.; Li, X. Low-Spin Co³⁺ Make Great Contributions to the Magnetism of BiFeO₃. *J. Mater. Sci. Mater. Electron.* 2018, 29, 18593–18599.

- (19) Quan, C.; Han, Y.; Gao, N.; Mao, W.; Zhang, J.; Yang, J.; Li, X.; Huang, W. Comparative Studies of Pure, Ca-Doped, Co-Doped and Co-Doped BiFeO₃ Nanoparticles. *Ceram. Int.* 2015, 42, 537–544.
- (20) Bernardo, M. S. Synthesis, Microstructure and Properties of BiFeO₃-Based Multiferroic Materials: A Review. *Bol. la Soc. Esp. Ceram. y Vidr.* 2014, 53, 1–14.
- (21) Palai, R.; Katiyar, R. S.; Schmid, H.; Tissot, P.; Clark, S. J.; Robertson, J.; Redfern, S. A. T.; Catalan, G.; Scott, J. F. β Phase and γ - β Metal-Insulator Transition in Multiferroic BiFeO₃. *Phys. Rev. B.* 2008, 77, 014110.
- (22) Morozov, M. I.; Lomanova, N. A.; Gusarov, V. V. Specific Features of BiFeO₃ Formation in a Mixture of Bismuth(III) and Iron(III) Oxides. *Russ. J. Gen. Chem.* 2003, 73, 1676–1680.
- (23) Maître, A.; François, M.; Gachon, J. C. Experimental Study of the Bi₂O₃-Fe₂O₃ Pseudo-Binary System. *J. Phase Equilibria Diffus.* 2004, 25, 59–67.
- (24) Valant, M.; Axelsson, A. K.; Alford, N. Peculiarities of a Solid-State Synthesis of Multiferroic Polycrystalline BiFeO₃. *Chem. Mater.* 2007, 19, 5431–5436.
- (25) Hull, S.; Norberg, S. T.; Tucker, M. G.; Eriksson, S. G.; Mohn, C. E.; Stølen, S. Neutron Total Scattering Study of the Δ and β Phases of Bi₂O₃. *J. Chem. Soc. Dalton Trans.* 2009, 40, 8737–8745.
- (26) Koizumi, H.; Niizeki, N.; Ikeda, T. An X-Ray Study on Bi₂O₃-Fe₂O₃ System. *Jpn. J. Appl. Phys.* 1964, 3, 495–496.
- (27) Speranskaya, E. I.; Skorikov, V. M.; Rode, E. Y.; Terekhova, V. A. The Phase Diagram of the System Bismuth Oxide-Ferric Oxide. *Bull. Acad. Sci. USSR, Div. Chem. Sci.* 1965, 14, 873–874.
- (28) Lu, J.; Qiao, L. J.; Fu, P. Z.; Wu, Y. C. Phase Equilibrium of Bi₂O₃-Fe₂O₃ Pseudo-Binary System and Growth of BiFeO₃ Single Crystal. *J. Cryst. Growth* 2011, 318, 936–941.
- (29) Liu, H.; Yang, P.; Yao, K.; Ong, K. P.; Wu, P.; Wang, J. Origin of a Tetragonal BiFeO₃ Phase with a Giant *c/a* Ratio on SrTiO₃ Substrates. *Adv. Funct. Mater.* 2012, 22, 937–942.
- (30) Xie, L.; Li, L.; Heikes, C. A.; Zhang, Y.; Hong, Z.; Gao, P.; Nelson, C. T.; Xue, F.; Kioupakis, E.; Chen, L.; Schlom, D. G.; Wang, P.; Pan, X. Giant Ferroelectric Polarization in Ultrathin Ferroelectrics via Boundary-Condition Engineering. *Adv. Mater.* 2017, 29, 1–7.
- (31) Sando, D.; Young, T.; Bulanadi, R.; Cheng, X.; Zhou, Y.; Weyland, M.; Munroe, P.; Nagarajan, V. Designer Defect Stabilization of the Super Tetragonal Phase in >70-Nm-Thick BiFeO₃ Films on LaAlO₃ Substrates. *Jpn. J. Appl. Phys.* 2018, 57, 0902B2.
- (32) Sando, D.; Xu, B.; Bellaiche, L.; Nagarajan, V. A Multiferroic on the Brink: Uncovering the Nuances of Strain-Induced Transitions in BiFeO₃. *Appl. Phys. Rev.* 2016, 3, 011106.
- (33) Nakashima, S.; Fujisawa, H.; Kobune, M.; Shimizu, M.; Kotaka, Y. Growth and Local Structure of BiFeO₃ Thin Films with Giant Tetragonality on SrRuO₃-Buffered SrTiO₃(001) Substrate by Ion Beam Sputtering. *Jpn. J. Appl. Phys.* 2014, 53, 05FE05.
- (34) Béa, H.; Dupé, B.; Fusil, S.; Mattana, R.; Jacquet, E.; Warot-Fonrose, B.; Wilhelm, F.; Rogalev, A.; Petit, S.; Cros, V.; Anane, A.; Petroff, F.; Bouzouane, K.; Geneste, G.; Dkhil, B.; Lisenkov, S.; Ponomareva, I.; Bellaiche, L.; Bibes, M.; Barthélémy, A. Evidence for Room-Temperature Multiferroicity in a Compound with a Giant Axial Ratio. *Phys. Rev. Lett.* 2009, 102, 217603.
- (35) Chen, Z.; You, L.; Huang, C.; Qi, Y.; Wang, J.; Sritharan, T.; Chen, L. Nanoscale Domains in Strained

- Epitaxial BiFeO₃ Thin Films on LaSrAlO₄ Substrate. *Appl. Phys. Lett.* 2010, 96, 252903.
- (36) Mazumdar, D.; Shelke, V.; Iliev, M.; Jesse, S.; Kumar, A.; Kalinin, S. V.; Baddorf, A. P.; Gupta, A. Nanoscale Switching Characteristics of Nearly Tetragonal BiFeO₃ Thin Films. *Nano Lett.* 2010, 10, 2555–2561.
- (37) Iliev, M. N.; Abrashev, M. V.; Mazumdar, D.; Shelke, V.; Gupta, A. Polarized Raman Spectroscopy of Nearly Tetragonal BiFeO₃ Thin Films. *Phys. Rev. B.* 2010, 82, 1–5.
- (38) Huang, R.; Ding, H. C.; Liang, W. I.; Gao, Y. C.; Tang, X. D.; He, Q.; Duan, C. G.; Zhu, Z.; Chu, J.; Fisher, C. A. J.; Hirayama, T.; Ikuhara, Y.; Chu, Y. H. Atomic-Scale Visualization of Polarization Pinning and Relaxation at Coherent BiFeO₃/LaAlO₃ Interfaces. *Adv. Funct. Mater.* 2014, 24, 793–799.
- (39) Yun, K. Y.; Ricinschi, D.; Kanashima, T.; Noda, M.; Okuyama, M. Giant Ferroelectric Polarization beyond 150 MC/cm² in BiFeO₃ Thin Film. *Jpn. J. Appl. Phys.* 2004, 43, L647–L648.
- (40) Wang, J.; Neaton, J. B.; Zheng, H.; Nagarajan, V.; Ogale, S. B.; Liu, B.; Viehland, D.; Vaithyanathan, V.; Schlom, D. G.; Waghmare, U. V.; Spaldin, N. A.; Rabe, K. M.; Wuttig, M.; Ramesh, R. Epitaxial BiFeO₃ Multiferroic Thin Film Heterostructures. *Science* 2003, 299, 1719–1722.
- (41) Das, R. R.; Kim, D. M.; Baek, S. H.; Eom, C. B.; Zavaliche, F.; Yang, S. Y.; Ramesh, R.; Chen, Y. B.; Pan, X. Q.; Ke, X.; Rzechowski, M. S.; Streiffer, S. K. Synthesis and Ferroelectric Properties of Epitaxial BiFeO₃ Thin Films Grown by Sputtering. *Appl. Phys. Lett.* 2006, 88, 242904
- (42) Nelson, C. T.; Winchester, B.; Zhang, Y.; Kim, S. J.; Melville, A.; Adamo, C.; Folkman, C. M.; Baek, S. H.; Eom, C. B.; Schlom, D. G.; Chen, L. Q.; Pan, X. Spontaneous Vortex Nanodomain Arrays at Ferroelectric Heterointerfaces. *Nano Lett.* 2011, 11, 828–834.
- (43) Ivanov, Y. P.; Kubicek, M.; Siebenhofer, M.; Viernstein, A.; Hutter, H.; Fleig, J.; Chuvilin, A.; Zhang, Z. Strain-Induced Structure and Oxygen Transport Interactions in Epitaxial La_{0.6}Sr_{0.4}CoO_{3-δ} Thin Films. *Commun. Mater.* 2020, 1, 25.
- (44) Ivanov, Y. P.; Meylan, C. M.; Panagiotopoulos, N. T.; Georgarakis, K.; Greer, A. L. In-Situ TEM Study of the Crystallization Sequence in a Gold-Based Metallic Glass. *Acta Mater.* 2020, 196, 52–60.
- (45) Ivanov, Y. P.; Soltan, S.; Albrecht, J.; Goering, E.; Schütz, G.; Zhang, Z.; Chuvilin, A. The Route to Supercurrent Transparent Ferromagnetic Barriers in Superconducting Matrix. *ACS Nano* 2019, 13, 5655–5661.
- (46) Haselmann, U.; Suyolcu, Y. E.; Wu, P.; Ivanov, Y. P.; Knez, D.; Aken, P. A. Van; Chu, Y.; Zhang, Z. Negatively Charged In-Plane and Out-Of-Plane Domain Walls with Oxygen-Vacancy Agglomerations in a Ca-Doped Bismuth-Ferrite Thin Film. *ACS Appl. Electron. Mater.* 2021, 3 (10), 4498–4508.
- (47) Gubbens, A.; Barfels, M.; Trevor, C.; Twesten, R.; Mooney, P.; Thomas, P.; Menon, N.; Kraus, B.; Mao, C.; McGinn, B. The GIF Quantum, a next Generation Post-Column Imaging Energy Filter. *Ultramicroscopy* 2010, 110, 962–970.
- (48) Schlossmacher, P.; Klenov, D. O.; Freitag, B.; von Harrach, H. S. Enhanced Detection Sensitivity with a New Windowless XEDS System for AEM Based on Silicon Drift Detector Technology. *Microsc. Today* 2010, July, 14–20.
- (49) Campanini, M.; Erni, R.; Rossell, M. D. Probing Local Order in Multiferroics by Transmission Electron Microscopy. *Phys. Sci. Rev.* 2020, 5, 20190068.
- (50) Lichtert, S.; Verbeeck, J. Statistical Consequences of Applying a PCA Noise Filter on EELS Spectrum Images.

- Ultramicroscopy 2013, 125, 35–42.
- (51) Lucas, G.; Burdet, P.; Cantoni, M.; Hébert, C. Multivariate Statistical Analysis as a Tool for the Segmentation of 3D Spectral Data. *Micron* 2013, 52–53, 49–56.
- (52) Blochl, P. E. Projector Augmented-Wave Method. *Phys. Rev. B* 1994, 50, 17953.
- (53) Kresse, G.; Hafner, J. Ab Initio Molecular Dynamics for Liquid Metals. *J. Non. Cryst. Solids* 1993, 47, 558–561.
- (54) Kresse, G.; Hafner, J. Ab Initio Molecular-Dynamics Simulation of the Liquid-Metamorphous-Semiconductor Transition in Germanium. *Phys. Rev. B* 1994, 49, 14251–14269.
- (55) Kresse, G.; Furthmüller, J. Efficient Iterative Schemes for Ab Initio Total-Energy Calculations Using a Plane-Wave Basis Set. *Phys. Rev. B* 1996, 54, 11169–11186.
- (56) Kresse, G.; Joubert, D. From Ultrasoft Pseudopotentials to the Projector Augmented-Wave Method. *Phys. Rev. B* 1999, 59, 1758.
- (57) Perdew, J. P.; Ruzsinszky, A.; Csonka, G. I.; Vydrov, O. A.; Scuseria, G. E.; Constantin, L. A.; Zhou, X.; Burke, K. Restoring the Density-Gradient Expansion for Exchange in Solids and Surfaces. *Phys. Rev. Lett.* 2008, 100, 136406.
- (58) Dudarev, S. L.; Botton, G. A.; Savrasov, S. Y.; Humphreys, C. J.; Sutton, A. P. Electron-Energy-Loss Spectra and the Structural Stability of Nickel Oxide: An LSDA+U Study. *Phys. Rev. B* 1998, 57, 1505.
- (59) Shenton, J. K.; Bowler, D. R.; Cheah, W. L. Effects of the Hubbard U on Density Functional-Based Predictions of BiFeO₃ Properties. *J. Phys. Condens. Matter* 2017, 29, 445501.
- (60) Chen, C.; Lv, S.; Li, J.; Wang, Z.; Liang, X.; Li, Y.; Viehland, D.; Nakajima, K.; Ikuhara, Y. Two-Dimensional Electron Gas at the Ti-Diffused BiFeO₃/SrTiO₃ Interface. *Appl. Phys. Lett.* 2015, 107, 031601.
- (61) Haselmann, U.; Haberfehlner, G.; Pei, W.; Popov, M. N.; Romaner, L.; Knez, D.; Chen, J.; Ghasemi, A.; He, Y.; Kothleitner, G.; Zhang, Z. Study on Ca Segregation toward an Epitaxial Interface between Bismuth Ferrite and Strontium Titanate. *ACS Appl. Mater. Interfaces* 2020, 12, 12264–12274.
- (62) Kubel, F.; Schmid, H. Structure of a Ferroelectric and Ferroelastic Monodomain Crystal of the Perovskite BiFeO₃. *Acta Crystallogr. Sect. B* 1990, 46, 698–702.
- (63) MacLaren, I.; Wang, L.; Morris, O.; Craven, A. J.; Stamps, R. L.; Schaffer, B.; Ramasse, Q. M.; Miao, S.; Kalantari, K.; Sterianou, I.; Reaney, I. M. Local Stabilisation of Polar Order at Charged Antiphase Boundaries in Antiferroelectric (Bi_{0.85}Nd_{0.15})(Ti_{0.1}Fe_{0.9})O₃. *APL Mater.* 2013, 1, No. 021102.
- (64) Zhang, J. X.; He, Q.; Trassin, M.; Luo, W.; Yi, D.; Rossell, M. D.; Yu, P.; You, L.; Wang, C. H.; Kuo, C. Y.; Heron, J. T.; Hu, Z.; Zeches, R. J.; Lin, H. J.; Tanaka, A.; Chen, C. T.; Tjeng, L. H.; Chu, Y. H.; Ramesh, R. Microscopic Origin of the Giant Ferroelectric Polarization in Tetragonal-like BiFeO₃. *Phys. Rev. Lett.* 2011, 107, 147602.
- (65) Campanini, M.; Trassin, M.; Ederer, C.; Erni, R.; Rossell, M. D. Buried In-Plane Ferroelectric Domains in Fe-Doped Single-Crystalline Aurivillius Thin Films. *ACS Appl. Electron. Mater.* 2019, 1, 1019–1028.
- (66) Hallstedt, B.; Risold, D.; Gauckler, L. J. Thermodynamic Assessment of the Bismuth-Calcium-Oxygen Oxide System. *J. Am. Ceram. Soc.* 1997, 80, 2629–2636.
- (67) Hidayat, T.; Shishin, D.; Decterov, S. A.; Jak, E. Thermodynamic Optimization of the Ca-Fe-O System. *Metall. Mater. Trans. B* 2016, 47, 256–281.

Publication C – Supporting Information

Ca Solubility in a BiFeO₃ Based System with a Secondary Bi₂O₃ Phase on a Nanoscale

Ulrich Haselmann¹, Thomas Radlinger², Weijie Pei³, Maxim N. Popov⁴, Tobias Spitaler⁵, Lorenz Romaner^{4,5}, Yurii P. Ivanov^{6,7}, Jian Chen³, Yunbin He^{*3}, Gerald Kothleitner^{2,8} and Zaoli Zhang^{*1,9}

1 Erich Schmid Institute of Materials Science, Austrian Academy of Sciences, 8700 Leoben, Austria

2 Institute for Electron Microscopy and Nanoanalysis, Graz University of Technology, 8010 Graz, Austria

3 School of Materials Science & Engineering, Hubei University, 430062 Wuhan, Hubei, China

4 Materials Center Leoben Forschung GmbH, 8700 Leoben, Austria

5 Department of Materials Science, Montanuniversität Leoben, 8700 Leoben, Austria

6 Department of Materials Science & Metallurgy, University of Cambridge, Cambridge CB3 0FS, U.K.

7 School of Natural Sciences, Far Eastern Federal University, 690950 Vladivostok, Russia

8 Graz Centre for Electron Microscopy, Austrian Cooperative Research, 8700 Graz, Austria

9 Institute of Material Physics, Montanuniversität Leoben, 8700 Leoben, Austria

***Corresponding authors:** zaoli.zhang@oeaw.ac.at, ybhe@hubu.edu.cn

In Table. S1 shows complementary imaging parameters of the HAADF and analytical data, which have not been mentioned in section 2. *Experimental and Calculation Details* in subsection 2.2. *Data acquisition.*

Table. S1. Complementary imaging parameters of the STEM data.

	collection angle [mrad]	pixel time [μ s]	step size [pm]	scanning-frame size [pixel*pixel]
Figure 1a	49-242	0.95	11	2048 * 2048
Figure 1d	62-214	0.57	11	2048 * 2048
Figure 2	49-242	0.14	3.1	4096 * 4096
Figure 3a	117-177	11.4	65	512 * 512
Figure 3b	117-177	10^5	91	20 * 83
Figure 4a	124-200	30	17	121 * 357
Figure S1a	117-177	11.4	46	512 * 512
Figure S1b	117-177	10^5	92	26 * 72
Figure S2a	124-200	40	17	157 * 581
Figure S3a	39-200	2.5	4.24	2048 * 2048
Figure S3b	10-37	2.5	4.24	2048 * 2048

Figure S1 and Figure S2 show elemental maps of the BCFCO-STO interface. Figure S1a shows a HAADF survey image with the area from where the spectrum images were taken indicated by the white rectangle. Figure S1b shows the HAADF image recorded simultaneously during the mapping. The areal density elemental maps Ca, Ti, Fe, and Ti combined with Fe can be seen in Figure S1c, d, e, and f. Figure S2a shows the HAADF image of the area of the EDS maps. The maps of the elemental ratios of the single elements and in some combinations can be seen in Figure S2b-j. Figure S1 and Figure S2 demonstrate that the interface between the substrate and the film is sharp and well defined.

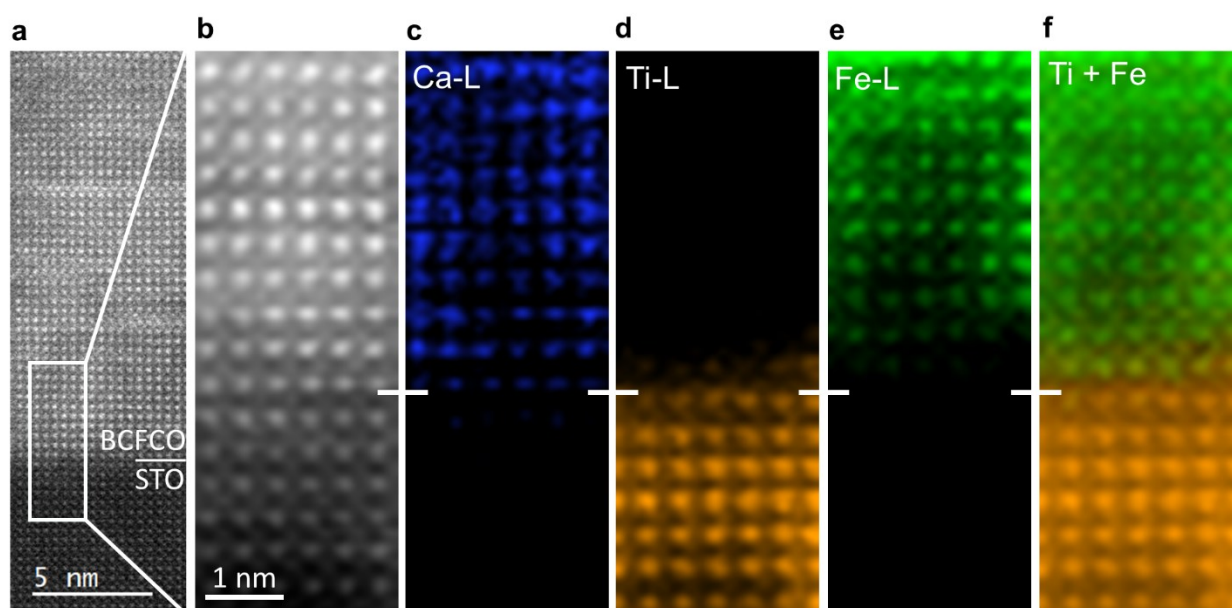


Figure S1. EELS elemental map of the interface between the BCFCO film and the STO substrate. (a) HAADF survey image of the interface area. The white rectangle indicates the area of the EELS elemental map. (b) Simultaneous HAADF image during mapping. EELS elemental maps of (c) Ca-L, (d) Ti-L, (e) Fe-L, and (f) Ti and Fe combined. The white lines indicate the interface.

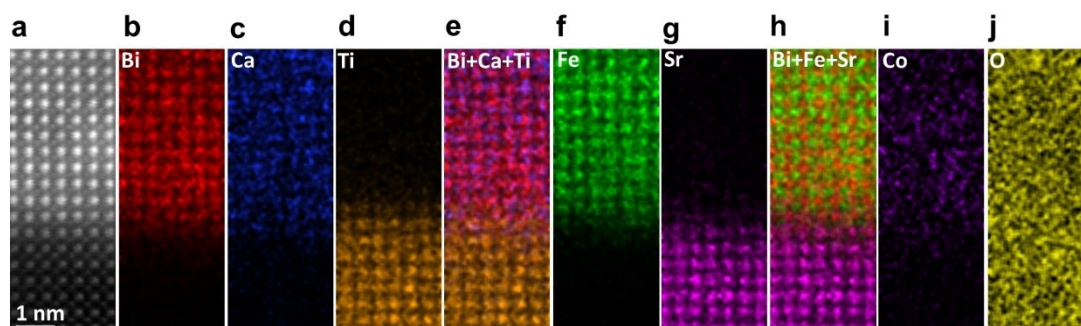


Figure S2. EDS elemental ratio map of the interface between the BCFCO film and the STO substrate. (a) HAADF image of the EDS mapping area. EDS elemental ratio maps of (b) Bi, (c) Ca, (d) Ti, (e) Bi, Ca and Ti combined, (f) Fe, (g) Sr, (h) Bi, Fe, and Sr combined, (i) Co, and (j) O.

In Figure S3, the example of a BO plate acting as a domain wall can be seen. Figure S3a show the HAADF image with the location of the BO plate in the image marked on the left and right side. The BO plate divides the $\text{Bi}_{0.8}\text{Ca}_{0.2}\text{Fe}_{0.95}\text{Mg}_{0.05}\text{O}_3$ film (grown on a STO substrate) in a top and bottom area. The vector plot of the electric field¹ retrieved from the DPC signal in Figure S3b shows that in the top area above the BO plate, the ferroelectric polarization has a different orientation than in the bottom area below the plate. Therefore, the BO plate is the domain wall where the orientation changes.

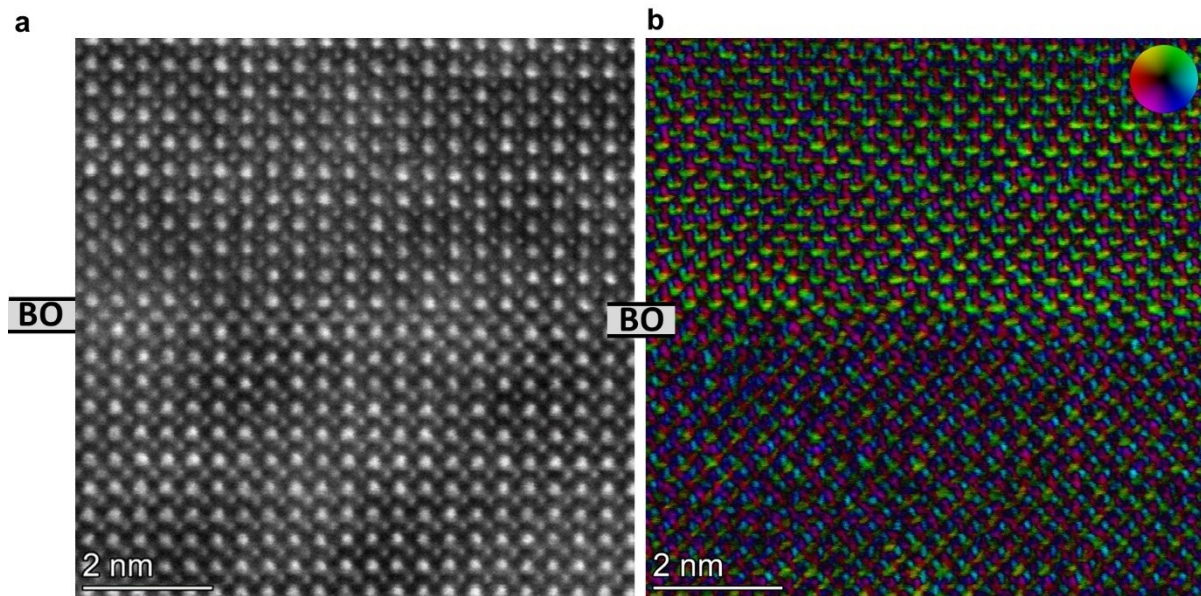


Figure S3. DPC analysis of the ferroelectric polarization at a BO plate, which acts as a domain wall (a) HAADF STEM image of the BO plate and the area around it. The location of the BO plate is marked on the left and right side. (b) vector plot of the electric field retrieved from the DPC signal showing the two ferroelectric domains above and below the BO plate.

Figure S4a and b show that the secondary BO phase can't be detected in the XRD data of the BCFCO film. Figure S4c shows a topographic AFM image of the BCFCO film surface with a root mean square (RMS) value of 4 nm.

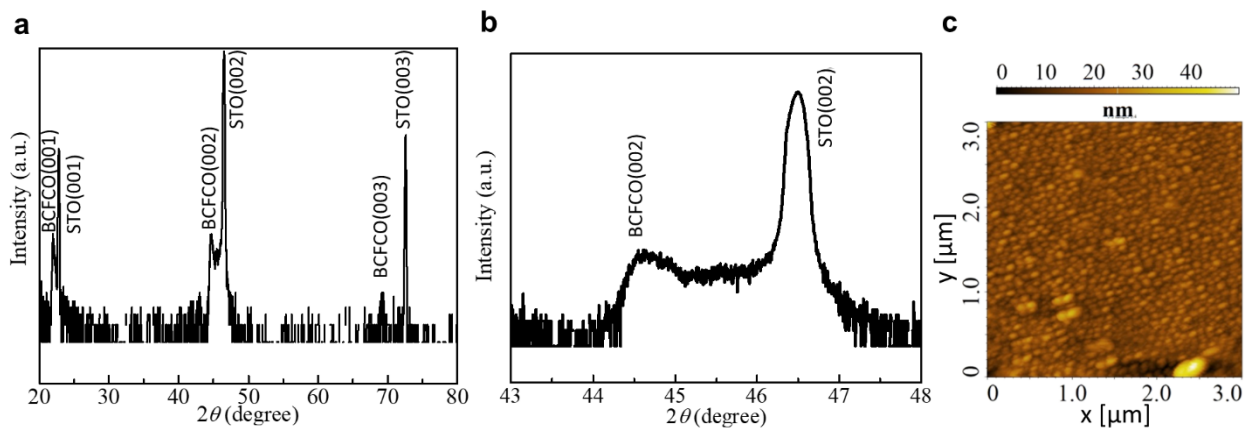


Figure S4. (a), (b) XRD data of the BCFCO film. (c) topographic AFM image of the BCFCO film surface.

References

- (1) Campanini, M.; Erni, R.; Rossell, M. D. Probing Local Order in Multiferroics by Transmission Electron Microscopy. *Phys. Sci. Rev.* 2020, 5, 20190068.

8. Appendix

The two Matlab Script used for data analysis of publication B can be found below – one for in-plane defects and one for out-of-plane defects:

For analysis of in-plane defects:

```
clear all;
close all;
M=load('addcsvfilenamehere.csv'); %here type in the csv file name
[x,b]=size(M);
%Add the number of lines on the A-site
a=xx; %Add the number of A-sites in [100] and [001] direction, which
must be the same (square image area necessary).

c=floor(x/(a-0.5));
M3=nan(a,b,c);
Msort=a*ones(a,c);
m=1;

[h,s1]=sort(M(:,2));
M=M(s1,:);

%Can't get this variant to work
%for k=1:c
%   if mod(k,2)==1, [h,Msort(:,k)]=sort(M(m:(m+13-1),3));
H=M(m:(m+13-1),:); M3(:, :, k)=H(Msort(:,k),:); m=m+13;
%   else
%       [h,Msort(1:end-1,k)]=sort(M(m:(m+12-1),3));
H=M(m:(m+12-1),:); M3(1:end-1, :, k)=H(Msort(1:end-1,k));...
%       m=m+12;
%   end
%end

for k=1:c
    if mod(k,2)==1, [h,Msort(:,k)]=sort(M(m:(m+a-1),3));
M3(:, :, k)=M(m:(m+a-1),:); m=m+a;
    else
        [h,Msort(1:end-1,k)]=sort(M(m:(m+a-2),3));
M3(1:end-1, :, k)=M(m:(m+a-2),:); m=m+a-1;
    end
end

for k=1:c
    H=M3(:, :, k); s=Msort(:,k); H=H(s,:); M3(:, :, k)=H;
end

%Transformation of x,y and I values in Matrices with the according
%positions.

%cordinates and intensities for A-site cations
cA=ceil(c/2);
XA=nan(a,cA);
YA=XA;
```

```

IA=YA;

for m=1:a
    n=1;
    for k=1:2:c
        XA(m,n)=M3(m,2,k);
        YA(m,n)=M3(m,3,k);
        IA(m,n)=M3(m,6,k);
        n=n+1;
    end
end

%coordinates and intensities for B-site cations
cB=cA-1;
aB=a-1;
XB=nan(aB,cB);
YB=XB;
IB=YB;

for m=1:aB
    n=1;
    for k=2:2:c
        XB(m,n)=M3(m,2,k);
        YB(m,n)=M3(m,3,k);
        IB(m,n)=M3(m,6,k);
        n=n+1;
    end
end

%center of gravity for quadruplet of A-site cations
XAG=nan(aB,cB);
YAG=XAG;
for m=1:aB
    for n=1:cB
        H=XA([m,m+1],[n,n+1]);
        XAG(m,n)=mean(H(:));
        H=YA([m,m+1],[n,n+1]);
        YAG(m,n)=mean(H(:));
    end
end

%polarization vector and plotting
figure('Name','Polarization');
dx=XAG-XB; dy=YAG-YB;
hold on
quiver(XAG(:),YAG(:),dx(:),dy(:));
pointsize = 30;
scatter(XA(:), YA(:), pointsize, IA(:),'filled');
colormap jet;
%scatter(XB(:), YB(:), pointsize, IB(:),'filled');
v = colorbar;
v.Label.String = 'A-site intensity [counts]';
axis equal;
xlim([0,max(M(:,2))+0.5]); ylim([0,max(M(:,3))+0.5]);
hold off;

%Plotting displacement (Polarization) in x and y direction
figure('Name','x and y displacement of Fe atom')

```

```

mdx=mean(dx,2);
sdx=std(dx,[],2);
mdy=mean(dy,2);
sdy=std(dy,[],2);
errorbar(mdx,[1:length(mdx)]+0.5,sdx,'bx-','horizontal');
hold on
errorbar(mdy,[1:length(mdy)]+0.5,sdy,'mx-','horizontal');
plot([0,0],[1.5,length(mdx)+0.5],'--','Color',[0.66 0.66 0.66]);
hold off
legend('x-displacement','y displacement','Location','South');

%lattice spacing in differently styled plot

%Map of A-A spacing in x direction
figure('Name','Map of A-A spacing in x direction');
XAA=diff(XA,[],2);
[m1,n1]=size(XAA);
[M1,N1]=meshgrid(1:n1,1:m1);
scatter(M1(:), N1(:), 300, XAA(:),'filled','s');
v = colorbar;
v.Label.String = 'A-A spacing in x-direction [nm]';
axis equal;
xlim([0.5,n1+0.5]); ylim([0.5,m1+0.5]);

%Map of A-A spacing in y-direction
figure('Name','Map of A-A spacing in y-direction');
YAA=diff(YA,[],1);
[m1,n1]=size(YAA);
[M1,N1]=meshgrid(1:n1,1:m1);
scatter(M1(:), N1(:), 300, YAA(:),'filled','s');
v = colorbar;
v.Label.String = 'A-A spacing in y-direction [nm]';
axis equal;
xlim([0.5,n1+0.5]); ylim([0.5,m1+0.5]);

%calculation lattice expansion
MeanXAA=mean(mean(XAA));
MeanYAA=mean(YAA,2);
def=mean(MeanYAA([8]))
non_def=mean(MeanYAA([1:7,9:end]))
ratio_def=def/MeanXAA
ratio_non_def=non_def/MeanXAA
ratio=def/non_def

%Map of B-B spacing in x direction
figure('Name','Map of B-B spacing in x direction');
XBB=diff(XB,[],2);
[m1,n1]=size(XBB);
[M1,N1]=meshgrid(1:n1,1:m1);
scatter(M1(:), N1(:), 300, XBB(:),'filled','s');
colormap hot;
v = colorbar;
v.Label.String = 'B-B spacing in x-direction [nm]';
axis equal;
xlim([0.5,n1+0.5]); ylim([0.5,m1+0.5]);

```

```

%Map of B-B spacing in y direction
figure('Name','Map of B-B spacing in y direction');
YBB=diff(YB,[],1);
[m1,n1]=size(YBB);
[M1,N1]=meshgrid(1:n1,1:m1);
scatter(M1(:), N1(:), 300, YBB(:),'filled','s');
colormap hot;
v = colorbar;
v.Label.String = 'B-B spacing in y-direction [nm]';
axis equal;
xlim([0.5,n1+0.5]); ylim([0.5,m1+0.5]);

%return;

%PLOTS - Data display
%LOTS OF FOR LOOPS

%Plot interatomic A-site distances along vertical rows
figure('Name','Plot interatomic A-site distances along vertical
rows');
m=1;
x1=ceil(sqrt(ceil(c/2)));
for k=1:2:c
    d=diff(M3(:,3,k));
    subplot(x1,x1,m);
    plot(1:a-1,d,'b');
    ylim([0.4,0.6]);
    title(mean(d)); m=m+1;
end

%Plot interatomic A-site distances along horizontal rows

figure('Name','Plot interatomic A-site INTENSITIES and distances along
horizontal rows');
m=1;
D_HOR=[];
I_HOR=[]; %Horizontal Intensity
x2=ceil(sqrt(a));
for l = 1:a
    d_hor=[];
    i_hor=[];
    for k = 1:2:c
        d_hor=cat(1,d_hor,M3(l,2,k));
        i_hor=cat(1,i_hor,M3(l,6,k));
    end
    d=diff(d_hor);
    subplot(x2,x2,m);
    plot(1:length(1:2:c)-1,d,'g');
    ylim([0.4,0.6]);
    title(mean(d)); m=m+1;
    D_HOR=cat(2,D_HOR,d_hor);
    I_HOR=cat(2,I_HOR,i_hor);
end

figure('Name','A-site intensity averaged along x direction');
ix_plot=mean(I_HOR);

```



```

ix_std=std(I_HOR);
y4=1:length(ix_plot);
errorbar(ix_plot,y4,ix_std,'ro-','horizontal');

%Plot interatomic A- and B-site INTENSITIES and distances along
horizontal rows

figure('Name','Plot interatomic B-site distances along horizontal
rows');
m=1;
D_HORB=[];
I_HORB=[]; %Horizontal Intensity
x2=ceil(sqrt(a));
for l = 1:a
    d_hor=[];
    i_hor=[];
    for k = 2:2:c
        d_hor=cat(1,d_hor,M3(l,2,k));
        i_hor=cat(1,i_hor,M3(l,6,k));
    end
    d=diff(d_hor);
    subplot(x2,x2,m);
    plot(1:length(2:2:c)-1,d,'m');
    ylim([0.4,0.6]);
    title(mean(d)); m=m+1;
    D_HORB=cat(2,D_HORB,d_hor);
    I_HORB=cat(2,I_HORB,i_hor);
end

figure('Name','A and B-site intensity averaged along x direction');
ix_plotb=mean(I_HORB);
ix_stdb=std(I_HORB);
ix_plotb=ix_plotb(1:end-1);
ix_stdb=ix_stdb(1:end-1);

y4b=1:length(ix_plotb);
y4b=y4b+0.5;
errorbar(ix_plot,y4,ix_std,'ro-','horizontal');
hold on
errorbar(ix_plotb,y4b,ix_stdb,'go-','horizontal');
plot([mean(ix_plot),mean(ix_plot)], [y4(1),y4(end)], '--','Color',[0.66
0.66 0.66]);
plot([mean(ix_plotb),mean(ix_plotb)], [y4b(1),y4b(end)], '--
','Color',[0.66 0.66 0.66]);
hold off
legend('A-site intensities','B-site intensities','Location','North');

% %Plot interatomic A-site intensities along vertical rows
% figure('Name','Test');
% m=1;
% for k=1:2:c
%     int=M3(:,6,k);%/(10^7);
%     subplot(x1,x1,m);

```

Appendix

```
%      plot(1:a,int,'r');
%      m=m+1;
% end

%Plot only intensity on both sites
figure('Name','Intensities on A and B sites');
pointsize = 40;
scatter(M(:,2), M(:,3), pointsize, M(:,6), 'filled');
colormap jet;
v = colorbar;
v.Label.String = 'Intensities on A and B sites [counts]';
axis equal;
xlim([0,max(M(:,2))+0.5]); ylim([0,max(M(:,3))+0.5]);

M2_B=[];

for k=2:2:c
    M2_B=cat(1,M2_B,M3(:, :, k));
end

M2_A=[];

for k=1:2:c
    M2_A=cat(1,M2_A,M3(:, :, k));
end

%Plot intensity only on A-sites
figure('Name','Intensities on A sites')
pointsize = 60;
scatter(M2_A(:,2), M2_A(:,3), pointsize, M2_A(:,6), 'filled');
colormap jet;
v = colorbar;
v.Label.String = 'Intensities only on A [counts]';
axis equal;
xlim([0,max(M(:,2))+0.5]); ylim([0,max(M(:,3))+0.5]);

%Plot intensity only on B-sites
figure('Name','Intensities on B sites')
pointsize = 60;
scatter(M2_B(:,2), M2_B(:,3), pointsize, M2_B(:,6), 'filled');
colormap jet;
v = colorbar;
v.Label.String = 'Intensities only on B [counts]';
axis equal;
xlim([0,max(M(:,2))+0.5]); ylim([0,max(M(:,3))+0.5]);
```

For analysis of out-of-plane defects:

```

clear all;
close all;
M=load('addcsvfilenamehere');%here type in the csv file name

%Add the number of lines on the A-site
a=xx; %Add the number of A-sites in [100] and [001] direction, which
must be the same (square image area necessary).
%Add the dimension where it should be averaged for the input
parameters
dim=1;

[x,b]=size(M);
c=floor(x/(a-0.5));
M3=nan(a,b,c);
Msort=a*ones(a,c);
m=1;

[h,s1]=sort(M(:,2));
M=M(s1,:);

%Doesn't get this variant to work.
%for k=1:c
%   if mod(k,2)==1, [h,Msort(:,k)]=sort(M(m:(m+13-1),3));
H=M(m:(m+13-1),:); M3(:, :, k)=H(Msort(:,k),:); m=m+13;
%   else
%       [h,Msort(1:end-1,k)]=sort(M(m:(m+12-1),3));
H=M(m:(m+12-1),:); M3(1:end-1, :, k)=H(Msort(1:end-1,k));...
%       m=m+12;
%   end
%end

for k=1:c
    if mod(k,2)==1, [h,Msort(:,k)]=sort(M(m:(m+a-1),3));
M3(:, :, k)=M(m:(m+a-1),:); m=m+a;
    else
        [h,Msort(1:end-1,k)]=sort(M(m:(m+a-2),3));
M3(1:end-1, :, k)=M(m:(m+a-2),:); m=m+a-1;
    end
end

for k=1:c
    H=M3(:, :, k); s=Msort(:,k); H=H(s,:); M3(:, :, k)=H;
end

%Transformation of x,y and I values in Matrices with the according
%positions.

%coordinates and intensities for A-site cations
cA=ceil(c/2);
XA=nan(a,cA);
YA=XA;
IA=YA;

for m=1:a
    n=1;
    for k=1:2:c

```

```

        XA(m,n)=M3(m,2,k);
        YA(m,n)=M3(m,3,k);
        IA(m,n)=M3(m,6,k);
        n=n+1;
    end
end

%coordinates and intensities for B-site cations
cB=cA-1;
aB=a-1;
XB=nan(aB,cB);
YB=XB;
IB=YB;

for m=1:aB
    n=1;
    for k=2:2:c
        XB(m,n)=M3(m,2,k);
        YB(m,n)=M3(m,3,k);
        IB(m,n)=M3(m,6,k);
        n=n+1;
    end
end

%center of gravity for quadruplet of A-site cations
XAG=nan(aB,cB);
YAG=XAG;
for m=1:aB
    for n=1:cB
        H=XA([m,m+1],[n,n+1]);
        XAG(m,n)=mean(H(:));
        H=YA([m,m+1],[n,n+1]);
        YAG(m,n)=mean(H(:));
    end
end

%polarization vector and plotting
figure('Name','Polarization');
dx=XAG-XB; dy=YAG-YB;
hold on
quiver(XAG(:),YAG(:),dx(:),dy(:));
pointsize = 30;
scatter(XA(:), YA(:), pointsize, IA(:),'filled');
colormap jet;
%scatter(XB(:), YB(:), pointsize, IB(:),'filled');
v = colorbar;
v.Label.String = 'A-site intensity [counts]';
axis equal;
xlim([0,max(M(:,2))+0.5]); ylim([0,max(M(:,3))+0.5]);
hold off;

%Plotting displacement (Polarization) in x (in-plane) and z (out-of-
plane) direction
figure('Name','x and y displacement of Fe atom')
mdx=mean(dx,dim);
sdx=std(dx,[],dim);
mdy=mean(dy,dim);
sdy=std(dy,[],dim);

```

```

errorbar([1:length(mdx)]+0.5,mdx,sdx,'bx-','horizontal');
hold on
errorbar([1:length(mdy)]+0.5,mdy,sdy,'mx-','horizontal');
plot([1.5,length(mdx)+0.5],[0,0],'--','Color',[0.66 0.66 0.66]);
hold off
legend('x-displacement','y displacement','Location','South');

%lattice spacing in differently styled plot

%Map of A-A spacing in x direction
figure('Name','Map of A-A spacing in x direction');
XAA=diff(XA,[],2);
[m1,n1]=size(XAA);
[M1,N1]=meshgrid(1:n1,1:m1);
scatter(M1(:), N1(:), 300, XAA(:),'filled','s');
v = colorbar;
v.Label.String = 'A-A spacing in x-direction [nm]';
axis equal;
xlim([0.5,n1+0.5]); ylim([0.5,m1+0.5]);

%Map of A-A spacing in y-direction
figure('Name','Map of A-A spacing in y-direction');
YAA=diff(YA,[],1);
[m1,n1]=size(YAA);
[M1,N1]=meshgrid(1:n1,1:m1);
scatter(M1(:), N1(:), 300, YAA(:),'filled','s');
v = colorbar;
v.Label.String = 'A-A spacing in y-direction [nm]';
axis equal;
xlim([0.5,n1+0.5]); ylim([0.5,m1+0.5]);

%calculation lattice expansion
MeanYAA=mean(mean(YAA));
MeanXAA=mean(XAA,dim);
def=MeanXAA(7)
non_def=mean(MeanXAA([1:6,8:end]))
ratio_def=def/MeanYAA
ratio_non_def=non_def/MeanYAA
ratio=def/non_def

%Map of B-B spacing in x direction
figure('Name','Map of B-B spacing in x direction');
XBB=diff(XB,[],2);
[m1,n1]=size(XBB);
[M1,N1]=meshgrid(1:n1,1:m1);
scatter(M1(:), N1(:), 300, XBB(:),'filled','s');
colormap hot;
v = colorbar;
v.Label.String = 'B-B spacing in x-direction [nm]';
axis equal;
xlim([0.5,n1+0.5]); ylim([0.5,m1+0.5]);

%Map of B-B spacing in y direction
figure('Name','Map of B-B spacing in y direction');
YBB=diff(YB,[],1);
[m1,n1]=size(YBB);
[M1,N1]=meshgrid(1:n1,1:m1);
scatter(M1(:), N1(:), 300, YBB(:),'filled','s');

```

```

colormap hot;
v = colorbar;
v.Label.String = 'B-B spacing in y-direction [nm]';
axis equal;
xlim([0.5,n1+0.5]); ylim([0.5,m1+0.5]);

%return;

%PLOTS - Data display
%LOTS OF FOR LOOPS

%Plot interatomic A-site distances along vertical rows
figure('Name','Plot interatomic A-site distances along vertical
rows');
m=1;
D_VER=[];
I_VER=[];
x1=ceil(sqrt(ceil(c/2)));
for k=1:2:c
    d=diff(M3(:,3,k));
    subplot(x1,x1,m);
    plot(1:a-1,d,'b');
    ylim([0.4,0.6]);
    title(mean(d)); m=m+1;
    D_VER=cat(2,D_VER,M3(:,3,k));
    I_VER=cat(2,I_VER,M3(:,6,k));
end

% %Plot interatomic A-site distances along vertical rows
% figure('Name','Plot interatomic A-site distances along vertical
% rows');
% m=1;
% x1=ceil(sqrt(ceil(c/2)));
% for k=1:2:c
%     d=diff(M3(:,3,k));
%     subplot(x1,x1,m);
%     plot(1:a-1,d,'b');
%     ylim([0.4,0.6]);
%     title(mean(d)); m=m+1;
% end

%Plot interatomic A-site distances along horizontal rows

figure('Name','Plot interatomic A-site distances along horizontal
rows');
m=1;
D_HOR=[];
I_HOR=[]; %Horizontal Intensity
x2=ceil(sqrt(a));
for l = 1:a
    d_hor=[];
    i_hor=[];
    for k = 1:2:c
        d_hor=cat(1,d_hor,M3(l,2,k));
        i_hor=cat(1,i_hor,M3(l,6,k));
    end
end

```

```

end
d=diff(d_hor);
subplot(x2,x2,m);
plot(1:length(1:2:c)-1,d,'g');
ylim([0.4,0.6]);
title(mean(d)); m=m+1;
D_HOR=cat(2,D_HOR,d_hor);
I_HOR=cat(2,I_HOR,i_hor);
end

%Plot interatomic B-site distances and Intensities along vertical rows
figure('Name','Plot interatomic B-site distances along vertical
rows');
m=1;
D_VERB=[];
I_VERB=[];
x1=ceil(sqrt(ceil(c/2)));
for k=2:2:c
    d=diff(M3(:,3,k));
    subplot(x1,x1,m);
    plot(1:a-1,d,'b');
    ylim([0.4,0.6]);
    title(mean(d)); m=m+1;
    D_VERB=cat(2,D_VERB,M3(:,3,k));
    I_VERB=cat(2,I_VERB,M3(:,6,k));
end

%Plot interatomic B-site distances along horizontal rows
figure('Name','Plot interatomic B-site distances along horizontal
rows');
m=1;
D_HORB=[];
I_HORB=[]; %Horizontal Intensity
x2=ceil(sqrt(a));
for l = 1:a
    d_hor=[];
    i_hor=[];
    for k = 2:2:c
        d_hor=cat(1,d_hor,M3(l,2,k));
        i_hor=cat(1,i_hor,M3(l,6,k));
    end
    d=diff(d_hor);
    subplot(x2,x2,m);
    plot(1:length(2:2:c)-1,d,'m');
    ylim([0.4,0.6]);
    title(mean(d)); m=m+1;
    D_HORB=cat(2,D_HORB,d_hor);
    I_HORB=cat(2,I_HORB,i_hor);
end

figure('Name','A and B-site intensity averaged along z direction');
%A-sites
ix_plot=mean(I_VER);
ix_std=std(I_VER);
y4=1:length(ix_plot);

```

```

%B-sites
%only with Z-direction defects
I_VERB=I_VERB(1:end-1,:);
ix_plotb=mean(I_VERB);
ix_stdb=std(I_VERB);
%only with x-direction defects
%ix_plotb=ix_plotb(1:end-1);
%ix_stdb=ix_stdb(1:end-1);

y4b=1:length(ix_plotb);
y4b=y4b+0.5;

%FOR Z-DIRECTION
errorbar(y4,ix_plot,ix_std,'ro-'); %'horizontal' if rotated
hold on
errorbar(y4b,ix_plotb,ix_stdb,'go-'); %'horizontal' if rotated
plot([y4(1),y4(end)],[mean(ix_plot),mean(ix_plot)],'--','Color',[0.66
0.66 0.66]);
plot([y4b(1),y4b(end)],[mean(ix_plotb),mean(ix_plotb)],'--
','Color',[0.66 0.66 0.66]);
hold off
legend('A-site intensities','B-site intensities','Location','West');

% %FOR X DIRECTION
% errorbar(ix_plot,y4,ix_std,'ro-','horizontal');
% hold on
% errorbar(ix_plotb,y4b,ix_stdb,'go-','horizontal');
% plot([mean(ix_plot),mean(ix_plot)],[y4(1),y4(end)],'--
','Color',[0.66 0.66 0.66]);
% plot([mean(ix_plotb),mean(ix_plotb)],[y4b(1),y4b(end)],'--
','Color',[0.66 0.66 0.66]);
% hold off
% legend('A-site intensities','B-site
intensities','Location','North');

% %Plot interatomic A-site intensities along vertical rows
% figure('Name','Test');
% m=1;
% for k=1:2:c
%     int=M3(:,6,k);%/(10^7);
%     subplot(x1,x1,m);
%     plot(1:a,int,'r');
%     m=m+1;
% end

%Plot only intensity on both sites
figure('Name','Intensities on A and B sites');
pointsize = 40;
scatter(M(:,2), M(:,3), pointsize, M(:,6),'filled');
colormap jet;
v = colorbar;
v.Label.String = 'Intensities on A and B sites [counts]';
axis equal;
xlim([0,max(M(:,2))+0.5]); ylim([0,max(M(:,3))+0.5]);

```



```
M2_B=[];

for k=2:2:c
    M2_B=cat(1,M2_B,M3(:,:,k));
end

M2_A=[];

for k=1:2:c
    M2_A=cat(1,M2_A,M3(:,:,k));
end

%Plot intensity only on A-sites
figure('Name','Intensities on A sites')
pointsize = 60;
scatter(M2_A(:,2), M2_A(:,3), pointsize, M2_A(:,6), 'filled');
colormap jet;
v = colorbar;
v.Label.String = 'Intensities only on A [counts]';
axis equal;
xlim([0,max(M(:,2))+0.5]); ylim([0,max(M(:,3))+0.5]);

%Plot intensity only on B-sites
figure('Name','Intensities on B sites')
pointsize = 60;
scatter(M2_B(:,2), M2_B(:,3), pointsize, M2_B(:,6), 'filled');
colormap jet;
v = colorbar;
v.Label.String = 'Intensities only on B [counts]';
axis equal;
xlim([0,max(M(:,2))+0.5]); ylim([0,max(M(:,3))+0.5]);
```